Unraveling Barite Scale Crystallization Mechanisms In The Presence Of Polyprotic Acids

by

Ricardo David Sosa

A Dissertation submitted to the William A. Brookshire Department of Chemical and Biomolecular Engineering, University of Houston

in partial fulfillment of the requirements for the degree of

Doctor of Philosophy

in Chemical and Biomolecular Engineering

Chair of Committee: Dr. Jeffrey D. Rimer

Committee Member: Dr. Jacinta C. Conrad

Committee Member: Dr. Jeremy C. Palmer

Committee Member: Dr. Michael A. Reynolds

Committee Member: Dr. Allan J. Jacobson

University of Houston
August 2021

Dedication

This dissertation is dedicated to my parents, David and Belem Sosa whose love, support, and success through adversity provided the foundation and opportunity to choose this path in life.

Acknowledgements

First, I would like to thank my advisor Dr. Jeffrey D. Rimer for his incredible guidance and mentorship throughout my graduate studies, and for giving me the opportunity to begin and develop my research career early on in my undergraduate career. I would like to give thanks to my committee members for thoughtful discussion in our project meetings. I express my sincerest gratitude for Dr. Jacinta C. Conrad for the wonderful experience in writing my first – first author paper in graduate school, for her mentorship in helping me gain a deeper understanding of transport phenomena, and her continued guidance and support throughout my PhD. I am grateful to have had the opportunity to work with Dr. Michael A. Reynolds, who brought the birth of this project to the Rimer group. I am grateful to have had the opportunity to present my work to committee member Dr. Allan J. Jacobson. I am eternally thankful to have shared some of the best and toughest years with my dear friend, Doyoung.

To my sisters, Syndy, Kyra, and Selene, thank you for your love, and humor, which kept my mind afloat amidst the most stressful occasions. I am incredibly blessed to have remained near my family and friends throughout my graduate studies. To my best friend and partner, Amy Le, thank you for standing by my side all these years – your patience and encouragement drive me to be better with each day. To my friends, Eduardo Medina, Sunil Shahani, Trung Do, and Nick Dias, thank you for your continued support. Finally, I would like to acknowledge the National Science Foundation for providing me award funding for three years through the NSF Graduate Research Fellowship.

Abstract

Mineral scale occurs in processes ranging from water treatment and purification to oil and gas production systems, posing significant challenges to the upstream petroleum industry. Designing effective biodegradable chemical treatments to reduce scale formation requires understanding the molecular-scale interactions of inhibitors during nucleation, growth, and dissolution of scale. Crystal growth modifiers (or impurities), in the form of ions (Na^{+}, Zn^{2+}, Mg^{2+}, etc.), small molecules, or macromolecules such as peptides, proteins, or polymers can be introduced to growth or dissolution media to aid in controlled crystal growth (inhibition or promotion) or dissolution as demineralizing agents. The precise effect of hydrodynamics, which alters modifier-crystal interactions, on inhibitor and dissolver efficacy remains elusive. This dissertation has established a robust microfluidic platform that systematically characterizes the effects of hydrodynamics on crystallization processes for barium sulfate (barite). These studies focused on elucidating the effects of small molecules and bio-derived macromolecules on barite crystallization and dissolution kinetics. In situ atomic force microscopy (AFM) was used to track surface growth and dissolution in real time. Findings in this dissertation provide mechanistic insight into the unique modes of barite dissolution via the use of demineralizing agents, such as the naturally-derived macromolecule alginate, and the cooperative synergy achieved through the use of binary combinations of demineralizing agents with commercial scale dissolvers, such as diethylenetriaminepentaacetic acid (DTPA). An irreversible inhibition mechanism is gleaned from these studies in which amorphous surface features are formed on barite surfaces in the presence of small polyprotic carboxylate-based molecules. In summary, this dissertation details studies using a combination of state-of-

the-art characterization that elucidate growth, inhibition, and dissolution mechanisms for barite scale in media containing molecular modifiers of varying chemistry for the improved design of chemical scale treatments.

Table of Contents:

List of Tables

List of Figures

Chapter 1: Introduction to Crystallization

Crystallization is a ubiquitous phenomenon that occurs in both natural and synthetic processes at varying scales. In general, crystallization is the ordered assembly of repeat units that is driven by the oversaturation of the parent solution to form a solid product. The properties that govern crystallization include (but are not limited to) temperature, pressure, pH, ionic strength, and impurities. This assembly process yields crystalline solid materials often with desirable properties (optical, physicochemical, electrical, etc.) that make them integral to developments in many industries ranging from pharmaceuticals[1-2] to semiconductors[3-4]. On the other hand, crystallization can be quite problematic in biological processes (e.g., pathological diseases) and to a number of industries including wastewater treatment and energy production (e.g., scale formation).[5-7] In each of these cases, controlling crystallization of these materials is imperative. For instance, in the semiconductor industry, where crystalline materials are integral to the functionality of products, it is desirable to tune organic crystallization for the formation of highly ordered thin films used for organic electronic devices.[8-10] Similarly, controlling the crystallization of organic molecules is desirable in the development of active pharmaceutical ingredients (APIs).[11-13] The buildup of crystalline material in pathological diseases (e.g., kidney stones and atherosclerosis) as well as industrial processes (e.g., scale formation in pipelines) presents situations where the primary interest of controlling crystallization is suppression or reversal (i.e., dissolution).[5, 14-21] Controlling crystallization is a topic that has garnered significant attention among a wide range of research communities. Inspiration for the use of impurities (or more generally "modifiers") to tailor crystallization has been drawn from natural compounds (or their derivatives) that regulate biomineralization.[22-27] Evidently,

there is a need for understanding crystallization pathways for the design of functional materials as well as the design of treatments for crystals associated with human diseases.

1.1 Crystallization Mechanisms

Crystallization processes can be characterized by unique sequences of molecule attachment to the crystal surface through either classical or nonclassical pathways. Classical crystal growth occurs via monomer attachment, whereas nonclassical crystal growth can occur through the involvement of diverse growth precursors. In many applications it is desirable to understand the precise crystallization pathway materials follow with molecular-level resolution in order to optimize the parameters of the growth medium to engineer and optimize functional materials. Furthermore, knowledge of crystallization mechanisms allows for the design of crystal growth modifiers that can alter crystallization pathways or hinder specific steps in the mechanism to suppress crystallization. The latter is ideal for systems where crystallization poses a threat to functionality, such as scale formation in industrial pipelines.

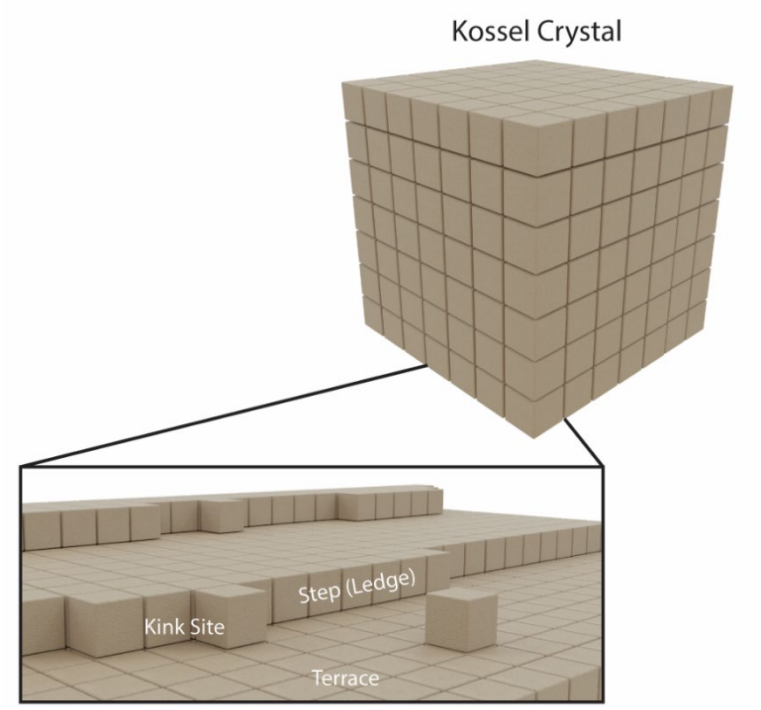

Figure 1. Idealized schematic of a Kossel crystal displaying terrace, step, and kink sites for solute attachment during classical layer-by-layer growth.[28]

1.1.1 Classical Crystal Growth

In classical crystal growth, solutes (monomer) adsorb to an existing crystal surface with the rate of growth determined by the supersaturation of growth media. The Terrace-Ledge-Kink model describes the thermodynamics governing the formation of a basic crystal, referred to as a Kossel crystal. Figure 1 displays a rendering of a Kossel crystal featuring common growth sites: kinks, edges, and terraces. In the classical crystal growth pathway, monomer attachment can occur at a variety of crystal growth sites, as represented in Figure 2, to promote growth by layer generation and spreading.

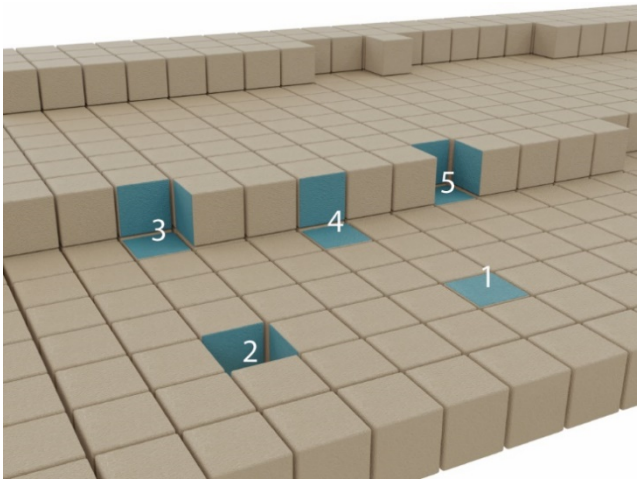

Figure 2. Idealized schematic of surface growth sites for attachment of monomers (classical pathway).

Kinks (site 3 in Figure 2) are growth sites with three neighboring surfaces, namely, two stepped surfaces and one terrace surface. Steps (site 4 in Figure 2) feature a series of growth units in succession that represent the leading edge of layer growth. A terrace (site 1 in Figure 2) displays a flat surface where monomers may attach during growth. Crystal growth rates, which are proportional to the rates of step propagation, are dependent on kink site density.[29] Furthermore, monomer attachment may occur by directly incorporating to the growth sites, or by adsorbing to the crystal surface and subsequently diffusing to a growth site (Figure 3), which has been demonstrated for organic crystallization (e.g., hematin).[30]

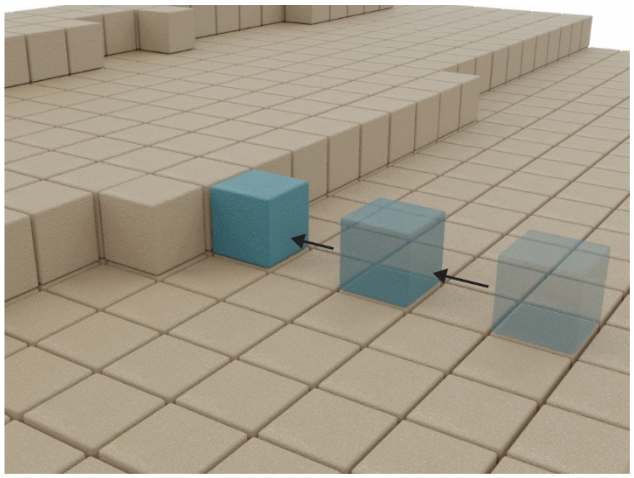

Figure 3. Surface diffusion of a monomer (depicted as a square basic building unit) adsorbed to the crystal surface and attaching to a nearly step edge.

Classical growth mechanisms generally lead to the formation of growth hillocks, and/or 2-dimensional single layers that spread laterally. A growth hillock emanates from a screw dislocation on the crystal surface, which consists of a single atomic plane rolled into a helicoid. This dislocation continually acts as a layer source; therefore, the growing crystal simply experiences monomer attachment to the existing layer from the dislocation source resulting in a spiral morphology (Figure 4).[28, 31-33] In this type of growth, which occurs at relatively low supersaturation, step velocity and curvature are proportional to supersaturation. By further increasing supersaturation of the growth media, a transition in growth mechanism occurs. At higher supersaturation, growth is primarily observed to occur via 2-dimensional (2D) nucleation of new layers that follow a birth and spread model.[29] Growth units continuously attach and detach at rates that are dependent on supersaturation.

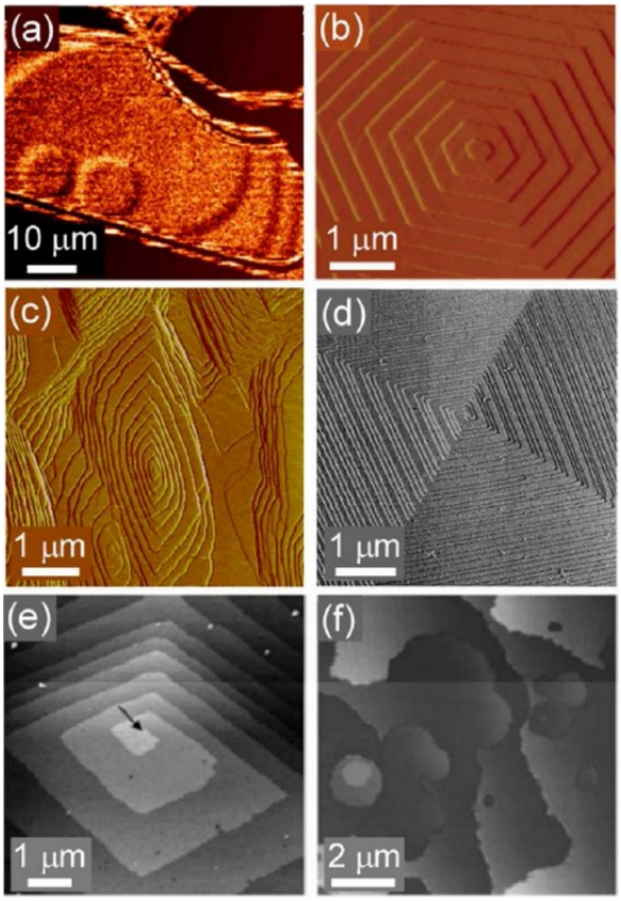

Figure 4. Examples of crystal systems that exhibit classical growth features: (a) 2D nuclei on growing ice crystals, and atomic force micrographs of screw dislocations on the following crystals (b) L-cystine (001, (c) calcium oxalate (010), (d) calcite {1014}, (e) insulin (100), and (f) ferritin (111).[34]

Nucleation of 2D layers occurs when the adsorbed molecules on the crystal surface generate islands of a critical radius (r_c), which decreases concomitantly with increasing supersaturation.[35] When the critical radius of an emerging layer is greater than r_c, there is a high probability the layer will continue to spread laterally (Figure 5) and eventually merge with other layers advancing across the crystal surface. In some systems, 2D islands and growth hillocks display a morphology dictated by periodic bond chain theory and resemble the habit of the larger crystal.[33, 36-38]

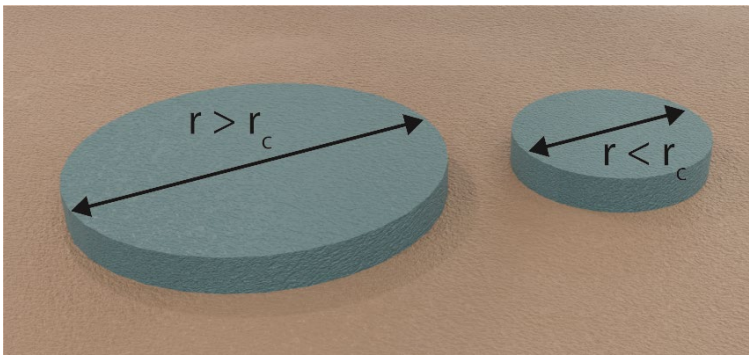

Figure 5. Idealized schematic of 2D islands with radii (left) greater than and (right) smaller than the critical radius.

1.1.2 Classical Nucleation Theory (CNT)

The birth phase in classical crystallization known as Classical Nucleation Theory (CNT) comprises the emergence of a crystal embryo in solution whereby the growth of the nuclei occurs by the addition of one monomer at a time, modeled as spherical droplets with uniform densities. The critical radius of embryos represents the point where there are equal probabilities of growth and dissolution, indicating crystal nucleation is a stochastic process. This model assumes the monomers are highly ordered building blocks, thus the molecular arrangement of the crystal embryo resembles that of the grown crystal (Figure 6).[39] CNT, however, has been reported to predict nucleation rates 1-2 orders of magnitude higher than rates determined experimentally.[40] It is evident that there are limitations to the CNT model.

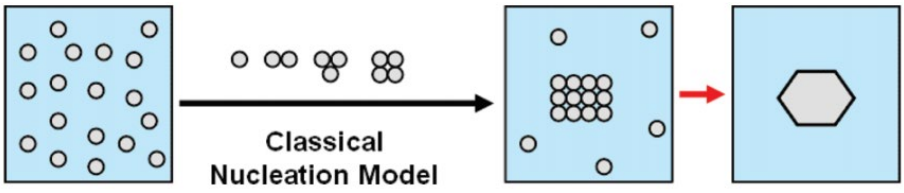

Figure 6. Schematic showing the classical nucleation model (CNT). This model involves the ordered assembly of monomer units that may grow after approaching a critical size.[39]

Furthermore, CNT assumes the nucleus has a uniform composition; however, it is reported that in certain binary phase systems (organic-aqueous) the clusters may have varying composition relative to the bulk, owing to the enrichment of the droplet surface.[39] Thus, CNT cannot predict absolute nucleation rates and often may not accurately depict the assembly of crystal nuclei for many systems. While classical crystallization and nucleation models provide a fundamental framework for our understanding of crystal assembly, there are a vast number of systems that deviate from this model and follow more complex nonclassical models.

1.1.3 Nonclassical Crystallization and Two-Step Nucleation

Many crystal systems have been discovered to assemble via pathways that differ from the classical growth mechanism, where growth may occur via the attachment of precursors that are not limited to monomers (Figure 7).[39-45] One such example is a class of crystals known as zeolites, which are porous crystalline aluminosilicates featuring inherently complex crystal structures that yield microporous geometries and are often found in nature, such as in basalt cavities.[46-47]

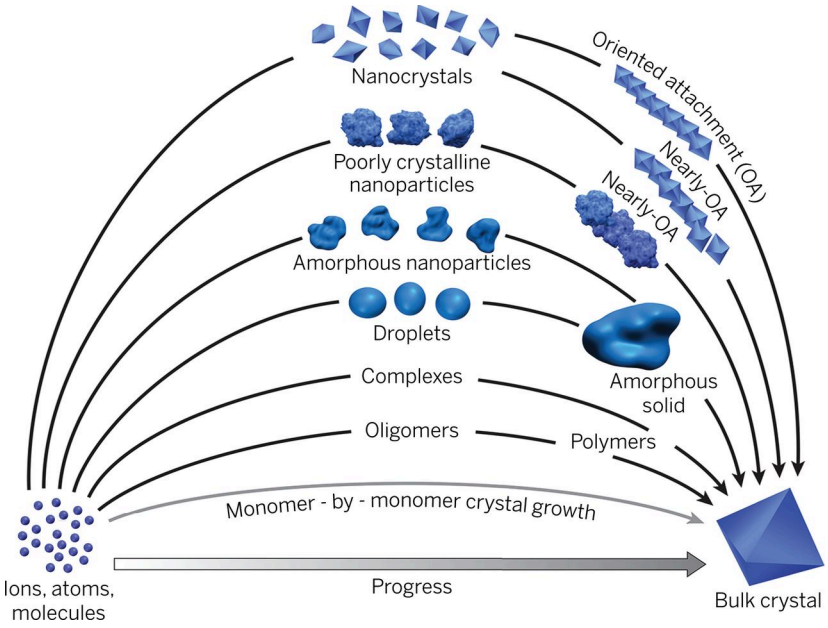

Figure 7. Examples of potential crystallization pathways, including classical (monomer addition) and nonclassical mechanisms. The latter can involve a diverse set of precursors (depicted here) ranging from oligomers to amorphous particles and nanocrystallites.[48]

The intricate nature of zeolite crystallization has made it challenging to obtain a clear understanding of zeolite nucleation and growth pathways, which generally comprises the attachment of growth units including (but not limited to) oligomers, amorphous particles, and small crystallites.[48-54] Significant steps have been taken to elucidate nonclassical crystallization mechanisms, including the observation of gel-like particles forming on zeolite crystal surfaces that enables further 3-dimensional layered growth.[52-53] Other examples of nonclassical growth include: the non-oriented attachment of amorphous primary particles on magnetite (Fe^3O^4) surfaces, worm-like particles serving as precursors of zeolite crystallization, and amorphous calcium carbonate precursors exhibiting liquid-like properties that feed vaterite crystal growth.[34]

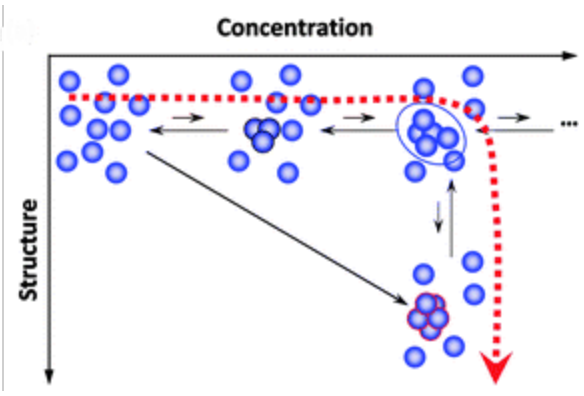

Figure 8. Scheme outlining the two-step nucleation model (dashed red line) with the arrow indicating the direction of nucleation. Monomers first form a dense liquid cluster, which then undergoes an ordering phase to form a crystal nucleus.[42]

There have been numerous efforts to understand more clearly how crystal nucleation differs from CNT. Research groups have developed a more representative model known as the two-step nucleation model.[39-40, 42, 44] Contrary to CNT, the two-step model first involves the formation of a metastable dense liquid precursor that may lack the ordering found in the crystalline phase, followed by a stage(s) involving rearrangement into ordered crystalline segments (Figure 8).[39-44] This phenomenon is observed for a wide range of crystalline materials such as proteins, organic small molecules, polymers, and inorganic minerals.[55-56] For example, the crystallization of calcium carbonate ($CaCO_3$) has been shown to exhibit an amorphous calcium carbonate phase prior to the formation of various crystalline forms.[56-59] Similar behavior has been shown for other mineral systems such as calcium oxalate monohydrate (COM),[49] and barium sulfate ($BaSO_4$).[50, 60-61]

1.1.2 Crystal Dissolution

Dissolution is another integral field of crystallization that is driven primarily by the solution thermodynamics (i.e., solubility), namely the degree of undersaturation in the dissolution media, which is analogous to crystal growth where supersaturation is the

driving force for crystallization.[31, 62-66] Dissolution often occurs by the formation of shallow etch pits that dissolve layer-by-layer or alternatively deep etch pits with less lateral spread. Dissolution can be altered by tuning parameters that impact the material's solubility, such as pH, temperature, pressure, ionic strength, and concentration of impurities. Analogous to classical growth, mildly undersaturated conditions leads to "spiral dissolution", and depicted by the propagation of a dissolving pit.[62, 67-68] Additionally, the kinetics that define crystal dissolution are also highly dependent on the crystal's intrinsic properties, which include surface defects, kink sites, and crystal size.[62, 68-70] A key distinction between growth and dissolution is that crystals in growth media tend to be in conditions much closer to equilibrium than crystals in media promoting dissolution. In far from equilibrium conditions, the dissolving crystal undergoes significantly more changes in morphology owing to the rise in different crystal planes that are exposed.[71] Thus, a high degree of control over the dissolution process can be quite challenging. Controlling both crystal growth and dissolution processes can be facilitated by introducing molecular modifiers to respective media.

1.2 Crystal modifiers

Additives can be introduced to growth or dissolution media to aid in controlled crystal growth (crystal growth modifiers) and dissolution (demineralizing agents).[72-76] These additives may be in the form of ions (Na^+, Zn^{2+}, Mg^{2+}, etc.), small molecules, or macromolecules such as peptides, proteins, or polymers. Many of these species are either derived or inspired from nature (e.g., polysaccharides).[77-78] Modifiers can bind to crystal surface sites (kinks, step edges, or terraces) where they impede solute attachment via distinct modes of action.[31, 79] Demineralizing agents are another subset of modifiers that

also adsorb or bind to crystal surface sites, however, in undersaturated conditions they elicit various modes of solute detachment.

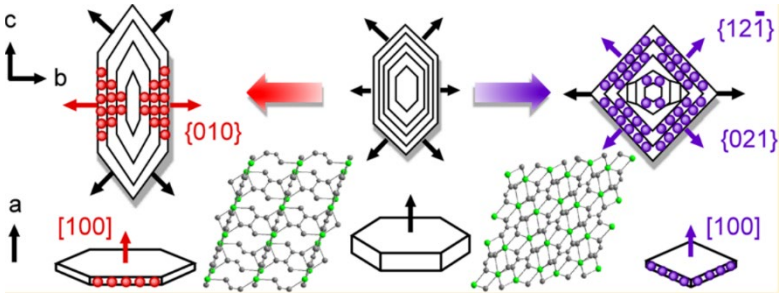

Figure 9. Preferential binding specificity of impurities on different facets of a calcium oxalate monohydrate (COM) crystal.[80]

Modifiers are capable of altering anisotropic rates of growth with concomitant impact on crystal shape and size, often demonstrating binding specificity for one or more facets (Figure 9).[80-81] A key component of a modifier's ability to induce these interactions with crystal surfaces is the abundance of functional groups (motifs) that aid the molecule in binding with crystal surface sites to alter the morphology, size, and/or structure of crystals. One such example of these interactions involve calcium (Ca^{2+}) bridging, where modifiers containing carboxylic acid groups (COO^-) can bind to Ca^{2+} ions near the crystal surface to create a bridge interaction between the modifier and crystal (Figure 10).[80] There is great interest in identifying the mode of action by which select modifiers direct crystallization.

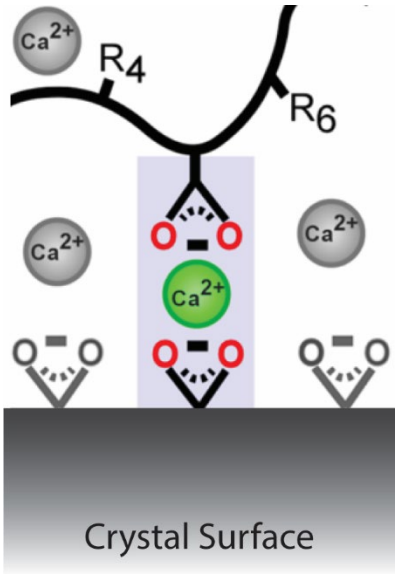

Figure 10. Schematic showing calcium bridging between carboxylic acid groups on a negatively-charged COM surface, Ca^{2+} ions near the crystal surface, and a carboxylic acid group on a modifier.[80]

1.2.1 Kink Blocking

One of the most common crystal inhibition mechanisms is kink blocking (Figure 11), in which a molecule binds to kinks thereby occupying a potential growth site preventing the incorporation of solute and concomitantly impeding layer advancement.[15, 17, 32-33] An increase in modifier concentration generally results in increased coverage adsorbed modifier on crystal surfaces, leading to enhanced growth suppression; however, owing to the continuous and rapid generation of kink sites, full suppression is often not observed for modifiers that operate through this mode of action. In a kink blocking mechanism, the inhibitor may or may not permanently suppress step advancement but merely reduce the rate of step propagation. Thus, in this mode of action the crystal growth inhibitor does not affect the local solubility. Moreover, modifiers acting as kink blockers can induce changes to the crystal habit owing to altered anisotropic rates of crystal growth.

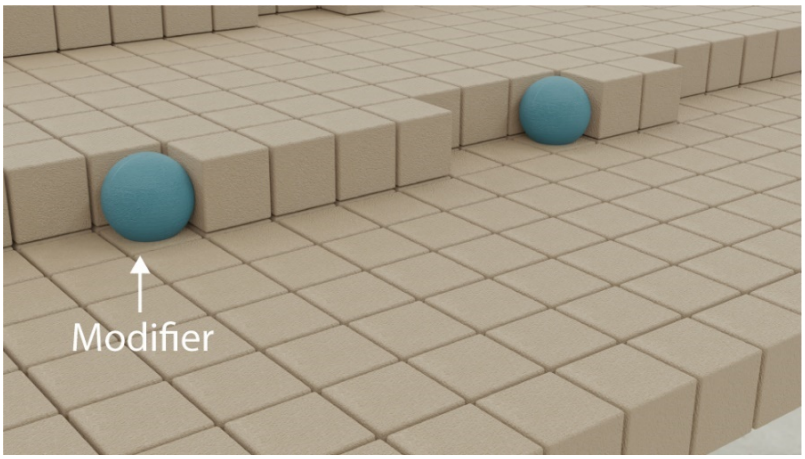

Figure 11. An idealized schematic of a kink blocking mechanism where a modifier (blue sphere) is occupying a kink site in a Kossel crystal.

1.2.2 Step Pinning

Another common classical inhibition mechanism involves the adsorption of additives to terraces on crystal surfaces, which can block the attachment of molecules to step edges. When a molecule adsorbs to the surface, two possibilities arise for the advancing layer.[32-33, 82] If two adsorbed molecules are within a distance, Δx, and this distance is smaller than the critical curvature (r_c), which is dependent on the supersaturation, the layer will cease growth and become pinned by the inhibitor. If the distance between two adsorbed molecules is greater than r_c then the layer will continue to grow past the bound modifier unimpeded. This step pinning mechanism reduces layer advancement based on a thermodynamic effect where the localized supersaturation is reduced. For instance, when the radius of curvature of the advancing layer falls below r_c, the solution becomes locally undersaturated, which is followed by layer dissolution until the curvature radius approaches r_c.[35]

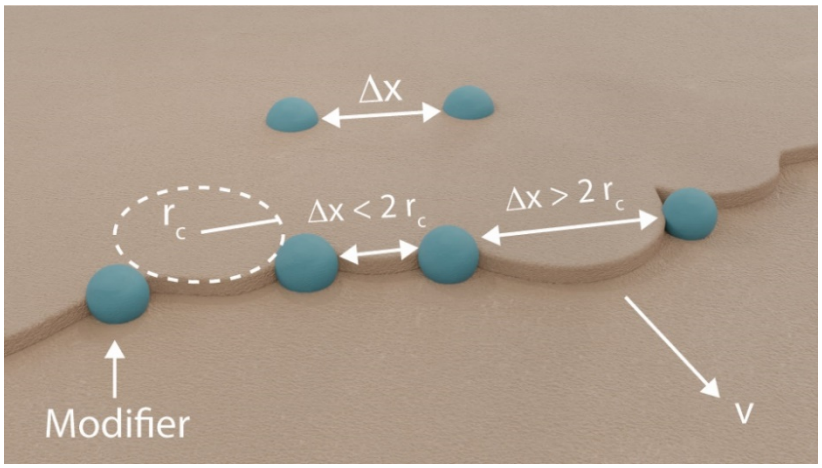

Figure 12. Step pinning mode of action depicting adsorbed molecules (blue circles) pinning the advancement of an unfinished layer.

1.2.3 Demineralizing Agents

Additives can also be used as demineralization agents to facilitate the dissolution of crystals. This approach is of particular interest to industries where regulating crystal solubility is essential to product safety and functionality (e.g., active pharmaceutical ingredients)[1-2, 11-13] or cases where crystallization is harmful to system processes (e.g., kidney stone diseases, scale formation, etc.).[14-19, 21, 58, 83-87] In the latter case, additives are generally introduced to sequester ions (solute) in the bulk solution, which is equivalent to increasing crystal solubility. When additive concentrations are sufficiently high to lower solute levels below saturation, this induces crystal dissolution. These additives are selected on the basis of their ability to chelate solute ions. Generally, a greater degree of chelation results in enhanced dissolution.[73-74, 78, 88-93]

Crystal dissolution kinetics have been widely investigated in the presence of various additives believed to be effective demineralizing agents for ions associated in common mineral scales, such as calcium, strontium, and barium.[62, 70, 75, 94-99] The simplest

of additives used to enhance mineral dissolution is ions (Ca^{2+}, Mg^{2+}, Na^{+}), which increase the ionic strength of the solution and thus increase solubility for many crystal systems. The majority of compounds investigated as demineralizing agents are small molecules decorated with acid groups (carboxylic, phosphonic, etc.) owing to their ability to effectively chelate monovalent and divalent cations.[100-104] Due to the polyprotic nature of these molecules, special consideration must go into the solution properties, such as ionic strength and pH. These properties dictate the speciation of the polyprotic acids and their affinity to interact with free ions. Few studies have investigated the effects of larger molecules such as polymers and proteins on crystal dissolution.[77] The selection criteria for macromolecules, however, is similar to that of small molecules. The most effective macromolecular demineralizing agents are populated with acid groups, where examples include alginate (carboxylic acid) and polyphosphinocarboxylic acid (PPCA, polyphosphate chain decorated with carboxylic acid groups).[78, 105] Although it is generally reported that demineralizing agents enhance dissolution via sequestration of free ions, our work[78] showcases examples of increased dissolution where the primary mechanism involves unique modifier-crystal interactions that deviate from classical dissolution mechanisms.

1.3 Industrial-Scale Crystallization

Mineralization in the oil and gas industry is pervasive and exemplifies how crystallization (scale formation) can have a detrimental effect by significantly hindering energy production, which costs industry hundreds of millions of dollars in lost production alone.[5-7, 106] Scale is the assemblage of minerals that forms as a result of the oversaturation of fluid traveling through production pipelines. This oversaturation of fluid is an

undesirable byproduct of hydraulic fracturing. The generation of supersaturated fluid, accentuated by changes in temperature, pressure, and flow, can result in the precipitation of multiple inorganic scale components.[107-108] During this process, a fracture fluid (high SO_4^{2-} concentration) is injected into the oil reservoir, which contains formation water high in mineral content (Ca^{2+}, Ba^{2+}, Sr^{2+}, Mg^{2+}, etc.), to enhance oil recovery (Table 1).[109]

Table 1. Ion concentrations in formation water found in oil reservoirs, and in fracturing fluid that is introduced during hydraulic fracturing.[109]

Ion Species	Formation (ppm)	Injection (ppm)
Sodium	31275	10890
Potassium	654	460
Magnesium	379	1368
Barium	269	0
Strontium	771	0
Sulfate	0	2960
Chloride	60412	19766
Calcium	5038	428

The mixing of these incompatible fluids leads to the precipitation of many mineral systems and results in the formation of scale accumulates within pipelines and downhole equipment. Scale treatment can be divided into two categories: (i) preventative methods, and (ii) scale removal when preventative methods fail. Inhibitor formulations (e.g., squeeze treatments) have been designed to suppress scale formation primarily by using additives such as diethylenetriaminepenta(methylene phosphonic acid) (DTPMP) that can sequester

ions thereby impeding crystal formation.[101-102, 104, 110-113] However, these treatments only suppress crystallization at early timescales and eventually are rendered ineffective owing to the high degree of supersaturation in the fluid. Thus, the second approach is taken, which involves the use of acids or highly alkaline chelating agents to promote dissolution. For certain scales (e.g., $CaCO_3$) an abrasive acid wash is often implemented, whereby a mixture of abrasive material and acid is jetted into the affected pipeline. The abrasives and high pressure of the fluid aid in breaking down the hard scale, while a strong acid (e.g., HCl) is used to reverse the crystallization reaction chemistry to promote scale dissolution.[114-115] On the other hand, scale dissolver formulations make use of polyprotic acids that can chelate divalent cations (Ca^{2+}, Ba^{2+}, etc.) and increase the solute saturation limit in the bulk, thereby promoting dissolution. Aminopolycarboxylic acids such as ethylenediaminetetraacetic acid (EDTA) and diethylenetriaminepentaacetic acid (DTPA) are used commercially as demineralizing agents for hard scales such as calcium carbonate and barite.[94, 116-119] Both additives are productive dissolvers of pure mineral systems, however, they require high solution pH to be fully deprotonated and thus "active" for chelating metal ions. One major drawback of these additives is the caustic nature of the solution required for effective demineralization, which poses a threat to the equipment used as well as the environment.[120] Another shortcoming of chemical demineralization treatment is that in practice, these solutions dissolve scale but not with high efficiency, which often requires mechanical drilling to remove the scale from the pipelines.[5] Thus, there is a need for the design of more efficient chemical scale treatments, which necessitates efforts to better understand the mechanisms that drive crystallization and

dissolution processes as well as the interactions between chemical additives and crystal surfaces.

1.4 Barite Crystallization

Barite is a commonly encountered, water insoluble scale component (K_{sp} = 1.08 × 10^{-10} at 25 °C) in the oil and gas industry, and poses difficulty for treatment relative to other scales.[108-109, 121-122] Furthermore, the North American shale boom has highlighted the need for new techniques for studying inorganic scale in the pores of tight shales, where porosity is high (8 – 10%) while pore size (1 – 100 nm) and permeability (< 0.1 mD) are low.[123] A lack of available chemical treatments has led the industry to use mechanical means for barite scale remediation, including drill-based milling.[124] Controlling its formation requires a fundamental understanding of growth, inhibition, and dissolution mechanisms in dynamic environments. Barite mineralization occurs via classical growth pathways with second-order kinetics[111, 125-126] and typically results in coffin-shaped crystals bound by (001), (210), and (100) facets (Figure 13).

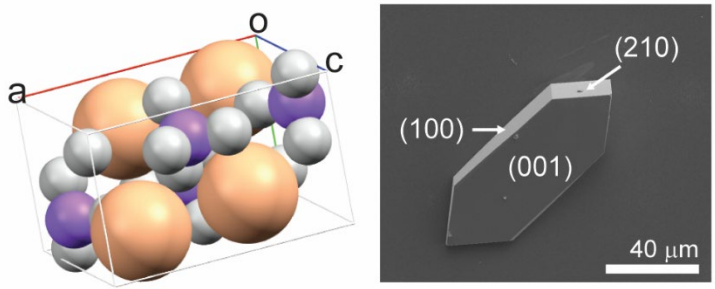

Figure 13. Barite crystal lattice with the unit cell outlined (left) and a representative electron micrograph of a synthetic barite crystal grown at room temperature.

Co-precipitation of Ba^{2+} with Sr^{2+}, Ra^{2+} and other metal ions adds to the complexity of barite formation. Suppressing crystal growth requires the use of molecular additives that,

through various modes of action, retard barite precipitation. Surprisingly few compounds have been successfully used as treatments to dissolve barite. Chelating agents represent one class of compounds used to dissolve scale. Indeed, ethylendiaminetetraacetic acid (EDTA), diethylenetriaminepentaacetic acid (DTPA), and similar polyprotic acids have been commercially employed as scale inhibitors and dissolving agents,[109, 113, 127-131] and certain 18-membered macrocycles have been shown to be effective chelators of Ba^{2+} ions.[90] Collectively, studies investigating the effect of additives largely focus on prevention and dissolution mechanisms in quiescent conditions. Scale, however, typically forms under dynamic flow conditions. Understanding the effects of fluid flow on barite crystallization processes is thus expected to improve the design of scale treatments.

A majority of barite mineralization studies under quiescent conditions have investigated crystallization kinetics using bulk assays or batch processes by tracking solute depletion (conductivity, turbidity, or elemental analysis) or characterizing temporal changes in crystal size and morphology via *ex situ* microscopy (optical or scanning electron).[89, 97, 126, 132-134] These techniques capture crystallization kinetics that may be influenced by mass transport limitations or require rigorous and time-consuming experimental methods. Kinetic studies relying on the measurement of target ion concentration (conductivity or ion selective analysis) may be vulnerable to interference from spectator ions. Growth, inhibition, and dissolution mechanisms have also been probed in various chemical environments through the use of *in situ* atomic force microscopy (AFM), which provides insight on surface chemistry such as etch pit kinetics, hydration structure, and modes of action of modifiers.[36-37, 110, 135-140]

In this dissertation, we address hydrodynamic effects and crystal growth and dissolution pathways in the presence and absence of molecular modifiers. In Chapter 2, the development of a novel microfluidic platform for investigating crystallization and crystal dissolution, and the effects of hydrodynamics on crystallization processes will be reviewed, using the commercial additive diethylenetriaminepentaacetic acid (DTPA) as a benchmark. In Chapter 3, we investigate barite dissolution in greater depth and elucidate key dissolution mechanisms that result in synergistic cooperativity in barite demineralization in the presence of naturally derived macromolecules. In Chapter 4, we screen a library of molecular modifiers as putative inhibitors of barite crystallization. Here we examine barite growth inhibition kinetics and mechanisms in the presence of a bio-derived macromolecule through a cooperative study using bulk assays, in situ microfluidics, and in situ atomic force microscopy (AFM). In Chapter 5, we investigate the effects of citrate and two of its analogues as molecular modifiers in barite crystallization. We reveal a unique inhibition mechanism that irreversibly suppresses barite crystal growth at micromolar concentrations. In Chapter 6, we show the inhibition of a naturally derived phosphate-based additive, which demonstrates comparable barite inhibition potency relative to the commercial phosphonic acid. In Chapter 7, we summarize key findings in this dissertation and provide future outlook in this field.

Chapter 2: Microfluidic Platform for Probing Barite Crystallization

A majority of barite mineralization studies under quiescent conditions have investigated crystallization kinetics using bulk assays or in batch processes by tracking solute depletion (conductivity, turbidity, or elemental analysis) or characterizing temporal changes in crystal size and morphology via *ex situ* microscopy (optical, scanning electron,

or scanning probe).[89, 97, 126, 132-134] These techniques capture crystallization kinetics that may be influenced by mass transport limitations or require rigorous and time-consuming experimental methods. Kinetic studies relying on the measurement of target ion concentration (conductivity or ion selective analysis) may be vulnerable to interference from spectator ions. Growth, inhibition, and dissolution mechanisms have also been probed in various chemical environments through the use of *in situ* atomic force microscopy (AFM), which provides insight on surface phenomena such as etch pit kinetics, hydration structure, and modes of action of modifiers.[36-37, 110, 135-140] For growth, interfacial studies have been shown to correlate well with bulk (macroscopic) kinetics.[141] Although the combination of bulk crystallization and crystal surface kinetics provides valuable insight into crystallization mechanisms, microscopic studies (AFM) are limited by a specified set of parameters per trial, sample size, and flow rate range. Furthermore, in AFM studies the flow patterns may be influenced by fluid cell design, and crystallization kinetics can be affected by tip interference with solute transport.[142-143] There remains a need for non-pervasive *in situ* methods that probe crystallization processes under flow while allowing for efficient parametric analyses. Microfluidics offers an excellent alternative for addressing the limitations of traditional methods by eliminating external interference and enabling the sampling of multiple parameters simultaneously under stable flow conditions.

Droplet microfluidics, as one example, allows single crystal nucleation and growth to be decoupled in high-throughput platforms.[144-149] Temporal changes in solution conditions within the droplets (e.g., supersaturation), however, preclude facile measurement of anisotropic crystal growth rates. As a second example, single-phase microfluidic platforms used to investigate organic and inorganic crystallization bridge the

gap between bulk crystallization measurements and interfacial studies.[148, 150-153] These studies have demonstrated that flow of adjoining solute streams imposes mass transport limitations, which affect local stability of supersaturation within microchannels and thus govern crystallization kinetics as well as nucleation and growth mechanisms of minerals such as calcium carbonate ($CaCO_3$). These mass transport limitations have been shown to influence $CaCO_3$ growth in the presence of inhibitors.[57, 148, 154] Microfluidics as a tool for mineralization studies has been applied to other forms of scale, such as gypsum ($CaSO_4 \cdot 2H_2O$) and $CaCO_3$, and integrated with methods such as synchrotron Fourier transform infrared spectroscopy to show that the absence of convection extends the lifetime of typically unstable polymorphs of $CaCO_3$ in confinement.[153] The emerging use of microfluidics for crystallization studies demonstrates the promise for time-resolved measurements of individual crystals. Hence microfluidic techniques represent an ideal platform to explore the effect of flow velocity on crystallization processes for sparingly soluble minerals such as barite.

In this work we develop a microfluidic platform for rapid screening of barite growth, inhibition, and dissolution kinetics under controlled hydrodynamic conditions. Under a pseudo-steady-state growth environment, increasing the solution flow rate of $Ba^{2+}_{(aq)}$ drives a transition in the crystallization kinetics from a transport-limited to a reaction-controlled regime, parameterized by a local Péclet number that describes transport through the boundary layer adjacent to the crystal surface. Coupling the microfluidic platform with optical microscopy enables time-resolved observation of anisotropic crystal growth, revealing face-specific inhibition in the presence of commercial chemical additives. Finally, we demonstrate the versatility of the microfluidic platform by showing

that barite dissolution is promoted under flow of alkaline aqueous solutions. These methods provide new insights into the effects of dynamic conditions on mineralization processes. Moreover, our approach allows bulk dissolution phenomenon to be systematically elucidated in a controlled laminar flow environment using a combination of optical microscopy and microfluidics.

2.1 Experimental Methods

Materials. The following reagents were purchased from Sigma Aldrich: barium chloride dihydrate (99+%), sodium sulfate (>99%), diethylenetriaminepentaacetic acid (DTPA) (>99%), sodium hydroxide (>97%), and sodium chloride (>99.5%). Polydimethylsiloxane (PDMS, Dow Corning SYLGARD 184) was purchased from Essex Brownell. SU-8 2150 photoresist and SU-8 developer were purchased from Microchem. All chemicals were used as received without further purification. Silicone tubing was purchased from Cole-Parmer. Single side polished 4 in P-type silicon wafers <100> were purchased from University Wafer and were cleaned using a piranha solution. Deionized (DI) water (18.2 MΩ·cm) filtered with an Aqua Solutions RODI-C-12A purification system was used in all experiments.

Fabrication of microfluidic devices. The microfluidic platform consisted of two chips placed in series: a chip with a concentration gradient generator was linked downstream with a chip featuring individual straight channels (Fig. 1). The microchannel design, which was adapted from gradient generators in the literature,[155-157] was drafted using AutoCAD software (Autodesk) and fabricated using standard photolithography and polymer casting techniques.[158] A negative photoresist with 400 μm thick features was patterned on a 4-inch silicon wafer using photolithography. Subsequently, a mixture of

PDMS prepolymer and curing agent (volume ratio of 10:1) was degassed for 30 min and poured over the microchannel molds to 7 mm thickness. PDMS molds were cured at 65 °C for 4 h, after which devices were extracted with a razor blade. Inlet and outlet ports were created using a 2 mm biopsy punch. PDMS devices were cleaned with scotch tape to remove any dust and organic debris. Glass substrates were carefully washed with DI water and isopropyl alcohol and dried with N_2 gas. PDMS devices were bound onto the glass substrates after corona plasma treatment using a BD-10A high-frequency generator.

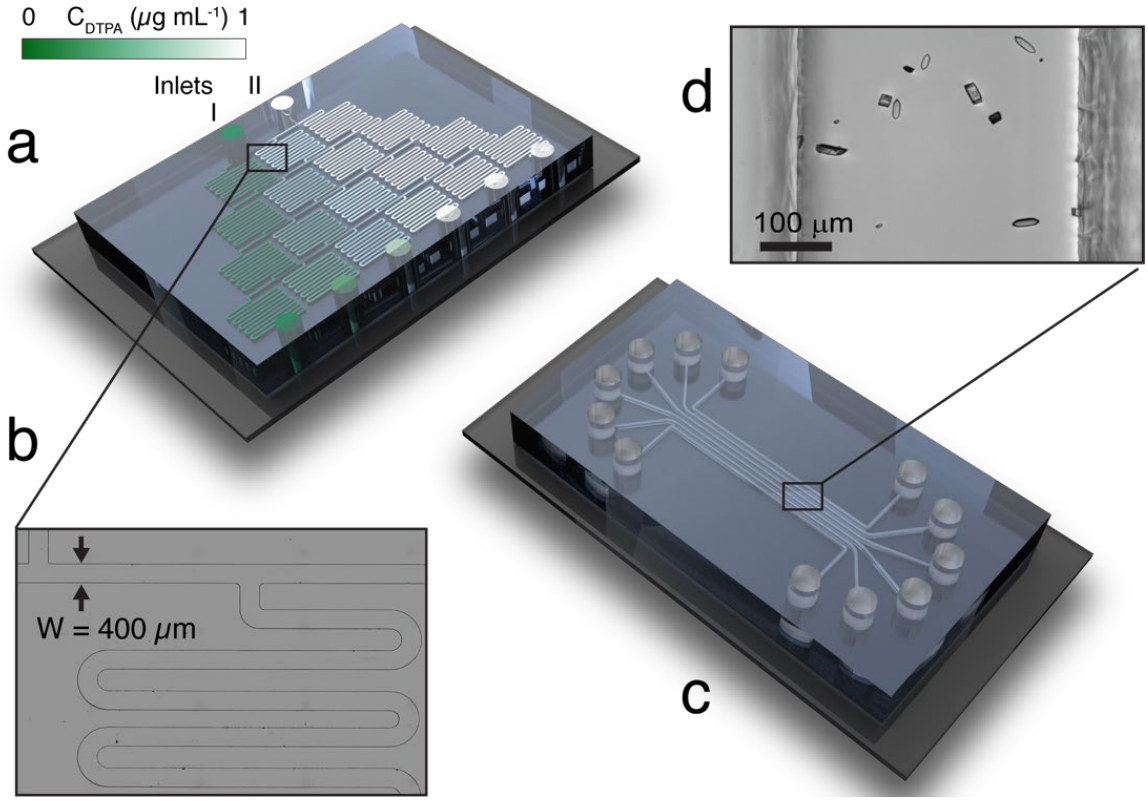

Figure 14. (a) Three-dimensional rendering of the gradient generator. (b) Optical micrograph of the microchannels in the gradient generator (c) A microfluidic device containing barite crystals. (d) Optical micrograph of barite seed crystals.

2.2 Bulk crystallization assays

Barite crystals were synthesized using a protocol modified from procedures reported in the literature.[96, 113, 126, 141, 159-160] In a typical synthesis, $NaCl_{(aq)}$ was first added

into a 20-mL glass vial followed by aliquot addition of 10 mM $BaCl_{2,(aq)}$ and 10 mM $Na_2SO_{4,(aq)}$ stock solutions under mild agitation for 10 s. Samples containing molecular modifier DTPA were prepared by adding aliquots of $DTPA_{(aq)}$ to the reaction mixture prior to the addition of Na_2SO_4. The final growth solutions with a total volume of 10 mL had a pH of 7.1 ± 0.3 and a composition of 0.5 mM $BaCl_2$: 0.5 mM Na_2SO_4 : 600 mM NaCl : x μg mL^{-1} modifier ($0 \leq x \leq 10$). The pH of growth solutions was measured using an Orion 3-Star Plus pH benchtop meter equipped with a ROSS Ultra electrode (8102BNUWP). The sample vials were left undisturbed at 22 °C for 24 h to allow crystallization of hexagonal barite platelets with well-defined (001), (210), and (100) facets (Figure 2a and b).

2.3 In situ preparation of seed crystals in the microfluidic channels.

For *in situ* crystallization studies, the microchannels (Fig. 14) were first flushed thoroughly with DI water. Growth solutions were then delivered into the channels using a dual syringe pump (CHEMYX Fusion 200) at a rate of 12 mL h^{-1} for 90 min. A solution containing 1.0 mM Ba^{2+} was mixed through a y-connector with a second solution component containing 1.0 mM SO_4^{2-} and 550 mM NaCl to circumvent interfacial crystallization in the microchannel caused by diffusion limitations.

2.4 Real-time study of growth, inhibition and dissolution kinetics.

Time-resolved imaging of barite crystal growth, inhibition, and dissolution using an inverted optical microscope was performed to quantify the kinetics of barite crystallization. For growth, two solution components were prepared in individual syringes. One solution contained 0.7 mM $BaCl_{2,(aq)}$ and the second solution contained 0.7 mM Na_2SO_4 and 1.2 M NaCl. The two solutions were mixed using an inline flow configuration that produced a final composition of 0.35 mM $BaCl_2$, 0.35 mM Na_2SO_4, and 600 mM NaCl.

The fully mixed growth solution was introduced into seeded PDMS chips using a dual syringe pump.

Inhibition studies required the use of two dual syringe pumps, each containing syringes of the same growth solution composition but different quantities of growth modifier (DTPA). The first syringe pump contained syringes prepared with no growth modifier (control) and the second syringe pump contained syringes prepared with 1 μg mL^{-1} DTPA, where DTPA was added to the syringe containing SO_4^{2-} to minimize formation of ion complexes. Growth solution components from each dual syringe pump were mixed via silicon tubing and a y-connector and successively fed into the corresponding inlet of the concentration gradient generator. Both pumps were programmed with the same flow parameters to ensure a linear concentration gradient at the outlet of the microfluidic channels (Fig. A1).

Dissolution studies of barite were performed in an alkaline solution that was prepared by adding appropriate amounts of NaOH to DI water. The flow configuration for carrying out barite dissolution entailed a dual syringe pump that fed two separate solutions, one control and one containing 500 μg mL^{-1} $DTPA_{(aq)}$ solution, into the respective inlets of the concentration gradient generator (Figure 14a). All dissolution cocktails were adjusted to pH 9, which is near the upper limit of the environmentally acceptable pH range for industrial scale treatment.

Barite crystal size and morphology were determined using a Leica DMi8 inverted optical microscope equipped with HC PL Fluotar 5×, 10×, 20×, and N Plan L 50× objectives. At least ten brightfield images of representative areas on the bottom of the glass vials were captured in transmittance mode for characterization of crystals grown in the bulk

assay. The average [010] length, [100] width, and [001] thickness of crystals in optical micrographs were measured from a minimum of 90 crystals per trial and three individual trials. An inverted optical microscope equipped with a motorized stage was used to image crystals in the bulk crystallization assays as well as time-resolved crystal growth, inhibition, and dissolution in the microfluidic assays (Fig. A2 – A4). For *in situ* time-resolved studies, LAS X software was used to program a minimum of 10 positions along a seeded microchannel, at which images were captured in transmittance mode at 5 min intervals for at least 3 h. Crystals observed *in situ* were analyzed using ImageJ (NIH) (Fig. A5). Images were converted to 8-bit followed by a threshold adjustment to outline the edges of barite crystals. An ellipse was fit to each crystal to obtain major and minor axis dimensions corresponding to the length and width of the crystal. At least 90 crystals located in different channels per batch were analyzed over time. Crystal lengths were measured every 5 min during inhibition studies. From the change in crystal length over time, a growth rate *r* was determined for each experimental condition. The relative growth rate (RGR) was calculated as

$$RGR = \frac{r_{\mathrm{DTPA}}}{r_{\mathrm{control}}} \qquad \text{Eq. (1)}$$

where r_{DTPA} and $r_{control}$ represent growth rates in the presence and absence of DTPA, respectively.

For *ex situ* microscopy measurements, a clean glass slide (1×1 cm^2) was positioned at the bottom of the vials to collect barite crystals. After crystallization, the glass slide was removed from its solution, gently rinsed with DI water, and dried in air prior to analysis. Crystal size and morphology were investigated using a FEI 235 dual-beam focused ion beam scanning electron microscope (SEM). SEM samples were prepared by attaching

carbon tape to SEM studs and subsequently attaching glass slides to carbon tape by gently pressing the glass slide to the tape using tweezers. SEM samples were coated with 15 – 20 nm gold to reduce electron beam charging.

2.5 Barite synthesis in quiescent conditions.

Barite crystals grown in a bulk batch synthesis formed hexagonal platelets with an average length of 15 μm and a length-to-width ([010]/[100]) aspect ratio of 2.2 ± 0.2 (Fig. 15a and b). Barite crystals grown under quiescent conditions in the microfluidic channels also formed hexagonal platelets with a length-to-width aspect ratio of 2.4 ± 0.1 (Fig. A2), nearly identical to that for crystals grown in the batch process at larger volume. Supersaturation and total reservoir volume govern the solute concentration gradient between the bulk solution and crystal surface. The former provides the driving force for crystal growth, whereas the latter dictates the total time of crystallization.[96, 126] Under quiescent conditions, solute transport is dominated by diffusion to the crystal surface through a boundary layer, which can be treated as a stagnant film. As solute is depleted from the bulk, the chemical potential gradient is reduced due to desupersaturation with a concomitant minimization of the driving force for crystal growth. In bulk assays, both nucleation and crystal growth consume solute. The effects of growth on solute consumption can be isolated using the method of seeding, in which seed crystals are grown at supersaturation ratios S in the region of metastability where nucleation does not occur. Under these conditions, S dictates the net change in crystal size.

2.6 Design of the microfluidics device.

To provide reproducible kinetic data for crystal growth, inhibition, and dissolution with time-resolved imaging, we designed a microfluidic platform to efficiently mix two

streams with different concentrations of DTPA (at either supersaturated or undersaturated conditions) and produce a concentration gradient across the six outlet channels (Fig. 14). To ensure complete mixing of two streams, the total length of each serpentine channel was set by the time required for small molecules, such as DTPA (with a diffusion coefficient approximated as $D = 1 \times 10^{-9}$ m^2 s^{-1}),[161] to diffuse across a channel of width $W = 400$ μm to obtain a linear concentration gradient of DTPA at the outlet channels. Specifically, we used the relation $W = \sqrt{tD}$, where $t = AL/Q$ is the minimum residence time of fluid in the microchannels based on the channel length $L = 2.4 \times 10^{-1}$ m, cross-sectional area $A = 1.6 \times 10^{-7}$ m^2, and the maximum volumetric flow rate $Q = 3.3 \times 10^{-8}$ m^3 s^{-1} used in this study. A linear concentration gradient of Ba^{2+} was obtained across the outlets (Fig. A1), confirming the reliability of the microfluidic concentration gradient generator. This experimental design enables simultaneous testing of multiple concentrations of molecular modifiers for barite dissolution, thus greatly reducing both screening time and the number of individual experiments required. Here we characterized the growth of seed crystals within the channels of the microfluidic device. Performing bulk crystallization studies in a microfluidic device allows individual crystals to be tracked over time and across a broad range of conditions. Thus, microfluidic devices can be used as a platform for rapid parametric analyses of anisotropic crystal growth at a macroscopic scale.

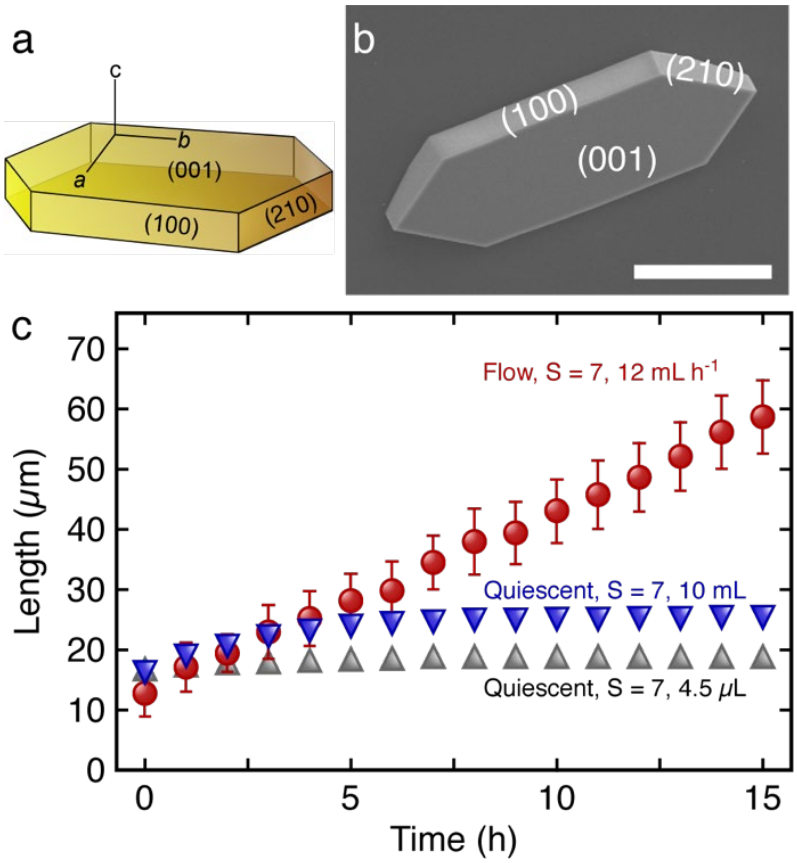

Figure 15. (a) Barite schematic with crystallographic indices labeled. (b) Barite crystal synthesized at room temperature. Scale bar is equal to 15 µm. (c) Barite crystal [010] length over time. The error bars for the quiescent experiments are smaller than the symbol size.

2.7 Crystal growth in quiescent and flow conditions.

During seeded bulk crystallization experiments in supersaturated solution (S = 7) under quiescent conditions, the rate of crystal growth decreases over time, leading to the emergence of a plateau in crystal size as solute is incorporated into the crystals (blue triangles in Fig. 15). Identical experiments at higher solute concentration (S = 10, Fig. S3) extend the duration of crystal growth beyond what is achieved in less supersaturated media, resulting in larger crystals.

Seeded growth in the small microchannel volume (ca. 4.5 µL) under quiescent conditions reveals a twofold reduction in the growth kinetics of barite compared to

measurements in a batch process using larger volume (20 mL) vials. Barite crystals grown at $S = 7$ in the microfluidic channels (grey triangles in Fig. 15c) increase only slightly in size over time, commensurate with the rapid depletion of solute from the growth solution in a smaller volume. This observation confirms that the relatively small volume of each individual microchannel leads to a more rapid reduction of the driving force for crystal growth. Furthermore, we observe that the growth rate of crystals is uniform across microchannels (Fig. A4). Because concentration gradients in solute would generate corresponding gradients in crystal number density and size,[57, 148, 154, 162-164] which are not observed in these measurements, this result confirms that aqueous solutes are fully mixed in our device.

In addition to enabling *in situ* imaging during growth, a key advantage of microfluidic devices for studies of crystallization is the ability to generate well-defined flow conditions. Seeded crystal growth experiments confirm that faceted barite crystals can be obtained uniformly across microchannels owing to the complete mixing of inlet solutions (Fig. A4), which allows macroscopic growth kinetics to be quantified under laminar flow (for Reynolds numbers Re of $0.92 < \mathrm{Re} < 92$). To identify the transport process that controls the delivery of solute, we calculate a macroscopic Péclet number $\mathrm{Pe}_{\mathrm{macro}} = Wv/D$, where v is the average fluid velocity across the microchannel, $W = 400$ μm is the channel width, and $D = 8.47\times10^{-10}$ m^2 s^{-1} is the diffusivity of Ba^{2+} ions in water. In our experiments $\mathrm{Pe}_{\mathrm{macro}}$ varies from 10^3 to 10^5 and advection governs transport of solute across microchannels,[164] in accord with the uniformity in crystal size observed across the width of the channel. Under flow of supersaturated solution, the driving force for crystallization is constant because solute is continuously replenished; therefore, seeded

growth in the microfluidic device under continuous flow and the same solute concentration (S = 7, red circles in Fig. 15c) results in crystals of sizes much larger than those produced via quiescent batch synthesis (S = 7, blue triangles in Fig. 15c). The length of crystals grown under flow increases linearly with time, indicating that the constant supersaturation produces a steady driving force for crystal growth.

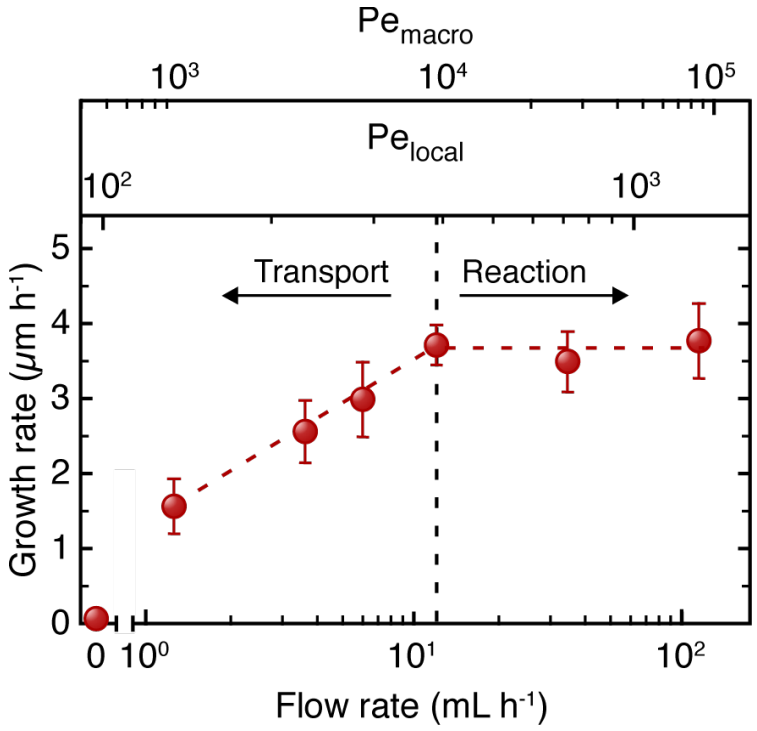

Figure 16. Effect of flow rate on seeded growth of barite. The growth rate (left axis) was measured by linear regression of length versus time data sets over 3 h in microchannels. Dashed lines are fits in each regime and error bars span two standard deviations.

The fluid flow rate affects crystal growth kinetics during continuous crystallization processes. Microfluidics enables the rate of solute delivery to be tuned via the flow rate in the laminar regime. In this regime, the boundary layer thickness δ defined as

$$\delta = 5\left(\frac{D}{\nu}\right)^{\frac{1}{3}}\left(\frac{Wx}{Re}\right)^{\frac{1}{2}} \qquad \text{Eq. (2)}$$

on a crystal of length x in a square channel of width W is proportional to $Re^{-1/2}$.[165-167]

Increasing the flow rate narrows the boundary layer and thereby reduces the time for solute to diffuse to the crystal surface. Thus, increasing the flow rate of barite growth solution is anticipated to lead to an increase in crystal growth kinetics until the growth rate is limited by the rate at which solute incorporates in the crystal surface. In a reaction-controlled regime, the crystal growth kinetics reflect adsorption/desorption of solute ions/molecules at the crystal surface established by supersaturation.

We investigate the relative importance of transport versus surface kinetics by varying the flow rate in the microfluidic device. The rate of crystal growth increases monotonically when the flow rate is lower than 12 mL h^{-1} (Re < 9.2) (Fig. 16). This result indicates that the rate of solute delivery to the crystal surface controls the crystal growth rate. When flow rates are higher than 12 mL h^{-1} (Re > 9.2), the barite growth rate plateaus at 4 μm h^{-1} and does not change even when the flow rate is further increased. The independence of crystal growth rate from flow rate indicates a transition to a reaction-controlled regime on the macroscopic scale.

The macroscopic Péclet number, describing the diffusion of solute across the channel, ranges between $10^3 < Pe_{macro} < 10^5$. Crystallization typically depends on diffusion of solute through the stagnant boundary layer near the crystal surface. We define a local Péclet number $Pe_{local} = \delta v/D$, where the relevant length scale is the boundary layer thickness δ (Eq. (2)),[168] that ranges between $140 < Pe_{local} < 1400$. When flow rates are low (Re < 9.2, $140 < Pe_{local} < 435$), crystal growth is controlled by the rate of delivery of solute. Pe_{local} is high in this regime, suggesting that bulk advection still governs solute transport. The dependence of growth kinetics on flow rate suggests that crystal growth is under mixed transport-surface kinetic control. The well-defined flow conditions in the microfluidic

device allow us to identify a flow rate regime where mass transport limitations are minimized and crystal growth is predominantly governed by surface kinetics.

2.8 Inhibition of barite growth using a molecular additive.

DTPA is a common chelating agent for divalent cations, including barium, and is used commercially to treat scale mineralization.[122, 133] Introducing this commercial scale inhibitor in microfluidic growth experiments retards barite growth preferentially along the [010] direction of the crystal, as revealed using time-resolved optical microscopy (Fig. 17a). The apical tips become blunted over time, suggesting that growth is inhibited along the crystal length, b-axis, due to the development of a new facet (Fig. 17a, 3 h image). Analysis of optical micrographs (Fig. A6) indicates that the new facet corresponds to the (011) plane. This result, coupled with a decrease in aspect ratio (Fig. A6), suggests that DTPA preferentially binds to the (011) facet of barite. To understand the effects of DTPA on barite growth, we compare to earlier studies using another chelating agent, ethylenediaminetetraacetic acid (EDTA), which shares a similar backbone structure with DTPA but contains three fewer CH_2 groups, one fewer amine moiety, and one fewer carboxylic acid group. Carboxylates such as EDTA and DTPA are often assumed to modify crystal growth by forming complexes with divalent cations and lowering the supersaturation. At low modifier concentration, however, we observe that DTPA principally inhibits barite crystallization through adsorption on crystal surfaces, which impedes solute incorporation. Adsorption of EDTA was reported to be energetically more favorable on the (011) facet of barite.[129, 134] This comparison between two crystal growth modifiers suggests that both polyprotic acids appear to operate under similar modes of action, despite differences in their physicochemical properties.

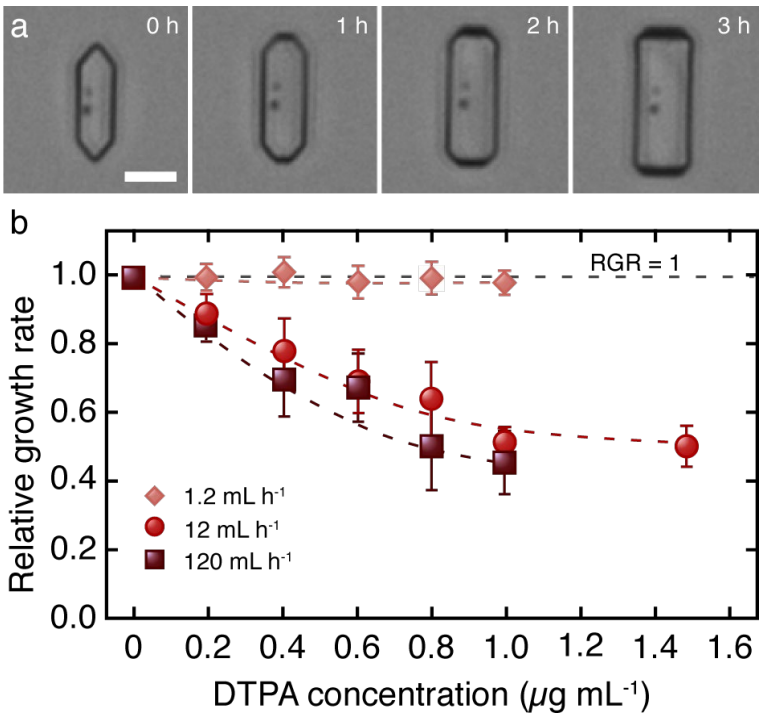

Figure 17. (a) Time-elapsed optical micrographs demonstrating the effects of 1 μg mL^{-1} DTPA on barite growth under solution flow. The scale bar for all images is equal to 10 μm. (b) Relative growth rate (RGR) as a function of DTPA concentration.

Quiescent studies confirm that DTPA is an inhibitor of barite crystallization. Given that fluid flow also affects barite growth kinetics in the laminar regime, we hypothesize that the inhibition mechanism and efficacy of DTPA may be affected by the fluid flow rate. To probe the effects of fluid flow on inhibition of barite in the presence of DTPA, we conducted *in situ* microfluidic experiments at flow regimes where growth in the absence of DTPA is controlled by either mass transport or surface kinetics. At a low flow rate (1.2 mL h^{-1}; Re = 0.92; Pe_{local} = 140) barite growth kinetics are independent of DTPA concentration (Fig. 17b, diamonds), although slight blunting of the apical tips is observed in optical micrographs (Fig. A8). The lack of dependence of crystal growth on modifier concentration at low flow rate is indicative of mass transport limitations (i.e., the organic

modifier exhibits a slower rate of diffusion compared to more mobile Ba^{2+} and SO_4^{2-} ions). The longer diffusion time for DTPA, relative to the mobile ions, suggests that its coverage on crystal surfaces at thermodynamic equilibrium may be difficult to achieve even at high DTPA concentrations; this idea is consistent with the inability of DTPA to inhibit crystal growth at low flow rates. Conversely, time-resolved optical micrographs of barite crystal growth acquired at a higher flow rate of 12 mL h^{-1} reveal that the crystal morphology changes with increasing DTPA concentration to generate new {011} facets (Fig. A6), suggesting that DTPA preferentially binds to sites located on {210} surfaces.

Relative growth rate (RGR) and crystal morphology of barite depend more strongly on DTPA concentration at higher flow rates. At a flow rate of 12 mL min^{-1} (Re = 9.2; Pe_{local} = 435), the RGR of barite initially decreases monotonically with increasing DTPA concentration and reaches a plateau near 1 μg mL^{-1} DTPA (Fig. 17b, circles) that corresponds to 55% inhibition of crystal growth. The plateau in RGR suggests that inhibitor coverage on crystal surfaces approaches thermodynamic equilibrium, and that barite growth in this fluid flow regime is kinetically controlled by advection of solute to growth sites on the crystal surface (Pe_{local} = 435). The molar ratio of DTPA/Ba^{2+} is less than 0.005, indicating the effect of modifier sequestration of Ba^{2+} ions is negligible compared to those imposed by DTPA-crystal interactions.

Under the highest flow rate condition tested (120 mL h^{-1}; Pe_{local} = 1400; Re = 92), the RGR again decreases with increasing DTPA concentration (Fig. 17b, squares), reaching a maximum *ca.* 60% inhibition of barite growth. An order of magnitude increase in flow rate leads to a negligible increase in DTPA efficacy (as the RGRs at 12 and 120 mL h^{-1} are equivalent within the error of measurement). Collectively, these studies indicate that barite

crystallization at flow rates of 12 mL h^{-1} or higher (Re ≥ 9.2) in the laminar regime is controlled by surface kinetics. Inhibitor efficacy is influenced by flow, which suggests that eliminating mass transport limitations is necessary to maximize barite inhibition. Overall, the microfluidic platform allowed us to elucidate preferential binding modes of DTPA on barite in real time and confirm that an increase in flow enhances inhibition of barite growth.

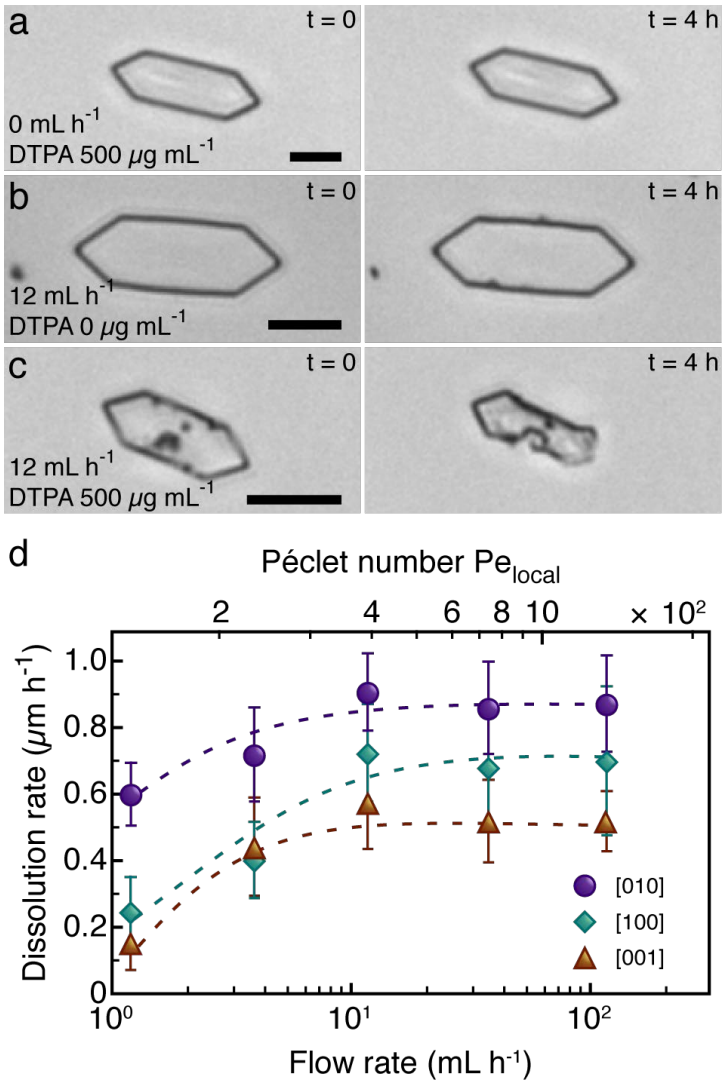

Figure 18. Optical micrographs of barite seed crystals (a) in the presence of 500 µg mL^{-1} DTPA and quiescent conditions, (b) in the absence and (c) in the presence of DTPA under the same flow rate. (d) Dissolution rate of barite as a function of flow rate.

2.9 Barite dissolution in the presence of DTPA.

Barite dissolution has been widely investigated in the presence and absence of organic ligands. In pure water under flow, the basal surface of barite is mostly stable with a slow rate of formation of shallow etch pits.[92, 135] In ligand-promoted dissolution, the Ba-DTPA complex is most stable at pH ≥ 12 where DTPA is fully deprotonated. Due to this stability, $DTPA^{5-}$ anions chelate surface barium and weaken the Ba-SO_4 bonds.[92] DTPA may coordinate with multiple surface barium atoms and promote dissolution in an aqueous environment with desorption of the surface being the rate-limiting step.[89, 91, 98, 135, 169-171] Dissolution ultimately occurs *via* hydration of surface barium atoms. The effects of flow rate, however, have remained elusive and the magnitude of the flow velocity is likely to affect dissolution kinetics.

We investigated the importance of flow and the role of DTPA for the dissolution of barite in microchannels using alkaline solutions (10 μM NaOH, pH 9) in the absence of barium sulfate. In quiescent conditions, exposure to DTPA for 4 h negligibly affected the morphology and size of barite crystals (Fig. 18a). This result is inconsistent with previous reports of DTPA-promoted dissolution in quiescent conditions with larger reservoir volumes,[133] suggesting that the finite volume (4.5 μL) of solution in the microchannels under quiescent conditions may not contain sufficient amounts of DTPA to promote macroscopic dissolution. Interestingly, barite crystals exposed to flow using the same alkaline solution, but without DTPA, did not exhibit macroscopic changes in size or morphology (Fig. 18b). This result, however, is consistent with previous reports that indicate a low solubility of barite in alkaline solution.[98] By contrast, striking differences in final barite crystal morphology and size are observed when 500 μg mL^{-1} DTPA is flowed

through the seeded microchannels. Optical micrographs reveal significant deterioration of the seed crystal over a 4 h experiment (Fig. 18c and A9). Although DTPA is not fully dissociated ($DTPA^{4-}$) at the pH of our experiments, these results are in accord with bulk dissolution experiments in the presence of stirring, which demonstrate deep etch pit formation and crystal dissolution at higher pH where DTPA is fully dissociated and $DTPA^{5-}$-Ba^{2+} chelation is optimal.[97]

We characterized the evolution of barite seed crystal length, width, and thickness under flow of 500 μg mL^{-1} DTPA at various rates ($0 < Re < 92$; $0 < Pe_{local} < 1400$). Dissolution occurs fastest along the [010] direction and appears to be nearly independent of flow rate. By contrast, barite mass loss along the [100] and [001] directions increases with flow rate and plateaus at rates above 3.6 mL h^{-1} ($168 < Pe_{local} < 1400$) indicating surface reaction-controlled kinetics (Fig. 18d). These results differ from dissolution kinetics reported for barite in a rotating disk, which do not depend on flow rate within the laminar regime.[172] These differences may be attributed to disparate experimental conditions. For barite, fast dissolution along the b-axis is consistent with microscopic observations of ligand-promoted dissolution in which etch pits propagate along the [010] direction, suggesting these microfluidic experiments may provide insight on microscopic surface dissolution. In contrast to reported etch pit formation rates where propagation along the *b*-axis is 2.5 times greater than along the *a*-axis, dissolution rates along the [010] direction are comparable to rates in the [100] direction under flow in microchannels.[92]

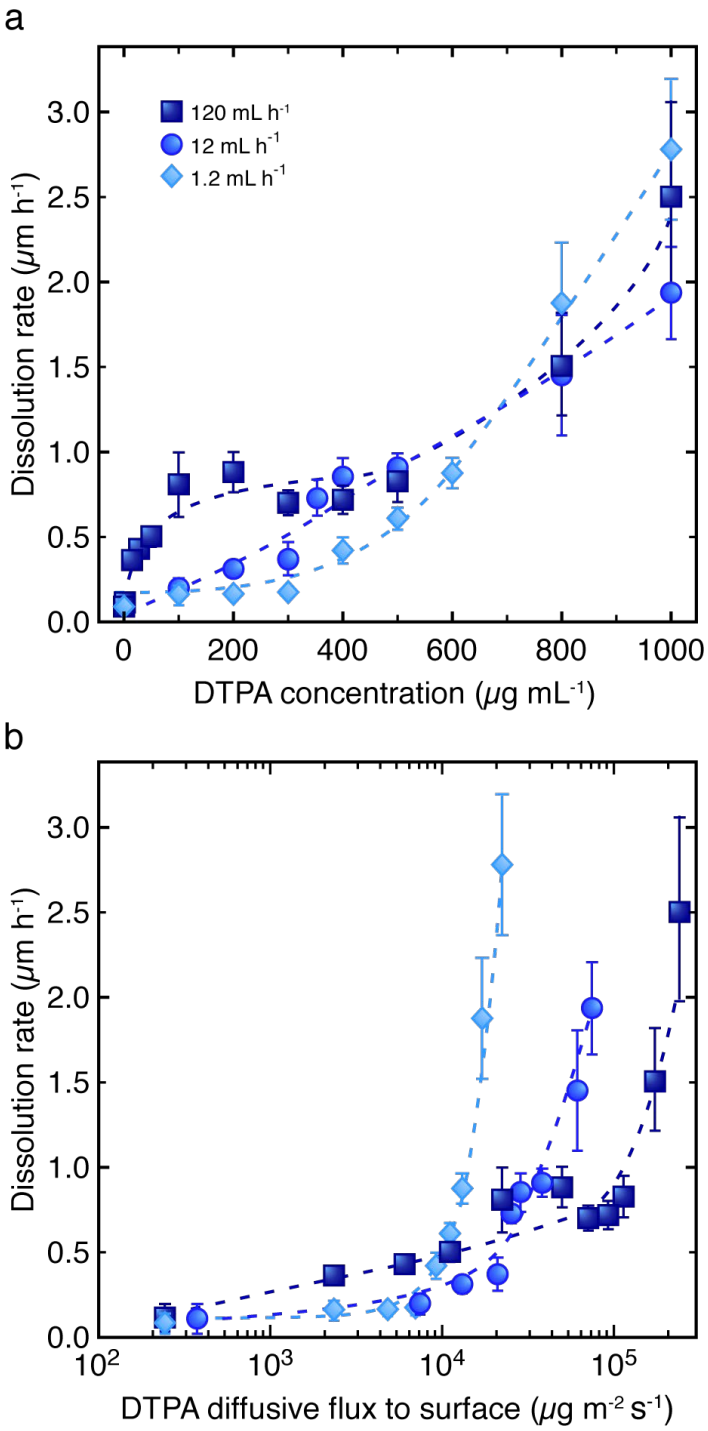

Figure 19. Rate of dissolution of barite seeds as a function of **(a)** DTPA concentration and **(b)** diffusive flux of DTPA to the crystal surface. Error bars represent two standard deviations and dashed curves are guides to the eye.

In separate experiments, we varied the DTPA concentration of undersaturated solutions (S = 0) and measured the extent of barite dissolution at several flow rates (Fig. 19). The alkalinity of solutions in these experiments was adjusted to pH = 9, the approximate upper limit for environmentally acceptable standards,[173] such that DTPA is not fully deprotonated (i.e., the predominant species is $DTPA^{4-}$). These conditions are in contrast to those of previous DTPA-promoted dissolution experiments that were carried out at higher pH (both quiescent and stirred), allowing for full deprotonation.[92, 97, 133] Increasing DTPA concentration enhances the dissolution rate for all flow rates evaluated in this study ($0 < Pe_{local} < 1400$). At a low flow rate (1.2 mL h^{-1}), the rate of dissolution increases monotonically with increasing DTPA concentration. At a higher flow rate (12 mL h^{-1}), the dissolution rate increases linearly with concentration. Under much higher flow rate (120 mL h^{-1}), the rate of barite dissolution initially increases sharply with concentration, then increases linearly at higher flow rates. At concentrations below 500 µg mL^{-1} dissolution is enhanced by an increase in flow rate. At higher concentrations, dissolution is linearly dependent on DTPA concentration and becomes independent of flow rate. While the underlying physics governing the trends in dissolution rates at lower DTPA concentrations remains unknown, these results indicate that the dependence of dissolution kinetics on DTPA concentration is influenced by changes in flow rate within a finite concentration regime.

We calculated the boundary layer profiles for barite under each flow rate tested experimentally (Fig. A10 – A13) and the diffusive flux of DTPA to the crystal surface (Fig. A14), $J = Dc_o/\delta$, to probe the dissolution kinetics of barite. For a fixed flow rate, the diffusive flux is dependent on the change in DTPA concentration from the bulk to the

crystal surface. Given that an increase in either flow rate or DTPA concentration enhances dissolution, we hypothesize that dissolution is controlled by the mass flux of DTPA to the surface. In support of this hypothesis, the rate of dissolution for barite is enhanced with increasing diffusive flux under all flow rates. A majority of studies in literature[91-92, 169] use DTPA concentrations that are 10- to 100-times greater than those employed in this study, and observe that the dissolution rates of barite first increase and then decrease with concentration. The results of our study suggest that there may be different, albeit unknown, molecular processes governing DTPA-induced dissolution of barite crystals. Additional microscopic studies are needed to fully resolve the physical processes governing the behavior in Fig. 19; nevertheless, barite dissolution is markedly enhanced under specific flow conditions that depend on DTPA concentration.

We presented a microfluidic platform for investigating bulk crystallization and dissolution kinetics of barite in dynamic flow conditions. We systematically investigate hydrodynamic contributions by varying the flow rate during crystallization of barite in the presence and absence of the scale inhibitor DTPA, and obtain time-resolved characterizations of crystal morphology for each case. Under flow of supersaturated growth solution, barite growth undergoes a transition from mass-transport-limited to surface-reaction-limited kinetics at a local Péclet number of ~250. Growth studies in the presence of DTPA reveal that this transport limitation also holds for inhibition of barite at low concentrations of DTPA. In a reaction-limited growth environment, DTPA induces the formation of a new facet, which remains stable through the duration of experiments. In undersaturated conditions, barite dissolution is enhanced with increasing diffusive flux of DTPA to the crystal surface. At low DTPA concentrations, however, our results suggest

that dissolution may occur *via* distinct, unique molecular processes that remain to be determined. Identifying these processes likely requires the use of methods, such as atomic force microscopy experiments or molecular simulation, that are capable of resolving dissolution at an atomic level. This microfluidic platform can be extended to characterize the kinetics of crystallization in systems in which hydrodynamics may play a significant role. Barite was chosen for these studies on the basis of its commercial relevance to demonstrate how microfluidics coupled with microscopy could serve as a quantitative method for determining crystal growth and inhibition under dynamic flow conditions. As one example, these techniques could be used to assess the transient surface area for materials for which kinetic parameters are difficult to estimate or determine. Together, these techniques offer an opportunity to investigate the crystal growth kinetics for other problematic and geochemically relevant biominerals under a controlled flow regime environment.

Chapter 3: Green Alternatives for Barite Scale Dissolution

Chemical options for dissolving industrial scale include using chelating agents such as diethylenetriaminepentaacetic acid (DTPA), ethylenediaminepentaacetic acid (EDTA), and other aminopolycarboxylic acids.[94, 99, 118-119] Although many studies have investigated the dissolution of barite with commercial additives (termed demineralizing agents),[73-76, 91-93, 97, 133, 135, 169, 174-175] there is very little fundamental knowledge of dissolution mechanisms to aid in the rational design of new and improved alternatives. Moreover, commercial formulations used to treat barite scale require highly alkaline media (pH > 12)[117, 176], which has a negative impact on the environment.[120] Therefore, it is advantageous to identify a new class of green (i.e., biodegradable) demineralizing agents and develop improved understanding of their modes of action to establish well-defined guidelines for future design of scale dissolvers.[177] More broadly, this knowledge may also inform a broader spectrum of applications for applying (organic) growth modifiers to control crystallization, including (but not limited to) human diseases (e.g., kidney stones, malaria, atherosclerosis) and biomineralization (e.g., bone, nacre, coral).[48, 178-184]

Most demineralizing agents explored in literature are small molecules. Some studies have shown evidence of synergistic cooperativity when combining a newly assayed demineralizing agent with either EDTA or DTPA.[94, 116, 119] More recently, certain 18-membered macrocycles have been shown to be effective chelators of Ba^{2+} ions with efficiencies comparable to DTPA.[90] Studies have also shown that barite solubility is enhanced in the presence of bacteria, which is attributed to their putative generation of organic acids to chelate Ba^{2+} ions.[185]

In contrast to small molecules, polymers potentially offer improved efficacy arising from the presence of multiple functional groups along the backbone. The use of polymeric demineralization agents has been investigated for calcite, another mineral commonly associated with scale formation. Studies of calcite crystallization in the presence of polyaspartic acid and alginate found that these polymers are effective demineralizing agents.[77, 186] By examining macroscopic changes in crystals during bulk dissolution, these studies identified polymer specificity for distinct facets of calcite, but were unable to provide mechanistic understanding into their mode(s) of action at a molecular level. Alginate is of particular interest owing to its abundance in brown algae,[187] and its extensive use in the food, pharmaceutical, and biomedical industries.[188-189] Alginate is composed of mannuronic acid and guluronic acid residues, both of which participate in the gelling mechanism. Typically, two adjacent guluronic acid residues are reported to bind a single divalent cation through the formation of a buckling structure in the polymer, whereas mannuronic acid incorporation in the sequence reportedly provides flexibility in the polymer chain to facilitate gelation.[190]

In this study, we test the hypothesis that multiple functional moieties of polysaccharides, including the acid and alcohol side groups of alginate and related analogues, are efficient binding groups for barite crystal surfaces. Comparison of seven biopolymers (both polysaccharides and their acid derivatives) reveals that alginate dissolves barite at rates much greater than other candidates. Moreover, direct comparison between alginate and DTPA shows that alginate has greater efficacy in neutral media, whereas the combination of both demineralizing agents in alkaline media leads to synergistic cooperativity. The efficacy of barite dissolution is quantified at the macroscopic

level using a microfluidic device that allows for the analysis of average dissolution kinetics in the absence and presence of demineralizing agents, showing that the rates of dissolution can be markedly enhanced under flow conditions. These studies are complemented by *in situ* atomic force microscopy to probe specific interactions between demineralizing agents and crystal surfaces at a molecular level, and to extract mechanistic details of their modes of action. These studies show that alginate is a highly efficient barite scale dissolver. Moreover, we uncover new insights for its potential replacement of long-standing commercial dissolvers.

3.1 Screening Biopolymers as Demineralizing Agents

We examined a wide array of biopolymers (Figure 20) as potential green demineralizing agents for barite. The macromolecules selected for this study can be subdivided according to their primary functional groups: alcohols (I), carboxylates (II – IV), and sulfates (V – VII). Barite dissolution kinetics were assessed by time-resolved optical imaging of multiple single crystals under quiescent conditions and in a neutral (pH 7) medium containing an equal mass of each additive (200 μg mL^{-1}). Crystal dissolvers can be grouped into three categories based on their efficacy, as shown in Figure 20. The least effective polysaccharides identified in our measurements were carboxymethyl cellulose (II, where R = CH_2CO_2H, H, etc.), κ-carrageenan (V), and ι-carrageenan (VII). Three additives exhibited moderate efficacy: agarose (I), polygalacturonic acid (III), and λ-carrageenan (VI). Each of these molecules is decorated with chemically distinct binding groups (-OH, $-COO^-$, $-SO_3^-$), indicating that all three functional moieties are influential in barite dissolution. Interestingly, only one of the polysaccharides, alginate (IV), was a standout in its ability to dissolve barite crystals. Alginate contains similar functional groups

as polygalacturonic acid (i.e., alcohols and carboxylates); however, these molecules differ in their stereochemistry. Notably, alginate contains two monomers, mannuronic and guluronic acids, that alter the spatial distribution and orientation of the carboxylate functional groups interacting with barite crystal surfaces.

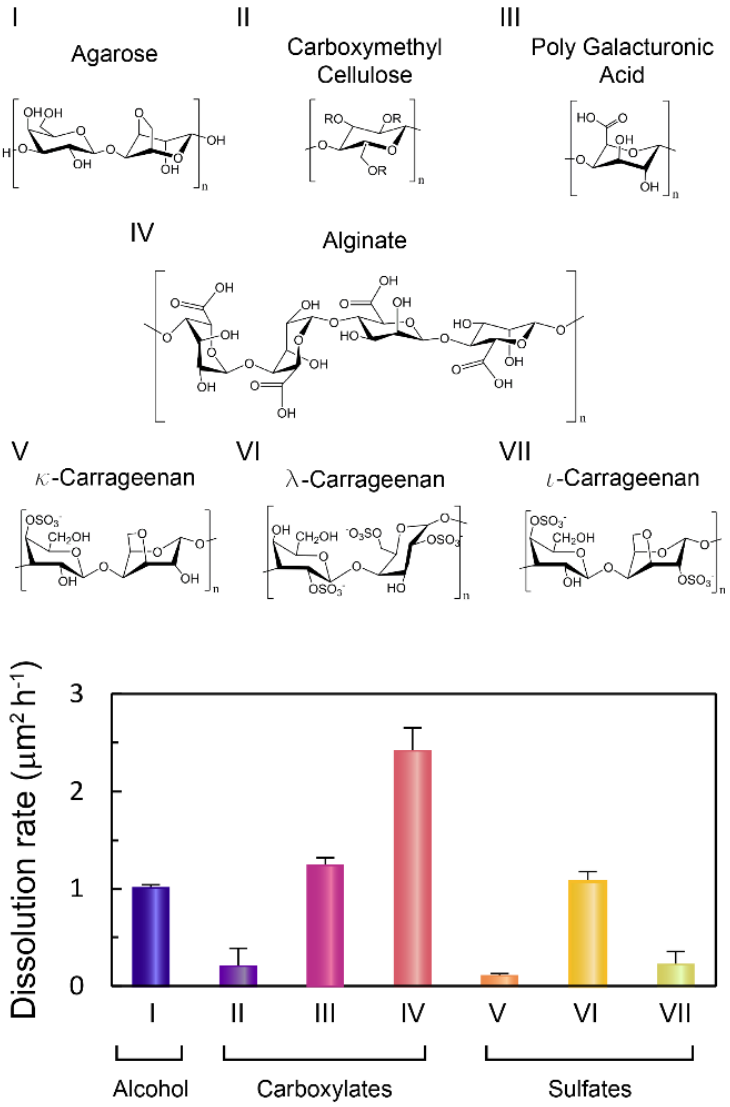

Figure 20. (top) List of molecules with (I) alcohol, (II-IV) carboxylate, and (V-VII) sulfate functional moieties. (bottom) Rate of barite crystal dissolution in the presence of 200 μg mL^{-1} of additives in pH neutral aqueous media at 21 ±1 °C (quiescent conditions).

We examined the effect of alginate on barite dissolution in comparison with a commercial dissolver, DTPA, used as a benchmark. The kinetics of barite dissolution in the presence of 200 μg mL^{-1} additive at neutral pH and quiescent conditions was measured using elemental analysis (ICP-MS) of the supernatant to track the release of Ba^{2+} ions over time (Figure 21a). The nonlinear dissolution profile of alginate starkly contrasts to the nearly flat profile of DTPA. In the presence of alginate, the concentration of free Ba^{2+} ions increases rapidly at early times owing to the high degree of undersaturation, but approaches a plateau at later times as the solution becomes saturated (i.e., the solubility product K_{sp} for barite at 25 °C is 1.08×10^{-10}).[121] The thermodynamic upper limit of free Ba^{2+} ions can be enhanced by the presence of chelating agents. Using a titration technique adapted from a reported protocol,[90] we confirmed that DTPA sequesters free Ba^{2+} ions from solution with moderately better efficiency than alginate (Figure A15).

Barite crystals grown in the absence of additives exhibit a coffin-shape habit with basal {001}, side {100}, and apical {210} facets (Figure 21b). After exposure to alginate at neutral pH, barite dissolution is observed at the intersecting corners of the (100) and (210) faces, whereas the (001) surface displays striated etch pits elongated in the [010] direction (Figure 21c). Time-resolved optical images acquired during quiescent bulk dissolution over a 5-day period reveal anisotropic etching that seemingly originates from the corners of the barite crystal (Figure 21d). In the presence of DTPA at pH 7, we observe mild dissolution over a 5-day period leading to dissolution features originating from the corners (Figure 21e), similar to those observed for alginate.

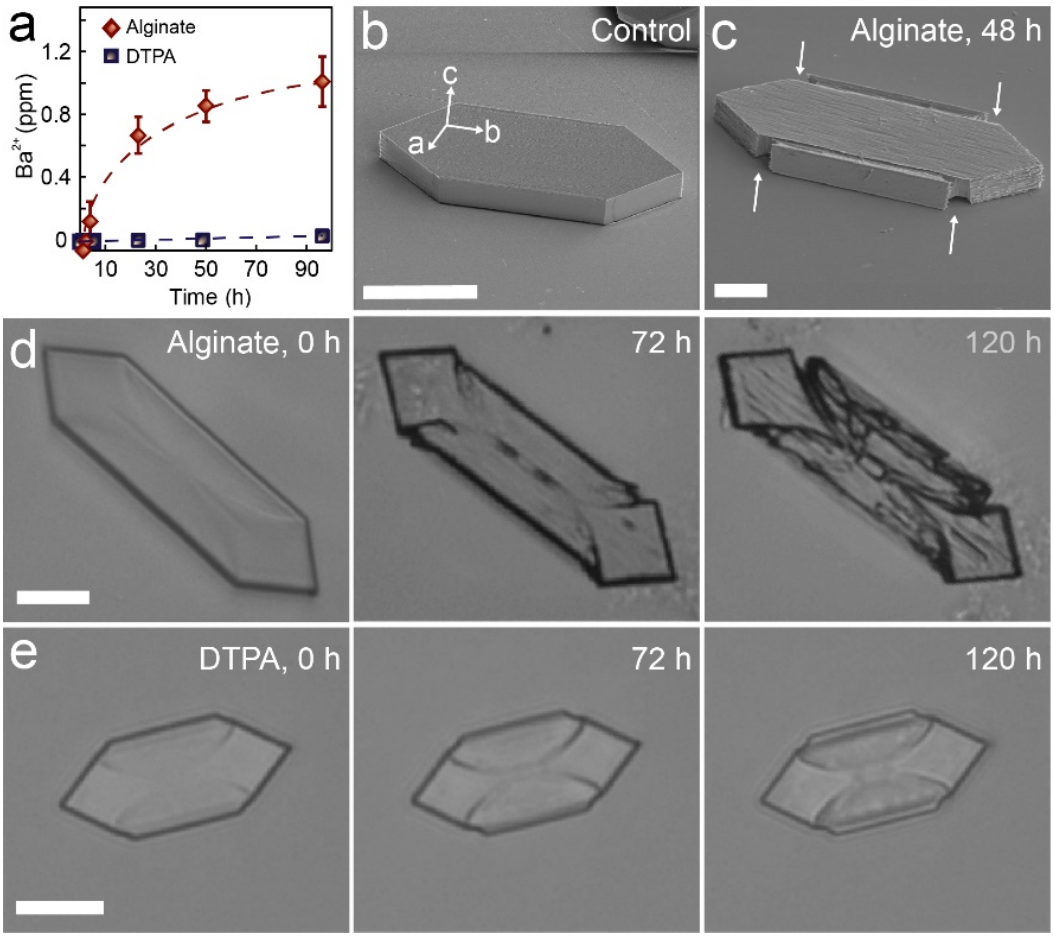

Figure 21. (a) Bulk assays of barite dissolution under quiescent conditions. (b and c) Scanning electron micrographs of barite crystals before and after exposure alginate. (d and e) Optical micrographs of barite crystals partially dissolved in the presence of additives.

It has been reported that the efficacy of DTPA as a barite dissolver is highly pH dependent.[76, 92] DTPA is composed of five carboxylic acids (pKa = -0.1, 0.7, 1.6, 2.0, and 2.6) and three amine groups (pKa = 4.3, 8.6, and 10.5).[191] A speciation model (Figure 22a) shows that all five of its carboxylates are dissociated and all three of its amines remain in free-base form (i.e., $DTPA^{5-}$) at high pH (> 11). At neutral conditions, however, DTPA is zwitterionic. This property may explain its poor efficacy to dissolve barite under these conditions. For instance, the presence of positively charged amines can potentially lead to the formation of intramolecular hydrogen bonds ($C_3N\cdots H\cdots O_2C$) that render acid groups

on DTPA inaccessible for binding to barium sites on crystal surfaces. Alternatively, the positive charges on the amines may interact with sulfates on barite crystal surfaces, which have a net negative charge in aqueous media, as confirmed by zeta potential measurements (Figure A16).

3.2 Molecular Dynamics Calculations of DTPA-Mediated Barite Dissolution

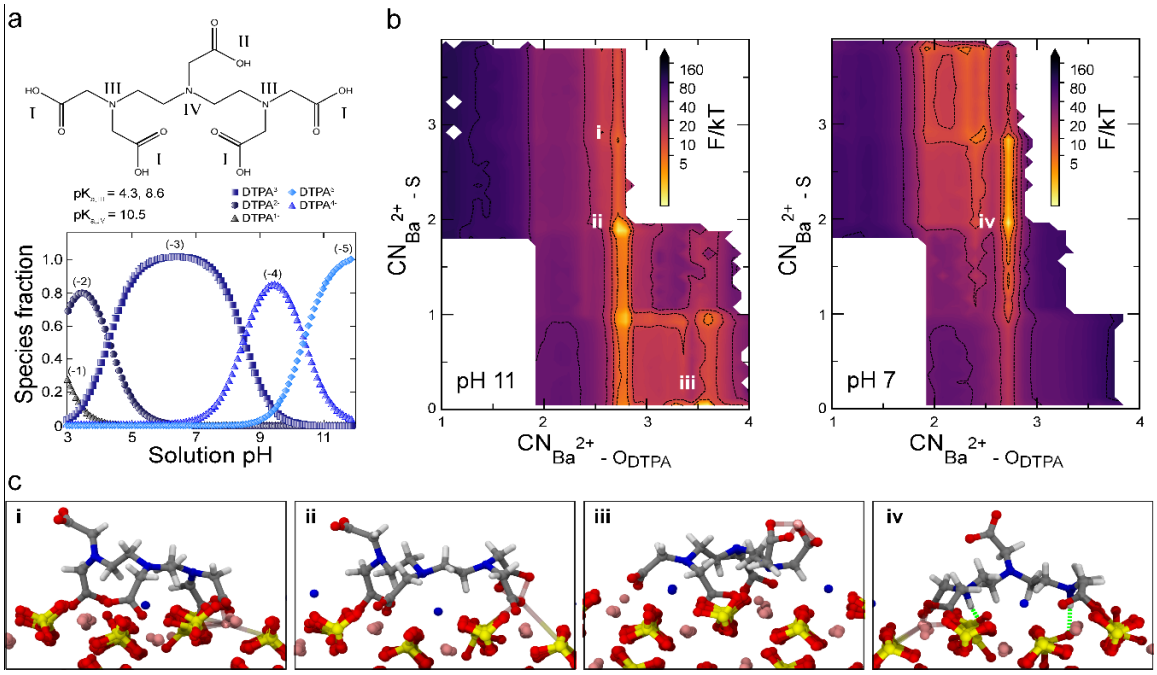

Figure 22. (a) (top) Molecular structure of DTPA.[191] (bottom) Speciation model for $DTPA^{n}$. (b) – (c) Free energy surfaces from USMD simulations of DTPA-assisted detachment of Ba^{2+} ions from the barite (001) surface at pH 11 and 7 (left and right panels, respectively).

To rationalize these observations, we performed umbrella sampling molecular dynamics (USMD) simulations[192-194] to investigate the mechanism of DTPA-assisted detachment of Ba^{2+} ions from the barite (001) surface. The USMD simulations were used to compute the free energy surface (FES) associated with two coordination numbers (CNs), $\{CN_{Ba^{2+}-S}, CN_{Ba^{2+}-O_{DTPA}}\}$, characterizing the extent of coordination of a central Ba^{2+} ion by S atoms in the barite crystal and by O atoms on DTPA's carboxyl groups (Figure 22b), respectively. Hence, regions in the FES where the values of $CN_{Ba^{2+}-S}$ and $CN_{Ba^{2+}-O_{DTPA}}$

are high and low, respectively, indicate that Ba^{2+} is strongly coordinated by sulfur atoms in barite and thus still attached to the crystal surface. Conversely, low values of $CN_{Ba^{2+}-S}$ and high values of $CN_{Ba^{2+}-O_{DTPA}}$ denote states were Ba^{2+} is (partially) detached from the barite crystal and predominately coordinated in DTPA's carboxyl groups. The free energy calculations suggest that DTPA promotes detachment through several metastable intermediate states. At pH 11, the fully detached state at $\{0.1, 3.6\}$ is at significantly lower free energy than the bound state at $\{4, 2.75 <\}$, indicating that detachment is highly favorable. The detachment process is facilitated by metastable partially unbound states at $\{1.9, 2.75\}$ and $\{0.9, 2.75\}$ (Figure 22b, i and ii) that are separated by low energy barriers ($< 5\ kT$), which can be overcome by thermal fluctuations. At pH 7, the stability of the intermediate state at $\{1.9, 2.75\}$ (Figure 22b, iv) is enhanced and there are relatively large free energy barriers (ca. $15 - 20\ kT$) along the pathways leading to complete detachment, implying slower detachment consistent with the slower dissolution rate observed in experiments. Inspection of the molecular configurations reveal that the state at $\{1.9, 2.75\}$ is stabilized at pH 7 by the formation of hydrogen (h)-bonds between DTPA's terminal amines and surface sulfate groups that are not present at pH 11 due to the deprotonation of the amine groups (Figure 22c, iv). These h-bonds inhibit the carboxylate group on DTPA from pulling away from the surface and thus detaching the coordinated Ba^{2+} ion.

3.3 Barite Dissolution Under Flow

Using an *in situ* microfluidic device, conditions such as solution flow rate, pH, and additive concentration were systematically varied to quantify their effect(s) on barite dissolution. In these studies, the change in basal surface area (i.e., projected area measured normal to the (001) surface) was used to assess the rate of dissolution. First, measurements

were performed over a range of flow rates (0 – 120 mL h^{-1}) and in the presence of 200 μg mL^{-1} additive (alginate or DTPA) at neutral pH. Consistent with quiescent conditions, measurements with DTPA showed little effect, whereas alginate increased the barite dissolution rate by approximately one order of magnitude (Figure 23a). Measurements of the crystals in alginate revealed that the rate of barite dissolution increased proportionally with flow rate until reaching a plateau at around 12 mL h^{-1}. This plateau indicates the transition from transport-limited to reaction-limited dissolution kinetics, similar to our previous study of barite growth.[195]

Holding the flow rate fixed at 12 mL h^{-1}, the rate of barite dissolution was measured in microfluidic channels at varying solution pH (Figure 23b) for both additives. In the presence of 200 μg mL^{-1} DTPA, barite dissolution increased monotonically with increasing pH above pH 5. The effect of DTPA becomes noticeable once the pH reaches a value where the speciation model (Figure 22a) indicates appreciable quantities of $DTPA^{4-}$ (pH 9) and $DTPA^{5-}$ (pH 11). Conversely, alginate dissolves barite over a broader range of alkalinity (pH 3 – 7) where both mannuronic and guluronic acid are fully dissociated (pKa = 3.38 and 3.65, respectively).[196] Interestingly, we observed a reduction in barite dissolution at pH > 7 that cannot be easily rationalized. For instance, gel permeation chromatography (Figure A17) and infrared spectroscopy (Figure A18) do not show any evidence of alginate chemical degradation after incubation in highly alkaline media.[197-199] Dynamic light scattering showed no evidence of alginate aggregation over a broad range of solution pH (Figure A19), and bulk dissolution does not give any indication of unfavorable coverage effects such as repulsive adsorbate-adsorbate interactions (Figure 23c,d). Thus, the

alginate's maximum efficacy is around pH 5 and the mechanism of its decline at higher pH remains elusive.

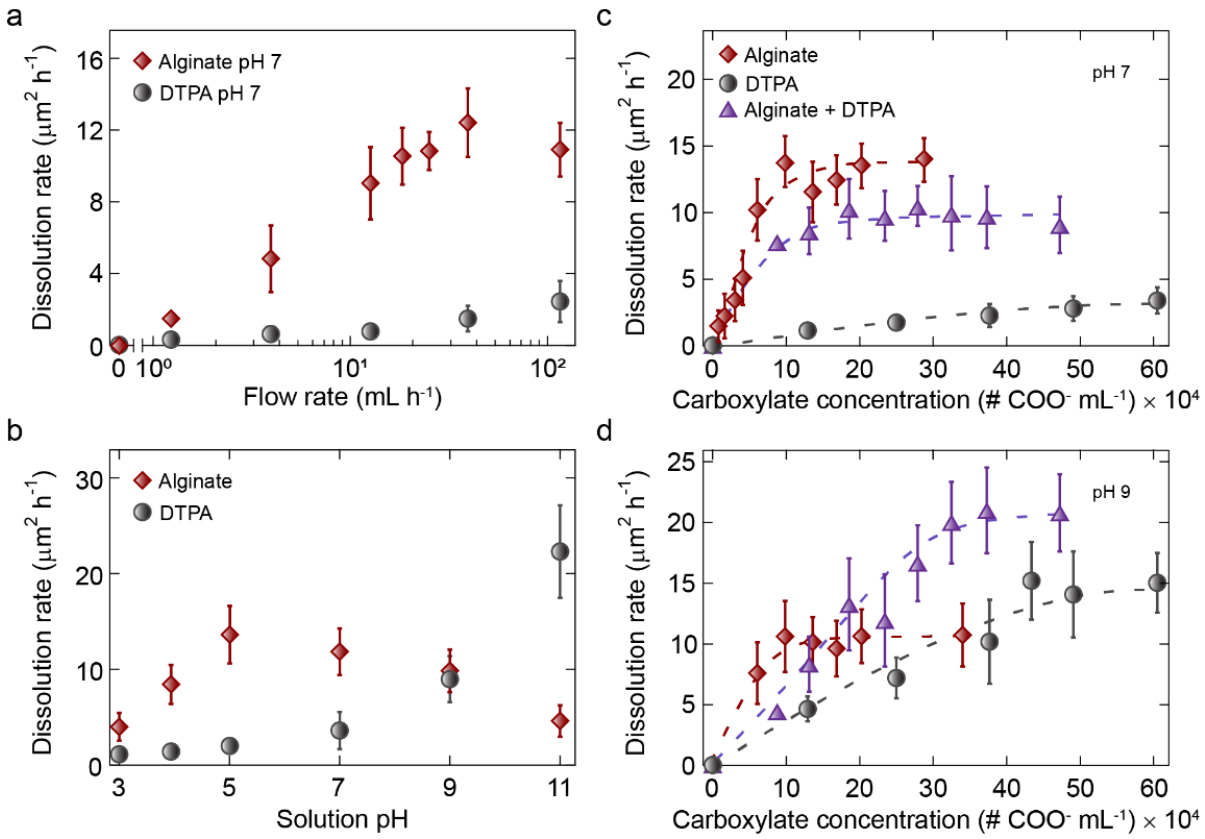

Figure 23. Microfluidic measurements of barite dissolution rate as a function of (a) flow rate and (b) solution pH, and (c and d) as a function of total dissolver concentration in microchannels under flow of solutions (pH 7 and 9) of alginate, DTPA, and 50/50 (wt%) alginate-DTPA binary mixtures.

Prior studies of crystal growth inhibition have shown that binary combinations of additives can result in either synergistic or antagonistic cooperativity.[80, 200] Here we examine the effect of using binary combinations of alginate and DTPA (50/50 by mass) on the rate of barite crystal dissolution at pH 7 (Figure 23c) and pH 9 (Figure 23d). To facilitate comparison, the concentration of each additive is reported with respect to the number of carboxylate (COO^-) groups for each dissolver cocktail. The general shape of dissolution curves is characteristic of Langmuir adsorption, where an increase in total

additive concentration results in an increased rate of dissolution until reaching a plateau (i.e., concentrations corresponding to an approximate monolayer coverage of additive(s) on crystal surfaces). Although DTPA has little effect on the rate of dissolution at pH 7, its presence nevertheless influences alginate-barite interactions given that the binary combination results in an overall lower rate of dissolution compared to alginate as the sole dissolver. These results are indicative of a mild antagonistic cooperativity.

At pH 9 we observed an unusual switch from antagonistic cooperativity at low concentration of binary dissolvers to synergistic cooperativity at higher concentrations (Figures 23d and A20). This same trend does not hold at higher alkalinity (e.g., pH 12) where binary combinations result in extreme antagonistic cooperativity (Figure A21) owing to the decreased efficacy of alginate. Although DTPA and alginate exhibited similar rates of barite dissolution at pH 9, alginate reaches its maximum efficacy at a much lower concentration of COO^- groups, indicating that it is a more potent dissolver than the commercial DTPA.

3.4 In Situ Atomic Force Microscopy Study of Barite Dissolution Mechanisms

Ex situ images of barite crystals that have been partially dissolved in alginate under quiescent conditions reveal unique dissolution features. We first focus on the dissolution of (210) and (100) side facets, which are often overlooked in studies of barite dissolution and growth owing to the anisotropy of barite crystals that makes it difficult to image these surfaces. After 24-h exposure to 200 μg mL^{-1} alginate solution at neutral pH, scanning electron microscopy (SEM) images reveal highly rough (210) surfaces with visible protrusions (Figure 24a and b). To gain molecular level insight into the mechanism of dissolution, we performed *in situ* atomic force microscopy (AFM) studies on surfaces with

exposed (210) surfaces. Time-resolved AFM images of these surfaces reveal highly corrugated steps (Figure 24c – e and A24 – A25) with an average height of 3.8 Å, corresponding to an approximate single unit cell dimension of barite. During continuous imaging, we observe dissolution layer-by-layer with each step receding at a constant rate (Figure A22). Conversely, dissolution of the (100) surface occurs by a different mechanism. The (100) facet features rectangular etch pits of varying widths and depths exceeding 60 nm, as shown in *ex situ* SEM images (Figure 24b, arrow) and AFM images (Figure 24f – h) of barite crystals dissolved in 200 μg mL^{-1} alginate. The high density of etch pits on these surfaces makes *in situ* AFM measurements of the (100) facet challenging; thus, we report *ex situ* images that seem to indicate that alginate preferentially dissolves barite in the a- and c-directions.

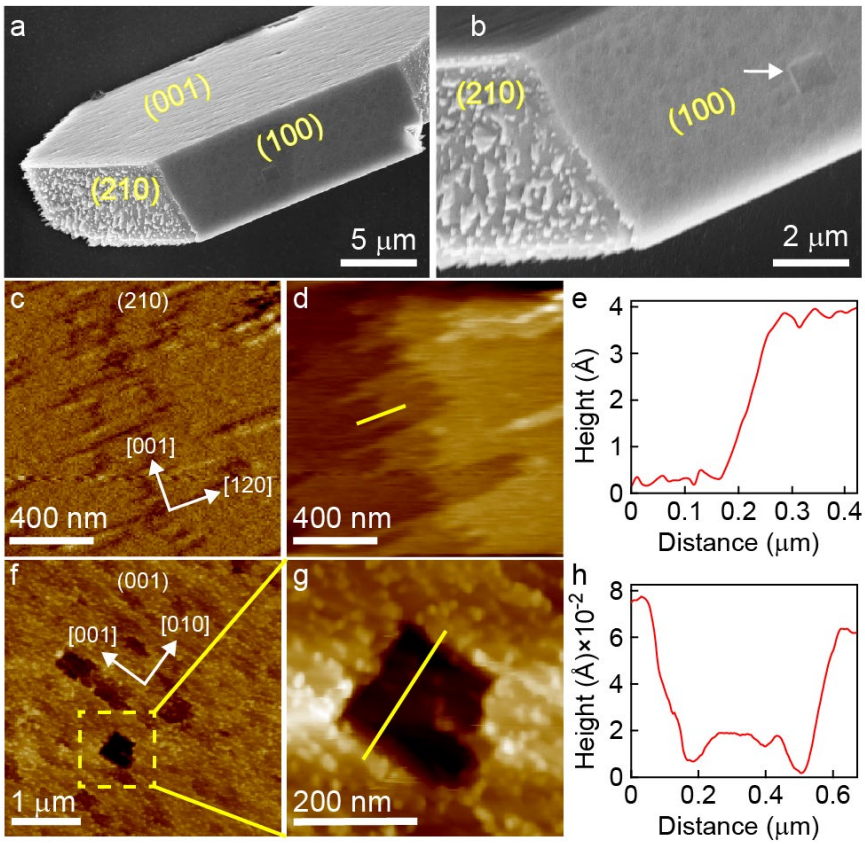

Figure 24. (a)-(b) Scanning electron micrograph of a partially dissolved barite crystal. (c – e) *In situ* measurements of (210) surface dissolution under a constant flow. (f)-(h) *Ex situ* AFM deflection image of the (100) surface.

Using *in situ* AFM, we measured barite crystal surface dissolution under constant flow (12 mL h^{-1}) for both the (001) and (210) surfaces. The results of the latter are described in the Supporting Information. Here, we focus on the basal (001) surface, where dissolution is more pronounced, and compare our findings for four distinct solutions: (i) a control of $NaOH_{(aq)}$ (pH = 9) without additives; (ii) the control modified by the addition of DTPA; (iii) an aqueous solution of alginate (pH = 7); and the control modified by the addition of alginate and DTPA (binary mixture). Time-resolved measurements of surface dissolution for the control revealed the birth and spread of triangular etch pits defined by the [010] and ⟨120⟩ directions (Figures 25a,b and A26). A representative height profile of a partially

dissolved surface shows etch pits with a depth of ca. 3.6 Å (Figure 25c), which corresponds to a one-half unit cell dimension (*c/2*). In the presence of DTPA, the etch pits exhibit an elongated triangular morphology with rounded sides where the fastest rate of dissolution occurs in the [010] direction for etch pits bounded by ⟨130⟩ and [010] edges (Figures 25d,e and A26). The height profiles of these etch pits reveal identical depths (ca. 3.6 Å, Figure 25f), indicating a layer-by-layer mechanism of dissolution. There is an inversion of etch pit orientation with each new layer owing to the 2_1 axis symmetry of barite with alternating sulfate group orientation between each half cell (Figure A26).[93, 135, 201]

In the presence of alginate, the flat surface of the original barite substrate is indistinguishable within 12 min of exposure due to the rapid proliferation of etch pits (Figure 25g and h). These etch pits have ill-defined morphologies and do not appear to be bound by any crystallographic directions, in contrast to the triangular features observed for the control and solution containing DTPA. Moreover, height profiles of these etch pits (Figure 25i) reveal depths in excess of 50 Å, corresponding to more than 7 unit cells. Etch pits appear randomly on the surface and become more elongated in the [010] direction, similar to DTPA. These results reveal that alginate dissolves barite by etching along the b-direction and into the (001) surface (c-direction). This unique mechanism may be facilitated by the ability of the flexible polymeric backbone of alginate and its many binding groups to interact with multiple Ba^{2+} ions in a concerted manner.

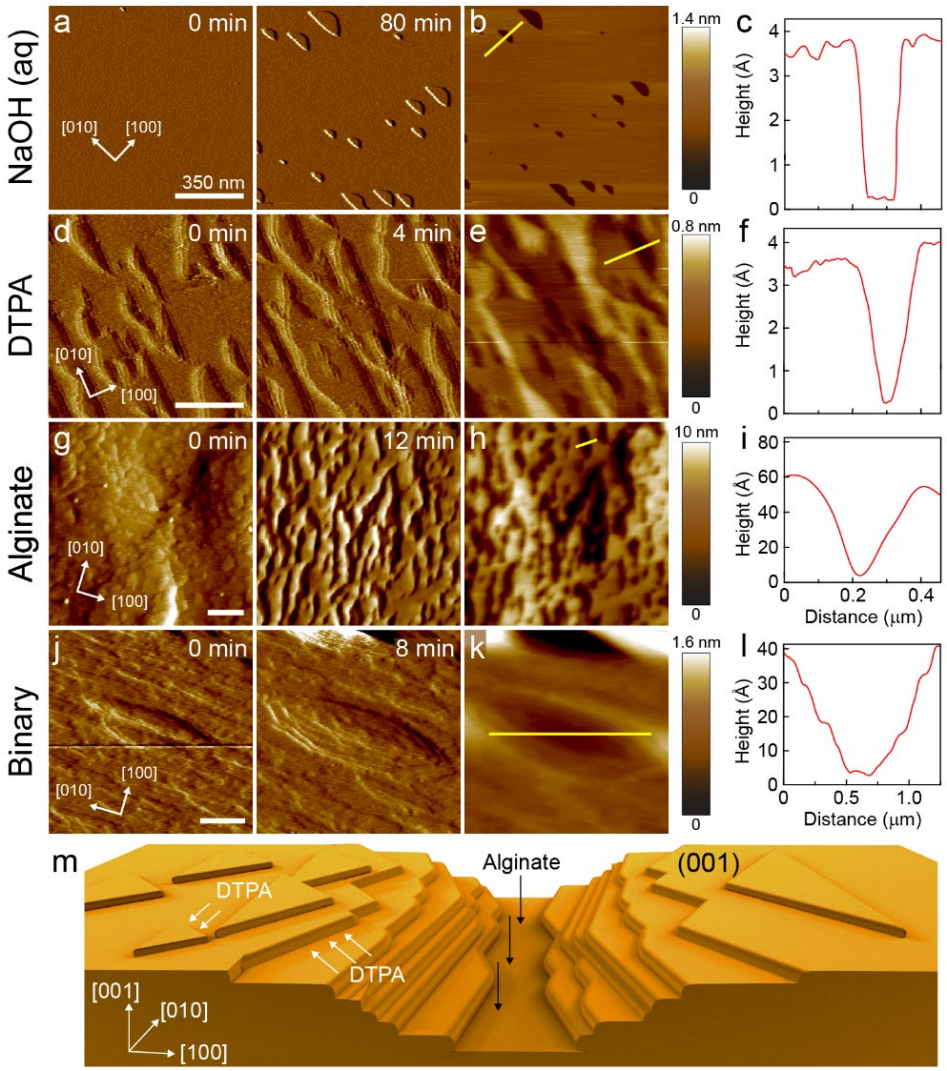

Figure 25. *In situ* AFM measurements of barite (001) surface dissolution in different media. Corresponding height images after the specified exposure time and height profiles of etch pits along the yellow lines of each height mode image are shown in (c), (f), (i), and (l)

We also probed the cooperative synergy between alginate and DTPA for surface dissolution in AFM experiments using binary combinations where the solution was adjusted to pH 9. Barite crystals exposed to binary combinations of DTPA and alginate exhibit a distribution of etch pit depths and diameters (Figure 25j-m and A27). A fraction of etch pits exhibit 3.6 Å (*c/2*) depth profiles (Figure A27), while the majority of etch pits are much deeper (10 Å or larger) and tend to have tiered profiles that are composed of

macro-steps (Figure 25*l*). The cooperative synergy appears to be associated with the ability of alginate to create newly exposed layers and the preferential dissolution of layers within the plane of imaging by DTPA, as illustrated in Figure 25m. This observed dual action of cooperative dissolvers leads to an overall rough (001) surface that is more similar to the single component solution of alginate compared to that of DTPA.

The dissolution of barite using natural, biocompatible additives at moderate pH has been underexplored. Through screening a series of polysaccharides, we identify alginate as an efficient alternative to DTPA. Using a combination of bulk dissolution assays and molecular dynamics, we show that DTPA is only active as a barite demineralizing agent at high pH owing to lower energetic barriers for its removal of Ba^{2+} ions from crystal surfaces. Microfluidic assays of barite dissolution under flow reveal a marked increase in the rate of barite dissolution compared to quiescent conditions. These studies demonstrate a high efficacy of alginate over a broad range of solution pH (4 – 9) relative to DTPA (pH ≥ 9). *In situ* atomic force microscopy measurements reveal that alginate and DTPA exhibit distinct modes of dissolution, wherein a binary combination of these two demineralizing agents in alkaline media results in synergistic cooperativity. On a molecular level, AFM imaging of the (001) barite surface reveals alginate induces deep (>50 Å) etch pits in the *c*-direction. Conversely, DTPA promotes layer-by-layer dissolution in the *a/b*-plane to generate shallow etch pits. For binary mixtures of alginate and DTPA, the origin of synergy derives from the fact that the two demineralizing agents promote dissolution in orthogonal directions, which enhances the overall rate of barite dissolution.

In many natural and synthetic crystallization processes, organics play a pivotal role in regulating crystal growth and dissolution. This is particularly true in biomineralization

where materials, such as calcium carbonates and phosphates, grow into exquisite hierarchical structures via highly specific organic-crystal interactions. Designing molecules to promote dissolution is desirable for cases where mineralization is unwanted or detrimental, such as barite (and other scale) formation in confined aqueous flow regimes, as well as numerous pathological diseases. Few studies in literature have elucidated molecular-level mechanisms of mineral dissolution at the solvent-crystal interface. Here, we do so for a newly identified naturally-abundant and environmentally-compatible biopolymer. These findings collectively demonstrate alginate's versatility and efficacy as a demineralizing agent, thereby opening new avenues for its use in formulations to treat barite (and potentially other scale) formation.

3.5 Methods of Barite Dissolution Kinetics and Mechanism

Barite crystallization and characterization. Barite crystals were prepared using a previously reported protocol.[195] A 5-mL solution of 1.2 M $NaCl_{(aq)}$ was first added into a 20-mL glass vial followed by 0.5-mL aliquot addition each of 10 mM $BaCl_{2,(aq)}$ and10 mM $Na_2SO_{4,(aq)}$ stock solutions. To this solution was added 4 mL DI water under mild agitation for 10 s to produce a growth solution (10 mL) with a composition of 0.5 mM $BaCl_2$: 0.5 mM Na_2SO_4 : 600 mM NaCl (pH = 7.1 ± 0.3). The pH of growth solutions was measured using an Orion 3-Star Plus pH benchtop meter equipped with a ROSS Ultra electrode (8102BNUWP). The sample vials were left undisturbed at 22 ± 1 °C for 24 h to allow crystallization of hexagonal barite platelets with well-defined (001), (210), and (100) facets (see Figure 2b). Natural barite samples were obtained from Amazon. The zeta potential ζ of natural and synthetic barite samples was measured with a NICOMP 380/ZLS instrument (Particle Sizing Systems, Santa Barbara, CA).

Dissolution assays under quiescent conditions. Demineralizing agent stock solutions were prepared by the addition of 40 mg reagent to 200 mL of DI water followed by pH neutralization with an appropriate amount of 100 mM $NaOH_{(aq)}$. After 24 h crystallization, the supernatant was removed via pipette and barite crystals adhered to the bottom of the 20 mL glass vials were rinsed in DI water in triplicate. Immediately after rinsing the crystals, 20 mL aliquots of demineralizing agents (200 μg mL^{-1}) were introduced into the glass vials containing the barite seed crystals and were left undisturbed for 7 days.

In a separate experiment intended for *ex situ* imaging, a clean glass slide (1 × 1 cm^2) was placed at the bottom of a 20 mL glass vial prior to the addition of reagents used for barite crystallization. Immediately after synthesis, the glass slide containing the newly formed barite crystals was removed from the supernatant and rinsed thoroughly in DI water and dried in air. The slide was then positioned at the bottom of a vial containing 20 mL of a selected demineralizing agent solution (200 μg mL^{-1}). Barite crystals were exposed to solutions between 1 to 10 days. The glass slide was removed from the solution and rinsed in DI water and dried in air.

Dissolution assays under flow conditions. Details of the microfluidic platform and procedures used to measure *in situ* rates of crystal dissolution under constant flow are described in a previous study.[195] Dissolution of barite was performed in solutions of varying pH that were prepared by adding appropriate amounts of $NaOH_{(aq)}$ or $HCl_{(aq)}$ to DI water. The flow configuration for carrying out barite dissolution is described in detail in our previous study[195] that made use of a dual syringe pump that fed two separate solutions,

one containing DI water and one containing 500 μg mL^{-1} demineralizing agent, into the respective inlets of the microchannels.

Barite crystal size and morphology were determined using a Leica DMi8 inverted optical microscope equipped with HC PL Fluotar 5×, 10×, 20×, and N Plan L 50× objectives. At least ten brightfield images of representative areas on the bottom of the glass vials were captured in transmittance mode for characterization of crystals dissolved in polysaccharide solutions. The average basal surface area of barite crystals in optical micrographs were measured from a minimum of 100 crystals per batch and three separate batches. An inverted optical microscope equipped with a motorized stage was used to image crystals in the bulk crystallization assays as well as time-resolved demineralization in microfluidics assays. For *in situ* time-resolved studies, LAS X software was used to program a minimum of 15 positions along a seeded microchannel. Images were captured in transmittance mode at 5 min intervals for a minimum of 3 h. Crystals observed *in situ* were analyzed using ImageJ (NIH) with a protocol previously reported.[195] At least 100 crystals located in different channels in a single batch were analyzed at 5 min intervals over a minimum of 3 h. From the change in crystal basal (001) surface area over time, a dissolution rate *r* was calculated for each experimental condition as $r_{dissolution} = \Delta S_A\ t^{-1}$, where ΔS_A is the change in (001) surface area and *t* is the time (in hours).

Scanning Electron Microscopy. *Ex situ* microscopy measurements were obtained using a FEI 235 dual-beam focused ion beam scanning electron microscope (SEM). For SEM imaging, a clean glass slide (1 × 1 cm^2) was positioned at the bottom of bulk crystallization vials to collect barite crystals. Samples containing either as-synthesized crystals or those after dissolution assays were removed from their native solutions, gently

rinsed with DI water, and dried in air prior to analysis. SEM samples were prepared by attaching glass slides to SEM studs (Ted Pella) using carbon tape and were coated with 15 – 20 nm gold to reduce electron beam charging.

Atomic force microscopy. All atomic force microscopy (AFM) measurements were performed with a Cypher ES instrument (Asylum Research, Santa Barbara, CA) using silicon nitride probes with gold reflex coating and a spring constant of 0.08 $N\ m^{-1}$ (Olympus, PNP-TR). The liquid cell (ES-CELL-GAS) contained two ports for inlet and outlet flow to maintain constant composition continuous imaging. Barite crystals prepared via bulk crystallization (described above) were synthesized directly onto on an AFM specimen disk (Ted Pella) covered with a thin layer of thermally curable epoxy (Loctite, China). The epoxy was first partially cured in an oven for ca. 5 min at 60 °C prior to drying in air overnight to completely cure. AFM specimen disks were placed at the bottom of 20 mL glass vials and reagents used for bulk crystallization of barite were subsequently introduced to the vials upon which crystals nucleated, sedimented onto the epoxy, and grew overnight. The samples were gently rinsed with DI water and dried in air for one hour prior to imaging.

For *ex situ* imaging of the (100) surface of barite, glass slides containing barite crystals used in quiescent dissolution assays were fixed onto an AFM specimen disk using epoxy and left undisturbed overnight to allow the epoxy to fully cure. These samples were imaged in air at ambient temperature and in contact mode with a scan rate of 2.44 Hz at 256 lines per scan. *In situ* AFM measurements of barite dissolution were carried out by introducing a growth solution with a composition of 0.06 mM $BaCl_2$ and 0.06 mM Na_2SO_4 (supersaturation ratio S = 5.3) in DI water into the fluid cell using an in-line mixing

configuration at a flow rate of 12 mL h^{-1} to obtain a smooth (001) surface with classical growth features. Measurements were performed using several concentrations of aqueous NaOH, alginate, and DTPA solutions (pH = 7 – 9) that were introduced into the fluid cell following a 30-min growth period. Continuous imaging was carried out at ambient temperature in contact mode with a scan rate of 9.77 Hz at 256 lines per scan.

Molecular dynamics simulations. Molecular dynamics (MD) simulations were conducted with GROMACS 2016.[202-203] Barite was described using the potential of Piana et al.,[128] DTPA was modeled using GROMOS force field parameters from the Automatic Topology Builder (ATB) server,[204] and the SPC model[205] was used for water. Water-barite interactions were described using the force field of Piana et al.,[128] and standard geometric mixing rules were used to parameterize all other van der Waals interactions, with parameters for O and S in barite from ATB and parameters for Ba from Rowley et al.[206] Umbrella sampling molecular dynamics (USMD) simulations were performed using the PLUMED 2.4.3[207-208] plugin for GROMACS to characterize the DTPA-assisted detachment of Ba^{2+} ions from the barite (001) surface. Additional details of the MD simulations are provided in the Supplementary Methods section within the Supporting Information.

Chapter 4: Green Inhibitors of Barite Nucleation and Growth

Mineralization of alkaline earth metals and iron-based scale components is an undesirable and ubiquitous phenomenon in industrial systems for wastewater treatment, energy production, and manufacturing.[106, 108-109] One of the most stubborn components of mineral scale is barium sulfate (i.e., barite).[209,210] Approaches to prevent barite scale include treatments with phosphonate-based commercial inhibitors such as diethylenetriamine penta(methylene phosphonic acid) (DETPMP), hydroxyethylidene diphosphonic acid (HEDP), or related analogues.[109, 112-113, 211-213] Carboxylate-based compounds are generally less potent, and thus have received less attention as commercial scale inhibitors, but are frequently employed as chelating agents of alkaline earth metals (e.g., Ba^{2+} and Ca^{2+}). Examples include ethylenediaminetetraacetic acid (EDTA) and diethylene-triaminepentaacetic acid (DTPA) owing to their strong binding affinity for metal ions.[100-104] Most commercial compounds used to treat barite scale are not easily biodegradable. Moreover, one drawback of carboxylate-based compounds is the required use of caustic (highly alkaline) solutions to dissociate acid groups for improved efficacy.[120, 214] Thus, there remains a need for environmentally friendly alternatives to effectively inhibit mineral scale.

Inspiration for the design of novel crystal growth inhibitors can be drawn from natural compounds (or their derivatives) that regulate biomineralization.[22-27] One class of natural carboxylate-based compounds with broad appeal are polysaccharides owing to their ability to regulate the crystallization of numerous minerals. These species are generally referred to as modifiers, but more specifically they are denoted as either promoters or inhibitors of crystallization. Polygalacturonic acid is a bioinspired compound reported to

inhibit barite crystallization.[111] Additional examples include carboxymethylcellulose (CMC) and carboxymethyl inulin,[215-217] which are effective inhibitors of calcium oxalate and calcium carbonate. One polysaccharide that has shown promise is alginate, a linear biopolymer constructed from mannuronic acid (M) and guluronic acid (G) monomers, which is extracted from brown sea algae and is used commercially as an additive in consumer goods.[188-190] Although its efficacy has not been tested previously for barite, it has been demonstrated that alginate is an effective inhibitor of calcium and magnesium based scales[218] and crystals such as calcite ($CaCO_3$), hydroxyapatite ($Ca_{10}(PO_4)_6(OH)_2$), and struvite ($NH_4MgPO_4 \cdot 6H_2O$), and a mild inhibitor of brushite ($CaHPO_4 \cdot 2H_2O$) crystallization.[219-226]

The efficacy of an inhibitor is determined by its ability to suppress nucleation and/or crystal growth. It is less common to encounter compounds capable of fully suppressing nucleation, and also unusual to find a compound with dual capability to inhibit both nucleation and growth. There are a few phosphonate-based compounds that inhibit barite nucleation.[227-229] To our knowledge there are no examples of barite nucleation inhibitors containing only carboxylate moieties; prior studies have instead reported exclusively on the efficacy of carboxylate-based compounds as inhibitors of crystal growth.[27, 100-102, 104, 111, 228, 230] Barite grows via a classical layer-by-layer process involving the addition of monomer (solute) from solution to crystal surface sites (i.e., kinks, steps, and terraces).[231] Growth inhibitors for a variety of systems reduce the rate of solute addition to crystal surfaces by two predominant mechanisms: kink blocking and step pinning.[17] Kinks are the most favorable sites for solute incorporation; thus, the adsorption of inhibitors to these sites can dramatically reduce (but not fully impede) the rate of step

advancement.[15, 31] A more effective mechanism of growth inhibition is step pinning wherein modifiers adsorb on terraces and suppress step growth by imposing a surface tension on advancing layers.[15-16] A common attribute of crystal growth inhibitors is their preference for binding to select crystallographic surfaces, which alters the anisotropic kinetics of growth.[17, 80] This binding specificity enables certain facets to grow at the expense of others that are either fully or partially inhibited, which can explain why there are few inhibitors that are capable of fully suppressing crystallization.

Hydrodynamics can play an important role in scale treatment. It has been demonstrated that higher rates of fluid flow minimize barriers for inhibitor diffusion to barite surfaces, thereby improving modifier efficacy.[18-19, 195] Turbulent rotary flow[232] in the presence of modifiers has been shown to enhance crystal growth inhibition, whereas stirring[19] can reduce an inhibitor's efficacy relative to quiescent conditions. The effects of laminar fluid flow conditions on crystal growth inhibition can be probed at different length scales.[209] Microfluidics offers a unique platform to investigate bulk crystallization kinetics and time-resolved morphological development of crystals at the macroscopic level,[18, 195] whereas *in situ* atomic force microscopy (AFM) can be used to extract mechanistic details of surface growth inhibition at near molecular level.[17, 53, 233-235]

In this study, we use a combination of microfluidics, AFM, and other techniques to assess a series of polycarboxylates as potential barite scale inhibitors under quiescent and flow conditions. Bulk assays reveal a wide disparity in efficacy of polycarboxylates as inhibitors of barite crystallization. Among the compounds investigated, we identified two macromolecules – alginate and polygalacturonic acid – that are capable of inhibiting barite nucleation. Microfluidic assays revealed that alginate was also a potent inhibitor of barite

crystal growth, showing that alginate fully suppresses barite crystallization. Furthermore, *in situ* AFM studies reveal two distinct mechanisms of layer growth inhibition on barite crystal surfaces that are dependent upon the concentration of alginate. Based on these findings, alginate emerges as a sustainable alternative to commercial additives owing to its dual role as a nucleation and growth inhibitor.

4.1 Experimental Methods of Barite Growth Inhibition

Materials. The following reagents were purchased from Sigma Aldrich: barium chloride dihydrate (99+%), sodium sulfate (>99%), sodium hydroxide (>97%), and sodium chloride (>99.5%), sodium citrate tribasic dihydrate (≥99.0%), sodium alginate from algae brown, succinic acid, tricarballylic acid, 1,2,3,4-butanetetracarboxylic acid, ethylenediaminetetraacetic acid (EDTA), and diethylenetriaminepentaacetic acid (DTPA). Sodium alginate (Grindsted FD 120) was provided by Danisco. Polydimethylsiloxane (PDMS, Dow Corning SYLGARD 184) was purchased from Essex Brownell, and SU-8 2150 photoresist and SU-8 developer were purchased from Microchem. All chemicals were used as received without further purification. Silicone tubing was purchased from Cole-Parmer. Single-side polished 4-inch P-type silicon wafers <100> were purchased from University Wafer and were cleaned using a piranha solution. Deionized (DI) water used in all experiments was filtered with an Aqua Solutions RODI-C-12A purification system (18.2 MΩ·cm).

Bulk crystallization assays. Barite crystals were synthesized using a protocol modified from procedures reported in the literature.[96, 113, 126, 141, 159-160] In a typical synthesis, $NaCl_{(aq)}$ was first added into a 20-mL glass vial followed by aliquot addition of 10 mM $BaCl_{2,(aq)}$ and 10 mM $Na_2SO_{4,(aq)}$ stock solutions under mild agitation for 10 s. Samples

prepared in the presence of molecular modifiers were carried out by adding aliquots of molecular modifiers $_{(aq)}$ to the reaction mixture prior to the addition of Na_2SO_4. The final growth solutions with a total volume of 10 mL had a pH of 7.1 ± 0.3 and a composition of 0.5 mM $BaCl_2$: 0.5 mM Na_2SO_4 : 600 mM NaCl : x μg mL^{-1} modifier ($0 \leq x \leq 10$). The sample vials were left undisturbed at 22 °C for 24 h to allow crystallization of hexagonal barite platelets with well-defined (001), (210), and (100) facets.

Microfluidic assays in the presence of inhibitors. To quantify the inhibition efficacy, the seeded growth of barite crystals was imaged over time using an inverted optical microscope. Microfluidic devices were assembled and seeded with barite crystals using a previously reported method.[195] Two solutions were prepared and transferred into separate syringes. One solution contained 0.5 mM $BaCl_2$ and the second solution contained 0.5 mM Na_2SO_4, 1.2 M NaCl and various quantities of growth modifiers (0 – 20 μg mL^{-1}). The two solutions were mixed using an inline flow configuration that produced a final composition of 0.35 mM $BaCl_2$, 0.35 mM Na_2SO_4, 600 mM NaCl and inhibitors at varied concentration. The fully mixed growth solution was introduced into seeded PDMS chips using a dual syringe pump where inhibitors were added to the syringe containing SO_4^{2-} to minimize formation of ion complexes. Growth solutions were mixed through silicon tubing attached to a y-connector, and then successively fed into the corresponding inlet of the concentration gradient generator.

Materials characterization and Instrumentation. Powder X-ray diffraction (PXRD) patterns of natural and as-synthesized samples were collected on a Rigaku Smart Lab X-ray diffractometer using a Cu-Kα radiation source (λ = 1.5406 Å, 40 kV, 30 mA). Reference PXRD patterns were selected from the ICDD PDF-2 2013 database.[236] Dual star

benchtop pH/ISE meters (Orion) equipped with a ROSS Ultra electrode (8102BNUWP) was used for adjusting pH with 10 mM solutions of NaOH and HCl. Conductivity measurements were carried out to assess the crystallization kinetics in the presence of crystal modifiers. Conductivity probe (VWR, 515 conductivity dip cell coated with Au) was vertically immersed into the growth solution under magnetic stirring (600 rpm) and the readings were recorded by the conductivity meter (VWR EC meter, model 2052). The conductivity probe was calibrated with 0.005 M KCl standard solutions prior to the experiments.

For *ex situ* microscopy measurements, a clean glass slide (1 cm^2) was positioned at the bottom of the vials to collect barite crystals. After crystallization, the glass slide was removed from its solution, gently rinsed with de-ionized (DI) water, and dried in air prior to analysis. SEM samples were prepared by attaching carbon tape to SEM studs and subsequently attaching glass slides to carbon tape by gently pressing the glass slide to the tape using tweezers. Scanning electron microscope (SEM) images were obtained on a FEI 235 dual-beam (focused ion-beam) system operated at an accelerating voltage of 15 kV and a working distance of 5 mm. As-synthesized samples were prepared by gently pressing the glass slide containing crystals onto the carbon tape. All the samples were coated with a thin layer of gold (ca. 5 – 10 nm) prior to imaging.

The size and morphology of barite crystals were examined using Leica DM2500-M optical microscope in transmittance mode, and *in situ* imaging of crystal growth was performed on the Leica DMi8 inverted optical microscope using transmittance mode equipped with HC PL Fluotar 5×, 10×, 20×, and N Plan L 50× objectives. To characterize crystals grown in the quiescent bulk assay, at least ten brightfield images of representative

areas on the bottom of the glass vials were captured in transmittance mode. The average [010] length, [100] width, and [001] thickness of crystals in optical micrographs were measured from a minimum of 100 crystals per trial and three separate trials. *In situ* time-resolved studies were evaluated using a Leica DMi8 inverted optical microscope equipped with a motorized stage and LAS X software. Images were captured in transmittance mode along a minimum of 20 positions throughout a seeded microchannel at 10 – 30 min intervals for at least 3 h. Crystals observed *in situ* were analyzed using ImageJ (NIH) and the detailed analytical protocol is described in our previous work.[195] From the change in crystal length over time, a growth rate *r* was determined for each experimental condition. The relative growth rate (RGR) was calculated as

$$RLR = \frac{L_m}{L_c} \quad \text{Eq. (3)}$$

and

$$RGR = \frac{r_m}{r_c} \quad \text{Eq. (4)}$$

where L_m and L_c represent the length of crystals grown in the presence of a modifier (m) and in the absence of any additive (c, control). The parameters r_m and r_c represent growth rates in the presence and absence of a growth modifier, respectively.

Atomic force microscopy. In situ atomic force microscopy (AFM) was performed to examine the temporal changes in topographical features on barite crystal surfaces. Barite crystals prepared via the bulk crystallization method described previously were synthesized directly onto an AFM specimen disk (Ted Pella) covered with a thin layer of thermally curable epoxy (Loctite, China). The AFM specimen disks were placed at the bottom of 20 mL glass vials and reagents used for bulk crystallization of barite were subsequently introduced to the vials upon which crystals nucleated, sedimented onto the epoxy, and grew

overnight. The samples were then rinsed in DI water and exposed to a growth solution (supersaturation ratio of S = 4.4) containing only Ba^{2+} and SO_4^{2-} ions for 1 hour prior to imaging. All AFM measurements were performed in a Cypher ES instrument (Asylum Research, Santa Barbara, CA) using silicon nitride probes with fold reflex coating and a spring constant of 0.15 N/m (Olympus, TR800PSA). The liquid cell (ES-CELL-GAS) contained two ports for inlet and outlet flow to maintain constant supersaturation during AFM measurements. Growth solutions containing different concentrations of solute ($BaCl_2$, Na_2SO_4) and inhibitors were delivered to the liquid cell using a y-connector mixing configuration where both solute solutions were combined immediately before entering the cell (analogous to the microfluidics configuration). Continuous imaging was performed at ambient temperature in contact mode with a scan rate of 2.44 Hz at 256 lines per scan.

4.2 Identifying Potent Inhibitors of Barite Crystallization

We selected nine different polyprotic acids (Figure 26, molecules I – IX) as potential inhibitors of barite crystallization. These molecules include polycarboxylic acids (I – IV), aminopolycarboxylic acids (V and VI), and biomacromolecules such as alginate (VIII) that is composed of two different monomers, D-glucuronic acid (VII) and mannuronic acid, and lastly polygalacturonic acid (IX), which has a ring structure and chemical functionality similar to both monomers of alginate. The library of modifiers was screened in bulk crystallization assays under quiescent conditions to evaluate their efficacy *ex situ*, as determined from changes in the size, morphology, and number density of crystal populations. Growth solutions used for these bulk assays were prepared with a supersaturation ratio of S = 10 (pK_{sp} of barite = 9.97 at 25 °C).[121]

Barite crystals obtained from bulk assays in the absence of a modifier (control) exhibit a hexagonal coffin-shaped morphology (Figure 27a,e). At low modifier concentration (1 μg mL^{-1}), we observed no apparent change in barite crystal morphology (Figure A28) when using the following molecules: succinic acid (I), tricarballylic acid (II), tetracarboxylic acid (IV), and D-guluronic acid (VII). Conversely, the addition of 1 μg mL^{-1} of citrate (Figure 27b,f), EDTA (Figure A28), or DTPA (Figure 27c,g) had a pronounced impact on barite morphology. The latter two directed the formation of barite crystals with irregular features, whereas citrate preferentially binds to the apical tips of barite crystals to elongate them along the a-direction (Figure A28). Except for citrate, molecules containing fewer than 4 carboxylates had a moderate effect on barite crystal morphology. Interestingly, there were almost no crystals detected in bulk assays with 1 μg mL^{-1} of alginate (Figure 27d) in the timeframe of measurement (ca. 24 h). Trace particles with a globular, unidentifiable morphology (Figures 27h and A29) were observed at a lower alginate concentration.

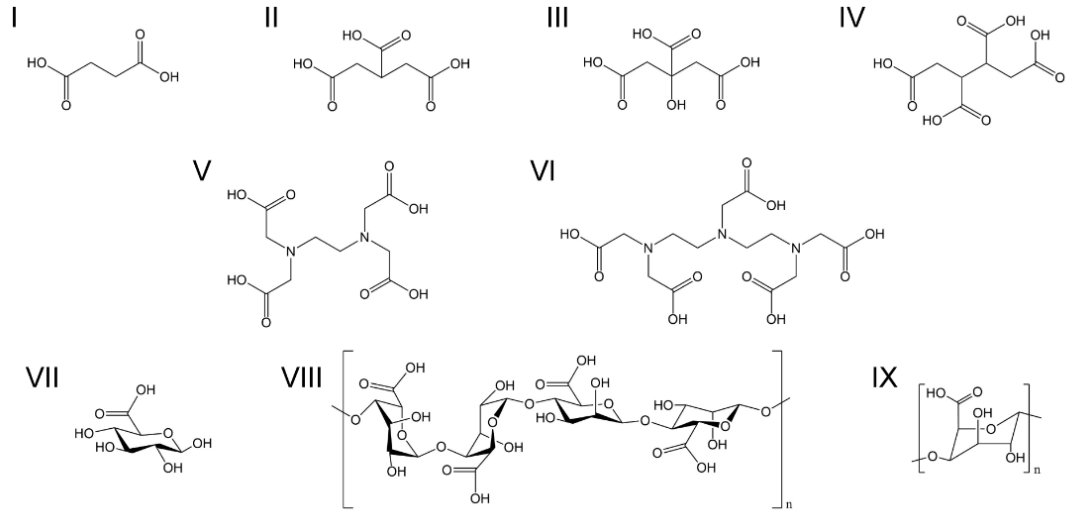

Figure 26. Chemical structures of molecules tested as putative growth modifiers of barite crystallization.

A ten-fold increase in a given modifier concentration (10 μg mL^{-1}) resulted in more pronounced changes to barite crystal morphology (Figure A30), apart from succinic acid, tricarballylic acid, and D-guluronic acid. Growth solutions containing 10 μg mL^{-1} of citrate produced crystals with spheroidal features. Tetracarboxylic acid produced crystals with shapes similar to those observed with EDTA at lower concentration (Figure A28), whereas EDTA at higher concentration resulted in thin, needle-like crystals that were often observed to form aggregates in a spherulitic conformation (Figure A30). Bulk assays in the presence of DTPA generated crystals with round edges (i.e., lack of distinct facets). Similarly, assays with 10 μg mL^{-1} polygalacturonic acid resulted in aggregates of spherical crystals, similar to those in the presence of alginate at much lower concentrations (Figure A29). Powder XRD patterns of all crystals confirmed the formation of crystalline barium sulfate (Figure A31); however, crystals synthesized in the presence of macromolecules resulted in number densities too low to determine crystallinity via powder XRD.

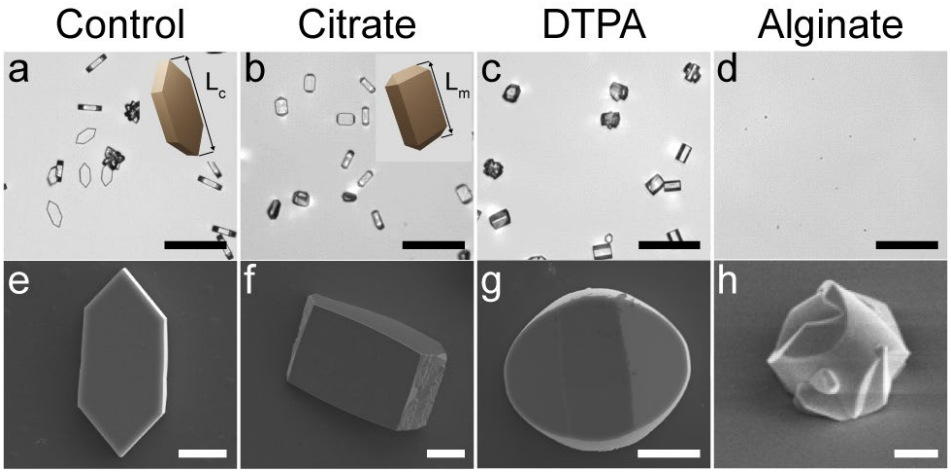

Figure 27. Optical (a – d) and scanning electron (e – h) micrographs of barite crystals synthesized in the absence of modifiers (a and e) and in the presence of (b and f) 1 μg mL^{-1} citrate, (c and g) 1 μg mL^{-1} DTPA, (d) 1 μg mL^{-1} alginate, and (h) 0.5 μg mL^{-1} alginate.

Crystal growth inhibition resulting from specific interactions between modifiers and crystal surfaces can be gleaned from changes in relative crystal dimensions (e.g., the length measured along the fastest growth direction, [010]). The effect of modifiers on crystal habit were grouped into one of two general categories, (i) well-defined morphologies and (ii) irregular particles, and quantified with respect to the control (i.e., no modifier) using a relative length ratio (RLR, Eq. 3). At the highest modifier concentration tested (10 μg mL^{-1}), only a subset of molecules resulted in more than 50% reduction in barite crystal length. These include citrate (III), tetracarboxylate (IV), EDTA (V), DTPA (VI), and alginate (VIII) (Figure 28a). The latter three stand out as exemplary inhibitors (i.e., >80% reduction in RLR). At the lowest modifier concentration tested (1 μg mL^{-1}), the impact of alginate on RLR is almost unchanged whereas the other molecules are far less effective (Figure 28b).

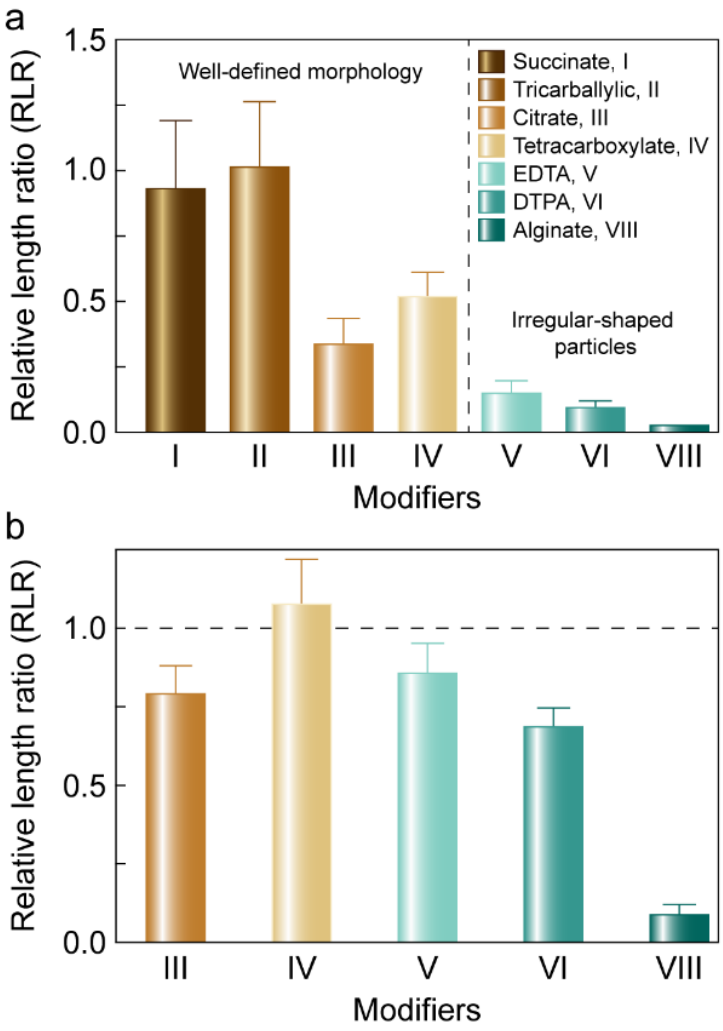

Figure 28. Histograms comparing the efficacy of modifiers based on their alteration of the relative length ratio (RLR), as defined in Eq. 3, at two different modifier concentrations: (a) 10 μg mL^{-1} and (b) 1 μg mL^{-1}.

Table 2. Number density of barite crystals in bulk crystallization assays.[a]

Polycarboxylate	Sample	Number density (mm^{-2}) [b]	
		1 µg mL^{-1}	10 µg mL^{-1}
Succinic acid	I	7.9 ± 0.4	4.8 ± 0.3
Tricarballylic acid	II	9 ± 1	11 ± 1
Citrate	III	7.1 ± 0.6	16 ± 1
Tetracarboxylic acid	IV	8.5 ± 0.4	4.9 ± 0.3
EDTA	V	4.0 ± 0.5	3.9 ± 0.2
DTPA	VI	13 ± 1	38 ± 2
D-Guluronic acid	VII	9.2 ± 0.7	3.0 ± 0.5
Polygalacturonic acid	IX	2.5 ± 0.1	1.0 ± 0.1
Alginate	VIII	0	0

a. measurements in supersaturated solutions (S = 10) under quiescent conditions; b. number density of the control is 5.2 ± 0.7 mm^{-2}

4.3 Impact of Inhibitors on Barite Nucleation

The effect of modifiers on barite nucleation was inferred by measuring changes in the number density of barite crystals as an indicator of a modifier's mode of action. Promotion of nucleation generally results in a larger population of crystals, whereas inhibition of nucleation yields the opposite effect. To assess the impact of each modifier, the average number density of crystals after bulk crystallization assays (Table 2) was compared against a control sample (5.2 ± 0.7 crystals mm^{-2}) synthesized at the same

supersaturation (S = 10) in the absence of any modifier. Within the error of measurement, most modifiers had negligible effect on nucleation. At the highest modifier concentration tested, three compounds appear to promote nucleation. DTPA produced the highest number density of crystals (nearly 8-fold higher than the control), and citrate and tricarballylic acid resulted in 4- and 2-fold increases, respectively. Conversely, both macromolecules (polygalacturonic acid and alginate) were the only modifiers that inhibit nucleation. Notably, alginate is unique among the modifiers tested based on its ability to prevent nucleation at both low and high concentration. To our knowledge, this is the first evidence that a single modifier is capable of fully suppressing barite nucleation at environmentally friendly conditions (pH = 7) without the use of Ba^{2+} sequestering agents.

4.4 Impact of Inhibitors on the Kinetics of Barite Crystallization

The kinetics of barite crystallization were evaluated by tracking the temporal depletion of Ba^{2+} and SO_4^{2-} ions from a supersaturated barite growth solution in the absence and presence of each modifier using ionic conductivity. Unlike the previous bulk crystallization assays, these studies were conducted under stirring (at 400 rpm) to reduce the induction period and overall time of crystallization. These measurements cannot fully decouple the effects of nucleation from crystal growth, but do allow for direct assessment of modifier efficacy. We determined the rate of crystallization from the initial (approximately linear) decrease in conductivity with time from de-supersaturation curves (Figure A32), and report the relative growth rate (RGR, Eq. 4) using as a reference the value obtained from a supersaturated growth solution (control) in the absence of modifier (Figure 29). A value of RGR = 1 signifies no change in the rate of growth, whereas RGR < 1 indicates crystal growth inhibition.

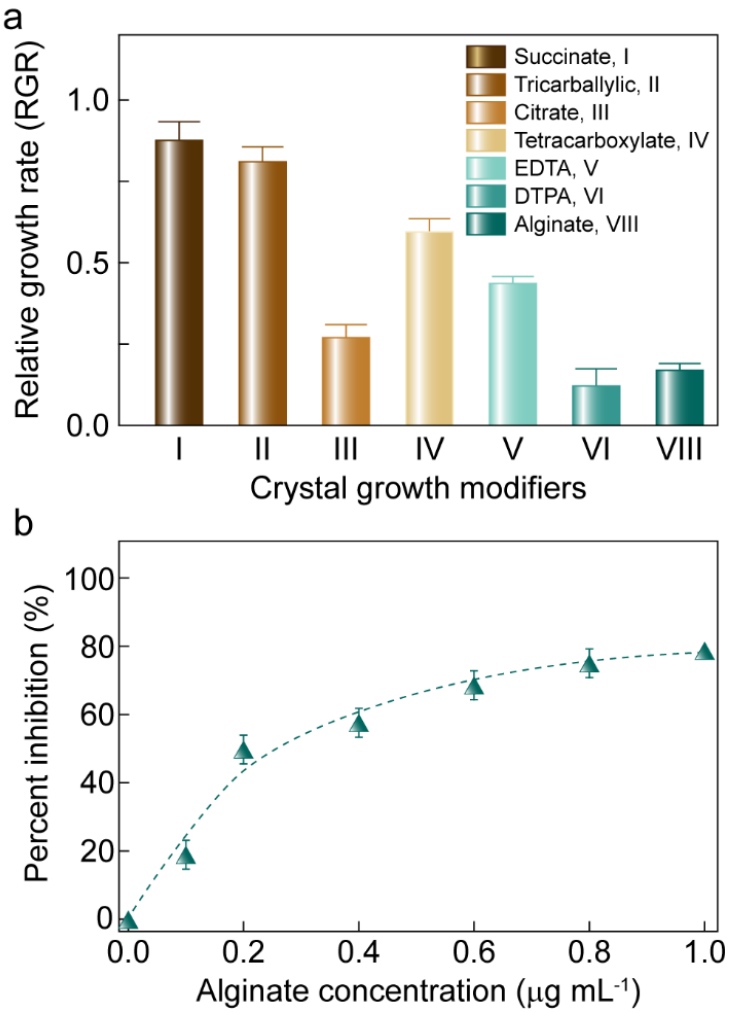

Figure 29. (a) Relative growth rate (RGR) determined from the linear slope of de-supersaturation curves (Figure S5) of growth solutions (S = 10) containing 1 μg mL^{-1} of each modifier. (b) Percent inhibition of barite growth as a function of alginate concentration.

The modifiers can be grouped in general categories based on their relative efficacy: weak inhibitors (I and II), moderate inhibitors with RGR ≈ 0.5 (IV and V), and strong inhibitors with RGR < 0.25 (III, VI, and VIII). These results contrast with those from the bulk assays under quiescent conditions (Figure 28b), in which alginate significantly outperforms all other modifiers. This comparison indicates that agitation (or stirring) reduces alginate's efficacy, leading to a maximum 80% inhibition of barite crystallization (Figure 29b) compared to the complete suppression of nucleation observed under quiescent

conditions (Table 2). These results are analogous to other mineral systems, such as struvite, in which a transition from stirring to quiescent conditions enhances the efficacy of crystal growth inhibitors.[19]

4.5 Effect of Potent Inhibitors on Anisotropic Crystal Growth

To evaluate the effects of alginate on the anisotropic rates of barite crystallization, we used a microfluidic platform to track temporal changes in the macroscopic dimensions of crystals under controlled flow rates (i.e., fixed Reynolds number Re = 9.2). Benefits of using microfluidics include the ability to (i) maintain a constant supersaturation, (ii) decouple the effect of modifiers on crystal growth relative to nucleation, and (iii) quantify the anisotropic rates of growth for all relevant crystal facets at a macroscopic level. For these studies we prepared seeded microfluidic devices and slightly reduced the supersaturation of the growth medium (S = 7.0) to prevent the formation of new nuclei. Seed crystals in the microchannels that are exposed to growth solutions without inhibitors grow anisotropically with a fixed aspect ratio. To account for alginate inhibition of growth, we monitored the basal (001) surface and tracked temporal changes in the length and width of crystals along the b- and a-directions, respectively. The growth rates in the presence of each additive (Figure 30) are compared against the control to calculate relative growth rates (RGR) for alginate as well as two additional compounds, DTPA and citrate, which were identified as moderately effective inhibitors (Figure 29a).

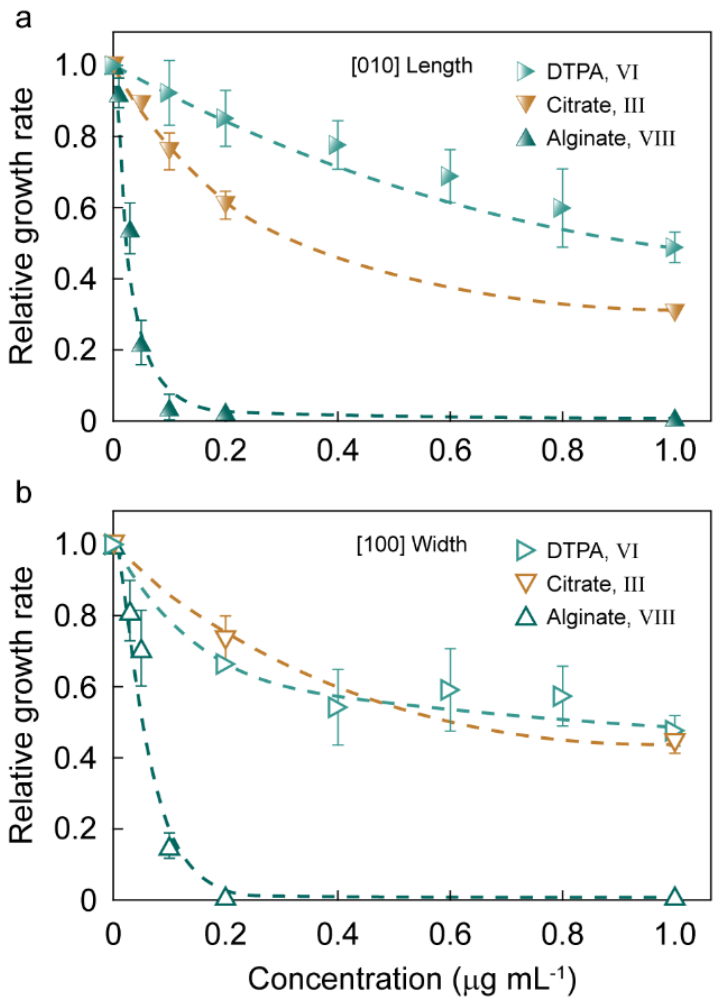

Figure 30. Relative growth rate (RGR) of barite crystallization based on (a) crystal width and (b) length dimensions as a function of modifier concentration. All experiments use conditions where molecules are mostly deprotonated: pH 7 for alginate and citrate[196, 237], and pH 9 for DTPA.[195]

Barite crystal growth is completely inhibited under low-Re (Re = 9.2) flow in the presence of 0.2 μg mL^{-1} alginate, which is similar to the results obtained under quiescent conditions (Figure 27) at higher alginate concentrations (Figure 30). This result highlights the potency of alginate in comparison with DTPA and citrate, which do not exceed 60% inhibition (where percent inhibition is defined as (1 – RGR) × 100%). The inhibition profiles for DTPA and citrate are similar, although the latter is slightly more effective at suppressing growth along the length of the crystal (Figure 30a). DTPA and citrate are

similarly effective at inhibiting barite growth along the width of crystals (Figure 30b). These observations indicate that DTPA has a minor preference for binding to barite (100) surfaces at lower concentrations (< 0.6 μg mL^{-1}), whereas citrate exhibits non-preferential interactions between (100) and (010) surfaces.

Prior studies of barite crystal growth inhibitors have predominantly assessed their impact on the kinetics of crystallization without examining specific influences on the physical properties of crystals (e.g., size and morphology).[27, 96, 104, 111, 126, 238-240] Here, we use *in situ* optical microscopy to track temporal changes in crystal morphology of barite seed crystals in microfluidic channels under the flow of supersaturated solutions containing alginate (Figures 31a and A35). Time-resolved images reveal that seed crystals grow disproportionately at the apical tips (i.e., {210} facets) and a fraction of crystals exhibit orientation-dependent anisotropic growth. These effects are observed for a minor population of crystals (labelled as "crystals affected by flow"). The asymmetric geometry develops after exposure to growth solutions containing alginate (indicated by white arrows in Figures 31a and A35), leading to crystals with aspect ratios that are much smaller than the average value measured in bulk crystallization assays (i.e., a higher percentage of length-to-width ratios $L/W \leq 2$; see Figure A36). Analysis of crystals affected by flow for different alginate concentrations reveals that asymmetric growth inhibition is more pronounced at lower alginate content (<0.05 μg mL^{-1}). Notably, the {210} facets oriented against the direction of flow grow at a slower rate than those on the opposite sides of the crystal, resulting in abnormal morphologies with longer imaging time. The percentage of crystals affected by flow monotonically decreases from 35% to less than 5% with increasing alginate concentration (Figure 31b). These features are consistent with faster

transport of alginate to facets directly facing oncoming solution flow. Previous literature has shown that laminar streams that encounter immobile crystals can generate different secondary flows depending on the crystal orientation.[241] Specifically, these secondary flows produce wakes near the trailing facets where solute transport to the crystal is reduced. These changes in flow surrounding the crystals can result in morphological instabilities, macrostep formation, and liquid inclusion.

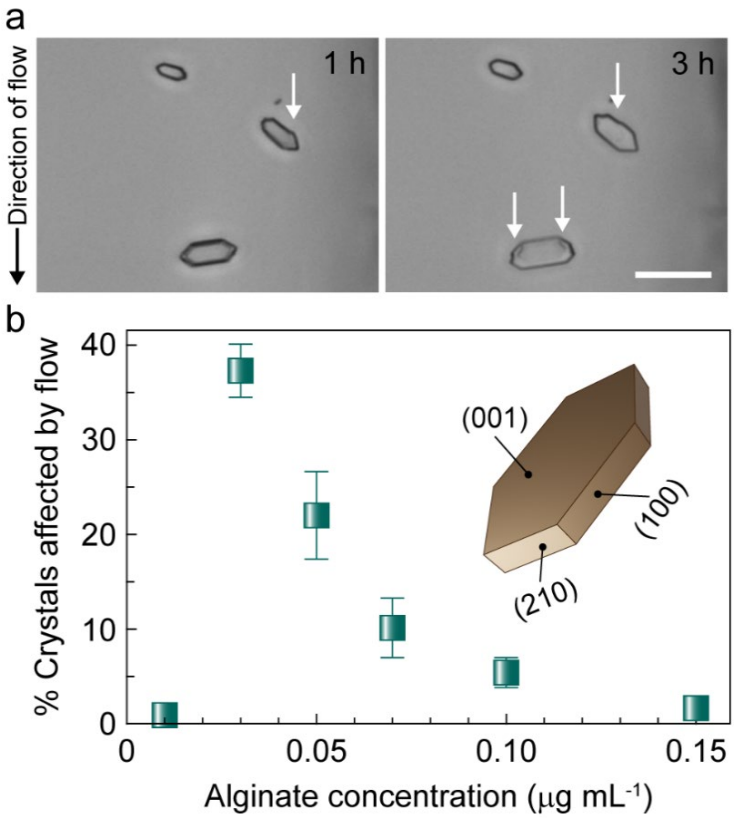

Figure 31. (a) Optical micrographs after 1 and 3 h of continuous imaging show asymmetric inhibition of barite {210}. Scale bar equals 20 μm. (b) Percentage of the crystal population in microchannels that demonstrate asymmetric growth as a function of alginate concentration.

4.6 Mechanism of Barite Growth Inhibition

Prior studies have used *in situ* AFM to show that barite surfaces grow classically (i.e., layer-by-layer).[38, 137-138, 242-243] This technique has also been used to examine conditions of barite surface dissolution[89, 137, 169] and with respect to the impact of select inhibitors on surface topography (e.g., layer morphology).[101, 110] To the best of our knowledge, AFM has not been used to elucidate the mechanism(s) of barite growth inhibition in the presence of carboxylate based modifiers. Here, we visualize the growth of barite (001) surfaces at near molecular level using *in situ* AFM to elucidate the mode of action by which alginate fully suppresses layer advancement. At low supersaturation (S = 4.4) barite growth is primarily governed by the formation of rhombohedral growth hillocks that emanate from screw dislocations (Figure 32a). In the presence of alginate, step velocities were measured and compared against step velocities in a pure growth solution. Step advancement is suppressed (Figure A37) with increasing inhibitor concentration (Figure 32b) via a step pinning mechanism (see Figure A38).[32, 244] The morphology of the growth hillock, however, remains largely unchanged after exposure to alginate. Barite growth at slightly higher supersaturation (S = 5.3) occurs by the birth and spread of 2-dimensional (2D) islands with a triangular morphology bound by the ⟨120⟩ and ⟨010⟩ directions (Figure 32c). These 2D nuclei have an average height of 3.6 Å (Figure 32d), which is equal to one-half the barite unit cell dimension (*c*/2). There is a 180-degree inversion of 2D island orientation with each new layer (Figure A39) owing to the 2_1 axis symmetry of barite with alternating sulfate group orientation between each half unit cell.[93, 135, 201]

At high alginate concentration (≥ 1 μg mL^{-1}), we observe complete suppression of layer advancement (Figure A40). At lower alginate concentration (e.g., 0.05 μg mL^{-1}), however, we observe bimodal behavior: One fraction of step edges advance at slower rates compared to layer growth in the control, whereas a second fraction of step edges at random orientations are fully suppressed (as indicated by the solid yellow lines in Figure 32e). Sequential images from in situ AFM show that islands growing on the upper terrace of immobilized layers advance until reaching the step edge where growth ceases, leading to the onset of step bunching. This finding is consistent with scanning electron micrographs (Figure A29) showing the presence of macrosteps on different surfaces of barite crystals obtained from bulk assays at quiescent conditions. Collectively, these results demonstrate a disconnect in modifier efficacy determined by microfluidic assays compared to *in situ* AFM studies.

Alginate demonstrates a greater inhibition potency in macroscopic (microfluidic) studies compared to molecular level studies (*in situ* AFM). Complete barite growth inhibition is observed at alginate concentrations > 0.2 μg mL^{-1} in microfluidic assays, while *in situ* AFM studies require modifier concentrations of 1.5 μg mL^{-1} or greater to achieve the same result. This discrepancy is attributed to the significant differences in fluid cell geometry, which influences flow patterns and mass transport, between rectangular microchannels in the microfluidic device and the AFM fluid cell. Simple geometries such as rectangular microchannels allow for controlled laminar and axial flow at the flow rate investigated (Re = 9.2, 12 mL h^{-1}), whereas the AFM fluid cell design generates a thin film of liquid with a primarily radial flow pattern owing to the perpendicular inlet and outlet relative to the sample. The radial flow pattern combined with the interference of the

cantilever probe in AFM studies poses a challenge in accurately mimicking macroscopic flow conditions, which results in mass transport limitations in the growth inhibition studies particularly with bulky modifiers such as alginate.[142]

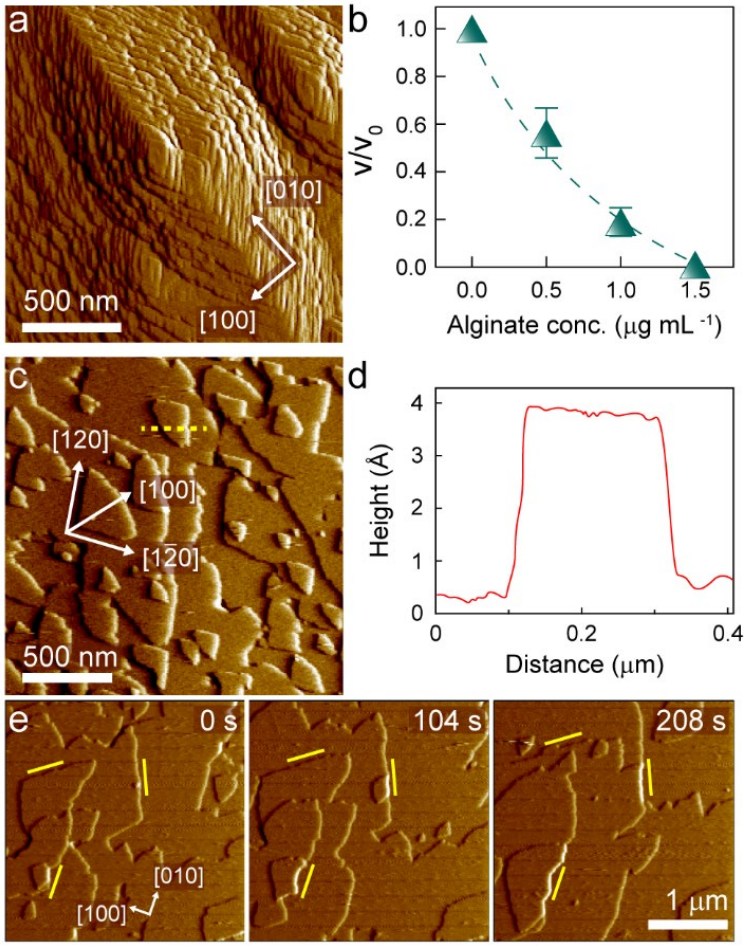

Figure 32. (a) Deflection mode image showing spiral growth from a screw dislocation. (b) Step velocity in the ⟨120⟩ direction. (c) Newly formed 2D growth layers. (d) a representative height profile along the dashed yellow line in panel c). (e) Snapshots of 2D layer nucleation and advancement.

In this article, we systematically evaluated diverse carboxylate-based molecules as inhibitors of barite crystallization under quiescent and flow conditions. A combination of microfluidics and atomic force microscopy was used to assess growth inhibition from the molecular to macroscopic scale. These findings demonstrated that alginate outperforms

other crystal growth modifiers, including common commercial scale treatments such as EDTA and DTPA. One of the unique observations is the full suppression of both nucleation and growth of barite crystals at relatively low alginate concentration (i.e., 0.2 μg mL^{-1}). The superior performance of alginate relative to other carboxylate-based compounds lies in its ability to interact with all principal surfaces of barite crystals. Time-resolved imaging of (001) surface growth during *in situ* AFM measurements reveals that alginate inhibits the advancement of layers via a step pinning mechanism at relatively low supersaturation (S = 4.4). At higher supersaturation (S = 5.3), we observe a transition in the dominant mechanism of inhibition to a step bunching mechanism, which is consistent with macro-step formation observed in bulk assays.

In addition to its dual role as an inhibitor of barite nucleation and crystal growth, there may be practical advantages for replacing current commercial scale inhibitors with alginate. The smaller acid dissociation constants of carboxylate moieties in alginate relative to more widely used analogues (e.g., DTPA) allow for alginate to be used at neutral pH, thus avoiding caustics (i.e., corrosive media) required in many commercial scale treatments. Moreover, the fact that alginate is readily available in nature and is biodegradable makes it an environmentally friendly alternative to products currently used to suppress the formation of barite scale.

Chapter 5: Irreversible Mechanism of Barite Growth Inhibition

Crystallization is a ubiquitous phenomenon in natural, biological, and synthetic processes that include (but are not limited to) biomineralization,[22-25, 48, 178-184, 245] pathological or infectious human diseases,[15-19, 237, 246] and scale formation in industrial pipelines.[21, 104, 106, 174, 218, 238, 240, 247-248] The latter two examples are cases where crystal growth is problematic and research efforts are focused on development economic, facile routes to inhibit crystallization. In this study we examine methods to curtail the formation of barium sulfate (barite), which is a persistent inorganic scale component with a sparing solubility that forms during energy production.[109, 121, 176] One of the most common methods of controlling crystallization is the use of molecular modifiers, which either promote or inhibit rates of crystal nucleation and/or growth.

Nucleation of a crystalline phase is a stochastic process that relies primarily on the supersaturation of the parent solution. Foreign additives can be introduced into growth media as a means of inhibiting crystal nucleation via sequestration of solutes (i.e., reducing supersaturation), disrupting the formation of a critical nucleus (within the context of classical nucleation theory), or altering self-assembly of clusters that participate in nonclassical mechanisms of crystallization.[55, 59, 249-251] Most common industrial modifiers of barite and other scale are rich in phosphate moieties (e.g., hydroxyethylidene diphosphonic acid or diethylenetriamine penta(methylene phosphonic acid)).[112-113, 211-213] Most of these commercial compounds are not easily biodegradable. Moreover, it is difficult to identify (macro)molecules that function as dual inhibitors of crystal growth and nucleation.

5.1 Citrate and Analogues as Crystal Growth Modifiers

Crystal growth modifiers are generally capable of altering the morphology, size, and/or structure of crystals, often through preferential interaction with different crystallographic facets.[80-81] Modifiers are typically decorated with functional groups (motifs) that have a strong binding affinity to crystal surface sites (kinks, step edges, or terraces) where they impede solute attachment via distinct modes of action[31, 79] that alter anisotropic rates of growth with concomitant impact on crystal shape.[81] Citric acid is a common modifier of numerous minerals, such as calcium oxalate monohydrate and calcium carbonate,[81, 252-256] and is an active component in formulations used to prevent pipe corrosion.[14, 83-87] Citrate is also commonly used as a capping agent for materials such as silver (Ag) and gold (Au) nanoparticles to elicit tailored crystal morphologies.[257-259] An analogue of citrate, hydroxycitrate (HCA), has also been found to be an effective inhibitor of calcium-based crystallization through a unique stain-induced mechanism.[260-264]

Here we implement a cooperative approach to investigate barite crystallization and inhibition pathways using bulk crystallization assays, microfluidics, and atomic force microscopy (AFM). These collective experiments reveal HCA to be the most effective inhibitor among molecules tested in this study. Through time-resolved microfluidic assays we identified that HCA exhibits a preferential binding to barite (010) and (100) facets. Using oblique illumination microscopy (OIM), we investigate barite nucleation events and observe a decrease in barium sulfate particles in the presence of 1 mM HCA suggesting that HCA acts as a potent barite nucleation inhibitor. Moreover, *in situ* AFM studies reveal a unique mechanism of irreversible (001) barite surface growth inhibition in the presence of HCA, thus identifying this naturally-derived molecule as a potent barite nucleation and

growth inhibitor that is capable under certain conditions to irreversible inhibit barite (001) surface growth.

5.2 Methods of Investigating Barite Nucleation and Growth

Materials. The following reagents were purchased from Sigma Aldrich: barium chloride dihydrate (99+%), sodium sulfate (>99%), sodium hydroxide (>97%), and sodium chloride (>99.5%), sodium citrate tribasic dihydrate (≥99.0%), DL-isocitric acid disodium hydrate (93%), potassium hydroxycitrate tribasic monohydrate (≥95%), sodium hydroxide (>97%), hydrochloric acid (37%). Polydimethylsiloxane (PDMS, Dow Corning SYLGARD 184) was purchased from Essex Brownell. SU-8 2150 photoresist and SU-8 developer were purchased from Microchem. All chemicals were used as received without further purification. Silicone tubing was purchased from Cole-Parmer. Deionized (DI) water (18.2 MΩ·cm) filtered with an Aqua Solutions RODI-C-12A purification system was used in all experiments.

Bulk crystallization assays. Barite crystals were synthesized using a protocol established in previous work.[195] Barite crystals are synthesized by adding $NaCl_{(aq)}$ into a 20-mL glass vial followed by aliquot addition of 10 mM $BaCl_{2,(aq)}$ and 10 mM $Na_2SO_{4,(aq)}$ stock solutions under mild agitation for 10 s. Samples prepared in the presence of inhibitors were carried out by adding aliquots of aqueous stock solutions of inhibitors to the reaction mixture prior to the addition of Na_2SO_4. The final growth solutions with a total volume of 10 mL had a pH of 7.1 ± 0.3 and a composition of 0.5 mM $BaCl_2$: 0.5 mM Na_2SO_4 : 600 mM NaCl : x μM modifier ($0 \leq x \leq 5$). The sample vials were left undisturbed at 21 ± 1.0 °C for 24 h to allow crystallization of hexagonal barite crystals exhibiting (001), (210), and

(100) facets (Figure 1C). Natural barite samples were obtained from Amazon and purity has been determined in previous work.[78]

Barite crystallization kinetics in bulk assays. Conductivity measurements were carried out to assess the crystallization kinetics in the absence and presence of inhibitors under stirred conditions (300 rpm). The conductivity cell (Thermo Scientific Orion DuraProbe), was vertically immersed into the growth solution and the readings are recorded by a conductivity meter (Thermo Scientific Orion Star A112 benchtop conductivity meter). The conductivity probe was calibrated with Orion conductivity standard 100 μS prior to each experiment. A linear fit was performed on the initial linear portion (30 min) of conductivity values over time, which represents the rate of solute consumption (i.e., crystallization) and is representative of the crystallization growth rate. Growth rates in the presence of inhibitors were divided by the growth rate in the absence of inhibitors were used to calculate percent inhibition as follows: % Inhibition = (1-RGR)×100%, where RGR represents the relative growth rate.

In situ microfluidic assays. The microfluidic platform used was adapted from previous work, in which a chip featuring individual straight channels houses barite seed crystals. To grow barite crystals without additional nucleation, a growth solution with lower supersaturation (S =7) was delivered into the microchannels using a dual syringe pump (CHEMYX Fusion 200) at a rate of 12 mL h^{-1} for 90 min. For growth, two solution components were prepared in individual syringes. One solution contained 0.5 mM $BaCl_{2,(aq)}$ and the second solution contained 0.5 mM Na_2SO_4 and 1.2 M NaCl. The two solutions were mixed using an inline flow configuration that produced a final composition of 0.35 mM $BaCl_2$, 0.35 mM Na_2SO_4, and 600 mM NaCl. Inhibition studies required the

use of two dual syringe pumps, each containing syringes of the same growth solution composition but different quantities of growth modifiers. Time-resolved imaging of barite crystal growth and inhibition using an inverted optical microscope was performed to quantify the kinetics of barite crystallization.

Materials characterization and Instrumentation. Dual star benchtop pH/ISE meters (Orion) equipped with a ROSS Ultra electrode (8102BNUWP). was used for adjusting pH as well as minoring pH change during crystallization. Speciation curves were plotted using Hyperquad Simulation and Speciation (HySS2009),[265] with pk_a values obtained from literature.[246, 266] For *ex situ* microscopy measurements, a clean glass slide (0.5×0.5 cm^2) was placed at the bottom of the glass vials to collect barite crystals. After crystallization, the glass slide was removed from its solution, thoroughly rinsed with DI water, and dried in air prior to further analysis. Scanning electron microscope (SEM) samples were prepared by attaching carbon tape to SEM studs and subsequently attaching glass slides to carbon tape by gently pressing the glass slide to the tape using tweezers. Scanning electron microscope (SEM) images were obtained on a FEI 235 dual-beam (focused ion-beam) system operated at an accelerating voltage of 15 kV and a working distance of 5 mm. as-synthesized samples were prepared by gently pressing the glass slide containing crystals onto the carbon tape. All the samples are coated with a thin layer of gold (ca. 5-10 nm) prior to imaging.

The size and morphology of barite crystals were examined using Leica DM2500-M optical microscope in transmittance mode, while *in situ* imaging of crystal growth was performed on the Leica DMi8 inverted optical microscope using transmittance mode equipped with HC PL Fluotar 5×, 10×, 20×, and N Plan L 50× objectives. At least fifteen

brightfield images of representative areas on the bottom of the glass vials were captured in transmittance mode for characterization of crystals grown in the bulk assay. The average [010] length, [100] width, and [001] thickness of crystals in optical micrographs were measured from a minimum of 100 crystals per trial and three separate trials. For *in situ* time-resolved studies, LAS X software was used to program a minimum of 30 positions along a seeded microchannel, at which images were captured in transmittance mode at 5 min intervals for at least 3 h. Crystals observed *in situ* were analyzed using ImageJ (NIH) using a procedure previously reported.[195] At least 90 crystals located in different channels per batch were analyzed at 5 min intervals over a minimum of 3 h. Crystal lengths were measured every 5 min during inhibition studies. From the change in crystal length over time, a growth rate *r* was determined for each experimental condition, which can be written as percent inhibition using the relative growth rate described previously.

Surface characterization by in situ atomic force microscopy. In situ atomic force microscopy (AFM) was performed to examine the temporal changes in topographical features on the (001) surface of barite. An AFM specimen disk (Ted Pella) covered with a thin layer of thermally curable epoxy (Loctite, China) was placed at the bottom of glass vials during barite synthesis in the bulk assay procedure outlined above. The epoxy was first partially cured in an oven for approximately 6 min at 60 °C and then dried in air overnight to completely cure the epoxy. All AFM measurements were performed in a Cypher ES instrument (Asylum Research, Santa Barbara, CA) using silicon nitride probes with a spring constant of 0.08 N m^{-1} (Oxford Instruments, PNP-TR 1). The liquid cell (ES-CELL-GAS) contained two ports for inlet and outlet flow to maintain constant

supersaturation during AFM measurements. Several concentrations of citrate (CA), isocitrate (ICA), and hydroxycitrate (HCA) were tested in growth solutions with supersaturation ratio S = 5.3. The growth solution was delivered to the liquid cell using an in-line mixing configuration where the two solute solutions (Ba^{2+}, and SO_4^{2-}) were combined immediately before being introduced into the cell (similar to the microfluidics configuration). Freshly prepared growth solutions were used for each experiment (within 2 hours of their preparation). Continuous imaging was performed at ambient temperature in contact mode with a scan rate of 2.44 Hz and 9.77 Hz at 256 lines per scan. For extended time experiments (>4 hours), images were taken in contact mode at 30 min intervals. Relative step velocities were determined by measuring the temporal change in 2D island length in the [010] direction for a minimum of 50 2D islands in the presence of inhibitors (v) and in the absence of inhibitors (v_0).

Nucleation: The onset of nucleation and aggregation of particles was characterized by using Nanosight LM10-HS oblique illumination microscopy (OIM) equipped with a green laser (532 nm) illuminating a solution film with a thickness of 500 μm at an oblique angle. This method relies on light scattered at wavevectors of order μm^{-1} and probes length scales in the range 10^{-3} to 10 μm. 1 mL samples of supersaturated solution (S = 10) in the absence and presence of inhibitors are injected into the OIM chamber, creating the 500 μm film between two glass substrates, at varying times of solution incubation at room temperature 21 ± 1.0 °C. The Brownian trajectory, and the average number density of the particles can be determined through OIM analysis.[267] A minimum of 10 regions within the liquid film were recorded and at least 50 particles were analyzed to obtain particle number density for each inhibitor concentration.

5.3 Evaluating the efficacy of citrate analogues

Here we compare three polyprotic acids of similar structure (Figure 33A): citrate (CA), its isomer isocitrate (ICA), and its derivative hydroxycitrate (HCA). Bulk crystallization assays were performed in the presence and absence of each modifier using optical and electron microscopy to evaluate changes in crystal size, morphology, and population, while solution conductivity measurements were used to assess crystallization kinetics. For all studies reported herein, solution pH of the growth medium was adjusted to 7 in order to evaluate the effects of CA, ICA, and HCA in their fully deprotonated states (Figure A41). Optical micrographs of glass slides placed at the bottom of crystallization vials were analyzed after 24 h under quiescent conditions to assess the number density of crystals. Our findings reveal that CA has no observable effect on crystal number density relative to the control (i.e., absence of modifier), whereas a monotonic reduction in barite crystal number density is observed with increasing ICA concentration (Figure A42). In contrast, we observed a sharp decline in crystal number density for solutions containing HCA at concentrations above 1.2 μM (Figure A42), which indicates HCA impedes barite nucleation (as will be discussed later).

Scanning electron microscopy (SEM) images revealed distinct changes in barite crystal morphology with each polyprotic acid. Citrate produces a barite morphology with a reduced length [010] to width [100] aspect ratio (Figure 34B) compared with that of the control (Figure A43), suggesting a preferential binding that influences growth along the [010] direction. In media containing ICA, growth is also affected along the [010] direction to yield a distinct crystal habit (Figures 33C and A43). Bulk assays in solutions containing HCA required significantly less modifier to inhibit crystal growth, and also resulted in the

generation of two uncommon crystal facets: (011) and (010) faces (Figures 33D and A43). The ability of all three modifiers to impart different crystal morphologies is indicative of their unique binding specificities to barite crystal surfaces, consistent with prior studies showing the unique effects of these homologous polyprotic acids as modifiers of other minerals.[237, 246, 268]

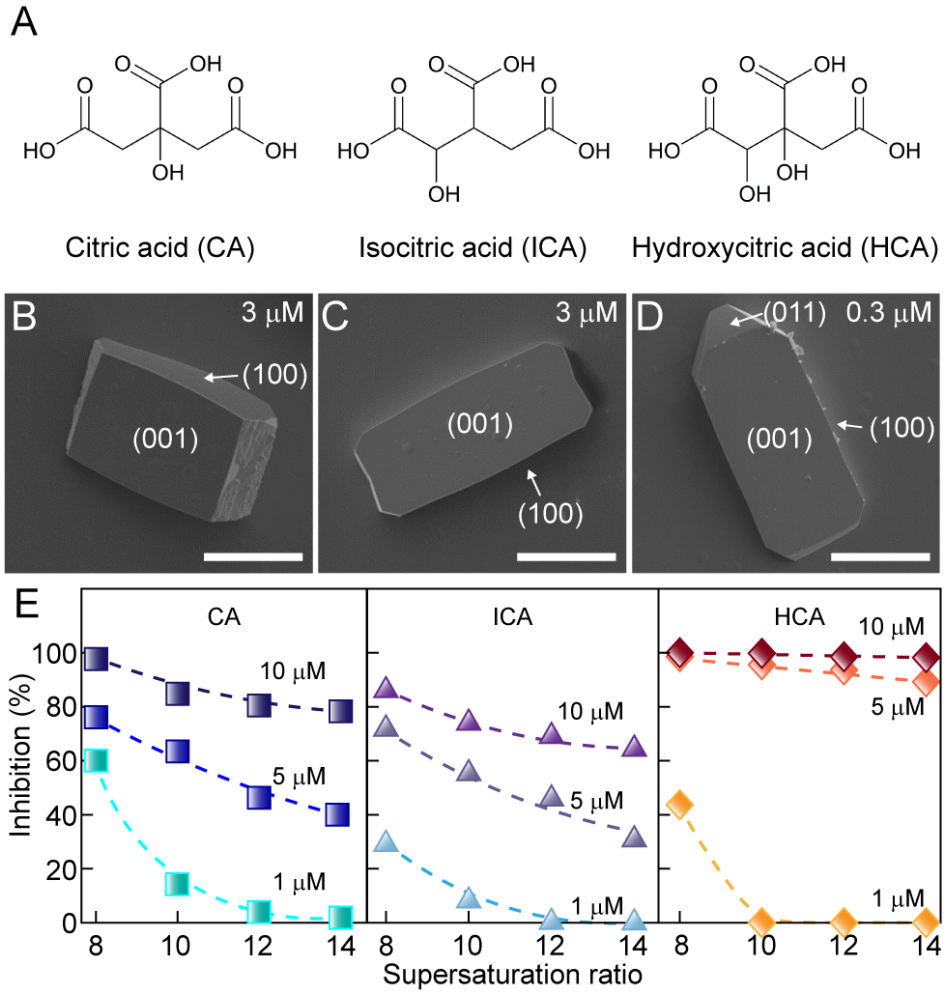

Figure 33. (A) Chemical structures of citrate (CA), isocitrate (ICA), and hydroxycitrate (HCA). (B-D) SEM images of representative barite crystals synthesized in the presence of 3 μM CA, 3 μM ICA, and 0.3 μM HCA. (E) Percent inhibition of barite crystallization as a function of supersaturation ratio.

Ionic conductivity has proven to be an effective method of screening the efficacy of crystal growth modifiers. Monotonic reduction in conductivity during the course of

crystallization allows for the quantification of desupersaturation rate (i.e., a surrogate for the kinetic rate of crystallization) in the presence and absence of modifiers (Figure A44). These experiments were performed over a range of barium sulfate supersaturation (S = 8 – 14) to assess the degree to which each modifier inhibits solute depletion over time (reported as a percent inhibition relative to the control) (Figures A45 and A46). At the lowest modifier concentration tested, all three inhibitors have similar trends (Figure 33E). General trends in percent inhibition for CA and ICA are nearly identical across all modifier concentrations; however, at concentrations of 5 μM HCA we observe a significant departure from these trends with HCA becoming a more potent crystallization inhibitor. Another unique characteristic of HCA is its ability to completely suppress barite crystallization over the entire range of supersaturation compared to CA and ICA, neither of which exceed 80% inhibition at the highest supersaturation tested.

5.4 Microfluidic analysis of barite growth inhibition.

Here we employ a previously developed microfluidic platform[195] to investigate the effects of CA, ICA, and HCA on the macroscopic rates of barite growth in all three principal crystallographic directions. In these experiments, growth solutions are supplied at a constant flow rate to maintain a fixed supersaturation under kinetically-controlled growth conditions.[195, 269] Optical micrographs taken at periodic time intervals capture the growth of individual barite crystals (Figure 34A and B), wherein it is possible to measure changes in crystal length, width, and thickness owing to orthogonal orientations of seed crystals deposited within the microchannel. In Figure 34C we compare the effects of each modifier on anisotropic rates of barite crystal growth. In the presence of 5 μM CA we observed a 75% reduction in growth rate along the crystal length ($\vec{b}$ direction), a 68%

reduction of growth along the thickness ($\vec{c}$ direction), and virtually no inhibition along the width ($\vec{a}$ direction). These results are consistent with quiescent bulk assays (Figure A43) showing CA binding specificity for the barite (010) surface.

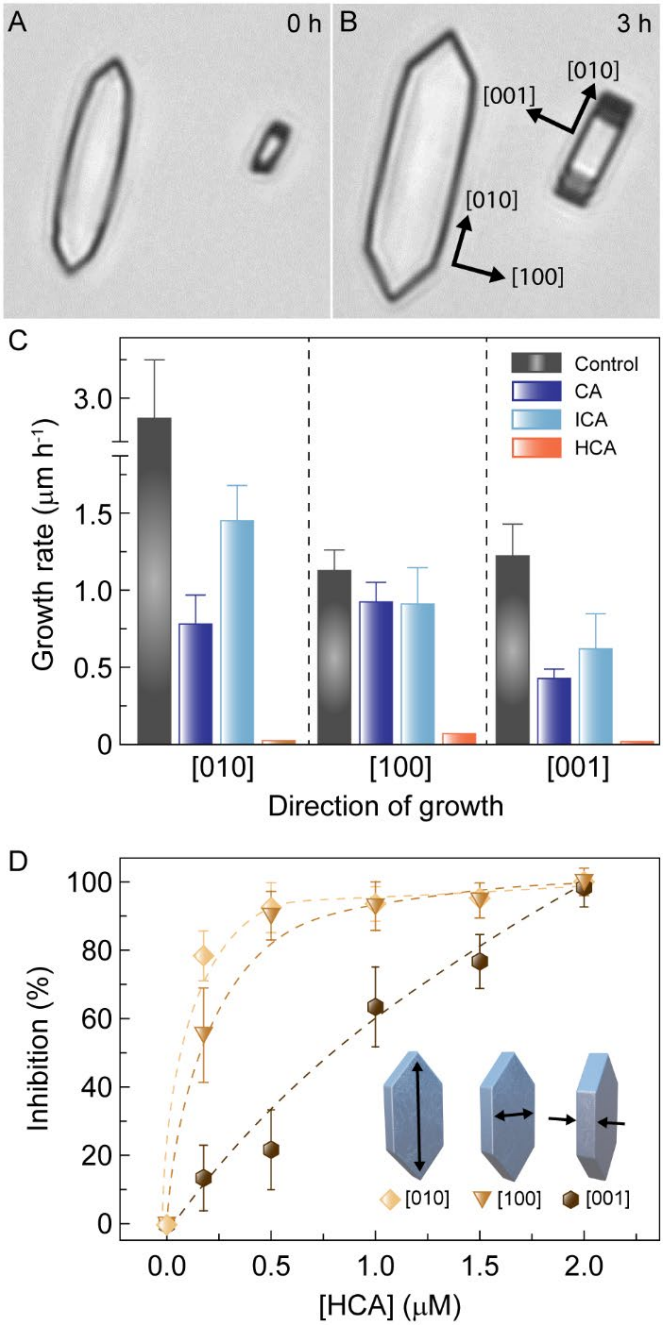

Figure 34. Optical micrographs of barite crystals growing in a microchannel. (C) Growth rate of barite crystals for all three principal crystallographic directions in the absence and presence of 5 μM CA, ICA, and HCA. (D) Percent inhibition of barite growth as a function of HCA concentrations.

Microfluidic assays of growth solutions containing ICA reveal similar specificity, but lower efficacy (i.e., growth inhibition of 50, 19, and 49% in length, width, and thickness, respectively).Analogous to quiescent bulk assays (Figure 33E), solutions containing 5 μM HCA result in nearly complete inhibition of all crystallographic directions; thus, studies conducted under both quiescent and flow conditions consistently show HCA to be a more potent growth inhibitor.

The specificity of HCA for barite crystal facets was more clearly differentiated by lowering modifier concentration below 2 μM (Figure 34D). Under these conditions, we observed that HCA preferentially impedes growth along the [010] and [100] directions (Figure A47) with complete suppression occurring around 0.5 μM HCA. On the contrary, time-resolved microfluidic assays reveal that HCA's impact on barite growth along the [001] direction is less effective. Indeed, our study reveals that a four-fold higher concentration of HCA is required to completely suppress growth along the [001] direction. To this end, these results demonstrate that HCA preferentially interacts with barite (010) and (100) surfaces.

5.5 Hydroxycitrate as a barite nucleation inhibitor.

Having identified HCA as a potent inhibitor of barite growth, we expanded bulk crystallization assays (Figure A43) to systematically assess the effects of HCA on barite nucleation. We conducted quiescent bulk assays using oblique illumination microscopy (OIM), which uses scattered laser light to track the Brownian motion of particles suspended in liquid. For these studies we compared supersaturated solutions of barium sulfate in the absence and presence of HCA (at fixed S = 10). In solutions without modifier, we measured 65 ± 6 particles μm^{-2} immediately after mixing all components and injecting the sample

into the OIM chamber. This observation is consistent with conductivity measurements (Figure A44) where there is an immediate reduction in the ion concentration upon mixing of reagents, which suggests an initial period of rapid precipitation.

The OIM measurement was repeated in the presence of HCA where we observed a monotonic reduction in particle number density with increasing HCA concentration (Figure 33A). In supersaturated growth solutions containing HCA at concentrations ≥ 1.75 μM, we did not observe particles in the OIM sample chamber, which indicates that HCA functions as an inhibitor of nucleation. Still frame images from time-resolved OIM measurements revealed that supersaturated solution (S = 10) in the absence of HCA contains large (mostly immobile) particles that have precipitated to the bottom of the sample chamber (Figure 35B). Conversely, the same experiment using a solution containing 3 μM HCA shows only trace particles (Figure 35C), consistent with bulk crystallization assays showing the absence of crystals after 24 h (Figure A44).

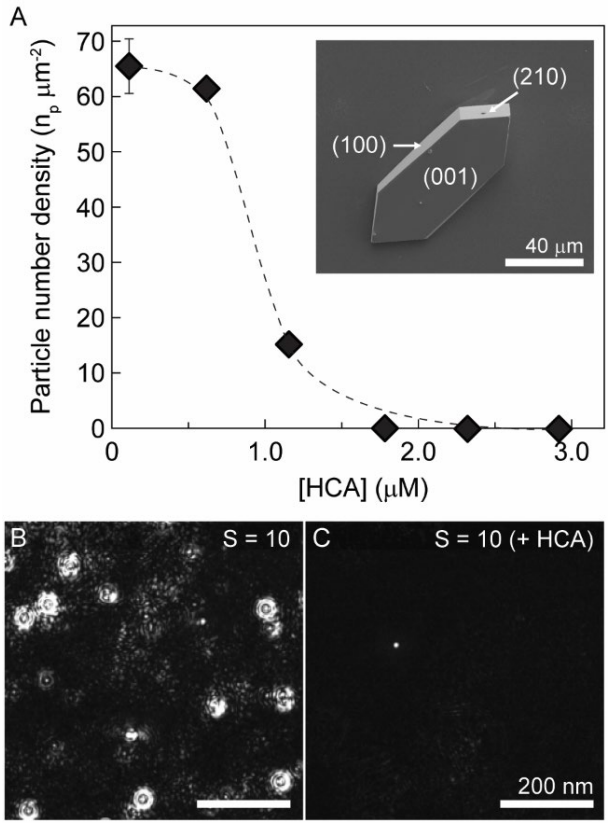

Figure 35. (A) Number density of barite particles decreasing as a function of HCA concentration in oblique illumination microscopy (OIM) assays.(B and C) OIM images of a supersaturated barium sulfate solution (S = 10) in a liquid sample chamber at 21 ± 1 °C.

OIM measurements of barium sulfate solutions at thermodynamic equilibrium (i.e., solubility) or at concentrations below saturation both show no evidence of particles or clusters with sizes that fall within the detection limit of the instrument (≥ 20 nm). As such, there is no evidence to suggest that barite nucleation involves a nonclassical two-step mechanism,[35, 39-43] but rather appears to abide by classical nucleation theory. Interestingly, nucleation can be fully suppressed using only a small quantity of HCA (i.e., 1 mol HCA: 250 mol Ba^{2+}). Using a reported potentiometric titration method in literature to assess ion chelation, there is no appreciable sequestration of free Ba^{2+} ions in solution by HCA

(Figure A48). This suggests that HCA suppresses barite crystallization, not by sequestering solute ions, but through processes that disrupt the formation of a critical nucleus.

5.6 Microscopic Assessment of Barite Growth Inhibition.

In situ atomic force microscopy (AFM) has proven to be a valuable technique for probing the dynamics of surface growth and its inhibition at near molecular level. Here, we use *in situ* AFM to compare the modes of action of CA, ICA, and HCA as inhibitors of barite surface growth, focusing on the (001) crystal surface. We selected a supersaturation (S = 5.3) within a range previously shown[269] to promote surface growth via 2-dimensional birth and spreading. Each single layer has an average height of 3.6 Å (equivalent to a *c/2* unit cell dimension) and a triangular morphology bound by [010] and [120] steps (Figure 36A). Step velocity in the [010] direction was measured from sequential images during continuous scanning (Figures 36B and A49). Here we report a relative step velocity v/v_o where measurements in the presence of each modifier, v, are scaled by the value in the absence of modifier, v_o. Comparison of all three modifiers reveal a similar trend of decreasing relative step velocity with increasing modifier concentration (Figure 36C). Among the molecules tested, HCA is more potent and results in complete suppression of step advancement above 2 μM HCA. Further analysis of the HCA step velocity profile reveals a linear scaling relation between $v_0(v_0\text{-}v)^{-1}$ and c^{-1} (where c is the concentration of modifier), which is indicative of a kink blocking mechanism (Figure A50).[15, 270] The same analysis for CA and ICA reveal a superlinear scaling relation that seems to suggest a combination of two mechanisms, with the second likely to be that of step pinning (one of the most common mechanisms of surface growth inhibition).[15, 17]

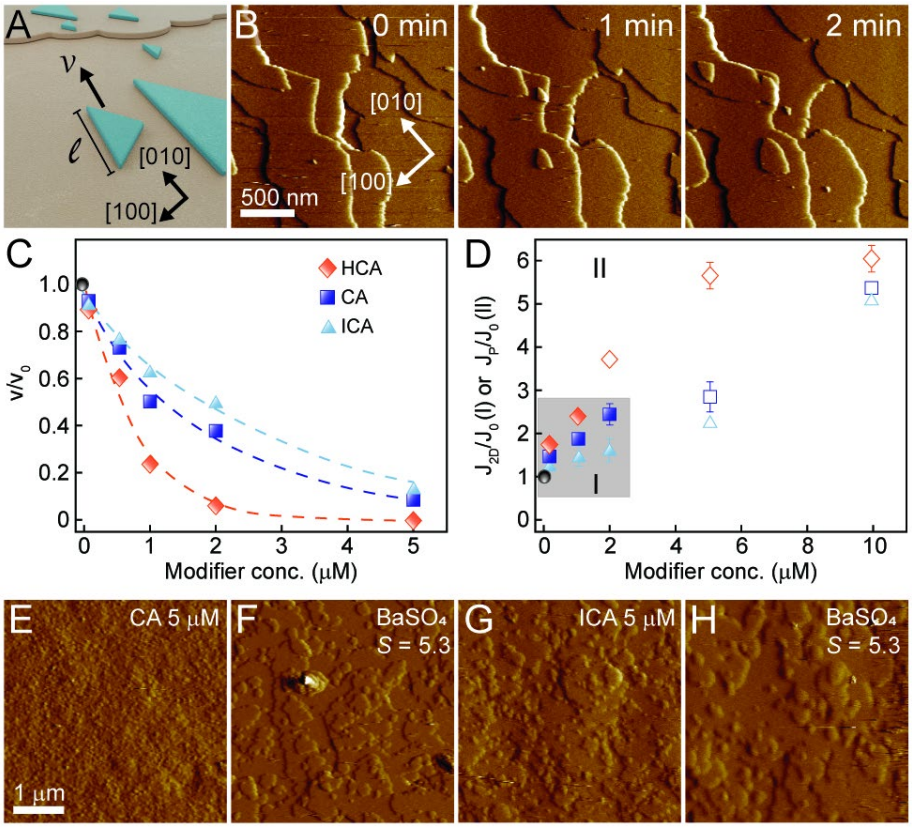

Figure 36. *In situ* AFM images of (001) surface growth (C) Step velocities of layers on the (001) barite surface and (D) the rate of 2D/particle nucleation of new layers J_{2D} relative to that in the absence of inhibitors $J_{2D,0}$, with increasing inhibitor concentration.

Previous examples of kink blockers have shown that layered growth by continuous generation of kink sites at step edges[15] leads to a plateau in the velocity profile (ca. 50% inhibition) with increasing modifier concentration whereby step advancement is not fully suppressed.[16] This seems to suggest that the mechanism(s) of growth inhibition for all three modifiers in Figure 36C may not be exclusively a kink blocking or step pinning mode of action. To test this hypothesis, we also measured the rate of 2D island generation J_{2D} (number of islands per surface area)[82] from time-resolved *in situ* AFM images. It is expected that the rate of layer generation decreases with increasing modifier concentration;[16] however, our measurements show an opposite trend for all three growth modifiers (Figure 36D). We report these results as a relative 2D nucleation rate $J_{2D}/J_{2D,0}$

where measurements in the presence of modifier are scaled by the value in the absence of modifier ($J_{2D,0}$ = 1.24 μm^{-2}).

At modifier concentrations below 2 μM (shaded grey region I in Figure 36D), we observe increases in the rate of 2D nucleation as high as 2.5-times that of the control. Interestingly, concentrations above 2 μM (labelled region II in Figure 36D) lead to further increases in the population of 2D features; however, there are several distinctions between the features observed in regions I and II. First, the 2D features observed in region II neither grow nor dissolve with imaging time. Second, the features in region II have much smaller heights (e.g., 1.8 Å, Figure A49) compared to the height of a single step (3.6 Å) on the barite (001) surface. The exact structure of these features is unknown, but we posit they are disordered islands (i.e., amorphous or possessing high defect density). The deposition of smaller features increases with increasing modifier concentration, with HCA producing the largest increase in the rate of appearance of surface protrusions, which we label J_P (Figure 36D, region II) to distinguish this phenomenon from layer nucleation J_{2D}. Time-resolved *in situ* AFM reveals that the (001) surface becomes covered in small features (Figure A51), which suppresses layer advancement once concentrations reach 5 μM for CA (Figure 36E) and ICA (Figure 36G). Experiments were performed to assess potential regeneration of layered growth upon removal of the modifier and reintroduction of fresh (modifier-free) supersaturated growth solution (S = 5.3) to the AFM liquid cell. Time-resolved images of barite (001) surfaces reveal that layered growth is recovered within one hour for surfaces that had been exposed to CA (Figure 36F) and ICA (Figure 36H); thus, the effects of CA and ICA on barite growth are reversible. In contrast, surfaces exposed to

5 μM HCA were not observed to recover within 10 h of intermittent AFM imaging, highlighting a unique mechanism of irreversible growth inhibition.

5.7 Irreversible Inhibition of Barite Growth.

We further investigated the effects of barite (001) surface exposure to HCA as a means of better understanding the mechanism governing irreversible inhibition of layered growth. In the presence of HCA, barite crystal surfaces become laden with small features (protrusions) that suppress step advancement. Here we present snapshots from in situ AFM studies where the layer growth on the barite surface is fully arrested within 8 min of imaging (Figure 37A) with no evidence of continued formation of surface features after 35 min. Attempts to recover surface growth via the introduction of a supersaturated barium sulfate solution resulted in no visible changes to surface features (Figure 37A, 90 min). The experiment was continued over 12-h period of time with continuous supply of fresh growth solution to the AFM sample cell. After 6 h of intermittent imaging we observed transient features with heights smaller than a single step and modes of feature changes that did not resemble classical island or layered surface growth (Figure A55). After 12-h of imaging, we observed only minor changes in surface topography, such as large features with highly corrugated steps resembling a barite growth hillock (Figure A55). This indicates that the effects of HCA are reversible only after a long period of regeneration. Additional tests showed that this timeframe for growth recovery can be reduced to ca. 1 h when the supersaturation ratio of the regenerating solution is increased from 5.3 to 6.5 (Figure A56).

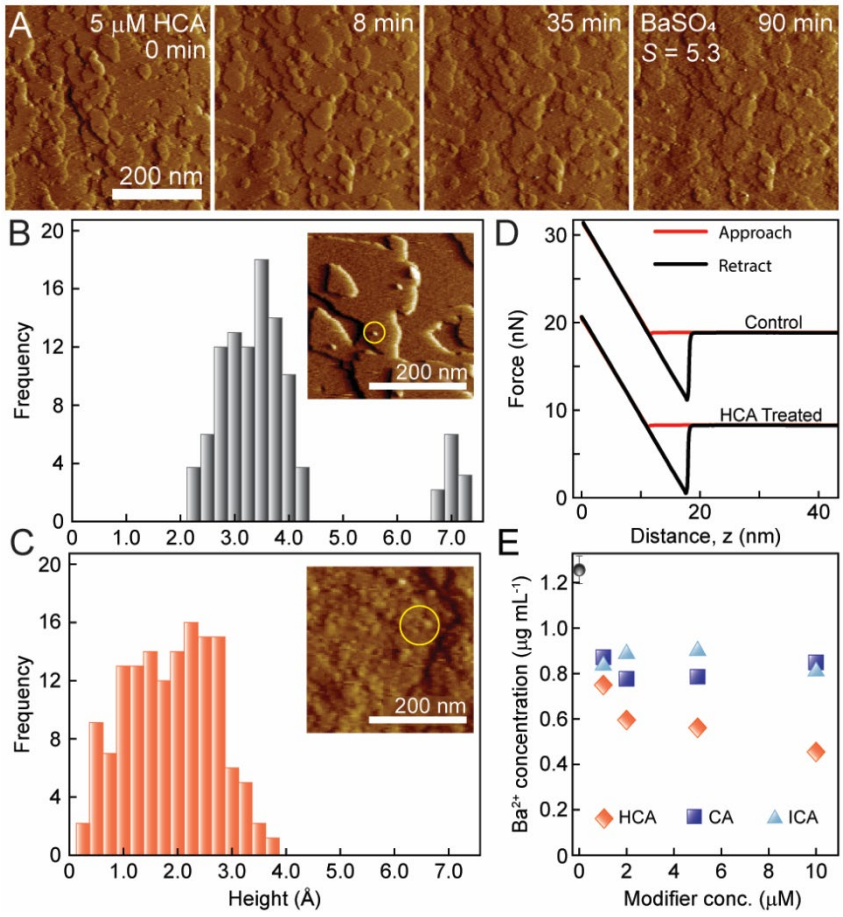

Figure 37. In situ AFM imaging, force measurements, and particle heigh distributions in the presence and absence of HCA.

Topographical analysis of barite (001) surfaces grown in the absence of modifier and in the presence of 5 μM HCA revealed distinct differences in the distributions of surface feature heights. Nucleation of islands in leads to a population of single layers with a Gaussian distribution centered around a step height of 3.2 Å (approximately *c*/2) and a small population of double layers (Figure 37B). The height distribution for protrusions observed on barite surfaces exposed to HCA is much broader with an average height nearly one-half that of the control (Figures 37C and A44). To test whether these small protrusions on barite (001) are either gel-or solid-like in structure, we performed chemical force microscopy (CFM)[30, 53] where AFM tip-crystal approach and retraction profiles are

characteristic of hard surfaces where we observe no appreciable difference between surfaces exposed to a pure growth solution (Figure 37D, top) and those exposed to HCA (Figure 37D, bottom). For instance, interfaces with soft or gel-like properties exhibit nonlinear profiles,[53] which is not observed in CFM profiles for barite.

All three modifiers promote the formation of disordered (or amorphous) protrusions on barite crystals to suppress growth; however, this effect is reversible for ICA and CA within a short period of time during regeneration. To quantify the degree of reversibility, we measured the solubility of natural barite crystals in the presence of varying concentrations of HCA, CA, and ICA. A fixed mass of crystals (ca. 50 mg) was placed in an aqueous solution, leading to dissolution until equilibrium was reached. This was determined by monitoring Ba^{2+} ion concentration in the solution during 14 days of incubation at room temperature. In the absence of modifiers (control), saturation occurs around 1.3 μg Ba^{2+} mL^{-1} (Figure 37E). Introduction of modifiers decreases the solubility with no apparent trends for increasing concentrations of ICA and CA; however, there is a monotonic reduction in Ba^{2+} ion concentration with increasing HCA concentration (orange diamonds in Figure 37E). This suggests that HCA adsorption on barite surfaces impedes dissolution, leading to an undersaturated (metastable) solution with respect to Ba^{2+} ion concentration. These results are consistent with AFM measurements showing irreversible inhibition of barite (001) surfaces. The irreversible effect of HCA, however, is only observed at moderately low supersaturation ($S < 6$), which was required to adjust step velocities within a range that was measurable by *in situ* AFM. Conversely, bulk crystallization and microfluidic assays required higher supersaturation (e.g., $S \geq 7$) to observe appreciable growth within a reasonable timeframe (i.e., order of hours). Under

conditions of higher supersaturation, we observed partial recovery of barite growth (Figure A57) where a regeneration procedure restored growth rates to 60 – 70% of their original value prior to exposing barite crystals to HCA.

In summary, we have compared the performance of citrate and two homologous analogues to assess their relative effect on barite crystallization. Our findings reveal that hydroxycitrate, a molecule differing from others by the presence of one additional alcohol group, is the most effective crystallization inhibitor with a distinct mode of action relative to citrate and isocitrate. We provide evidence that barite nucleation occurs through a classical mechanism, seemingly in accordance with the Szilard postulate stating that solutes from a supersaturated medium join a nucleus or a growing crystal individually.[271] We also observed that HCA completely suppresses solute assembly into pre-nucleation clusters, which is surprising given that nucleation is a stochastic process. Indeed, there are few examples of modifiers capable of blocking nucleation. In this study, we showed that HCA also has the ability to fully suppress barite crystal growth. This dual action of crystal nucleation and growth inhibition is rare, especially for barite crystallization where we are only aware of one previous example – a recent study by our group showing the macromolecule alginate having similar inhibitory effects on barite nucleation and growth.[269]

The exact mechanism by which HCA fully suppresses barite crystallization is not fully understood. Specifically, the structure and composition of protrusions that form on the surface of barite crystals in the presence of HCA is unknown. Using AFM, we showed these features are solid-like with heights much smaller than single layers of barite crystals. The fact that these features persist during periods of regeneration to impart sustained

(irreversible) inhibition suggests the crystal lattice is strained, possibly by incorporation of HCA and/or amorphous protrusions into barite crystals during growth regeneration. In general, crystal growth regeneration after exposure to a modifier is not widely tested in literature. Furthermore, among the few studies that have conducted regeneration assays,[272] the effects of modifiers tend to be reversible: specifically, the rate of crystal growth is restored to its original value once residual modifier is desorbed from the crystal surfaces. Factors differentiating whether a modifier has a reversible or irreversible effect on crystallization remain elusive; however, it is evident that the sustained inhibition of crystal growth after removing HCA from the supersaturated medium is a distinct characteristic among known modifiers of barite crystallization. Our findings indicate that HCA is a versatile disruptor of barite crystallization owing to its dual mode of action as a potent inhibitor of nucleation and growth. The ability of HCA to suppress nucleation has the potential to delay scale formation, making this naturally-derived compound a promising alternative to commercial compounds used for scale prevention. Moreover, the irreversible action of HCA on barite crystal growth indicates that this modifier may not have to be continuously supplied to the site of scale formation, which can potentially reduce operating costs associated with scale prevention.

Chapter 6: Suppressing Barite Crystallization with Organophosphorus Compounds

In this study we examine the efficacy and mechanism of phytic acid (or phytate) as a naturally-derived small molecule inhibitor of barite crystallization. Phytate is decorated with six phosphates and has been widely investigated for its application in the food industry due to its ability to chelate alkaline earth metals (e.g., Ca^{2+} ions) and form insoluble polyphosphate – ion complexes.[273-278] This reported functionality of phytate as a chelating agent and its use in commercial scale inhibitor formulations[279] motivated our investigation of its potential capacity to act as a crystal growth inhibitor.[56, 280-284] Here we compare the efficacy of phytate to that of DTPMP, which was used as a benchmark. Using a combination of microfluidics and scanning probe microscopy, we confirm that both modifiers exhibit dual characteristics as nucleation and growth inhibitors, with phytate being a more potent and potentially more cost-effective and environmentally friendly alternative to DTPMP.

Here we assess the efficacy of phytic acid (PA) as an inhibitor of barite crystallization using the commercial scale inhibitor diethylenetriamine penta(methylene phosphonic acid), or DTPMP, as a benchmark. DTPMP is a polyamine decorated with five phosphonic acids (Figure 38A) with 10 protons having pK_a values that span from 1.04 to 12.58.[285] Full deprotonation of this molecule is only achieved in severely caustic conditions; however, prior studies have shown that DTPMP is a highly effective inhibitor of barite crystallization in a partially dissociated state at near neutral pH.[286-287] PA comprises 12 protons (Figure 38B) where the first four to dissociate are strong acids (pK_a ~2) and the last 4 to dissociate are weak acids that require caustic conditions of pH > 10. Common operating conditions (pH 2 – 10) result in three dominant phytic acid speciations:

PA^{6-}, PA^{7-}, and PA^{8-}.[288] The presence of multiple acids decorating both molecules enables PA and DTPMP to sequester free barium ions in solution, as well as efficiently bind to barite crystal surfaces through proximal modifier-crystal interactions.

In bulk crystallization assays, barite is synthesized under quiescent conditions using a growth solution with supersaturation ratio S = 10. This nominal condition yields a large population of crystals (335 ± 86 crystals mm^{-2}), which is quantified by counting the number of crystals that sediment to the bottom of glass vials per unit area. Barite crystals exhibit an elongated hexagonal platelet morphology (Figure 38C) displaying three prominent facets: basal (001), apical (210), and side (100) surfaces (Figure 38D). Bulk crystallization assays in the presence of PA and DTPMP result in a sharp decline in crystal number density (Figure 38E) with increasing modifier concentration. Within 24 h of analysis, we observe complete suppression of barite nucleation at surprisingly low modifier concentration (ca. 50 nM) with little difference in trends for PA and DTPMP. As expected, the inhibition of nucleation rates leads to fewer crystals that are larger in size (inset of Figure 38E), but do not show any difference in aspect ratio (Figures A58 and A59). Extending the time of analysis to 14 days at 50 nM modifier reveals only a single crystal with [010] length greater than 500 μm (Figure A60).

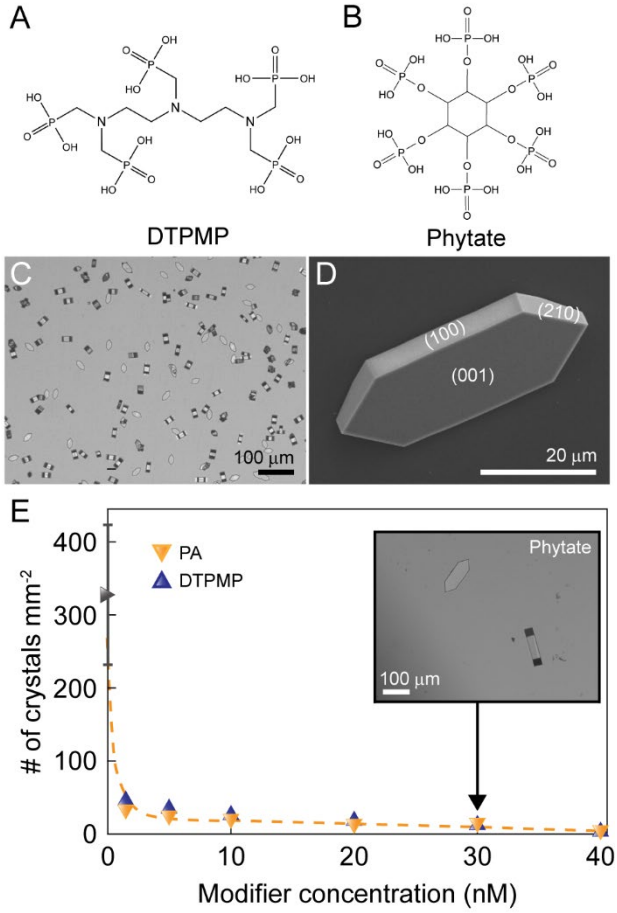

Figure 38. (A) Molecular structures of DTPMP and (B) phytate. (C) Representative optical micrograph of barite crystals. (D) Scanning electron image of a synthetic barite crystal displaying the three principal facets. (E) Crystal number density as a function of concentration.

It could be surmised that PA and DTPMP suppression of barite nucleation involves the inhibition of clusters (precursors) if the process were to involve a nonclassical two-step mechanism,[39-42] as has been suggested in prior literature for solutions containing polymeric additives.[50, 60] To test for this possibility, we also performed oblique illumination microscopy (OIM), which is a scattering technique used to identify particles by Brownian dynamics.[289-290] Solutions prepared at saturation (S = 1) did not show any evidence of clusters over a 3-day period (Figure A61), suggesting nucleation occurs via a classical pathway.[35, 39] Similar experiments were performed in a supersaturated solution (S = 10)

with various concentrations (10 – 50 nM) of each modifier. OIM measurements of these solutions over a much shorter timeframe (ca. 30 s) revealed nucleation and growth of crystals with sizes spanning from 30 to 200 nm (Figure A62). Our findings revealed that the population of particles decreased with increasing modifier concentration, such that the highest concentration (50 nM) completely suppressed nucleation (Figure A63), consistent with observations in bulk crystallization assays (Figure 38E).

In a recent study we have shown that certain modifiers (e.g., alginate) have the dual capability of inhibiting barite nucleation and growth.[269] Here we observe an identical behavior for both PA and DTPMP. Studies of crystal growth inhibition were performed using a combination of microfluidics and *in situ* atomic force microscopy (AFM). The microfluidics platform used in this study was adapted from a previous study[195] where microchannels are seeded with barite crystals and growth solutions with or without modifier are continuously flowing (12 mL h^{-1}) to maintain a constant supersaturation (S = 7) that is slightly less than that of bulk crystallization assays to prevent homogenous nucleation. Time-resolved microfluidic images show significant inhibition of barite growth at 40 nM PA with noticeable changes in crystal habit (Figure 39A), i.e., a blunting of apical tips to generate new (010) facets and a reduction in the length-to-width aspect ratio (or [010]/[100]). Microfluidic measurements reveal complete suppression of growth once the concentration of PA (or DTPMP) reaches 50 nM, which is identical to the concentration required to suppress nucleation. The inhibition of barite growth is evident in Figure 39B by the monotonic reduction in relative growth rate with increasing modifier concentration. Here we report the relative growth rate as the temporal change in (001) surface area in the presence of modifier scaled by its value in the absence of modifier. Comparison of PA and

DTPMP shows that the former is a more potent growth inhibitor (i.e., suppression of barite crystallization occurs at much lower PA concentration).

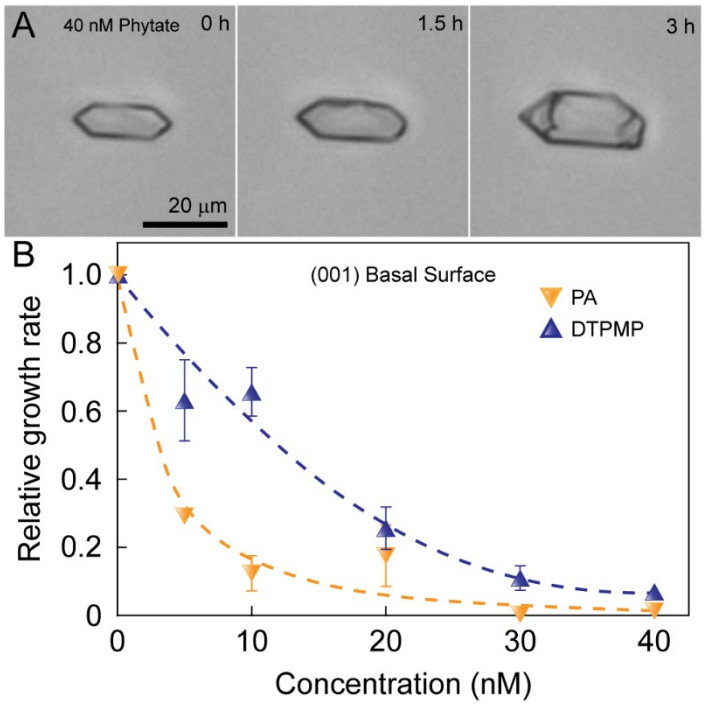

Figure 39. *In situ* microfluidic assays in the presence of DTPMP and PA. (A) optical images of a crystal growing in the presence of 40 nM phytate. (B) Relative growth rate of barite crystals exposed to flowing aqueous solutions of phytate and DTPMP as a function of inhibitor concentration.

In a previous study[269] we confirmed that barite surfaces grow by 2-dimensional layer generation and spreading to yield surfaces with triangular-shaped islands. Here we used *in situ* AFM to show that islands on barite (001) surfaces undergo a transition in geometry from triangular to rounded islands in the presence of PA (Figure 40A). Time-resolved images extracted from in situ AFM studies reveal that PA significantly reduces the rate of step advancement, thereby creating terraces with fixed surface area for subsequent island nucleation. Over the course of continuous imaging we observe an increased density of 2D islands populating the surface; however, the presence of PA

prevents further growth of newly generated layers, leading to a rough surface where growth is fully suppressed after 15 min.

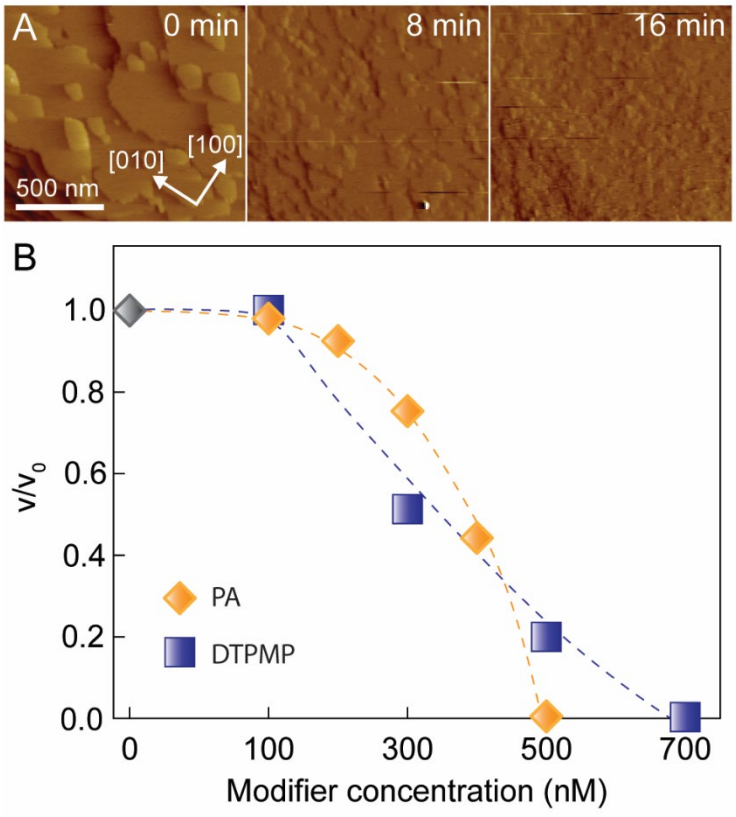

Figure 40. (A) Temporal *in situ* AFM images of growth suppression of the (001) barite surface upon exposure to growth solution (S = 7) containing 500 nM phytate. (B) Relative step velocities of 2D layers measured in the [010] direction in the presence of phytate and DTPMP.

Sequential AFM images were used to measure temporal advancement of layers in the [010] direction. From this data we extracted step velocity v in the presence of modifier, which was scaled by its value v_o in the absence of modifier. Plots of v/v_o as a function of modifier concentration (Figure 40B) reveal trends that are characteristic of the common step pinning mechanism of surface growth inhibition.[32, 291] Comparison of step velocity profiles for PA and DTPMP reveal subtle differences, with PA once again reaching complete suppression of growth at a lower concentration (500 vs. 700 nM). Interestingly,

the concentrations required to suppress growth on the basal (001) surface are nearly an order of magnitude higher than those required to impede growth along orthogonal [100] and [010] directions. Microfluidics measurements of barite crystals in Figure 39 show c-oriented crystals where temporal changes in thickness are not discernable (i.e., out of plane). Seeding of microchannels does result in a small population of a-oriented crystals (Figure A64) where time-resolved imaging shows growth along the [001] direction (i.e., increasing thickness) at low modifier concentrations where growth along the b- and a-directions is fully suppressed. These observations indicate PA and DTPMP inhibition is most effective on barite surfaces with the fastest growth rates, which is desirable from the standpoint of optimizing anti-scaling agents.

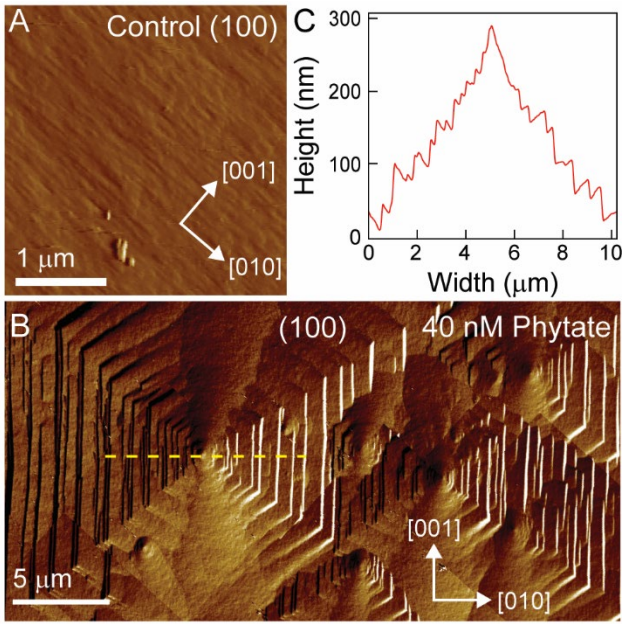

Figure 41. (A) Ex situ AFM image of the (100) surface of a barite crystal grown in the absence of any inhibitor (S = 10). (B) Tile-stitched ex situ images of the (100) surface of a barite crystal grown in the presence of 40 nM phytate in bulk assays. (C) Height profile of the macrostep.

The ability to seed microchannels with barite crystals with different orientations relative to the viewing area enables facile analysis of growth inhibition along all principle crystallization directions.[195] Although similar crystal orientations are achieved in AFM sample preparation, measurements of barite (100) surfaces typically result in topographies devoid of distinct layers (Figure 41A), which makes *in situ* analysis of step velocity impossible. Interestingly, we observe the appearance of distinct surface features on barite (100) surfaces when imaging in solutions containing PA whereas identical experiments with DTPMP do not produce the same effect. As shown in Figure 41B, the presence of PA generates pyramidal macrosteps where edges oriented along the [001] direction appear to be less defined, leading to asymmetric surface topography. A representative height profile measured along one of the pyramids (Figure 41C) shows that steps vary in height with sizes well exceeding single layers (i.e., macrosteps comprising close to 1000 unit cells). The exact mechanism of pyramidal feature generation on the (100) surface is not understood, nor is its relation (if any) to the enhanced efficacy of PA relative to DTPMP.

Chapter 7: Conclusions and Future Outlook

We designed a microfluidic platform for investigating bulk crystallization and dissolution kinetics of barite under dynamic flow conditions. This microfluidic setup allowed us to investigate hydrodynamic contributions to these processes by varying the flow rate during crystallization of barite in the presence and absence of the scale inhibitors (e.g., DTPA) and obtain time-resolved characterizations of crystal morphology. This work established the transition from mass-transport-limited to surface-reaction-limited kinetics for barite growth, inhibition, and dissolution processes. In a reaction-limited growth environment the presence of DTPA, used as a benchmark crystal growth modifier, causes the formation of a new facet, which remains stable through the duration of experiments. Our findings show that barite dissolution is enhanced with increasing diffusive flux of DTPA to the crystal surface. This microfluidic platform has been adapted to evaluate crystallization kinetics for other crystal systems.[18-19]

The dissolution of barite was further evaluated using natural, biocompatible additives by screening a series of polysaccharides with a combination of bulk dissolution assays, molecular dynamics, and *in situ* atomic force microscopy. From a list of biologically-derived polysaccharides we showed that alginate emerges as a clear standout in dissolving barium sulfate crystals. In comparison, the benchmark DTPA was shown to only dissolve barite effectively at high pH owing to lower energetic barriers for its removal of Ba^{2+} ions from crystal surfaces. Microfluidic assays of barite dissolution revealed an increase in barite dissolution kinetics compared to quiescent conditions. Alginate demonstrated a high efficacy over a broad range of solution pH (4 – 9) relative to DTPA (pH ≥ 9). *In situ* AFM imaging revealed that alginate and DTPA exhibit distinct modes of

dissolution, wherein a binary combination of these two demineralizing agents in alkaline media results in synergistic cooperativity. On a molecular level, AFM imaging of the (001) barite surface revealed alginate induces deep (>50 Å) etch pits in the *c*-direction. Conversely, DTPA promotes layer-by-layer dissolution in the *a/b*-plane to generate shallow etch pits. For binary mixtures of alginate and DTPA, the origin of synergy derives from the fact that the two demineralizing agents promote dissolution in orthogonal directions, which enhances the overall rate of barite dissolution. Limited studies in literature have elucidated molecular-level mechanisms of mineral dissolution at the solvent-crystal interface. In this dissertation, we presented a mechanistic interpretation of a newly identified naturally-abundant and environmentally-compatible biopolymer. Our findings demonstrated alginate's versatility and efficacy as a demineralizing agent, thereby opening new avenues for its use in formulations to treat barite (and potentially other scale) formation.

The versatility of alginate as a molecular modifier for barite crystallization was further unraveled through systematic evaluation of carboxylate-based molecules as inhibitors of surface growth. These findings demonstrated that alginate outperforms other crystal growth modifiers, including common commercial scale treatments such as EDTA and DTPA. One of the unique observations in this dissertation is the full suppression of both nucleation and growth of barite crystals at relatively low alginate concentration (i.e., 0.2 μg mL^{-1}). Time-resolved imaging of barite (001) surface growth during *in situ* AFM measurements revealed that alginate inhibits the advancement of layers via a step pinning mechanism at relatively low supersaturation (S = 4.4). At higher supersaturation (S = 5.3), we observed a transition in the dominant mechanism of inhibition to a step bunching

mechanism, which is consistent with macrostep formation observed in bulk crystallization assays. Ultimately, the fact that alginate is readily available in nature and is biodegradable makes it an environmentally friendly alternative to products currently used to suppress the formation of barite scale.

Few studies of crystal growth modifiers have tested recovery after exposure to inhibitors. Prior examples of inorganic crystallization (e.g., calcium oxalate monohydrate)[272] have reported instances where crystal surfaces that become pinned in the presence of macromolecules can be fully recovered within 30 min of introducing fresh growth solution absent of any inhibitor. Scanning probe microscopy studies revealed that citrate (CA) and its analogues ICA and HCA promote 2D layer generation on barite (001) surfaces with reduced step velocities (or rate of layer advancement). Moreover, above a threshold concentration, these additives induce the formation of surface features with heights smaller than classical barite layers (i.e., half unit cell height). Among the three citrates tested, HCA elicits a unique mechanism of barite inhibition, whereby the (001) surface of barite is irreversibly suppressed.

In this dissertation we also evaluated the efficacy of organophosphorus molecules as barite crystallization inhibitors. A cooperative study was conducted to identify the effect of dilute quantities of phytate on crystal habit, kinetics, and topology during growth, while using commercial DTPMP as a benchmark. Both inhibitors demonstrated comparable effects on crystal size and population in quiescent bulk crystallization assays, producing small populations of barite crystals larger than the control. These modifiers, however, induced negligible changes to barite crystal morphology. Microfluidic assays revealed that phytate emerges as a more potent growth inhibitor against DTPMP. From *in situ* AFM

studies we glean that phytate operates through a step pinning mechanism on the barite (001) surface and induces the formation of macrosteps on the (100) surface. The versatility that phytate exhibits as a barium sulfate inhibitor makes this naturally-derived molecule a potentially promising alternative to current commercial treatments.

Collectively, the studies in this body of work systematically evaluated the effects of small molecules and macromolecules of varying functionality (carboxylic acids, alcohols, phosphonic acids, and phosphoric acids). An array of microscopy techniques allowed us to measure crystal growth and dissolution kinetics, which provided mechanistic insight into modifier-mediated crystal inhibition mechanisms. *In situ* atomic force microscopy revealed unique dissolution and irreversible inhibition mechanisms in the presence of select molecular modifiers. These findings established a framework for new crystallization pathways and identified potentially viable alternatives to commercial barite scale treatments.

Crystallization and dissolution mechanisms still lack molecular clarity that is essential for controlling solute attachment/detachment from crystal interfaces and engineering modifiers to tailor crystal properties. An avenue that remains underexplored is the computational exploration of molecular modifiers and the dynamics between inhibitors/dissolvers and crystal facets. In particular, advances in molecular dynamics (MD) can aid in the understanding of the conformations and inter/intramolecular interactions that may occur with (macro)molecules. On the other hand, experimental techniques can benefit from temperature-dependent studies to identify thermal limitations to the inhibition and demineralization capabilities of molecular additives.

References

(1) Variankaval, N.; Cote, A. S.; Doherty, M. F. From Form to Function: Crystallization of Active Pharmaceutical Ingredients. **2008,** *54* (7), 1682-1688.

(2) Chekal, B. P.; Campeta, A. M.; Abramov, Y. A.; Feeder, N.; Glynn, P. P.; McLaughlin, R. W.; Meenan, P. A.; Singer, R. A. The Challenges of Developing an Api Crystallization Process for a Complex Polymorphic and Highly Solvating System. Part I. *Organic Process Research & Development* **2009,** *13* (6), 1327-1337.

(3) Lee, S. S.; Kim, C. S.; Gomez, E. D.; Purushothaman, B.; Toney, M. F.; Wang, C.; Hexemer, A.; Anthony, J. E.; Loo, Y.-L. Controlling Nucleation and Crystallization in Solution-Processed Organic Semiconductors for Thin-Film Transistors. **2009,** *21* (35), 3605-3609.

(4) Izawa, S.; Nakano, K.; Suzuki, K.; Chen, Y.; Kikitsu, T.; Hashizume, D.; Koganezawa, T.; Nguyen, T.-Q.; Tajima, K. Crystallization and Polymorphism of Organic Semiconductor in Thin Film Induced by Surface Segregated Monolayers. *Scientific Reports* **2018,** *8* (1), 481.

(5) Reynolds, M. A. A Technical Playbook for Chemicals and Additives Used in the Hydraulic Fracturing of Shales. *Energy & Fuels* **2020,** *34* (12), 15106-15125.

(6) García, A. V.; Thomsen, K.; Stenby, E. H. Prediction of Mineral Scale Formation in Geothermal and Oilfield Operations Using the Extended Uniquac Model: Part I. Sulfate Scaling Minerals. *Geothermics* **2005,** *34* (1), 61-97.

(7) Bellarby, J. Chapter 7 Production Chemistry. In *Developments in Petroleum Science*; Bellarby, J., Ed.; Elsevier: 2009; pp 371-432.

(8) Yu, L.; Niazi, M. R.; Ngongang Ndjawa, G. O.; Li, R.; Kirmani, A. R.; Munir, R.; Balawi, A. H.; Laquai, F.; Amassian, A. Programmable and Coherent Crystallization of Semiconductors. **2017,** *3* (3), e1602462.

(9) Riera-Galindo, S.; Tamayo, A.; Mas-Torrent, M. Role of Polymorphism and Thin-Film Morphology in Organic Semiconductors Processed by Solution Shearing. *ACS Omega* **2018,** *3* (2), 2329-2339.

(10) Chimmalgi, A.; Hwang, D. J.; Grigoropoulos, C. P. Nanoscale Rapid Melting and Crystallization of Semiconductor Thin Films. *Nano Letters* **2005,** *5* (10), 1924-1930.

(11) Takasuga, M.; Ooshima, H. Control of Crystal Size During Oiling out Crystallization of an Api. *Crystal Growth & Design* **2014,** *14* (11), 6006-6011.

(12) Furuta, M.; Mukai, K.; Cork, D.; Mae, K. Continuous Crystallization Using a Sonicated Tubular System for Controlling Particle Size in an Api Manufacturing Process. *Chemical Engineering and Processing: Process Intensification* **2016,** *102*, 210-218.

(13) Barrett, M.; McNamara, M.; Hao, H.; Barrett, P.; Glennon, B. Supersaturation Tracking for the Development, Optimization and Control of Crystallization Processes. *Chemical Engineering Research and Design* **2010,** *88* (8), 1108-1119.

(14) Zhang, W.; Li, H.-J.; Chen, L.; Sun, J.; Ma, X.; Li, Y.; Liu, C.; Han, X.; Pang, B.; Wu, Y.-C. Performance and Mechanism of a Composite Scaling–Corrosion Inhibitor Used in Seawater: 10-Methylacridinium Iodide and Sodium Citrate. *Desalination* **2020,** *486*, 114482.

(15) Olafson, K. N.; Nguyen, T. Q.; Rimer, J. D.; Vekilov, P. G. Antimalarials Inhibit Hematin Crystallization by Unique Drug–Surface Site Interactions. *Proceedings of the National Academy of Sciences* **2017,** *114* (29), 7531-7536.

(16) Olafson, K. N.; Ketchum, M. A.; Rimer, J. D.; Vekilov, P. G. Mechanisms of Hematin Crystallization and Inhibition by the Antimalarial Drug Chloroquine. *Proceedings of the National Academy of Sciences* **2015,** *112* (16), 4946-4951.

(17) Ma, W.; Lutsko, J. F.; Rimer, J. D.; Vekilov, P. G. Antagonistic Cooperativity between Crystal Growth Modifiers. *Nature* **2020,** *577* (7791), 497-501.

(18) Kim, D.; Olympiou, C.; McCoy, C. P.; Irwin, N. J.; Rimer, J. D. Time-Resolved Dynamics of Struvite Crystallization: Insights from the Macroscopic to Molecular Scale. *Chemistry-A European Journal* **2020,** *26* (16), 3555-3563.

(19) Kim, D.; Moore, J.; McCoy, C. P.; Irwin, N. J.; Rimer, J. D. Engaging a Battle on Two Fronts: Dual Role of Polyphosphates as Potent Inhibitors of Struvite Nucleation and Crystal Growth. *Chemistry of Materials* **2020,** *32* (19), 8672-8682.

(20) Frenier, W.; Ziauddin, M.; Davies, S.; Chang, F. Composition and Method for Treating a Subterranean Formation. 2007.

(21) Bassioni, G. Mechanistic Aspects on the Influence of Inorganic Anion Adsorption on Oilfield Scale Inhibition by Citrate. *Journal of Petroleum Science and Engineering* **2010,** *70* (3-4), 298-301.

(22) Li, M.; Cölfen, H.; Mann, S. Morphological Control of Baso 4 Microstructures by Double Hydrophilic Block Copolymer Mixtures. *Journal of Materials Chemistry* **2004,** *14* (14), 2269-2276.

(23) Qi, L.; Cölfen, H.; Antonietti, M. Control of Barite Morphology by Double-Hydrophilic Block Copolymers. *Chemistry of Materials* **2000,** *12* (8), 2392-2403.

(24) Qi, L.; Cölfen, H.; Antonietti, M.; Li, M.; Hopwood, J. D.; Ashley, A. J.; Mann, S. Formation of Baso4 Fibres with Morphological Complexity in Aqueous Polymer Solutions. *Chemistry–A European Journal* **2001,** *7* (16), 3526-3532.

(25) Yu, S.-H.; Antonietti, M.; Cölfen, H.; Hartmann, J. Growth and Self-Assembly of Bacro4 and Baso4 Nanofibers toward Hierarchical and Repetitive Superstructures by Polymer-Controlled Mineralization Reactions. *Nano Letters* **2003,** *3* (3), 379-382.

(26) Shaw, S. S.; Sorbie, K.; Boak, L. S. The Effects of Barium Sulfate Saturation Ratio, Calcium, and Magnesium on the Inhibition Efficiency: Part Ii Polymeric Scale Inhibitors. *SPE Production & Operations* **2012,** *27* (04), 390-403.

(27) Yan, C.; Kan, A. T.; Zhang, F.; Liu, Y.; Tomson, R. C.; Tomson, M. B. Systematic Study of Barite Nucleation and Inhibition with Various Polymeric Scale Inhibitors by Novel Laser Apparatus. *SPE Journal* **2015,** *20* (03), 642-651.

(28) Kossel, W. Extending the Law of Bravais. *J Nach. Ges. Wiss. Gottingen* **1927,** *143*, 25.

(29) Vekilov, P. G. What Determines the Rate of Growth of Crystals from Solution? *Crystal Growth & Design* **2007,** *7* (12), 2796-2810.

(30) Olafson, K. N.; Clark, R. J.; Vekilov, P. G.; Palmer, J. C.; Rimer, J. D. Structuring of Organic Solvents at Solid Interfaces and Ramifications for Antimalarial Adsorption on B-Hematin Crystals. *ACS Applied Materials & Interfaces* **2018,** *10* (35), 29288-29298.

(31) Chernov, A. A. Growth Mechanisms. In *Modern Crystallography Iii*; Springer: 1984; pp 104-158.

(32) Cabrera, N.; Vermilyea, D.; Doremus, R.; Roberts, B.; Turnbull, D. Growth and Perfection of Crystals. **1958,** *393*.

(33) Burton, W. K.; Cabrera, N.; Frank, F. C.; Mott, N. F. The Growth of Crystals and the Equilibrium Structure of Their Surfaces. **1951,** *243* (866), 299-358.

(34) Olafson, K. N.; Li, R.; Alamani, B. G.; Rimer, J. D. Engineering Crystal Modifiers: Bridging Classical and Nonclassical Crystallization. *Chemistry of Materials* **2016,** *28* (23), 8453-8465.

(35) De Yoreo, J. J.; Vekilov, P. G. Principles of Crystal Nucleation and Growth. *Reviews in Mineralogy and Geochemistry* **2003,** *54* (1), 57-93.

(36) Weber, J.; Bracco, J. N.; Poplawsky, J. D.; Ievlev, A. V.; More, K. L.; Lorenz, M.; Bertagni, A. L.; Jindra, S. A.; Starchenko, V.; Higgins, S. R.; Stack, A. G. Unraveling the Effects of Strontium Incorporation on Barite Growth—in Situ and Ex Situ Observations Using Multiscale Chemical Imaging. *Crystal Growth & Design* **2018,** *18* (9), 5521-5533.

(37) Bracco, J. N.; Gooijer, Y.; Higgins, S. R. Hydrothermal Atomic Force Microscopy Observations of Barite Step Growth Rates as a Function of the Aqueous Barium-to-Sulfate Ratio. *Geochimica et Cosmochimica Acta* **2016,** *183*, 1-13.

(38) Pina, C.; Bosbach, D.; Prieto, M.; Putnis, A. Microtopography of the Barite (0 0 1) Face During Growth:: Afm Observations and Pbc Theory. *Journal of Crystal Growth* **1998,** *187* (1), 119-125.

(39) Erdemir, D.; Lee, A. Y.; Myerson, A. S. Nucleation of Crystals from Solution: Classical and Two-Step Models. *Accounts of Chemical Research* **2009,** *42* (5), 621-629.

(40) Vekilov, P. G. Dense Liquid Precursor for the Nucleation of Ordered Solid Phases from Solution. *Crystal Growth & Design* **2004,** *4* (4), 671-685.

(41) Gebauer, D.; Kellermeier, M.; Gale, J. D.; Bergström, L.; Cölfen, H. Pre-Nucleation Clusters as Solute Precursors in Crystallisation. *Chemical Society Reviews* **2014,** *43* (7), 2348-2371.

(42) Vekilov, P. G. The Two-Step Mechanism of Nucleation of Crystals in Solution. *Nanoscale* **2010,** *2* (11), 2346-2357.

(43) Vekilov, P. G. Nucleation. *Crystal Growth & Design* **2010,** *10* (12), 5007-5019.

(44) Vekilov, P. G. Nonclassical Nucleation. In *Crystallization Via Nonclassical Pathways Volume 1: Nucleation, Assembly, Observation & Application*; American Chemical Society: 2020; Chapter 2, pp 19-46.

(45) Kashchiev, D.; Vekilov, P. G.; Kolomeisky, A. B. Kinetics of Two-Step Nucleation of Crystals. **2005,** *122* (24), 244706.

(46) Wise, W. S. Minerals Zeolites. In *Reference Module in Earth Systems and Environmental Sciences*; Elsevier: 2013.

(47) Ivanova, I. A.-O.; Kolyagin, Y. G.; Kasyanov, I. A.; Yakimov, A. V.; Bok, T. O.; Zarubin, D. N. Time-Resolved in Situ Mas Nmr Monitoring of the Nucleation and Growth of Zeolite Bea Catalysts under Hydrothermal Conditions. (1521-3773 (Electronic)).

(48) De Yoreo, J. J.; Gilbert, P. U.; Sommerdijk, N. A.; Penn, R. L.; Whitelam, S.; Joester, D.; Zhang, H.; Rimer, J. D.; Navrotsky, A.; Banfield, J. F. Crystallization by Particle Attachment in Synthetic, Biogenic, and Geologic Environments. *Science* **2015,** *349* (6247), aaa6760.

(49) Ruiz-Agudo, E.; Burgos-Cara, A.; Ruiz-Agudo, C.; Ibañez-Velasco, A.; Cölfen, H.; Rodriguez-Navarro, C. A Non-Classical View on Calcium Oxalate Precipitation and the Role of Citrate. *Nature Communications* **2017,** *8* (1), 768.

(50) Ruiz-Agudo, C.; Ruiz-Agudo, E.; Putnis, C. V.; Putnis, A. Mechanistic Principles of Barite Formation: From Nanoparticles to Micron-Sized Crystals. *Crystal Growth & Design* **2015,** *15* (8), 3724-3733.

(51) Kumar, M.; Luo, H.; Román-Leshkov, Y.; Rimer, J. D. Ssz-13 Crystallization by Particle Attachment and Deterministic Pathways to Crystal Size Control. *Journal of the American Chemical Society* **2015,** *137* (40), 13007-13017.

(52) Kumar, M.; Choudhary, M. K.; Rimer, J. D. Transient Modes of Zeolite Surface Growth from 3d Gel-Like Islands to 2d Single Layers. *Nature Communications* **2018,** *9* (1), 2129.

(53) Choudhary, M. K.; Kumar, M.; Rimer, J. D. Regulating Nonclassical Pathways of Silicalite-1 Crystallization through Controlled Evolution of Amorphous Precursors. *Angewandte Chemie* **2019,** *131* (44), 15859-15863.

(54) Choudhary, M. K.; Jain, R.; Rimer, J. D. In Situ Imaging of Two-Dimensional Surface Growth Reveals the Prevalence and Role of Defects in Zeolite Crystallization. **2020,** *117* (46), 28632-28639.

(55) Van Driessche, A. E.; Benning Lg Fau - Rodriguez-Blanco, J. D.; Rodriguez-Blanco Jd Fau - Ossorio, M.; Ossorio M Fau - Bots, P.; Bots P Fau - García-Ruiz, J. M.; García-Ruiz, J. M. The Role and Implications of Bassanite as a Stable Precursor Phase to Gypsum Precipitation. (1095).

(56) Xu, A.-W.; Yu, Q.; Dong, W.-F.; Antonietti, M.; Cölfen, H. Stable Amorphous Caco3 Microparticles with Hollow Spherical Superstructures Stabilized by Phytic Acid. **2005,** *17* (18), 2217-2221.

(57) Zeng, Y.; Cao, J.; Wang, Z.; Guo, J.; Lu, J. Formation of Amorphous Calcium Carbonate and Its Transformation Mechanism to Crystalline Caco3 in Laminar Microfluidics. *Crystal Growth & Design* **2018,** *18* (3), 1710-1721.

(58) Tobler, D. J.; Rodriguez-Blanco, J. D.; Dideriksen, K.; Bovet, N.; Sand, K. K.; Stipp, S. L. S. Citrate Effects on Amorphous Calcium Carbonate (Acc) Structure, Stability, and Crystallization. *Advanced Functional Materials* **2015,** *25* (20), 3081-3090.

(59) Bots, P.; Benning, L. G.; Rodriguez-Blanco, J.-D.; Roncal-Herrero, T.; Shaw, S. Mechanistic Insights into the Crystallization of Amorphous Calcium Carbonate (Acc). *Crystal Growth & Design* **2012,** *12* (7), 3806-3814.

(60) Ruiz-Agudo, C.; Ruiz-Agudo, E.; Burgos-Cara, A.; Putnis, C. V.; Ibáñez-Velasco, A.; Rodriguez-Navarro, C.; Putnis, A. Exploring the Effect of Poly(Acrylic Acid) on Pre- and Post-Nucleation Baso4 Species: New Insights into the Mechanisms of Crystallization Control by Polyelectrolytes. *CrystEngComm* **2016,** *18* (16), 2830-2842.

(61) Ruiz-Agudo, C.; McDonogh, D.; Avaro, J. T.; Schupp, D. J.; Gebauer, D. Capturing an Amorphous Baso4 Intermediate Precursor to Barite. *CrystEngComm* **2020,** *22* (8), 1310-1313.

(62) Lasaga, A. C.; Lüttge, A. Mineralogical Approaches to Fundamental Crystal Dissolution Kinetics. *American Mineralogist* **2004,** *89* (4), 527-540.

(63) Lacmann, R.; Heimann, R.; Franke, W. The Dissolution Forms of Single Crystal Spheres: Ii. Theory for the Molecular-Kinetics Interpretation. *Journal of Crystal Growth* **1974,** *26* (1), 117-121.

(64) Lacmann, R.; Franke, W.; Heimann, R. The Dissolution Forms of Single Crystal Spheres: I. Theory for the Molecular-Kinetics Interpretation. *Journal of Crystal Growth* **1974,** *26* (1), 107-116.

(65) Heimann, R.; Franke, W.; Lacmann, R. The Dissolution Forms of Single Crystal Spheres: Iv. Dissolution of Mgo. *Journal of Crystal Growth* **1975,** *28* (1), 151-156.

(66) Franke, W.; Heimann, R.; Lacmann, R. The Dissolution Forms of Single Crystal Spheres: Iii. Dissolution Forms of Ge and Si. *Journal of Crystal Growth* **1975,** *28* (1), 145-150.

(67) Lüttge, A. Crystal Dissolution Kinetics and Gibbs Free Energy. *Journal of Electron Spectroscopy and Related Phenomena* **2006,** *150* (2), 248-259.

(68) Lasaga, A. C.; Luttge, A. Variation of Crystal Dissolution Rate Based on a Dissolution Stepwave Model. **2001,** *291* (5512), 2400-2404.

(69) Heimann, R.; Franke, W.; Lacmann, R. Dissolution Forms of Single Crystal Spheres of Rutile. *Journal of Crystal Growth* **1972,** *13-14*, 202-206.

(70) Dove, P. M.; Han, N.; De Yoreo, J. J. Mechanisms of Classical Crystal Growth Theory Explain Quartz and Silicate Dissolution Behavior. **2005,** *102* (43), 15357-15362.

(71) Snyder, R. C.; Doherty, M. F. Faceted Crystal Shape Evolution During Dissolution or Growth. **2007,** *53* (5), 1337-1348.

(72) Campbell, J. R.; Nancollas, G. H. Crystallization and Dissolution of Strontium Sulfate in Aqueous Solution. *The Journal of Physical Chemistry* **1969,** *73* (6), 1735-1740.

(73) Wang, K.-S.; Resch, R.; Dunn, K.; Shuler, P.; Tang, Y.; Koel, B. E.; Yen, T. F. Dissolution of the Barite (001) Surface by the Chelating Agent Dtpa as Studied with Non-Contact Atomic Force Microscopy. *Colloids and Surfaces A: Physicochemical and Engineering Aspects* **1999,** *160* (3), 217-227.

(74) Shen, D.; Fu, G.; Al-Saiari, H. A.; Kan, A. T.; Tomson, M. B. Barite Dissolution/Precipitation Kinetics in Porous Media and in the Presence and Absence of a Common Scale Inhibitor. *SPE Journal* **2009,** *14* (03), 462-471.

(75) Lakatos, I.; Lakatos-Szabo, J.; Kosztin, B. In *Comparative Study of Different Barite Dissolvers: Technical and Economic Aspects*, International Symposium and Exhibition on Formation Damage Control, Society of Petroleum Engineers: 2002.

(76) Lakatos, I.; Lakatos-Szabo, J.; Kosztin, B. In *Optimization of Barite Dissolvers by Organic Acids and Ph Regulation*, International Symposium on Oilfield Scale, Society of Petroleum Engineers: 2002.

(77) Perry IV, T. D.; Duckworth, O. W.; McNamara, C. J.; Martin, S. T.; Mitchell, R. Effects of the Biologically Produced Polymer Alginic Acid on Macroscopic and

Microscopic Calcite Dissolution Rates. *Environmental science & technology* **2004,** *38* (11), 3040-3046.

(78) Sosa, R. D.; Geng, X.; Agarwal, A.; Palmer, J. C.; Conrad, J. C.; Reynolds, M. A.; Rimer, J. D. Acidic Polysaccharides as Green Alternatives for Barite Scale Dissolution. *ACS Applied Materials & Interfaces* **2020,** *12* (49), 55434-55443.

(79) Myerson, A. *Handbook of Industrial Crystallization*, Butterworth-Heinemann: 2002.

(80) Farmanesh, S.; Ramamoorthy, S.; Chung, J.; Asplin, J. R.; Karande, P.; Rimer, J. D. Specificity of Growth Inhibitors and Their Cooperative Effects in Calcium Oxalate Monohydrate Crystallization. *Journal of the American Chemical Society* **2014,** *136* (1), 367-376.

(81) Grohe, B.; O'Young, J.; Langdon, A.; Karttunen, M.; Goldberg, H. A.; Hunter, G. K. Citrate Modulates Calcium Oxalate Crystal Growth by Face-Specific Interactions. *Cells Tissues Organs* **2011,** *194* (2-4), 176-181.

(82) Markov, I. V. *Crystal Growth for Beginners*.

(83) Toujas, S.; Vázquez, M.; Valcarce, M. B. Unexpected Effect of Citrate Ions on the Corrosion Process of Carbon Steel in Alkaline Solutions. *Corrosion Science* **2017,** *128*, 94-99.

(84) Sobhi, M.; Abdallah, M.; Khairou, K. S. Sildenafil Citrate (Viagra) as a Corrosion Inhibitor for Carbon Steel in Hydrochloric Acid Solutions. *Monatshefte für Chemie - Chemical Monthly* **2012,** *143* (10), 1379-1387.

(85) Serdaroğlu, G.; Kaya, S.; Touir, R. Eco-Friendly Sodium Gluconate and Trisodium Citrate Inhibitors for Low Carbon Steel in Simulated Cooling Water System:

Theoretical Study and Molecular Dynamic Simulations. *Journal of Molecular Liquids* **2020,** *319*, 114108.

(86) Rachid, T.; Hayat, L. Tri-Sodium Citrate as Corrosion and Scale Inhibitor of Mild Steel in Synthetic Cooling Water System. In *New Challenges and Industrial Applications for Corrosion Prevention and Control*; Younes El, K.; Savas, K.; Rachid, T., Eds.; IGI Global: Hershey, PA, USA, 2020; pp 16-39.

(87) Müller, B. Citric Acid as Corrosion Inhibitor for Aluminium Pigment. *Corrosion Science* **2004,** *46* (1), 159-167.

(88) Zhen-Wu, B.; Dideriksen, K.; Olsson, J.; Raahauge, P.; Stipp, S. L. S.; Oelkers, E. Experimental Determination of Barite Dissolution and Precipitation Rates as a Function of Temperature and Aqueous Fluid Composition. *Geochimica et Cosmochimica Acta* **2016,** *194*, 193-210.

(89) Wang, K.-S.; Resch, R.; Dunn, K.; Shuler, P.; Tang, Y.; Koel, B. E.; Fu Yen, T. Dissolution of the Barite (001) Surface by the Chelating Agent Dtpa as Studied with Non-Contact Atomic Force Microscopy. *Colloids and Surfaces A: Physicochemical and Engineering Aspects* **1999,** *160* (3), 217-227.

(90) Thiele, N. A.; MacMillan, S. N.; Wilson, J. J. Rapid Dissolution of $Baso_4$ by Macropa, an 18-Membered Macrocycle with High Affinity for Ba^{2+}. *J. Am. Chem. Soc.* **2018,** *140* (49), 17071-17078.

(91) Putnis, C. V.; Kowacz, M.; Putnis, A. The Mechanism and Kinetics of Dtpa-Promoted Dissolution of Barite. *Applied Geochemistry* **2008,** *23* (9), 2778-2788.

(92) Putnis, A.; Putnis, C. V.; Paul, J. M., The Efficiency of a Dtpa-Based Solvent in the Dissolution of Barium Sulfate Scale Deposits. In *SPE International Symposium on*

Oilfield Chemistry, Society of Petroleum Engineers: San Antonio, Texas, 1995; p 13.

(93) Putnis, A.; Junta-Rosso, J. L.; Hochella, M. F. Dissolution of Barite by a Chelating Ligand: An Atomic Force Microscopy Study. *Geochimica et Cosmochimica Acta* **1995,** *59* (22), 4623-4632.

(94) Morris, R. L.; Paul, J. M., Sulfate Scale Dissolution. US 5084105: 1992.

(95) Lu, J.; Gabrysch, A.; Gao, S.; Yadav, M.; Lee, J.; LePage, J.; Daigle, B.; Tomson, R.; Guraieb, P.; Yan, C., Re-Visit Impact of High Temperature Conditions >150 °C on Sulphate Scale Dissolver Performance. In *SPE Annual Technical Conference and Exhibition*, Society of Petroleum Engineers: San Antonio, Texas, USA, 2017; p 7.

(96) Liu, S. T.; Nancollas, G. H.; Gasiecki, E. A. Scanning Electron Microscopic and Kinetic Studies of the Crystallization and Dissolution of Barium Sulfate Crystals. *Journal of Crystal Growth* **1976,** *33* (1), 11-20.

(97) Dunn, K.; Yen, T. F. Dissolution of Barium Sulfate Scale Deposits by Chelating Agents. *Environmental Science & Technology* **1999,** *33* (16), 2821-2824.

(98) Dove, P. M.; Czank, C. A. Crystal Chemical Controls on the Dissolution Kinetics of the Isostructural Sulfates: Celestite, Anglesite, and Barite. *Geochimica et Cosmochimica Acta* **1995,** *59* (10), 1907-1915.

(99) De Jong, R.; Torny-Schutte, G. J.; Reinhoudt, D. N., Dissolving Barium Sulfate Scale with Aqueous Solutions of Salts of Carboxymethyl Monocyclic Macrocyclic Polyamines. US 4215000: 1980.

(100) Uchida, M.; Sue, A.; Yoshioka, T.; Okuwaki, A. Morphology of Barium Sulfate Synthesized with Barium (Ii)–Aminocarboxylate Chelating Precursors. *CrystEngComm* **2001,** *3* (5), 21-26.

(101) Mavredaki, E.; Neville, A.; Sorbie, K. S. Initial Stages of Barium Sulfate Formation at Surfaces in the Presence of Inhibitors. *Crystal Growth & Design* **2011,** *11* (11), 4751-4758.

(102) Jones, F.; Jones, P.; De Marco, R.; Pejcic, B.; Rohl, A. L. Understanding Barium Sulfate Precipitation onto Stainless Steel. *Applied Surface Science* **2008,** *254* (11), 3459-3468.

(103) Freeman, S. R.; Jones, F.; Ogden, M. I.; Oliviera, A.; Richmond, W. R. Effect of Benzoic Acids on Barite and Calcite Precipitation. *Crystal Growth & Design* **2006,** *6* (11), 2579-2587.

(104) Bukuaghangin, O.; Neville, A.; Charpentier, T. In *Scale Formation in Multiphase Conditions*, Proceedings of the Oil Field Chemistry Symposium, Gielo, 2015.

(105) Jordan, M. M.; Graham, G. M.; Sorbie, K. S.; Matharu, A.; Tomlins, R.; Bunney, J. In *Scale Dissolver Application: Production Enhancement and Formation Damage Potential*, SPE Formation Damage Control Conference, 1998.

(106) Li, J.; Tang, M.; Ye, Z.; Chen, L.; Zhou, Y. Scale Formation and Control in Oil and Gas Fields: A Review. *Journal of Dispersion Science and Technology* **2017,** *38* (5), 661-670.

(107) Weintritt, D. J.; Cowan, J. C. Unique Characteristics of Barium Sulfate Scale Deposition. *Journal of Petroleum Technology* **1967,** *19* (10), 1381-1394.

(108) Hanor, J. S. Barite–Celestine Geochemistry and Environments of Formation. *Reviews in Mineralogy and Geochemistry* **2000,** *40* (1), 193-275.

(109) Mike Crabtree, D. E., Phil Fletcher, Matt Miller, Ashley Johnson, George King Fighting Scale - Removal and Prevention. *Oilfield Review* **1999**, 30-45.

(110) Pina, C. M.; Putnis, C. V.; Becker, U.; Biswas, S.; Carroll, E. C.; Bosbach, D.; Putnis, A. An Atomic Force Microscopy and Molecular Simulations Study of the Inhibition of Barite Growth by Phosphonates. *Surface Science* **2004,** *553* (1), 61-74.

(111) Leung, W. H.; Nancollas, G. H. A Kinetic Study of the Seeded Growth of Barium Sulfate in the Presence of Additives. *Journal of Inorganic and Nuclear Chemistry* **1978,** *40* (11), 1871-1875.

(112) Jones, F.; Oliveira, A.; Rohl, A.; Parkinson, G.; Ogden, M.; Reyhani, M. Investigation into the Effect of Phosphonate Inhibitors on Barium Sulfate Precipitation. *Journal of Crystal Growth* **2002,** *237*, 424-429.

(113) Black, S. N.; Bromley, L. A.; Cottier, D.; Davey, R. J.; Dobbs, B.; Rout, J. E. Interactions at the Organic/Inorganic Interface: Binding Motifs for Phosphonates at the Surface of Barite Crystals. *Journal of the Chemical Society, Faraday Transactions* **1991,** *87* (20), 3409-3414.

(114) Teir, S.; Eloneva, S.; Fogelholm, C.-J.; Zevenhoven, R. Dissolution of Steelmaking Slags in Acetic Acid for Precipitated Calcium Carbonate Production. *Energy* **2007,** *32* (4), 528-539.

(115) Fredd, C. N.; Fogler, H. S. In *Alternative Stimulation Fluids and Their Impact on Carbonate Acidizing*, SPE Formation Damage Control Symposium, 1996.

(116) Paul, J.; Fieler, E. In *A New Solvent for Oilfield Scales*, SPE Annual Technical Conference and Exhibition, Society of Petroleum Engineers: 1992.

(117) Morris, R. L.; Paul, J. M., Method for Removing Alkaline Sulfate Scale. US 4980077: 1990.

(118) Mason, D. J., Composition for Removing Naturally Occurring Radioactive Material (Norm) Scale. US 9896615: 2018.

(119) D'muhala, T. F., Barium Sulfate Removal and Anti-Deposition Compositions and Process of Use Therefor. US 4708805: 1987.

(120) Means, J. L.; Kucak, T.; Crerar, D. A. Relative Degradation Rates of Nta, Edta and Dtpa and Environmental Implications. *Environmental Pollution Series B, Chemical and Physical* **1980,** *1* (1), 45-60.

(121) Blount, C. W. Barite Solubilities and Thermodynamic Quantities up to 300 C and 1400 Bars. *American Mineralogist* **1977,** *62*, 942-957.

(122) Crabtree, M.; Eslinger, D.; Fletcher, P.; Miller, M.; Johnson, A.; King, G. Fighting Scale — Removal and Prevention. *Oilfield Rev.* **1999**, 30-45.

(123) Lee, K. S.; Kim, T. H. *Integrative Understanding of Shale Gas Reservoirs*, Springer International Publishing: 2016.

(124) Timmreck, T. C.; Shook, G. Environmental Health and Occupational Health Implications of Baritosis, a Pneumoconiosis. *Journal of Environmental Health* **1992,** *55* (1), 22-26.

(125) Nancollas, G. H.; Liu, S. T. Crystal Growth and Dissolution of Barium Sulfate. *Society of Petroleum Engineers Journal* **1975,** *15* (06), 509-516.

(126) Gardner, G. L.; Nancollas, G. H. Crystal Growth in Aqueous Solution at Elevated Temperatures. Barium Sulfate Growth Kinetics. *The Journal of Physical Chemistry* **1983,** *87* (23), 4699-4703.

(127) Sorbie, K. S.; Laing, N. In *How Scale Inhibitors Work - Mechanisms of Selected Barium Sulphate Scale Inhibitors across a Wide Temperature Range*, SPE Sixth International Symposium on Oilfield Scale; Exploring the Boundaries of Scale Control, Aberdeen, Scottland, United Kingdom, Aberdeen, Scottland, United Kingdom, 2004.

(128) Piana, S.; Jones, F.; Gale, J. D. Assisted Desolvation as a Key Kinetic Step for Crystal Growth. *Journal of the American Chemical Society* **2006,** *128* (41), 13568-13574.

(129) Jones, F.; Jones, P.; Ogden, M. I.; Richmond, W. R.; Rohl, A. L.; Saunders, M. The Interaction of Edta with Barium Sulfate. *Journal of Colloid and Interface Science* **2007,** *316* (2), 553-561.

(130) Mavredaki, E.; Neville, A.; Sorbie, K. Assessment of Barium Sulphate Formation and Inhibition at Surfaces with Synchrotron X-Ray Diffraction (Sxrd). *Applied Surface Science* **2011,** *257* (9), 4264-4271.

(131) Sorbie, K. S.; Laing, N., How Scale Inhibitors Work: Mechanisms of Selected Barium Sulphate Scale Inhibitors across a Wide Temperature Range. In *SPE International Symposium on Oilfield Scale*, Society of Petroleum Engineers: Aberdeen, United Kingdom, 2004; p 10.

(132) Todd, A. C.; Yuan, M. D. Barium and Strontium Sulfate Solid-Solution Scale Formation at Elevated Temperatures. *SPE Production Engineering* **1992,** *7* (01), 85-92.

(133) Dunn, K.; Daniel, E.; Shuler, P. J.; Chen, H. J.; Tang, Y.; Yen, T. F. Mechanisms of Surface Precipitation and Dissolution of Barite: A Morphology Approach. *Journal of Colloid and Interface Science* **1999,** *214* (2), 427-437.

(134) Jones, F.; Rohl, A. L. Empirical Molecular Modelling of Crystal Growth Modifiers. *Molecular Simulation* **2005,** *31* (6-7), 393-398.

(135) Bosbach, D.; Hall, C.; Putnis, A. Mineral Precipitation and Dissolution in Aqueous Solution: In-Situ Microscopic Observations on Barite (001) with Atomic Force Microscopy. *Chemical Geology* **1998,** *151* (1), 143-160.

(136) Higgins, S. R.; Jordan, G.; Eggleston, C. M.; Knauss, K. G. Dissolution Kinetics of the Barium Sulfate (001) Surface by Hydrothermal Atomic Force Microscopy. *Langmuir* **1998,** *14* (18), 4967-4971.

(137) Risthaus, P.; Bosbach, D.; Becker, U.; Putnis, A. Barite Scale Formation and Dissolution at High Ionic Strength Studied with Atomic Force Microscopy. *Colloids and Surfaces A: Physicochemical and Engineering Aspects* **2001,** *191* (3), 201-214.

(138) Kowacz, M.; Putnis, C. V.; Putnis, A. The Effect of Cation:Anion Ratio in Solution on the Mechanism of Barite Growth at Constant Supersaturation: Role of the Desolvation Process on the Growth Kinetics. *Geochimica et Cosmochimica Acta* **2007,** *71* (21), 5168-5179.

(139) Kuwahara, Y.; Makio, M. In Situ Afm Study on Barite (001) Surface Dissolution in Nacl Solutions at 30°C. *Applied Geochemistry* **2014,** *51*, 246-254.

(140) Bracco, J. N.; Lee, S. S.; Stubbs, J. E.; Eng, P. J.; Heberling, F.; Fenter, P.; Stack, A. G. Hydration Structure of the Barite (001)–Water Interface: Comparison of X-Ray Reflectivity with Molecular Dynamics Simulations. *The Journal of Physical Chemistry C* **2017,** *121* (22), 12236-12248.

(141) Godinho, J. R. A.; Stack, A. G. Growth Kinetics and Morphology of Barite Crystals Derived from Face-Specific Growth Rates. *Crystal Growth & Design* **2015,** *15* (5), 2064-2071.

(142) Peruffo, M.; Mbogoro, M. M.; Adobes-Vidal, M.; Unwin, P. R. Importance of Mass Transport and Spatially Heterogeneous Flux Processes for in Situ Atomic Force Microscopy Measurements of Crystal Growth and Dissolution Kinetics. *The Journal of Physical Chemistry C* **2016,** *120* (22), 12100-12112.

(143) Adobes-Vidal, M.; Shtukenberg, A. G.; Ward, M. D.; Unwin, P. R. Multiscale Visualization and Quantitative Analysis of L-Cystine Crystal Dissolution. *Crystal Growth & Design* **2017,** *17* (4), 1766-1774.

(144) Shim, J.-u.; Cristobal, G.; Link, D. R.; Thorsen, T.; Fraden, S. Using Microfluidics to Decouple Nucleation and Growth of Protein Crystals. *Crystal Growth & Design* **2007,** *7* (11), 2192-2194.

(145) Ildefonso, M.; Revalor, E.; Punniam, P.; Salmon, J. B.; Candoni, N.; Veesler, S. Nucleation and Polymorphism Explored Via an Easy-to-Use Microfluidic Tool. *Journal of Crystal Growth* **2012,** *342* (1), 9-12.

(146) Heymann, M.; Opthalage, A.; Wierman, J. L.; Akella, S.; Szebenyi, D. M. E.; Gruner, S. M.; Fraden, S. Room-Temperature Serial Crystallography Using a Kinetically Optimized Microfluidic Device for Protein Crystallization and on-Chip X-Ray Diffraction. *IUCrJ* **2014,** *1* (5), 349-360.

(147) Zhang, S.; Ferté, N.; Candoni, N.; Veesler, S. Versatile Microfluidic Approach to Crystallization. *Organic Process Research & Development* **2015,** *19* (12), 1837-1841.

(148) Gerard, C. J. J.; Ferry, G.; Vuillard, L. M.; Boutin, J. A.; Ferte, N.; Grossier, R.; Candoni, N.; Veesler, S. A Chemical Library to Screen Protein and Protein–Ligand Crystallization Using a Versatile Microfluidic Platform. *Crystal Growth & Design* **2018,** *18* (9), 5130-5137.

(149) Grossier, R.; Tishkova, V.; Morin, R.; Veesler, S. A Parameter to Probe Microdroplet Dynamics and Crystal Nucleation. *AIP Advances* **2018,** *8* (7), 075324.

(150) Schudel, B. R.; Choi, C. J.; Cunningham, B. T.; Kenis, P. J. A. Microfluidic Chip for Combinatorial Mixing and Screening of Assays. *Lab on a Chip* **2009,** *9* (12), 1676-1680.

(151) Gong, X.; Wang, Y.-W.; Ihli, J.; Kim, Y.-Y.; Li, S.; Walshaw, R.; Chen, L.; Meldrum, F. C. The Crystal Hotel: A Microfluidic Approach to Biomimetic Crystallization. *Advanced Materials* **2015,** *27* (45), 7395-7400.

(152) Laffite, G.; Leroy, C.; Bonhomme, C.; Bonhomme-Coury, L.; Letavernier, E.; Daudon, M.; Frochot, V.; Haymann, J. P.; Rouzière, S.; Lucas, I. T.; Bazin, D.; Babonneau, F.; Abou-Hassan, A. Calcium Oxalate Precipitation by Diffusion

Using Laminar Microfluidics: Toward a Biomimetic Model of Pathological Microcalcifications. *Lab on a Chip* **2016,** *16* (7), 1157-1160.

(153) Li, S.; Ihli, J.; Marchant, W. J.; Zeng, M.; Chen, L.; Wehbe, K.; Cinque, G.; Cespedes, O.; Kapur, N.; Meldrum, F. C. Synchrotron Ftir Mapping of Mineralization in a Microfluidic Device. *Lab on a Chip* **2017,** *17* (9), 1616-1624.

(154) Seo, S. W.; Ko, K. Y.; Lee, C.-S.; Kim, I. H. $CaCO_3$ Biomineralization in Microfluidic Crystallizer. *Hwahak Konghak* **2013,** *51*, 151– 156.

(155) Jeon, N. L.; Dertinger, S. K. W.; Chiu, D. T.; Choi, I. S.; Stroock, A. D.; Whitesides, G. M. Generation of Solution and Surface Gradients Using Microfluidic Systems. *Langmuir* **2000,** *16* (22), 8311-8316.

(156) Dertinger, S. K. W.; Chiu, D. T.; Jeon, N. L.; Whitesides, G. M. Generation of Gradients Having Complex Shapes Using Microfluidic Networks. *Analytical Chemistry* **2001,** *73* (6), 1240-1246.

(157) Ishida, T.; Shimamoto, T.; Ozaki, N.; Takaki, S.; Kuchimaru, T.; Kizaka-Kondoh, S.; Omata, T. Investigation of the Influence of Glucose Concentration on Cancer Cells by Using a Microfluidic Gradient Generator without the Induction of Large Shear Stress. *Micromachines* **2016,** *7* (9), 155.

(158) Xia, Y.; Whitesides, G. M. Soft Lithography. *Annu. Rev. Mater. Sci.* **1998,** *28* (1), 153-184.

(159) Nancollas, G. H.; Purdie, N. Crystallization of Barium Sulphate in Aqueous Solution. *Transactions of the Faraday Society* **1963,** *59* (0), 735-740.

(160) Blount, C. W. Synthesis of Barite, Celestite, Anglesite, Witherite, and Strontianite from Aqueous Solutions. *American Mineralogist* **1974,** *59*, 1209-1219.

(161) Vanysek, P. Ionic Conductivity and Diffusion at Infinite Dilution. *CRC handbook of chemistry and physics* **2000,** *83*, 76-78.

(162) Walter, S.; Malmberg, S.; Schmidt, B.; Liauw, M. A. Mass Transfer Limitations in Microchannel Reactors. *Catalysis Today* **2005,** *110* (1), 15-25.

(163) Gervais, T.; Jensen, K. F. Mass Transport and Surface Reactions in Microfluidic Systems. *Chemical Engineering Science* **2006,** *61* (4), 1102-1121.

(164) Squires, T. M.; Messinger, R. J.; Manalis, S. R. Making It Stick: Convection, Reaction and Diffusion in Surface-Based Biosensors. *Nature Biotechnology* **2008,** *26*, 417.

(165) Levich, V. G. *Physicochemical Hydrodynamics*, Prentice-Hall: Englewood Cliffs, N.J., 1962.

(166) Chernov, A. A. How Does the Flow within the Boundary Layer Influence Morphological Stability of a Vicinal Face? *Journal of Crystal Growth* **1992,** *118* (3), 333-347.

(167) Van Driessche, A. E. S.; García-Ruiz, J. M.; Delgado-López, J. M.; Sazaki, G. In Situ Observation of Step Dynamics on Gypsum Crystals. *Crystal Growth & Design* **2010,** *10* (9), 3909-3916.

(168) Juhasz, N. M.; Deen, W. M. Effect of Local Peclet Number on Mass Transfer to a Heterogeneous Surface. *Industrial & Engineering Chemistry Research* **1991,** *30* (3), 556-562.

(169) Kowacz, M.; Putnis, C. V.; Putnis, A. The Control of Solution Composition on Ligand-Promoted Dissolution: Dtpa−Barite Interactions. *Crystal Growth & Design* **2009,** *9* (12), 5266-5272.

(170) Bageri, B. S.; Mahmoud, M. A.; Shawabkeh, R. A.; Al-Mutairi, S. H.; Abdulraheem, A. Toward a Complete Removal of Barite (Barium Sulfate $$\Hbox {Baso}_{4}$$Baso4) Scale Using Chelating Agents and Catalysts. *Arab. J. Sci. Eng.* **2017,** *42* (4), 1667-1674.

(171) Mahmoud, M.; Ba Geri, B.; Abdelgawad, K.; Kamal, M. S.; Hussein, I.; Elkatatny, S.; Shawabkeh, R. Evaluation of the Reaction Kinetics of Diethylenetriaminepentaacetic Acid Chelating Agent and a Converter with Barium Sulfate (Barite) Using a Rotating Disk Apparatus. *Energy & Fuels* **2018,** *32* (9), 9813-9821.

(172) Herman, J. S.; White, W. B. Dissolution Kinetics of Dolomite: Effects of Lithology and Fluid Flow Velocity. *Geochimica et Cosmochimica Acta* **1985,** *49* (10), 2017-2026.

(173) McConchie, B. W.; Norris, H. H.; Bundoc, V. G.; Trivedi, S.; Boesen, A.; Urban, J. F.; Keane-Myers, A. M. Ascaris Suum-Derived Products Suppress Mucosal Allergic Inflammation in an Interleukin-10-Independent Manner Via Interference with Dendritic Cell Function. *Infect. Immun.* **2006,** *74* (12), 6632-6641.

(174) Bageri, B. S.; Mahmoud, M. A.; Shawabkeh, R. A.; Al-Mutairi, S. H.; Abdulraheem, A. Toward a Complete Removal of Barite (Barium Sulfate Baso4) Scale Using Chelating Agents and Catalysts. *Arabian Journal for Science and Engineering* **2017,** *42* (4), 1667-1674.

(175) Bao, H. Purifying Barite for Oxygen Isotope Measurement by Dissolution and Reprecipitation in a Chelating Solution. *Analytical chemistry* **2006,** *78* (1), 304-309.

(176) Abdelgawad, K.; Mahmoud, M.; Elkatatny, S.; Patil, S. In *Effect of Calcium Carbonate on Barite Solubility Using a Chelating Agent and Converter*, SPE International Conference on Oilfield Chemistry, Society of Petroleum Engineers: 2019.

(177) Harry, D.; Horton, D.; Durham, D.; Constable, D. J. C.; Gaffney, S.; Moore, J.; Todd, B.; Martinez, I. Grand Challenges and Opportunities for Greener Chemical Alternatives in Hydraulic Fracturing: A Perspective from the Acs Green Chemistry Institute Oilfield Chemistry Roundtable. *Energy Fuels* **2020,** *34* (7), 7837-7846.

(178) Addadi, L.; Berman, A.; Moradian-Oldak, J.; Weiner, S. Tuning of Crystal Nucleation and Growth by Proteins: Molecular Interactions at Solid-Liquid Interfaces in Biomineralization. *Croatica Chemica Acta* **1990,** *63* (3), 539-544.

(179) Aizenberg, J. Crystallization in Patterns: A Bio-Inspired Approach. *Advanced Materials* **2004,** *16* (15), 1295-1302.

(180) Aizenberg, J.; Lambert, G.; Weiner, S.; Addadi, L. Factors Involved in the Formation of Amorphous and Crystalline Calcium Carbonate: A Study of an Ascidian Skeleton. *Journal of the American Chemical Society* **2002,** *124* (1), 32-39.

(181) Dove, P. M.; De Yoreo, J. J.; Weiner, S. *Biomineralization*, Walter de Gruyter GmbH & Co KG: 2018; Vol. 54.

(182) Smeets, P. J.; Cho, K. R.; Kempen, R. G.; Sommerdijk, N. A.; De Yoreo, J. J. Calcium Carbonate Nucleation Driven by Ion Binding in a Biomimetic Matrix Revealed by in Situ Electron Microscopy. *Nature materials* **2015,** *14* (4), 394-399.

(183) Tambutté, S.; Holcomb, M.; Ferrier-Pagès, C.; Reynaud, S.; Tambutté, É.; Zoccola, D.; Allemand, D. Coral Biomineralization: From the Gene to the Environment. *Journal of Experimental Marine Biology and Ecology* **2011,** *408* (1-2), 58-78.

(184) Weiner, S.; Addadi, L. Crystallization Pathways in Biomineralization. *Annual review of materials research* **2011,** *41*, 21-40.

(185) Ouyang, B.; Akob, D. M.; Dunlap, D.; Renock, D. Microbially Mediated Barite Dissolution in Anoxic Brines. *Applied Geochemistry* **2017,** *76*, 51-59.

(186) Burns, K.; Wu, Y.-T.; Grant, C. S. Mechanisms of Calcite Dissolution Using Environmentally Benign Polyaspartic Acid: A Rotating Disk Study. *Langmuir* **2003,** *19* (14), 5669-5679.

(187) Lee, O. K.; Lee, E. Y. Sustainable Production of Bioethanol from Renewable Brown Algae Biomass. *Biomass and Bioenergy* **2016,** *92*, 70-75.

(188) Ching, S. H.; Bansal, N.; Bhandari, B. Alginate Gel Particles–a Review of Production Techniques and Physical Properties. *Critical Reviews in Food Science and Nutrition* **2017,** *57* (6), 1133-1152.

(189) Tam, S.; Bilodeau, S.; Dusseault, J.; Langlois, G.; Hallé, J.-P.; Yahia, L. Biocompatibility and Physicochemical Characteristics of Alginate–Polycation Microcapsules. *Acta Biomaterialia* **2011,** *7* (4), 1683-1692.

(190) Onsøyen, E. Alginates. In *Thickening and Gelling Agents for Food*; Springer: 1997; pp 22-44.

(191) Moulin, C.; Amekraz, B.; Steiner, V.; Plancque, G.; Ansoborlo, E. Speciation Studies on Dtpa Using the Complementary Nature of Electrospray Ionization Mass

Spectrometry and Time-Resolved Laser-Induced Fluorescence. *Applied Spectroscopy* **2003,** *57* (9), 1151-1161.

(192) Palmer, J. C.; Debenedetti, P. G. Recent Advances in Molecular Simulation: A Chemical Engineering Perspective. *AIChE Journal* **2015,** *61* (2), 370-383.

(193) Qin, W.; Agarwal, A.; Choudhary, M. K.; Palmer, J. C.; Rimer, J. D. Molecular Modifiers Suppress Nonclassical Pathways of Zeolite Crystallization. *Chemistry of Materials* **2019,** *31* (9), 3228-3238.

(194) Torrie, G. M.; Valleau, J. P. Nonphysical Sampling Distributions in Monte Carlo Free-Energy Estimation: Umbrella Sampling. *Journal of Computational Physics* **1977,** *23* (2), 187-199.

(195) Sosa, R. D.; Geng, X.; Reynolds, M. A.; Rimer, J. D.; Conrad, J. C. A Microfluidic Approach for Probing Hydrodynamic Effects in Barite Scale Formation. *Lab on a Chip* **2019,** *19* (9), 1534-1544.

(196) Chuang, J.-J.; Huang, Y.-Y.; Lo, S.-H.; Hsu, T.-F.; Huang, W.-Y.; Huang, S.-L.; Lin, Y.-S. Effects of Ph on the Shape of Alginate Particles and Its Release Behavior. *International Journal of Polymer Science* **2017,** *2017*, Article ID 3902704.

(197) Gómez-Ordóñez, E.; Rupérez, P. Ftir-Atr Spectroscopy as a Tool for Polysaccharide Identification in Edible Brown and Red Seaweeds. *Food Hydrocolloids* **2011,** *25* (6), 1514-1520.

(198) Papageorgiou, S. K.; Kouvelos, E. P.; Favvas, E. P.; Sapalidis, A. A.; Romanos, G. E.; Katsaros, F. K. Metal–Carboxylate Interactions in Metal–Alginate Complexes Studied with Ftir Spectroscopy. *Carbohydrate Research* **2010,** *345* (4), 469-473.

(199) Sarmento, B. Characterization of Insulin-Loaded Alginate Nanoparticles Produced by Ionotropic Pre-Gelation through Dsc and Ftir Studies. *Carbohydrate polymers* **2006,** *v. 66* (no. 1), pp. 1-7-2006 v.66 no.1.

(200) Ma, W.; Lutsko, J. F.; Rimer, J. D.; Vekilov, P. G. Antagonistic Cooperativity between Crystal Growth Modifiers. *Nature* **2020**, 1-5.

(201) Hill, R. A Further Refinement of the Barite Structure. *The Canadian Mineralogist* **1977,** *15* (4), 522-526.

(202) Abraham, M.; Van der Spoel, D.; Lindahl, E.; Hess, B., The Gromacs Development Team (2018) Gromacs User Manual, Version 2016.

(203) Abraham, M. J.; Murtola, T.; Schulz, R.; Páll, S.; Smith, J. C.; Hess, B.; Lindahl, E. Gromacs: High Performance Molecular Simulations through Multi-Level Parallelism from Laptops to Supercomputers. *SoftwareX* **2015,** *1*, 19-25.

(204) Malde, A. K.; Zuo, L.; Breeze, M.; Stroet, M.; Poger, D.; Nair, P. C.; Oostenbrink, C.; Mark, A. E. An Automated Force Field Topology Builder (Atb) and Repository: Version 1.0. *Journal of chemical theory and computation* **2011,** *7* (12), 4026-4037.

(205) Berendsen, H. J.; Postma, J. P.; van Gunsteren, W. F.; Hermans, J. Interaction Models for Water in Relation to Protein Hydration. In *Intermolecular Forces*; Springer: 1981; pp 331-342.

(206) Rowley, C. N.; Roux, B. A Computational Study of Barium Blockades in the Kcsa Potassium Channel Based on Multi-Ion Potential of Mean Force Calculations and Free Energy Perturbation. *Journal of General Physiology* **2013,** *142* (4), 451-463.

(207) Bonomi, M.; Branduardi, D.; Bussi, G.; Camilloni, C.; Provasi, D.; Raiteri, P.; Donadio, D.; Marinelli, F.; Pietrucci, F.; Broglia, R. A. Plumed: A Portable Plugin for Free-Energy Calculations with Molecular Dynamics. *Computer Physics Communications* **2009,** *180* (10), 1961-1972.

(208) Tribello, G. A.; Bonomi, M.; Branduardi, D.; Camilloni, C.; Bussi, G. Plumed 2: New Feathers for an Old Bird. *Computer Physics Communications* **2014,** *185* (2), 604-613.

(209) Reynolds, M. A. A Technical Playbook for Chemicals and Additives Used in the Hydraulic Fracturing of Shales. *Energy & Fuels* **2020**.

(210) Torres, L.; Yadav, O. P.; Khan, E. Risk Assessment of Human Exposure to Ra-226 in Oil Produced Water from the Bakken Shale. *Science of The Total Environment* **2018,** *626*, 867-874.

(211) Baynton, A.; Ogden, M. I.; Raston, C. L.; Jones, F. Barium Sulfate Crystallization Dependence on Upper Rim Calix [4] Arene Functional Groups. *CrystEngComm* **2012,** *14* (3), 1057-1062.

(212) Coveney, P. V.; Davey, R.; Griffin, J. L.; He, Y.; Hamlin, J. D.; Stackhouse, S.; Whiting, A. A New Design Strategy for Molecular Recognition in Heterogeneous Systems: A Universal Crystal-Face Growth Inhibitor for Barium Sulfate. *Journal of the American Chemical Society* **2000,** *122* (46), 11557-11558.

(213) Pina, C.; Putnis, C. V.; Becker, U.; Biswas, S.; Carroll, E.; Bosbach, D.; Putnis, A. An Atomic Force Microscopy and Molecular Simulations Study of the Inhibition of Barite Growth by Phosphonates. *Surface Science* **2004,** *553* (1-3), 61-74.

(214) Nowack, B.; Stone, A. T. Degradation of Nitrilotris(Methylenephosphonic Acid) and Related (Amino)Phosphonate Chelating Agents in the Presence of Manganese and Molecular Oxygen. *Environmental Science & Technology* **2000,** *34* (22), 4759-4765.

(215) Akın, B.; Öner, M.; Bayram, Y.; Demadis, K. D. Effects of Carboxylate-Modified, "Green" Inulin Biopolymers on the Crystal Growth of Calcium Oxalate. *Crystal Growth & Design* **2008,** *8* (6), 1997-2005.

(216) Boels, L.; Witkamp, G.-J. Carboxymethyl Inulin Biopolymers: A Green Alternative for Phosphonate Calcium Carbonate Growth Inhibitors. *Crystal Growth & Design* **2011,** *11* (9), 4155-4165.

(217) Zhang, H.-p.; Luo, X.-g.; Lin, X.-y.; Tang, P.-p.; Lu, X.; Yang, M.-j.; Tang, Y. Biodegradable Carboxymethyl Inulin as a Scale Inhibitor for Calcite Crystal Growth: Molecular Level Understanding. *Desalination* **2016,** *381*, 1-7.

(218) Charlesworth, M.; Kalli, C. J.; Thomas, D. G.; Shi, W.; Graham, B. F.; Aman, Z. M.; May, E. F. Compositions and Methods for Scale Inhibition. US 0221849, 2016.

(219) Malkaj, P.; Pierri, E.; Dalas, E. The Crystallization of Hydroxyapatite in the Presence of Sodium Alginate. *Journal of Materials Science: Materials in Medicine* **2005,** *16* (8), 733-737.

(220) Nielsen, J. W.; Sand, K. K.; Pedersen, C. S.; Lakshtanov, L.; Winther, J. R.; Willemoës, M.; Stipp, S. L. S. Polysaccharide Effects on Calcite Growth: The Influence of Composition and Branching. *Crystal Growth & Design* **2012,** *12* (10), 4906-4910.

(221) Olderøy, M. Ø.; Xie, M.; Strand, B. L.; Flaten, E. M.; Sikorski, P.; Andreassen, J.-P. Growth and Nucleation of Calcium Carbonate Vaterite Crystals in Presence of Alginate. *Crystal Growth & Design* **2009,** *9* (12), 5176-5183.

(222) Wei, L.; Hong, T.; Liu, H.; Chen, T. The Effect of Sodium Alginate on Struvite Crystallization in Aqueous Solution: A Kinetics Study. *Journal of Crystal Growth* **2017,** *473*, 60-65.

(223) Lakshtanov, L.; Bovet, N.; Stipp, S. L. S. Inhibition of Calcite Growth by Alginate. *Geochimica et Cosmochimica Acta* **2011,** *75* (14), 3945-3955.

(224) Manoli, F.; Dalas, E. The Effect of Sodium Alginate on the Crystal Growth of Calcium Carbonate. *Journal of Materials Science: Materials in Medicine* **2002,** *13* (2), 155-158.

(225) Ucar, S.; Bjørnøy, S. H.; Bassett, D. C.; Strand, B. L.; Sikorski, P.; Andreassen, J.-P. Formation of Hydroxyapatite Via Transformation of Amorphous Calcium Phosphate in the Presence of Alginate Additives. *Crystal Growth & Design* **2019,** *19* (12), 7077-7087.

(226) Ucar, S.; Bjørnøy, S. H.; Bassett, D. C.; Strand, B. L.; Sikorski, P.; Andreassen, J.-P. Nucleation and Growth of Brushite in the Presence of Alginate. *Crystal Growth & Design* **2015,** *15* (11), 5397-5405.

(227) Fan, C.; Kan, A. T.; Zhang, P.; Tomson, M. B. Barite Nucleation and Inhibition at 0 to 200* C with and without Thermodynamic Hydrate Inhibitors. *SPE Journal* **2011,** *16* (02), 440-450.

(228) He, S.; Oddo, J. E.; Tomson, M. B. The Inhibition of Gypsum and Barite Nucleation in Nacl Brines at Temperatures from 25 to 90 C. *Applied Geochemistry* **1994,** *9* (5), 561-567.

(229) Zhang, F.; Dai, Z.; Yan, C.; Bhandari, N.; Yan, F.; Liu, Y.; Zhang, Z.; Ruan, G.; Kan, A. T.; Tomson, M. B. Barite-Scaling Risk and Inhibition at High Temperature. *SPE Journal* **2017,** *22* (01), 69-79.

(230) Kashchiev, D.; Van Rosmalen, G. Nucleation in Solutions Revisited. *Crystal Research Technology: Journal of Experimental Industrial Crystallography* **2003,** *38* (7-8), 555-574.

(231) Burton, W.-K.; Cabrera, N.; Frank, F. The Growth of Crystals and the Equilibrium Structure of Their Surfaces. *Philosophical Transactions of the Royal Society of London. Series A, Mathematical Physical Sciences* **1951,** *243* (866), 299-358.

(232) Yan, F.; Dai, Z.; Ruan, G.; Alsaiari, H.; Bhandari, N.; Zhang, F.; Liu, Y.; Zhang, Z.; Kan, A.; Tomson, M. Barite Scale Formation and Inhibition in Laminar and Turbulent Flow: A Rotating Cylinder Approach. *Journal of Petroleum Science Engineering* **2017,** *149*, 183-192.

(233) Cho, K. R.; Kim, Y.-Y.; Yang, P.; Cai, W.; Pan, H.; Kulak, A. N.; Lau, J. L.; Kulshreshtha, P.; Armes, S. P.; Meldrum, F. C. Direct Observation of Mineral–Organic Composite Formation Reveals Occlusion Mechanism. *Nature Communications* **2016,** *7* (1), 1-7.

(234) Lupulescu, A. I.; Rimer, J. D. In Situ Imaging of Silicalite-1 Surface Growth Reveals the Mechanism of Crystallization. *Science* **2014,** *344* (6185), 729-732.

(235) Ma, X.; Zhang, S.; Jiao, F.; Newcomb, C. J.; Zhang, Y.; Prakash, A.; Liao, Z.; Baer, M. D.; Mundy, C. J.; Pfaendtner, J. Tuning Crystallization Pathways through Sequence Engineering of Biomimetic Polymers. *Nature Materials* **2017,** *16* (7), 767-774.

(236) Gates-Rector, S.; Blanton, T. The Powder Diffraction File: A Quality Materials Characterization Database. *Powder Diffraction* **2019,** *34* (4), 352-360.

(237) Chung, J.; Sosa, R.; Rimer, J. D. Elucidating the Effects of Polyprotic Acid Speciation in Calcium Oxalate Crystallization. *Crystal Growth & Design* **2017,** *17* (8), 4280-4288.

(238) Abd-El-Khalek, D.; Abd-El-Nabey, B.; Abdel-kawi, M. A.; Ebrahim, S.; Ramadan, S. The Inhibition of Crystal Growth of Gypsum and Barite Scales in Industrial Water Systems Using Green Antiscalant. *Water Supply* **2019,** *19* (7), 2140-2146.

(239) BinMerdhah, A. B.; Yassin, A. A. M.; Muherei, M. A. Laboratory and Prediction of Barium Sulfate Scaling at High-Barium Formation Water. *Journal of Petroleum Science Engineering* **2010,** *70* (1-2), 79-88.

(240) Mady, M. F.; Bayat, P.; Kelland, M. A. Environmentally-Friendly Phosphonated Polyetheramine Scale Inhibitors-Excellent Calcium Compatibility for Oilfield Applications. *Industrial & Engineering Chemistry Research* **2020**.

(241) Derby, J. J. Fluid Dynamics in Crystal Growth: The Good, the Bad, and the Ugly. *Progress in Crystal Growth and Characterization of Materials* **2016,** *62* (2), 286-301.

(242) Pina, C. M.; Becker, U.; Risthaus, P.; Bosbach, D.; Putnis, A. Molecular-Scale Mechanisms of Crystal Growth in Barite. *Nature* **1998,** *395* (6701), 483-486.

(243) Pina, C. M.; Enders, M.; Putnis, A. The Composition of Solid Solutions Crystallising from Aqueous Solutions: The Influence of Supersaturation and Growth Mechanisms. *Chemical Geology* **2000,** *168* (3-4), 195-210.

(244) Wang, L.; De Yoreo, J. J.; Guan, X.; Qiu, S. R.; Hoyer, J. R.; Nancollas, G. H. Constant Composition Studies Verify the Utility of the Cabrera− Vermilyea (Cv) Model in Explaining Mechanisms of Calcium Oxalate Monohydrate Crystallization. *Crystal Growth & Design* **2006,** *6* (8), 1769-1775.

(245) Weiner, S. Biomineralization: A Structural Perspective. *Journal of Structural Biology* **2008,** *163* (3), 229-234.

(246) Chung, J.; Taylor, M. G.; Granja, I.; Asplin, J. R.; Mpourmpakis, G.; Rimer, J. D. Factors Differentiating the Effectiveness of Polyprotic Acids as Inhibitors of Calcium Oxalate Crystallization in Kidney Stone Disease. *Crystal Growth & Design* **2018,** *18* (9), 5617-5627.

(247) Brown, A.; Merrett, S.; Putnam, J. In *Coil-Tubing Milling/Underreaming of Barium Sulphate Scale and Scale Control in the Forties Field*, Offshore Europe, Society of Petroleum Engineers: 1991.

(248) Kenneth Stuart Sorbie, N. L. In *How Scale Inhibitors Work - Mechanisms of Selected Barium Sulphate Scale Inhibitors across a Wide Temperature Range*, SPE Sixth International Symposium on Oilfield Scale; Exploring the Boundaries of Scale Control, Aberdeen, Scottland, United Kingdom, Aberdeen, Scottland, United Kingdom, 2004.

(249) Sommerdijk, N. A. J. M.; With, G. d. Biomimetic Caco3 Mineralization Using Designer Molecules and Interfaces. *Chemical Reviews* **2008,** *108* (11), 4499-4550.

(250) Gower, L. B. Biomimetic Model Systems for Investigating the Amorphous Precursor Pathway and Its Role in Biomineralization. *Chemical Reviews* **2008,** *108* (11), 4551-4627.

(251) Gebauer, D.; Völkel, A.; Cölfen, H. Stable Prenucleation Calcium Carbonate Clusters. **2008,** *322* (5909), 1819-1822.

(252) Wierzbicki, A.; Sikes, C. S.; Sallis, J. D.; Madura, J. D.; Stevens, E. D.; Martin, K. L. Scanning Electron Microscopy and Molecular Modeling of Inhibition of Calcium Oxalate Monohydrate Crystal Growth by Citrate and Phosphocitrate. *Calcified Tissue International* **1995,** *56* (4), 297-304.

(253) Wang, L.; Zhang, W.; Qiu, S. R.; Zachowicz, W. J.; Guan, X.; Tang, R.; Hoyer, J. R.; Yoreo, J. J. D.; Nancollas, G. H. Inhibition of Calcium Oxalate Monohydrate Crystallization by the Combination of Citrate and Osteopontin. *Journal of Crystal Growth* **2006,** *291* (1), 160-165.

(254) Tiselius, H.-G.; Fornander, A.-M.; Nilsson, M.-A. The Effects of Citrate and Urine on Calcium Oxalate Crystal Aggregation. *Urological Research* **1993,** *21* (5), 363-366.

(255) Qiu, S. R.; Wierzbicki, A.; Orme, C. A.; Cody, A. M.; Hoyer, J. R.; Nancollas, G. H.; Zepeda, S.; De Yoreo, J. J. Molecular Modulation of Calcium Oxalate Crystallization by Osteopontin and Citrate. *Proceedings of the National Academy of Sciences* **2004,** *101* (7), 1811-1815.

(256) Hess, B.; Zipperle, L.; Jaeger, P. Citrate and Calcium Effects on Tamm-Horsfall Glycoprotein as a Modifier of Calcium Oxalate Crystal Aggregation. **1993,** *265* (6), F784-F791.

(257) Hajfathalian, M.; Gilroy, K. D.; Hughes, R. A.; Neretina, S. Citrate-Induced Nanocubes: A Re-Examination of the Role of Citrate as a Shape-Directing Capping Agent for Ag-Based Nanostructures. *Small* **2016,** *12* (25), 3444-3452.

(258) Grys, D.-B.; de Nijs, B.; Salmon, A. R.; Huang, J.; Wang, W.; Chen, W.-H.; Scherman, O. A.; Baumberg, J. J. Citrate Coordination and Bridging of Gold Nanoparticles: The Role of Gold Adatoms in Aunp Aging. *ACS Nano* **2020,** *14* (7), 8689-8696.

(259) Bastús, N. G.; Comenge, J.; Puntes, V. Kinetically Controlled Seeded Growth Synthesis of Citrate-Stabilized Gold Nanoparticles of up to 200 Nm: Size Focusing Versus Ostwald Ripening. *Langmuir* **2011,** *27* (17), 11098-11105.

(260) Liu, X.; Yuan, P.; Sun, X.; Chen, Z. Hydroxycitric Acid Inhibits Renal Calcium Oxalate Deposition by Reducing Oxidative Stress and Inflammation. *Current Molecular Medicine* **2020,** *20* (7), 527-535.

(261) Hsu, Y.-C.; Lin, Y.-H.; Shiau, L.-D. Effects of Various Inhibitors on the Nucleation of Calcium Oxalate in Synthetic Urine. *Crystals* **2020,** *10* (4), 333.

(262) Han, S.; Zhao, C.; Pokhrel, G.; Sun, X.; Chen, Z.; Xu, H. Hydroxycitric Acid Tripotassium Inhibits Calcium Oxalate Crystal Formation in the Drosophila Melanogaster Model of Hyperoxaluria. *Med Sci Monit* **2019,** *25*, 3662-3667.

(263) Chen, W.-C.; Chen, H.-Y.; Lin, W.-Y.; Yang, Y.-R.; Tsai, M.-Y.; Chen, Y.-H. Inhibitory Effect of Hydroxycitrate on Calcium Oxalate Crystal Formation in a Drosophila Model. *Journal of Food and Nutrition Research* **2018,** *6* (11), 706-709.

(264) Ahmed, A.; Rodgers, A. L.; Elmagbari, F.; Jackson, G. E. In Support of Hydroxycitrate Being Clinically Investigated as a Potential Therapy of Calcium

Nephrolithiasis: Theoretical Modelling and in Vitro Investigation of Thermodynamic Effects. *Journal of Crystal Growth* **2021,** *558*, 125956.

(265) Alderighi, L.; Gans, P.; Ienco, A.; Peters, D.; Sabatini, A.; Vacca, A. Hyperquad Simulation and Speciation (Hyss): A Utility Program for the Investigation of Equilibria Involving Soluble and Partially Soluble Species. *Coordination chemistry reviews* **1999,** *184* (1), 311-318.

(266) Martell, A. E.; Smith, R. M. *Critical Stability Constants*, Springer: 1974; Vol. 1.

(267) Safari, M. S.; Byington, M. C.; Conrad, J. C.; Vekilov, P. G. Polymorphism of Lysozyme Condensates. *The Journal of Physical Chemistry B* **2017,** *121* (39), 9091-9101.

(268) Chung, J.; Granja, I.; Taylor, M. G.; Mpourmpakis, G.; Asplin, J. R.; Rimer, J. D. Molecular Modifiers Reveal a Mechanism of Pathological Crystal Growth Inhibition. *Nature* **2016,** *536* (7617), 446-450.

(269) Geng, X.; Sosa, R. D.; Reynolds, M. A.; Conrad, J. C.; Rimer, J. D. Alginate as a Green Inhibitor of Barite Nucleation and Crystal Growth. *Molecular Systems Design & Engineering* **2021**.

(270) Bliznakov, G. Adsorption Et Croissance Cristalline. *Editions du CNRS* **1965**, 291-301.

(271) Gutzow, I. S.; Schmelzer, J. W. P. Kinetics of Crystallization and Segregation: Nucleation in Glass-Forming Systems. In *The Vitreous State: Thermodynamics, Structure, Rheology, and Crystallization*; Springer Berlin Heidelberg: Berlin, Heidelberg, 2013; pp 219-288.

(272) Nene, S. S.; Hunter, G. K.; Goldberg, H. A.; Hutter, J. L. Reversible Inhibition of Calcium Oxalate Monohydrate Growth by an Osteopontin Phosphopeptide. *Langmuir* **2013,** *29* (21), 6287-6295.

(273) Zhou, J. R.; Erdman, J. W. Phytic Acid in Health and Disease. *Critical Reviews in Food Science and Nutrition* **1995,** *35* (6), 495-508.

(274) Oatway, L.; Vasanthan, T.; Helm, J. H. Phytic Acid. *Food Reviews International* **2001,** *17* (4), 419-431.

(275) Liang, J.; Han, B.-Z.; Nout, M. J. R.; Hamer, R. J. Effect of Soaking and Phytase Treatment on Phytic Acid, Calcium, Iron and Zinc in Rice Fractions. *Food Chemistry* **2009,** *115* (3), 789-794.

(276) Graf, E. Calcium Binding to Phytic Acid. *Journal of agricultural and food chemistry* **1983,** *31* (4), 851-855.

(277) Dendougui, F.; Schwedt, G. In Vitro Analysis of Binding Capacities of Calcium to Phytic Acid in Different Food Samples. *European Food Research and Technology* **2004,** *219* (4), 409-415.

(278) Caldwell, R. A. Effect of Calcium and Phytic Acid on the Activation of Trypsinogen and the Stability of Trypsin. *Journal of Agricultural and Food Chemistry* **1992,** *40* (1), 43-46.

(279) Amjad, Z. Inhibition of Alkaline Earth Sulfate Scales. US 4,652,377, 1987.

(280) Koutsoukos, P. G.; Amjad, Z.; Nancollas, G. H. The Influence of Phytate and Phosphonate on the Crystal Growth of Fluorapatite and Hydroxyapatite. *Journal of Colloid and Interface Science* **1981,** *83* (2), 599-605.

(281) Grases, F.; Costa-Bauzá, A.; Kroupa, M. Studies on Calcium Oxalate Monohydrate Crystallization: Influence of Inhibitors. *Urological Research* **1994,** *22* (1), 39-43.

(282) F. Grases, R. G.-G. J. J. T. A. L. Effects of Phytic Acid on Renal Stone Formation in Rats. *Scandinavian Journal of Urology and Nephrology* **1998,** *32* (4), 261-265.

(283) Celi, L.; Lamacchia, S.; Barberis, E. Interaction of Inositol Phosphate with Calcite. *Nutrient Cycling in Agroecosystems* **2000,** *57* (3), 271-277.

(284) Amjad, Z. Constant Composition Study of Crystal Growth of Calcium Fluoride. Influence of Poly(Carboxylic Acids), Polyphosphates, Phosphonates, and Phytate. *Langmuir* **1991,** *7* (3), 600-603.

(285) Tomson, M. B.; Kan, A. T.; Oddo, J. E. Acid/Base and Metal Complex Solution Chemistry of the Polyphosphonate Dtpmp Versus Temperature and Ionic Strength. *Langmuir* **1994,** *10* (5), 1442-1449.

(286) Shaw, S. S.; Sorbie, K. S. In *The Effect of Ph on Static Barium Sulphate Inhibition Efficiency and Minimum Inhibitor Concentration of Generic Scale Inhibitors*, SPE International Conference on Oilfield Scale, 2012.

(287) Al Hamad, M.; Al-Sobhi, S. A.; Onawole, A. T.; Hussein, I. A.; Khraisheh, M. Density-Functional Theory Investigation of Barite Scale Inhibition Using Phosphonate and Carboxyl-Based Inhibitors. *ACS Omega* **2020,** *5* (51), 33323-33328.

(288) Bieth, H.; Spiess, B. A Comparative Study of the Protonation of Myo-Inositol Hexakis(Phosphate). *Journal of the Chemical Society, Faraday Transactions 1: Physical Chemistry in Condensed Phases* **1986,** *82* (6), 1935-1943.

(289) Safari, M. S.; Wang, Z.; Tailor, K.; Kolomeisky, A. B.; Conrad, J. C.; Vekilov, P. G. Anomalous Dense Liquid Condensates Host the Nucleation of Tumor Suppressor P53 Fibrils. *iScience* **2019,** *12*, 342-355.

(290) Li, Y.; Lubchenko, V.; Vekilov, P. G. The Use of Dynamic Light Scattering and Brownian Microscopy to Characterize Protein Aggregation. **2011,** *82* (5), 053106.

(291) Poloni, L. N.; Ward, M. D. The Materials Science of Pathological Crystals. *Chemistry of Materials* **2014,** *26* (1), 477-495.

Appendix

Supplementary Figures

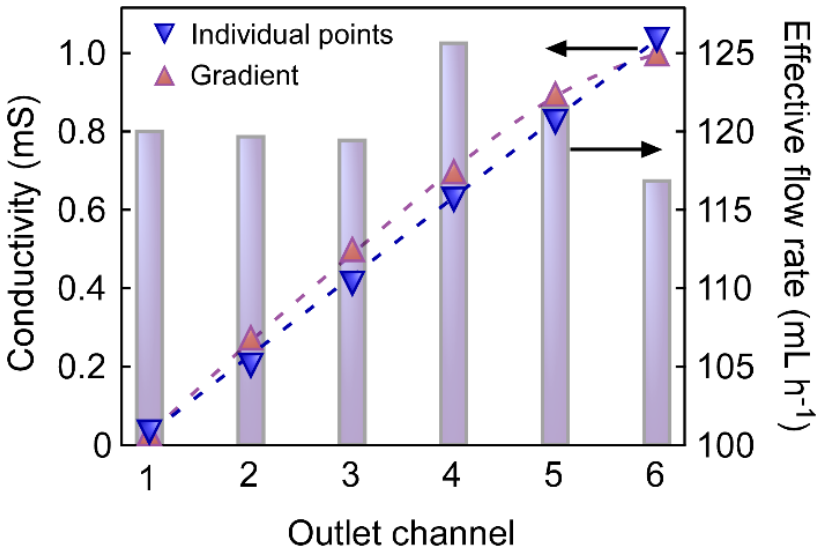

Figure A1: Ion concentration profile of Ba^{2+} (conductivity) of microchannel effluent. Conductivity measurements of the ion flux of $BaCl_2$ (aq) in each channel effluent are represented by the pink and blue data points.

Characterization of the gradient generator. The accuracy of the microfluidic gradient generator was examined by collecting and characterizing the six outlet effluents after flowing aqueous $BaCl_2$ in one inlet and DI water in the second inlet. Inlets were flowed into the microfluidic device using a dual syringe pump at a total flow rate of 720 mL h^{-1} to produce a flow rate of 120 mL h^{-1} in each outlet stream. The mass of effluents was measured after 10 min of collection using a Mettler Toledo balance. The effective flow rate, determined for each outlet was close to the theoretical value (120 mL h^{-1}) (Figure A1). The accuracy of the concentration gradient generator was determined by comparing the measured ion flux (mS) in each effluent against individually prepared $BaCl_2$ aqueous solutions within the concentration range tested. Conductivity measurements were obtained using a VWR International conductivity meter. The conductivity of effluents from each

channel are the same within experimental error as the conductivity of solutions prepared at several concentrations within the expected range, suggesting the gradient generator can successfully mix and split streams to obtain effluents corresponding to a linear concentration gradient.

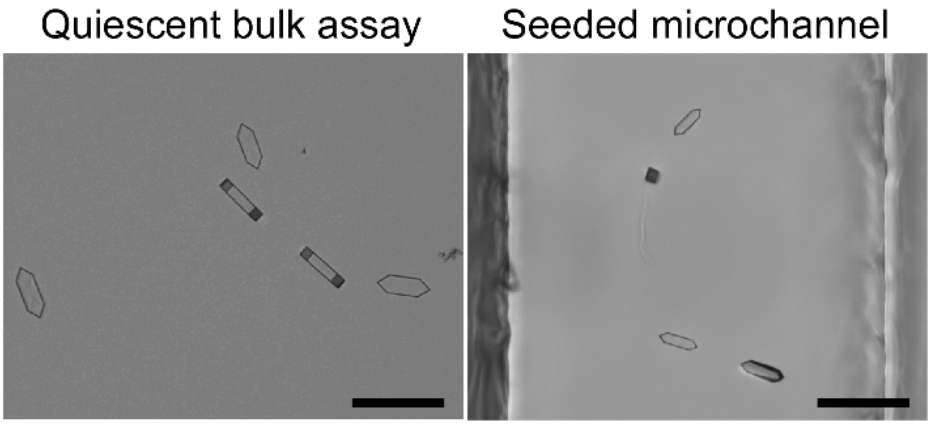

Figure A2: Optical micrographs of barite crystals grown (left) in vials and (right) in microchannels exhibit identical morphologies. Scale bars indicate 100 µm.

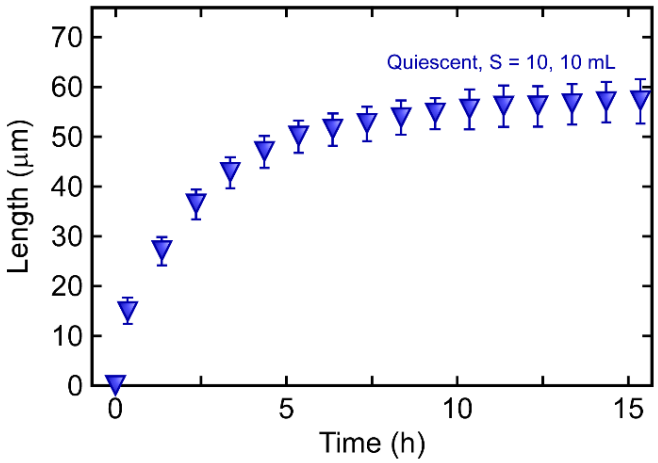

Figure A3: Growth kinetics for bulk crystallization assays under quiescent conditions and supersaturation ratio $S = 10$.

Growth kinetics for bulk crystallization. The length of barite crystals synthesized in 20 mL glass vials was captured from the earliest observable point of nucleation, by

optical microscopy, for a 15-h period during which equilibrium appears to be established between the crystals and bulk medium. The growth rate was greater within the first 5 h, after which the length begins to approach a plateau at ~60 μm due to the depletion of solute.

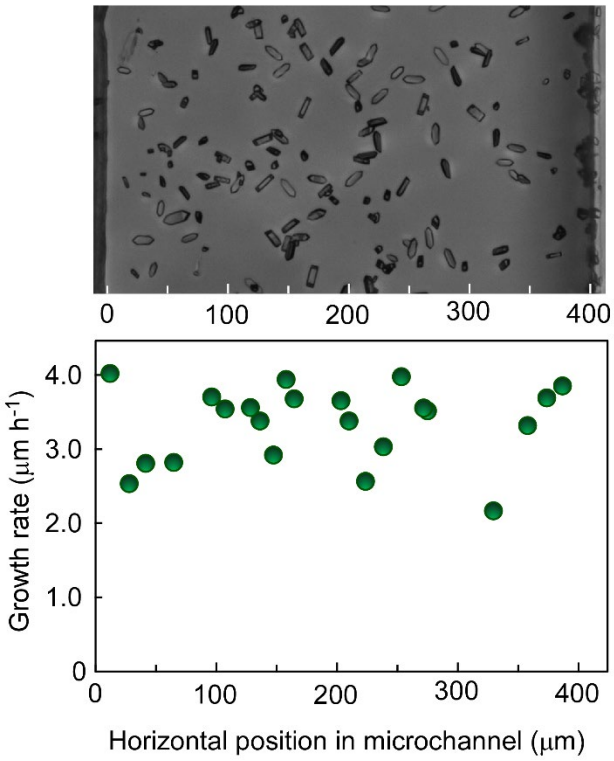

Figure A4: Growth kinetics as a function of position across the microchannel. (top) Representative optical micrograph of barite seed crystals in the microchannel. (bottom) Single crystal growth kinetics of barite seed crystals in the micrograph.

Homogeneous growth within microfluidic channels. The synthesis of seed crystals and growth rates in subsequent experiments were homogeneous across the width of the microchannels (Figure S3), consistent with the advection dominance at the flow rates used in all experiments. The optical micrograph in Figure S3 depicts a representative region of a seeded microchannel. Crystal growth rates across the width of the microchannel demonstrate no observable trend as a function of horizontal position in the microchannel,

indicating there is complete mixing of growth solution within the channel and no diffusion limitations.

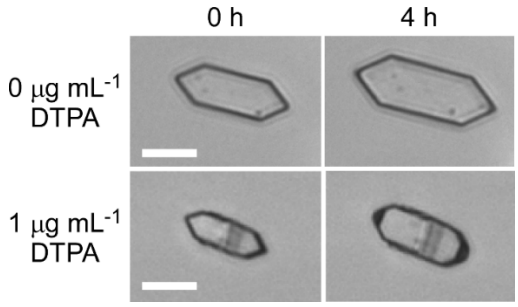

Figure A5: Optical micrographs of barite crystals at 0 h (left column) and 4 h (right column) under 1.2 mL h^{-1} flow of growth solutions (S=7) in the absence (top row) and presence (bottom row) of DTPA. Scale bars indicate 10 μm.

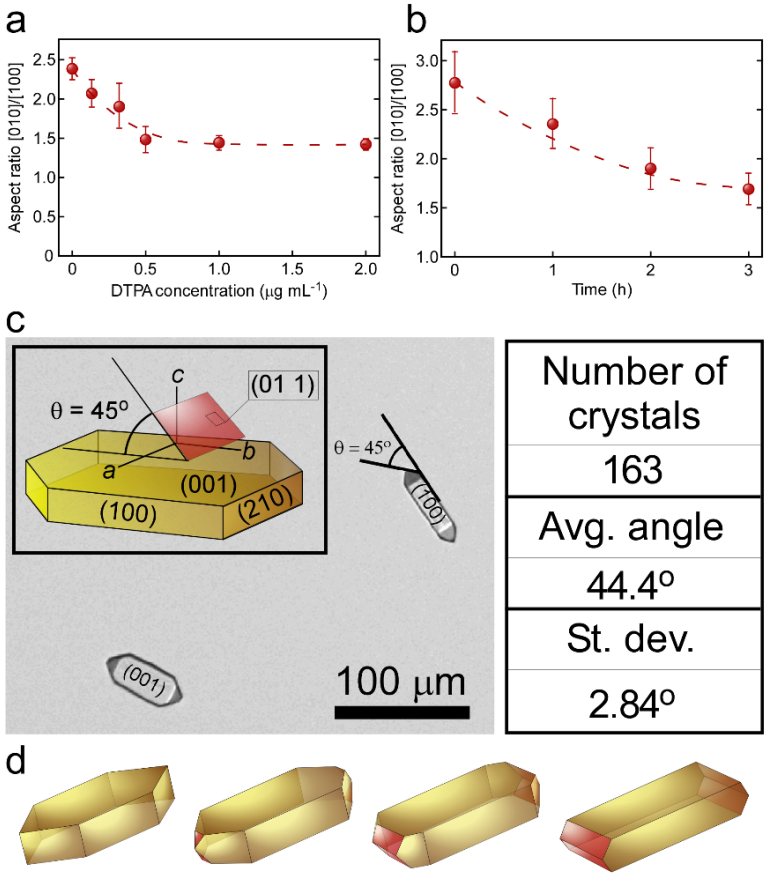

Figure A6: (a) Aspect ratio of the basal surface as a function of increasing concentration of DTPA. (b) Aspect ratio of the (001) basal surface in the presence of 0.5 μg mL^{-1} DTPA. (c) Optical micrograph analysis of {011} facets through measurements of dihedral angles.

Transformation of barite morphology. Barite inhibition in the presence of DTPA resulted in crystals with a morphology differing from the control. The measured aspect ratio decreased as a function of either DTPA concentration or time (Figure S6a and b), suggesting binding specificity near the apex of the crystals. Optical micrographs in which the (100) face of barite crystals was exposed suggest the apex is not completely blunted. Furthermore, a new facet develops, which intersects the (010) and (001) planes. The angle of the newly developed facet with respect to the (001) plane was measured to be ~45° (Figure S6c), suggesting the new facet corresponds to the (011) surface. The transformation of the morphology is illustrated schematically in Figure S6d.

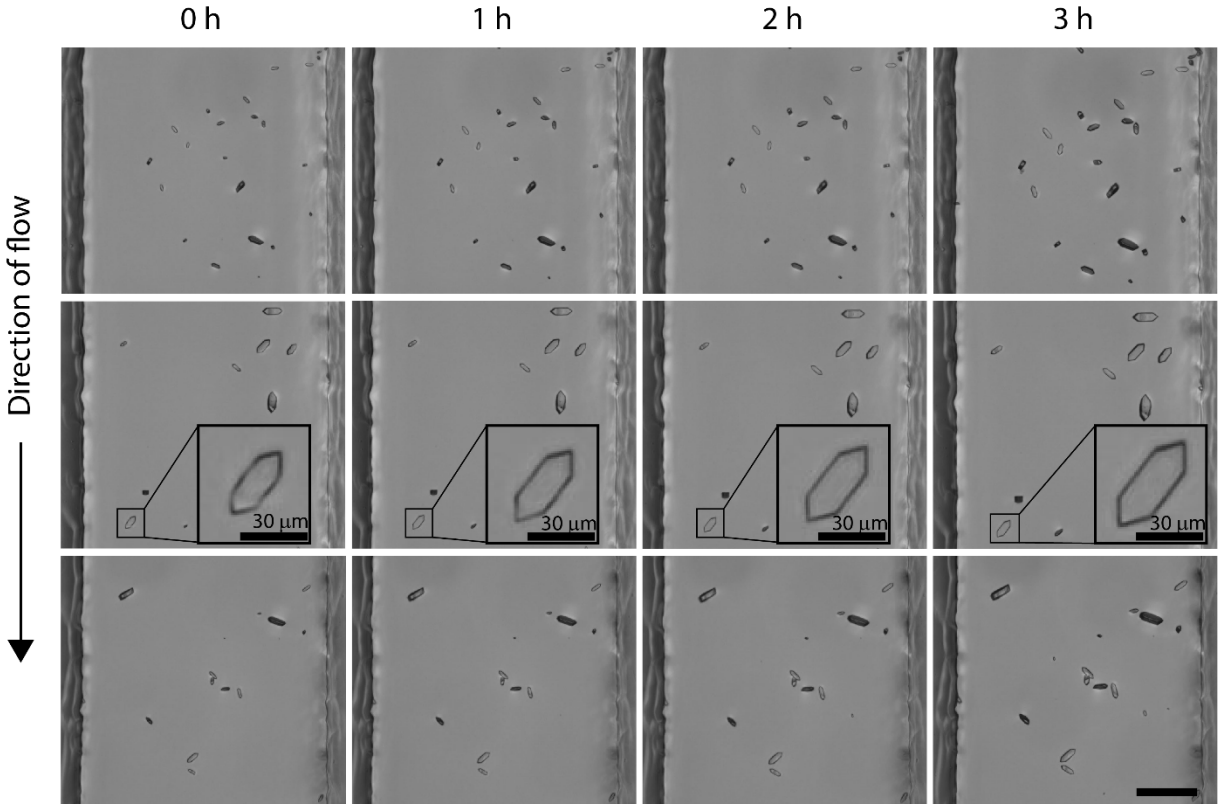

Figure A7: Large area field of view micrographs showing time elapsed growth of barite seed crystals in the microchannel under flow of a supersaturated growth solution (12 mL h^{-1}, S = 7). Scale bar indicates 100 µm for all images unless otherwise stated.

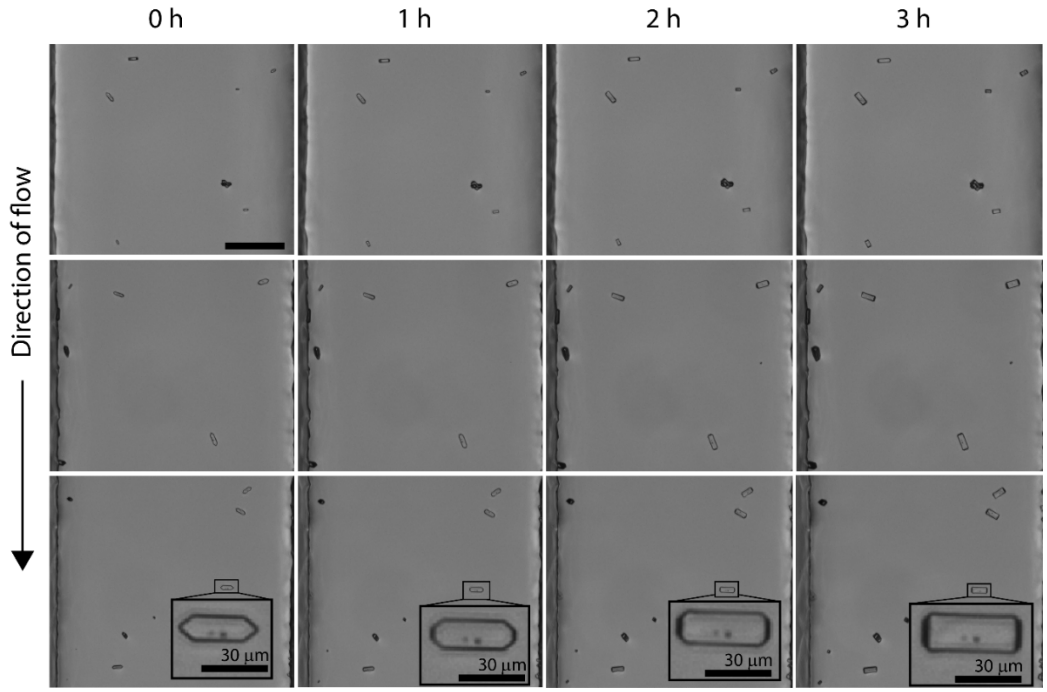

Figure A8: Large area field of view micrographs showing time elapsed growth of barite seed crystals in the microchannel under flow of a supersaturated growth solution (12 mL h^{-1}, $S = 7$) in the presence of 1 µg mL^{-1} DTPA. Scale bar indicates 100 µm for all images unless otherwise stated.

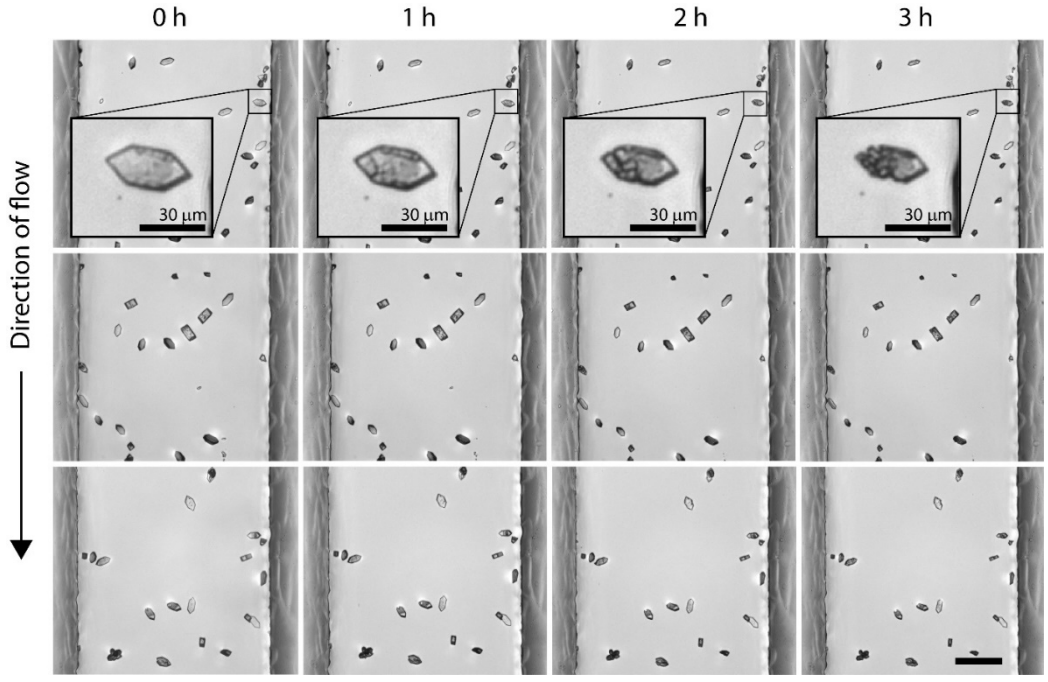

Figure A9: Large area field of view micrographs showing time elapsed dissolution of barite seed crystals in the microchannel under flow of alkaline solution (12 mL h^{-1}, pH = 9) in the presence of 200 µg mL^{-1} DTPA. Scale bar indicates 100 µm for all images unless otherwise stated.

Boundary layer analysis. The Schmidt number (Sc) represents the ratio of the rates of viscous diffusion to molecular diffusion. For Sc $\gg 1$, the diffusion boundary layer is much thinner than the hydrodynamic boundary layer. For $DTPA_{(aq)}$, $D \approx 1 \times 10^{-9}$ m^2 s^{-1} and $\nu \approx 9.06 \times 10^{-7}$ m^2 s^{-1}, and the dimensionless quantity Sc $\approx$ 850. Thus, the diffusion boundary layer thickness can be approximated by $\delta \approx 5\left(\frac{D}{\nu}\right)^{\frac{1}{3}}\left(\frac{Wx}{Re}\right)^{\frac{1}{2}}$ (eq. 2 in the main text), where x is the average length of the crystals and U_0 is the maximum fluid velocity.

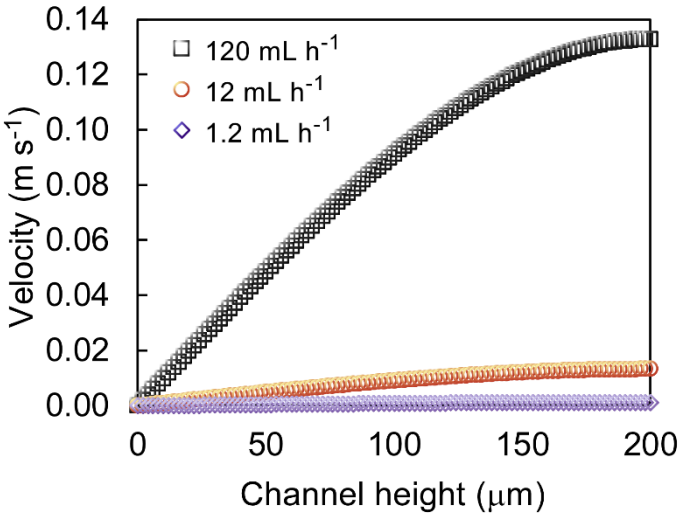

Figure A10: Velocity profiles through the microchannels. From the von Kármán momentum balance, velocity profiles can be approximated as $\frac{v_x}{v_\infty} = \frac{3}{2}\left(\frac{y}{\delta}\right) - \frac{1}{2}\left(\frac{y}{\delta}\right)^3$, where y is the dimension along the channel height and $\delta = 4.64\sqrt{\frac{\nu x}{U_0}}$. U_0 is the maximum fluid velocity in the microchannel.

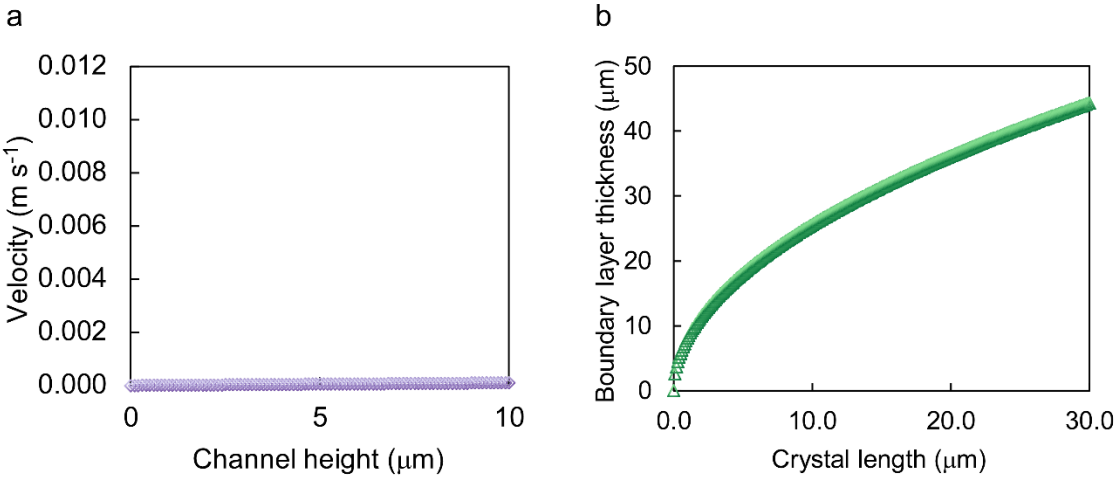

c

Crystal length (μm)	Concentration boundary layer thickness (μm)	Boundary layer velocity (μm s^{-1})
0	0.0	0.00
5	18	180
10	26	250
15	31	310
20	36	360
25	41	400
30	44	430

Figure A11: (a) Velocity profile for aqueous DTPA flowing through the microchannel at 1.2 mL h^{-1}. (b) Concentration diffusion boundary layer thickness as a function of crystal length for 1.2 mL h^{-1}. (c) Fluid velocity at the outer edge of the boundary layer.

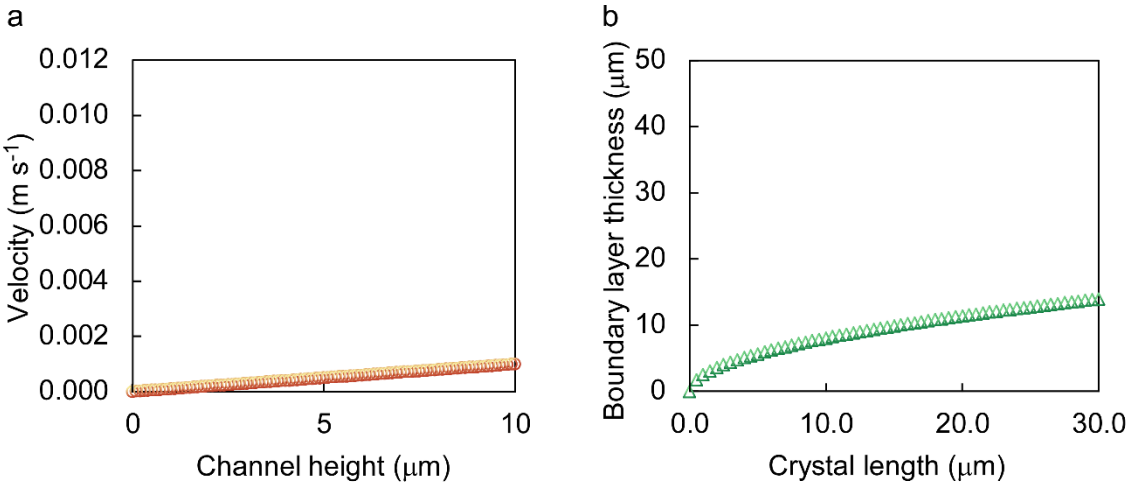

c

Crystal length (μm)	Concentration boundary layer thickness (μm)	Boundary layer velocity (μm s^{-1})
0	0.0	0.00
5	5.7	570
10	8.1	810
15	9.9	990
20	12	1100
25	13	1300
30	14	1400

Figure A12: (a) Velocity profile for aqueous DTPA flowing through the microchannel at 12 mL h^{-1}. (b) Concentration diffusion boundary layer thickness as a function of crystal length for 12 mL h^{-1}. (c) Fluid velocity at the outer edge of the boundary layer for different locations along the crystal length.

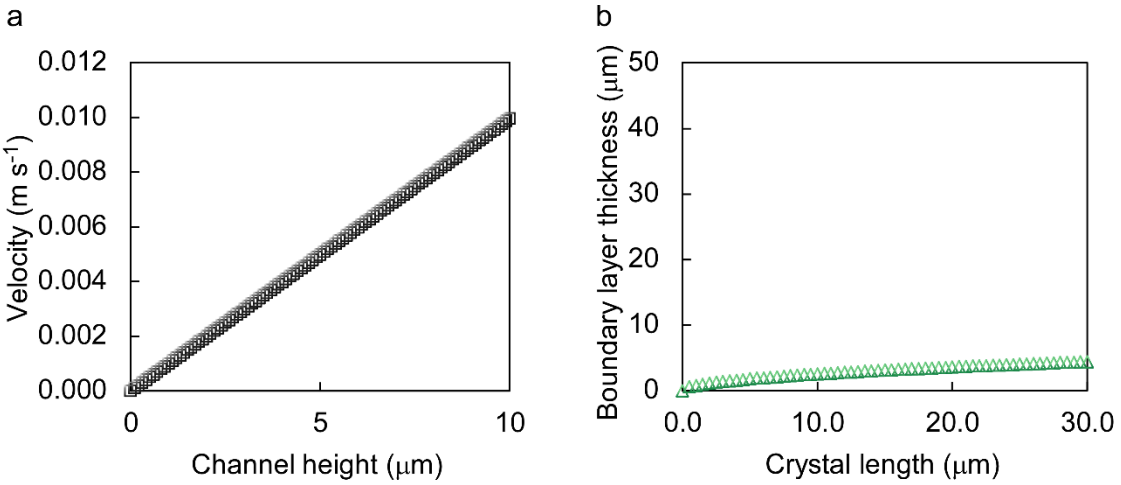

c

Crystal length (μm)	Concentration boundary layer thickness (μm)	Boundary layer velocity (μm s^{-1})
0	0.0	0.00
5	1.8	1800
10	2.6	2600
15	3.1	3100
20	3.6	3600
25	4.1	4000
30	4.4	4400

Figure A13: (a) Velocity profile for aqueous DTPA flowing through the microchannel at 120 mL h^{-1}. (b) Concentration diffusion boundary layer thickness as a function of crystal length for 120 mL h^{-1}. (c) Fluid velocity at the outer edge of the boundary.

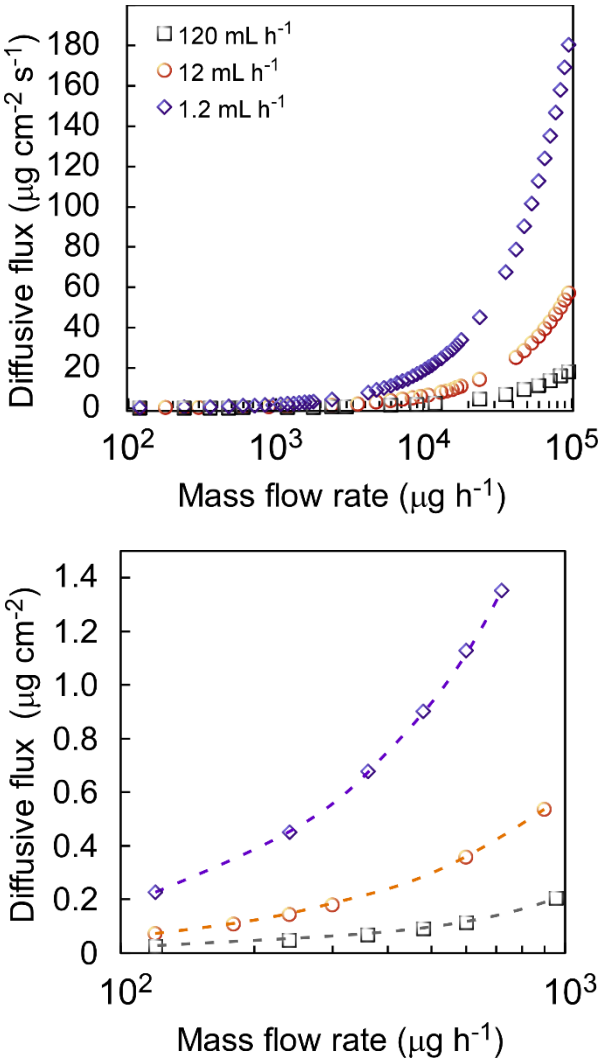

Figure A14: Diffusive flux of DTPA as a function of the DTPA mass flow rate. The molecular diffusional flux is of the order of magnitude $J = \frac{Dc_0}{\delta}$. The diffusional flux was calculated for each combination of flow rate and concentration, using the boundary layer based on the flow rate.

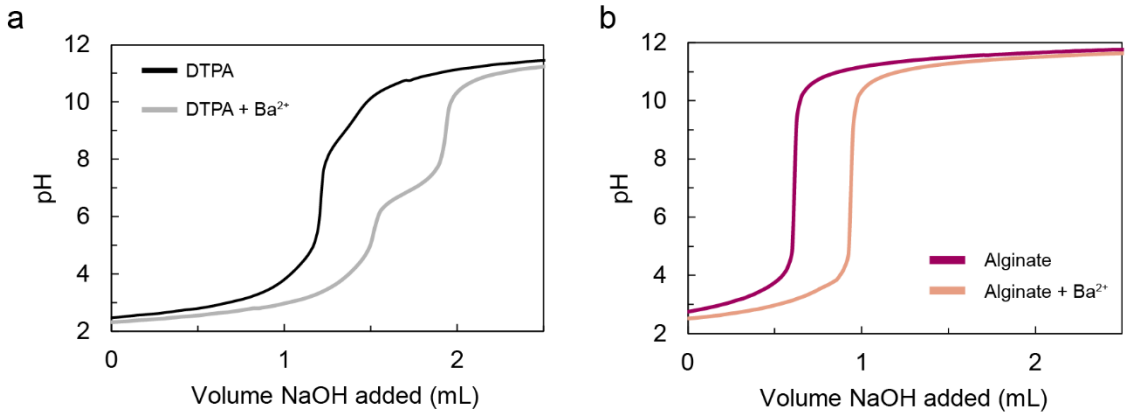

Figure A15. Titration of (a) 1 mM DTPA and (b) 400 µg mL^{-1} alginate with the addition of 0.1 M NaOH in 25 µL incremements in the absence and presence of 1 mM Ba^{2+}.

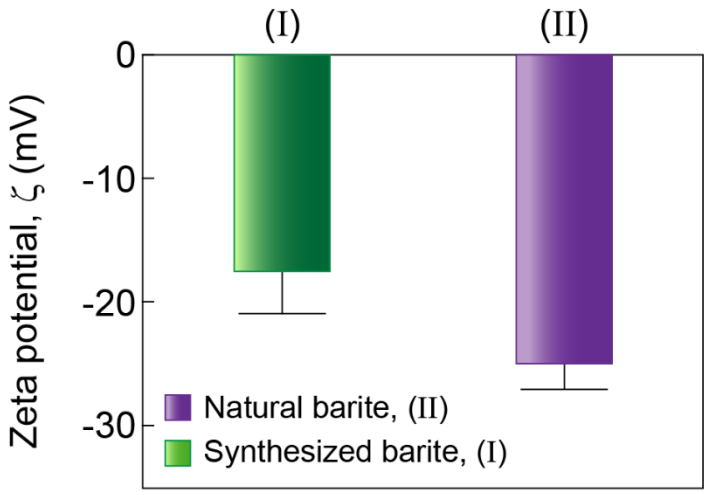

Figure A16. Zeta potential ζ measurements were performed using solutions that were prepared by adding 0.5 mg of barite crystals (seeds) to 10 mL of a saturated barium sulfate solution (0.011 mM $BaSO_4$). The electrophoretic mobility was calculated using the Smoluchowski equation.

a

	pH 7	pH 11
Ret. Vol (mL)	14.6	14.5
Mn (kDa)	226	211
Mw (kDa)	269	277
PDI	1.2	1.3

b

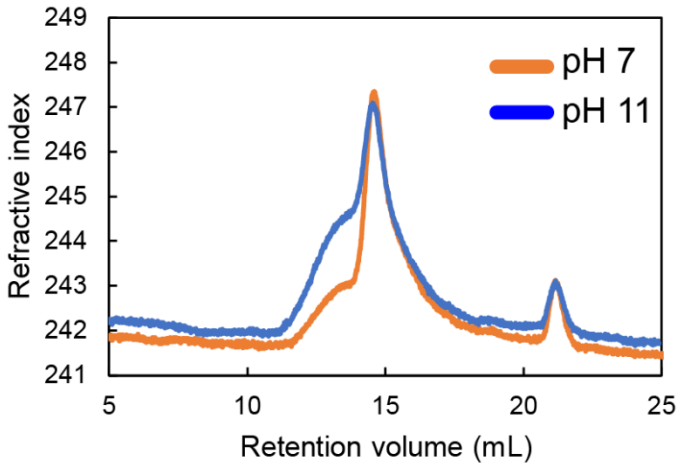

Figure A17. Results of gel permeation chromatography. (a) Retention volume, weight- and number-averaged molecular weights, and polydispersity index. (b) Gel permeation chromatography profiles of a 2% aqueous alginate solution by volume at pH 7 (orange) and pH 11 (blue).

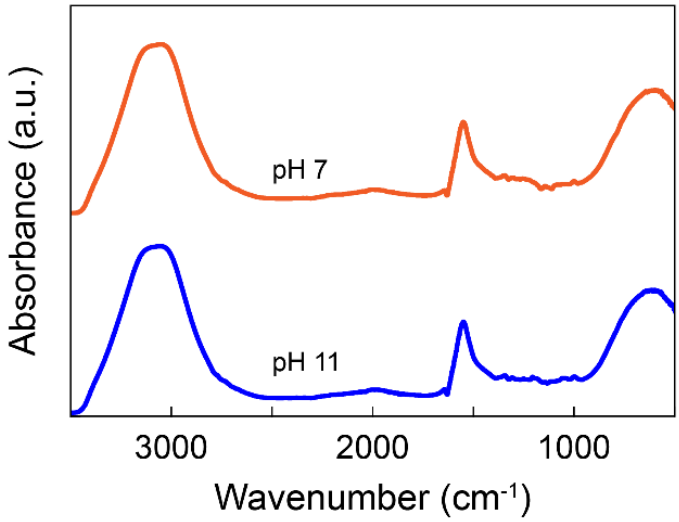

Figure A18. Infrared spectra of aliquots of 20 mg mL^{-1} aqueous alginate solutions (100 µL) adjusted to pH 7 (orange) and pH 11 (blue) with appropriate amounts of NaOH were placed on the ATR stage covering the diamond crystal detector.

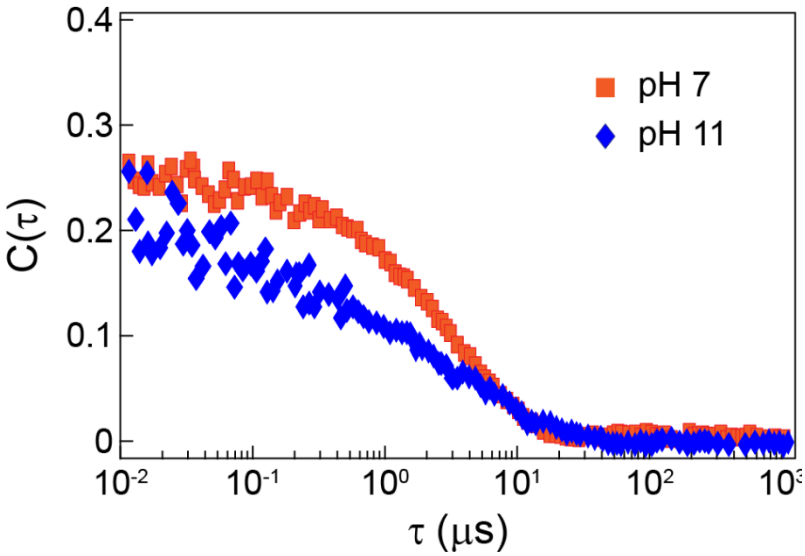

Figure A19. Representative dynamic light scattering (DLS) reporting the autocorrelation function, C(τ), as a function of delay time, τ, for aqueous solutions containing 500 μg mL^{-1} at pH 7 and pH 11.

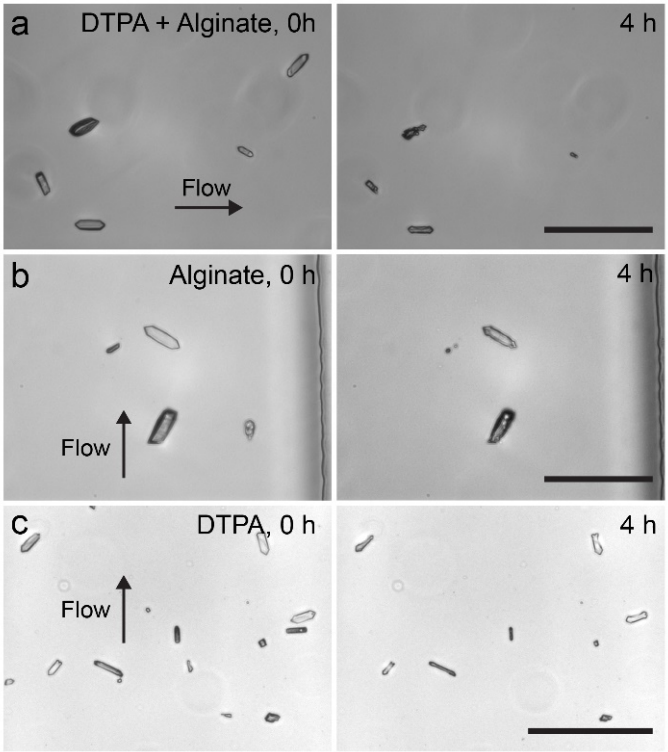

Figure A20. Barite dissolution in microfluidic channels under constant flow (12 mL h^{-1}) of alkaline solutions (pH 9) containing: (a) binary combination of 100 μg mL^{-1} DTPA and 100 μg mL^{-1} alginate, (b) 200 μg mL^{-1} alginate, and (c) 200 μg mL^{-1} DTPA.

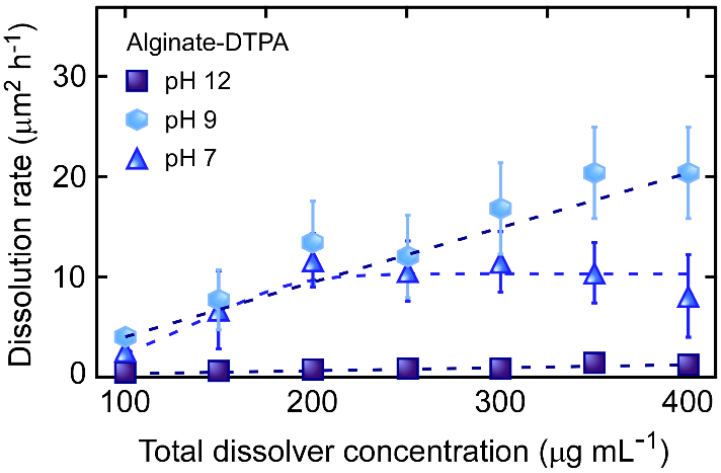

Figure A21. Effect of binary combinations of alginate and DTPA. The dissolution rate of barite as a function of total dissolver concentration in microchannels was measured under constant flow (12 mL h^{-1}) of a 50/50 (wt%) alginate-DTPA binary mixture at pH 7, 9, and 12.

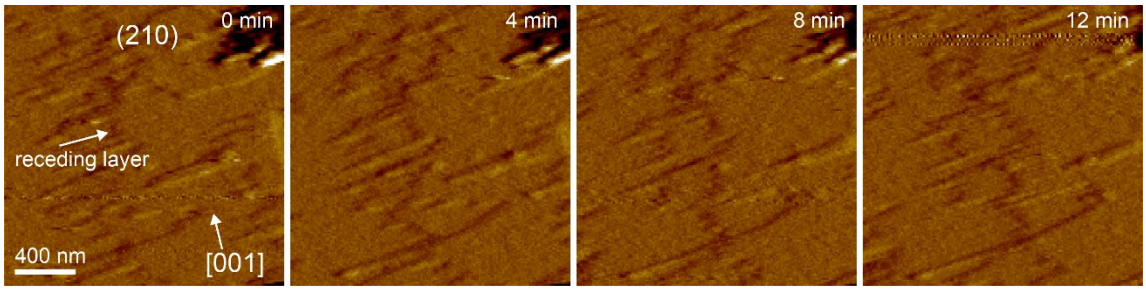

Figure A22. *In situ* AFM measurements of a (210) surface dissolving under a constant flow (12 mL h^{-1}) of an aqueous solution at pH 7 (without barium sulfate) containing 20 μg mL^{-1} alginate.

In situ AFM images of the (210) surface during barite dissolution show similar topological features in the presence of DTPA, alginate, and their binary combination (100 μg mL^{-1} alginate and 100 μg mL^{-1} DTPA in the absence of barium sulfate). In the presence of alginate, corrugated layers elongated in the [120] direction recede over time in a layer by layer fashion (Figure S8). Upon introducing 200 μg mL^{-1} DTPA, we observe the immediate presence of deposits on the surface (Figure S9). The deposits have an average height of 1.1 nm, which does not correspond to any unit cell dimension of barite. Moreover,

these features have no apparent orientation or morphology. Continuous imaging reveals the progressive removal of deposits with concomitant formation of 2-dimensional rectangular etch pits on the barite (210) surface. The latter are elongated in the [120] direction, and dissolve in a layer by layer fashion. Over time we observe rectangular etch pits with depths on the order of 1 nm (Figure S10). Similar observations are made when dissolving barite with a binary combination of DTPA-alginate (Figure S11). Interestingly, we observe a more rapid disappearance of deposits on the (210) surface compared to measurements with only DTPA.

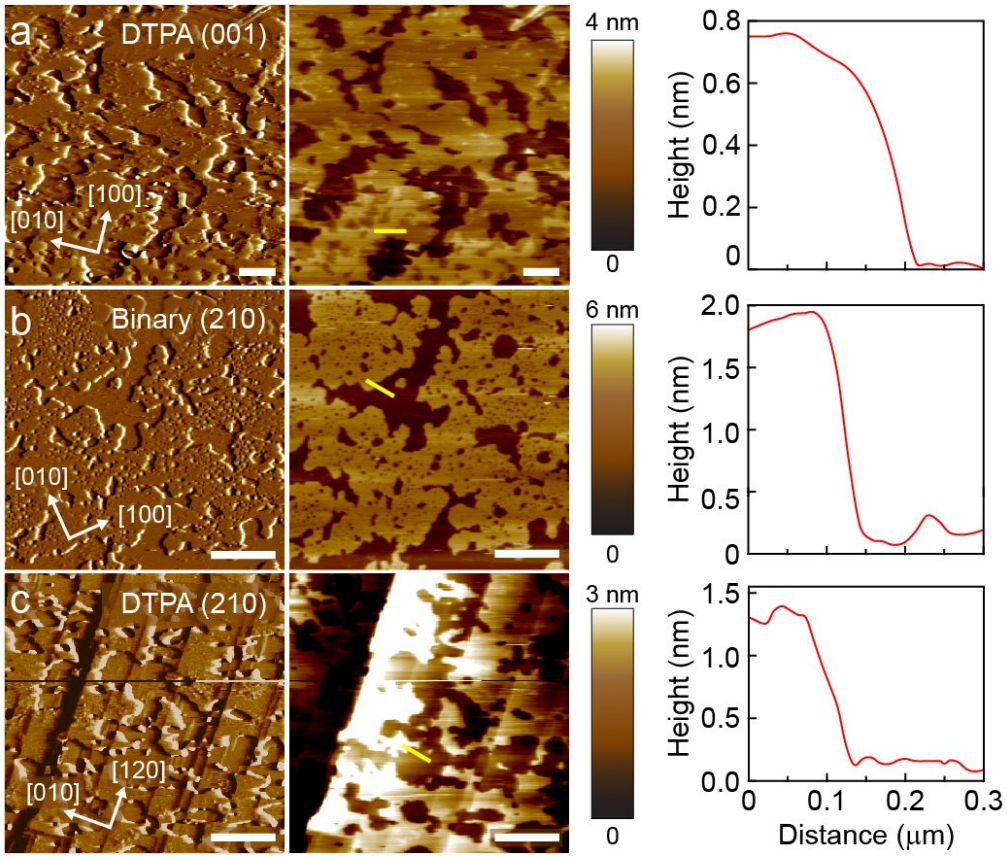

Figure A23. AFM images at t = 0 min corresponding to the introduction of demineralizing agents: (a) 200 μg mL^{-1} DTPA on the (001) surface; (b) binary combinations of alginate and DTPA (100 μg mL^{-1} each) on the (210) surface; and (c) 200 μg mL^{-1} DTPA on the (210) surface.

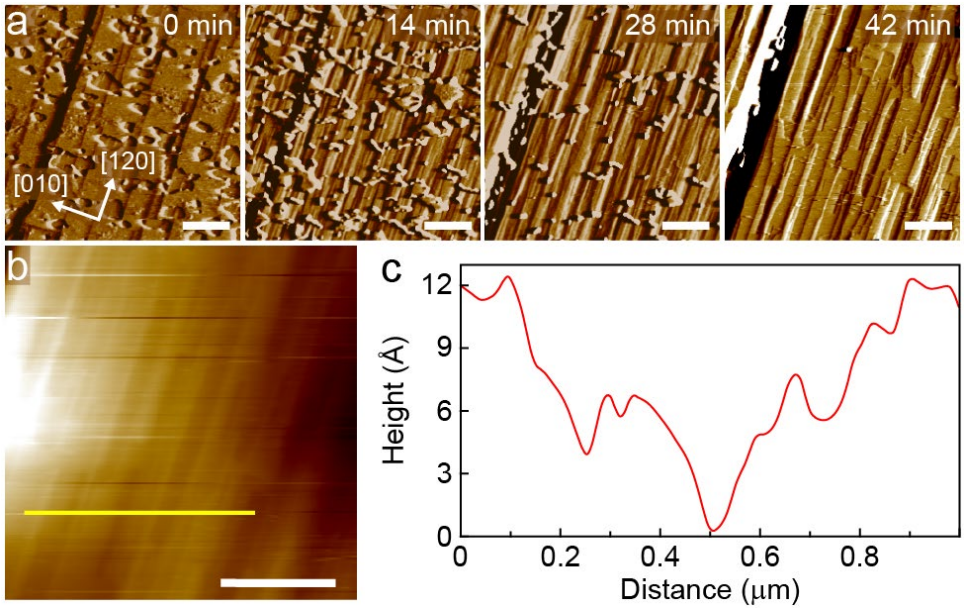

Figure A24. (a) *In situ* AFM deflection mode images of a barite (210) surface dissolving in an aqueous solution (pH 7) containing 200 μg mL^{-1} DTPA (without barium sulfate). (b) Height mode image of a partially dissolved (210) surface after 42 min. (c) Corresponding height profile.

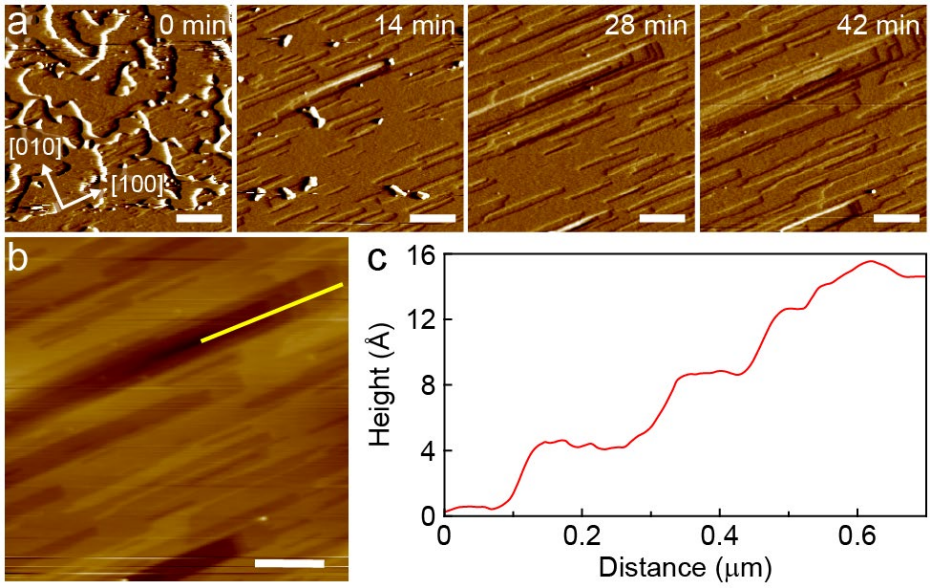

Figure A25. (a) *In situ* AFM deflection mode images of a barite (210) surface dissolving in an aqueous solution (pH 7) containing 100 μg mL^{-1} alginate and 100 μg mL^{-1} DTPA. (b) Height mode image of a partially dissolved (210) surface after 42 min. (c) Corresponding height profile.

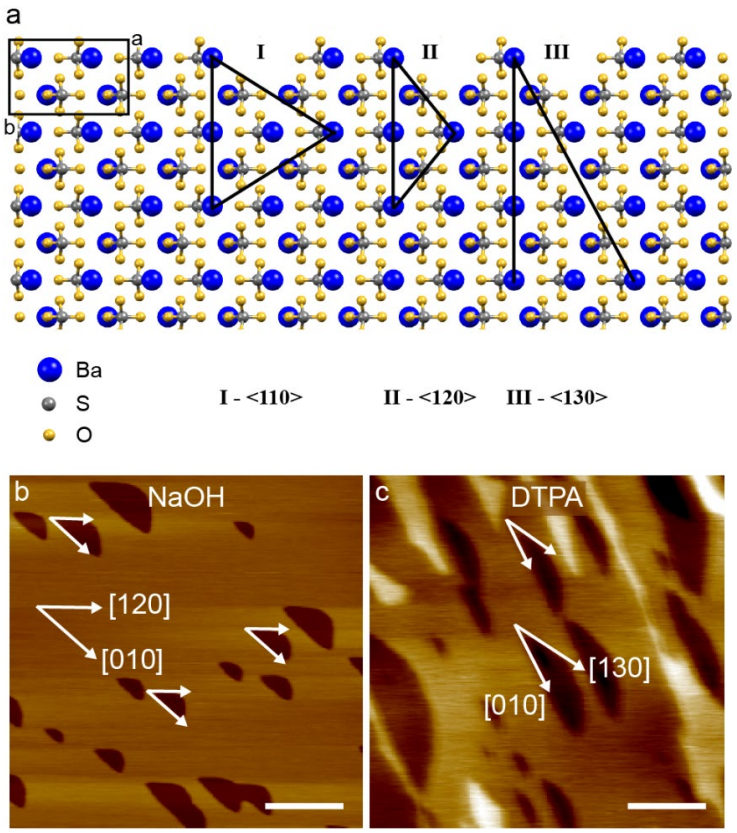

Figure A26. (a) Idealized [001] zone axis of barite with a single unit cell (black dashed box). Representative AFM height mode images of a barite (001) surface partially dissolved in (b) NaOH and (c) DTPA with etch pit morphologies identified along labelled crystallographic orientations.

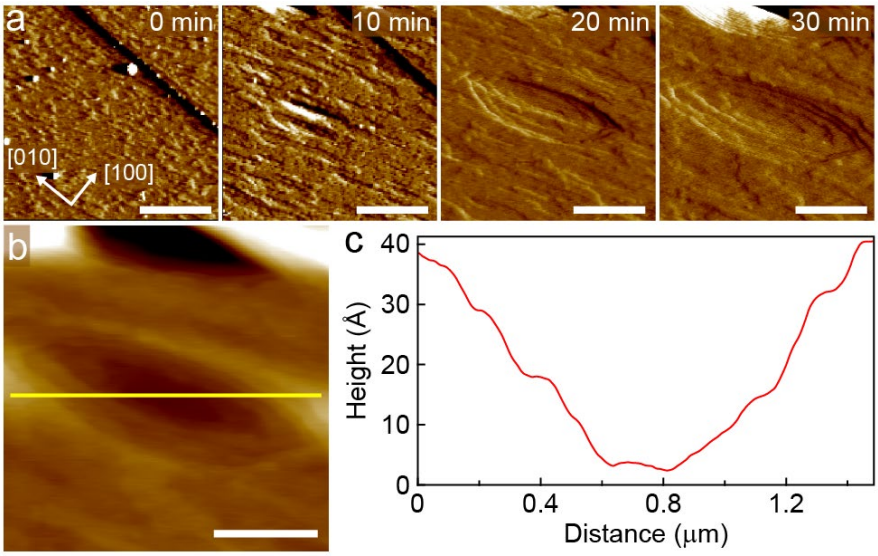

Figure A27. (a) *In situ* AFM deflection mode images of a barite (001) surface dissolving in an aqueous solution (pH 7) containing 100 μg mL^{-1} alginate and 100 μg mL^{-1} DTPA. (b) Height mode image of a partially dissolved (001) surface after 30 min. (c) Corresponding height profile.

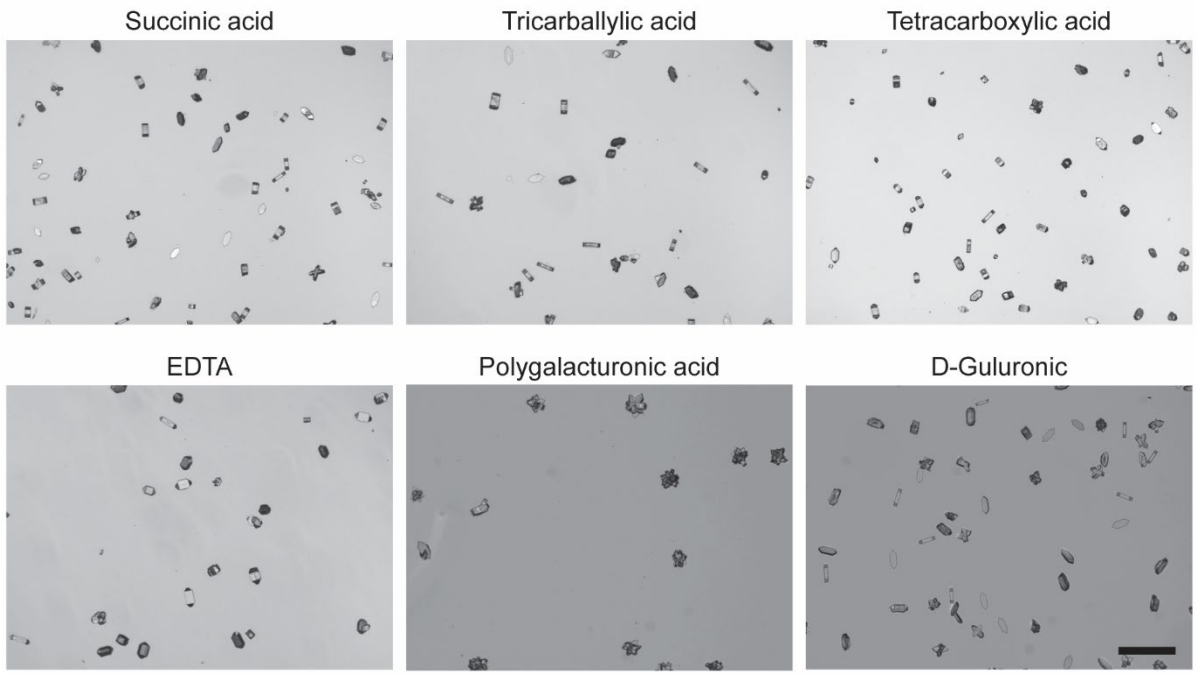

Figure A28. Representative optical images of barite crystals synthesized in the presence of 1 μg mL^{-1} of each additive with an initial supersaturation S = 10 under quiescent conditions at room temperature (21.0 ± 0.5 °C) for 24 h. Scale bar equals 100 μm.

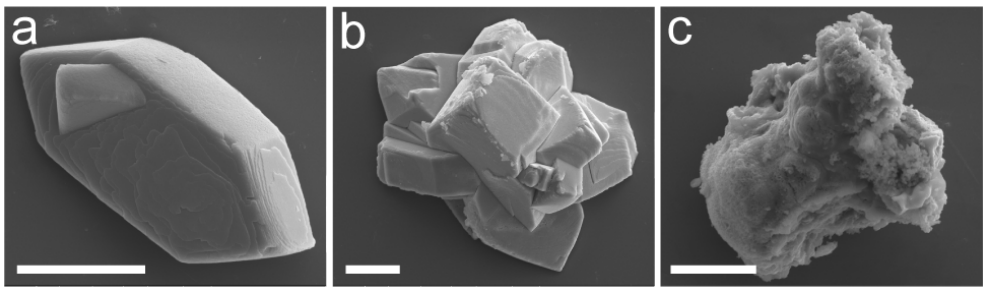

Figure A29. (a) SEM images of barite crystals synthesized under quiescent conditions in the presence of (a) 0.2, (b) 0.4, and (c) 0.8 μg mL^{-1} alginate with an initial supersaturation S = 10 under quiescent conditions at room temperature (21.0 ± 0.5 °C) for 24 h. Scale bars equal 10 μm.

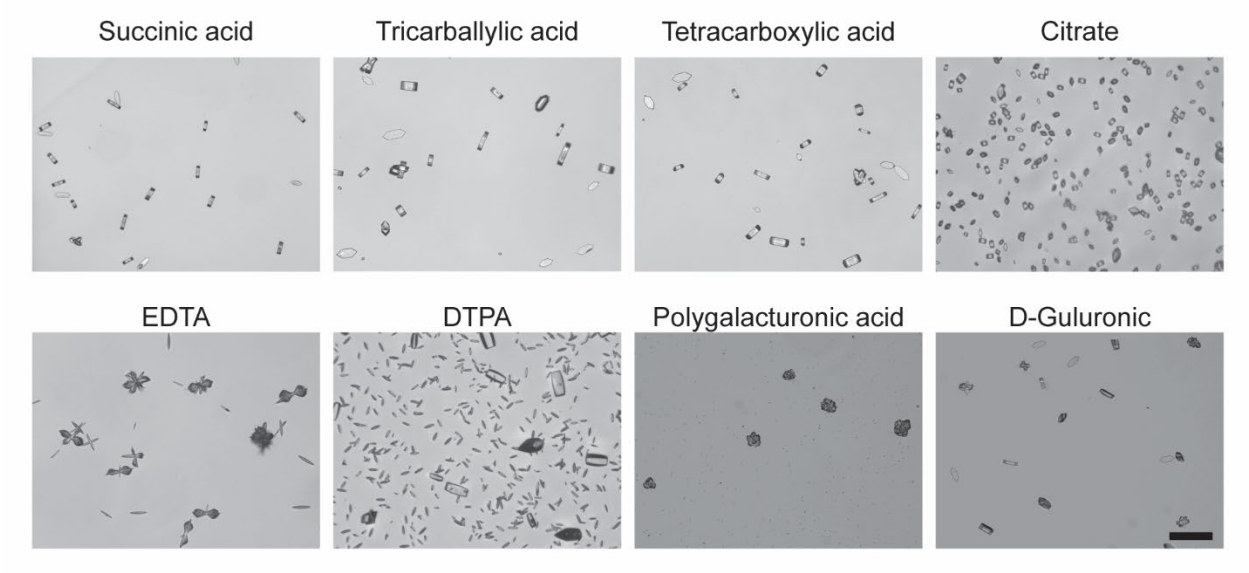

Figure A30. Representative optical images of barite crystals synthesized in the presence of 10 μg mL^{-1} of each additive with an initial supersaturation ratio S = 10 under quiescent conditions at room temperature (21.0 ± 0.5 °C) for 24 h. Scale bar equals 100 μm.

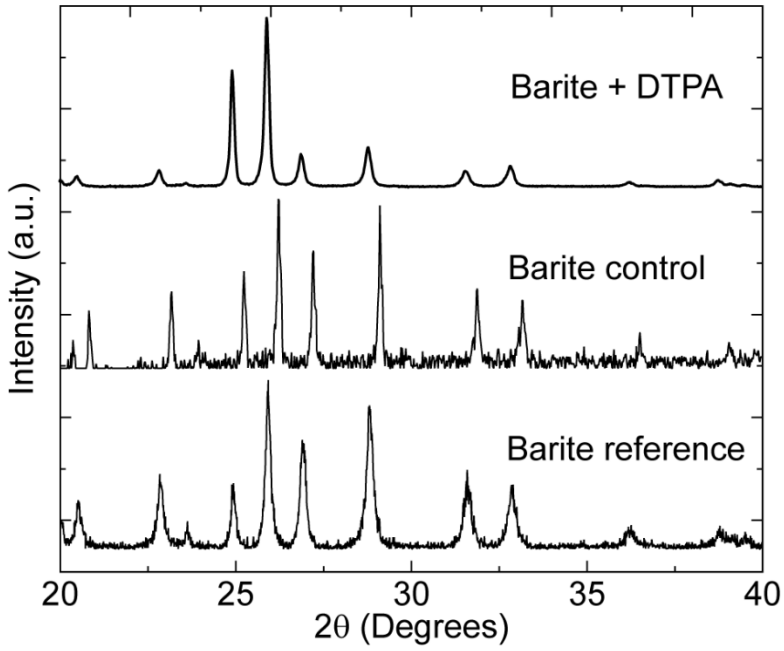

Figure A31. Powder XRD patterns of as-synthesized barite crystals from bulk assays in the presence and absence of 10 mg mL^{-1} DTPA and a reference sample from the ICDD PDF-2 2013 database.

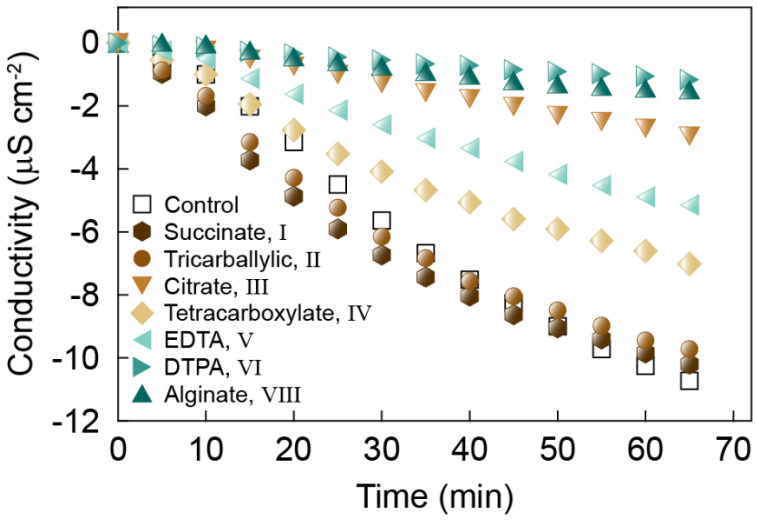

Figure A32. Representative desupersaturation curves tracking the conductivity of barite growth solutions (S = 10) at ambient temperature (21.0 ± 0.5 °C) during bulk assay synthesis while stirring (400 rpm).

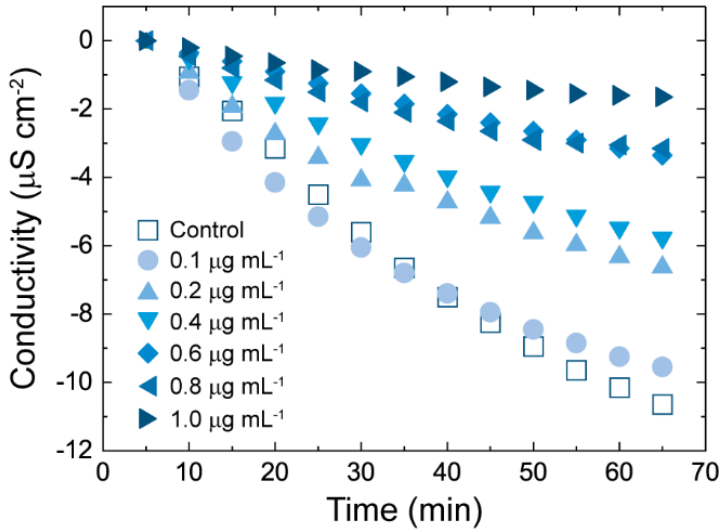

Figure A33. Representative desupersaturation curves tracking the conductivity of barite growth solutions (S = 10) at ambient temperature (21.0 ± 0.5 °C) during bulk assay synthesis in the presence of various alginate concentrations.

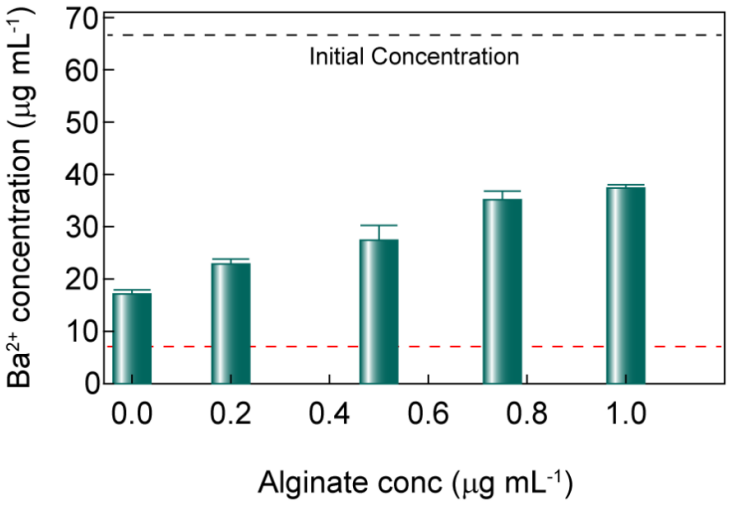

Figure A34. Elemental analysis (ICP-OES) of free Ba^{2+} ion concentration in the supernatant after a 24 synthesis. The grey dashed line indicates initial Ba^{2+} ion concentration (S = 10). The red dashed line corresponds to the solubility, C_e, of barite at 25 °C.[121]

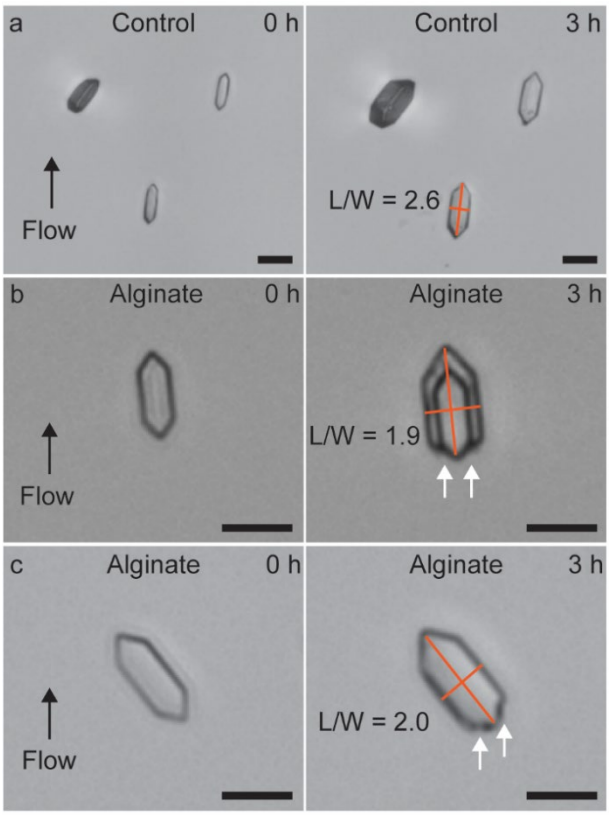

Figure A35. Time-resolved optical micrographs of seed crystals exposed to flow (12 mL h^{-1}) of supersaturated growth solutions (S = 7) in: (a) the absence of alginate, (b) the presence of 0.03 μg mL^{-1} alginate, and (c) 0.1 μg mL^{-1} alginate.

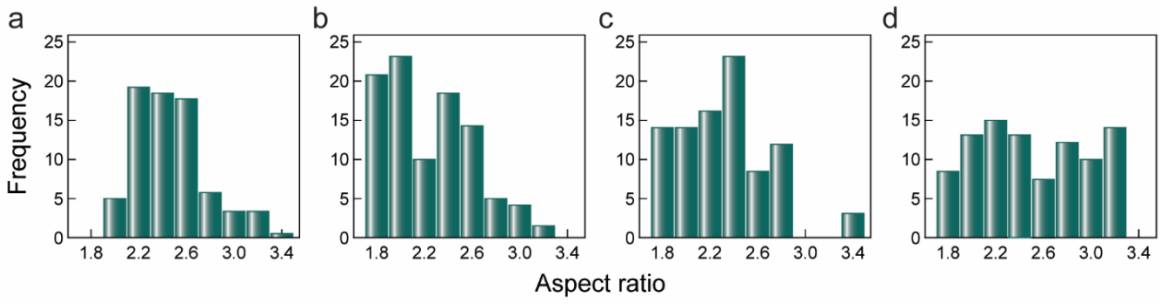

Figure A36. Aspect ratio measurements for crystals grown in microchannels under flow (12 mL h^{-1}) of supersaturated solutions (S = 7) containing Ba^{2+} and SO_4^{2-} ions and alginate concentrations of (a) 0 (b) 0.03 (c) 0.05, and (d) 1.0 μg mL^{-1} at pH 7.

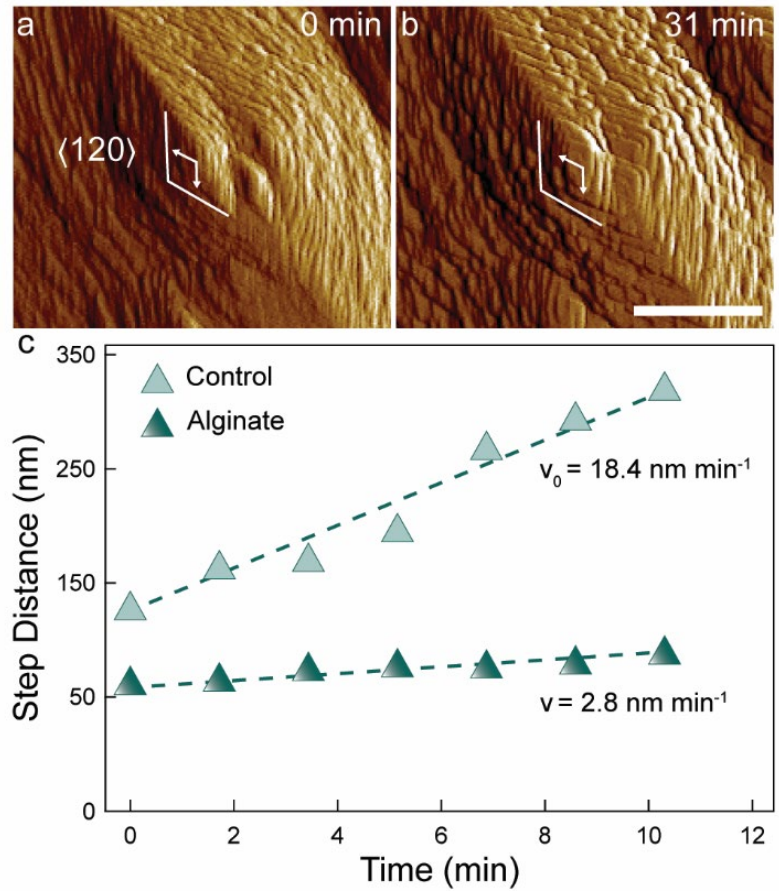

Figure A37. (a) - (b) In situ atomic force microscopy images (S = 4.4) in the presence of 1 μg mL^{-1} alginate. Scale bar equals 500 nm. (c) Measurements of single step advancement in the absence and presence of 1 μg mL^{-1} alginate.

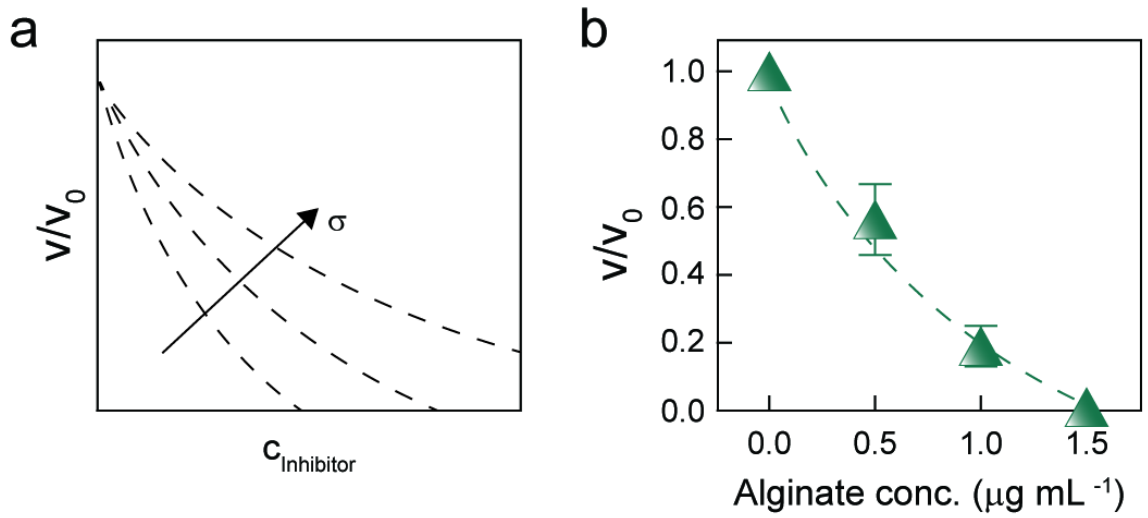

Figure A38. (a) Theoretical Cabrera-Vermilyea (CV) curves[32, 244] for inhibitors that follow a step-pinning mode of action. (b) Step velocity in the ⟨120⟩ direction for growth solutions containing alginate relative to those without any additive (control) as a function of increasing concentration.

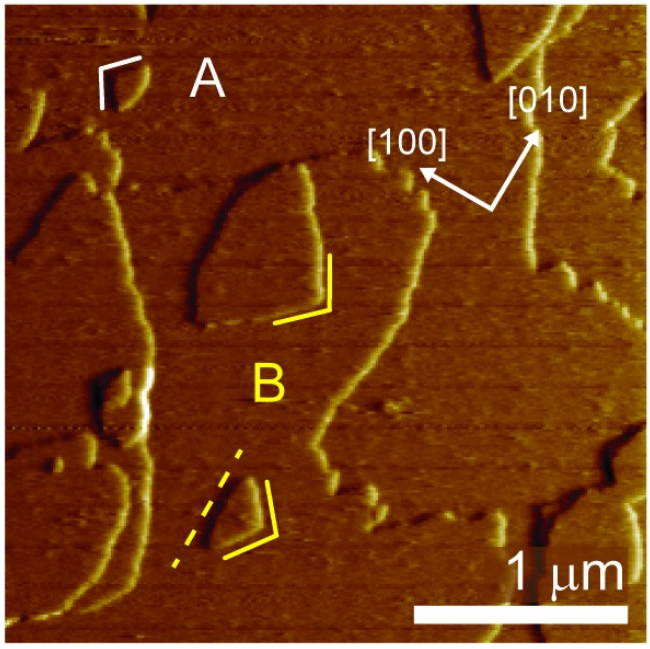

Figure A39. *In situ* atomic force microscopy deflection mode image extracted from Movie S3 showing the birth and spread of 2D nuclei on the (001) barite surface.

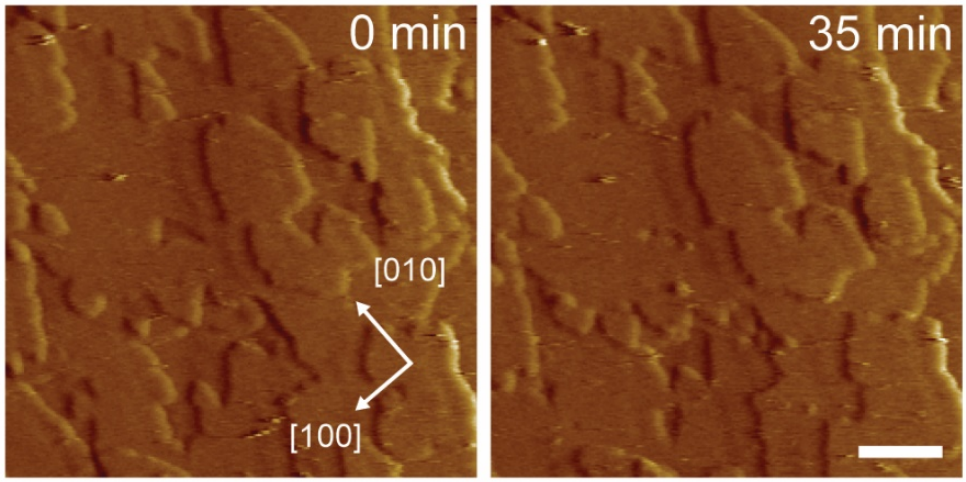

Figure A40. Time-resolved *in situ* atomic force microscopy images showing the suppression of step advancement of 2D layers on a (001) barite surface under flow of a growth solution (S = 5.3) containing Ba^{2+}, SO_4^{2-}, and 1 μg mL^{-1} alginate. Scale bar equals 500 nm.

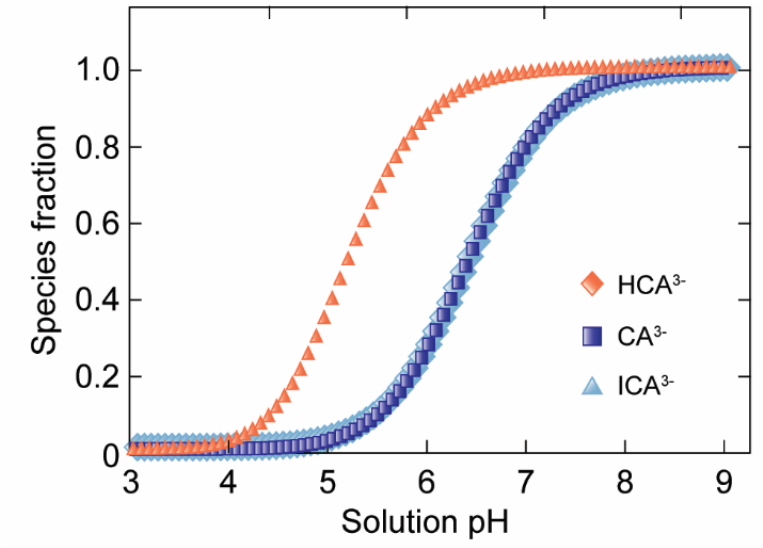

Figure A41. Speciation model for modifiers CA^{3-}, ICA^{3-}, and HCA^{3-} corresponding to fully dissociated carboxylic acids as a function of increasing solution pH. Data were produced with the software package HySS2009.[265]

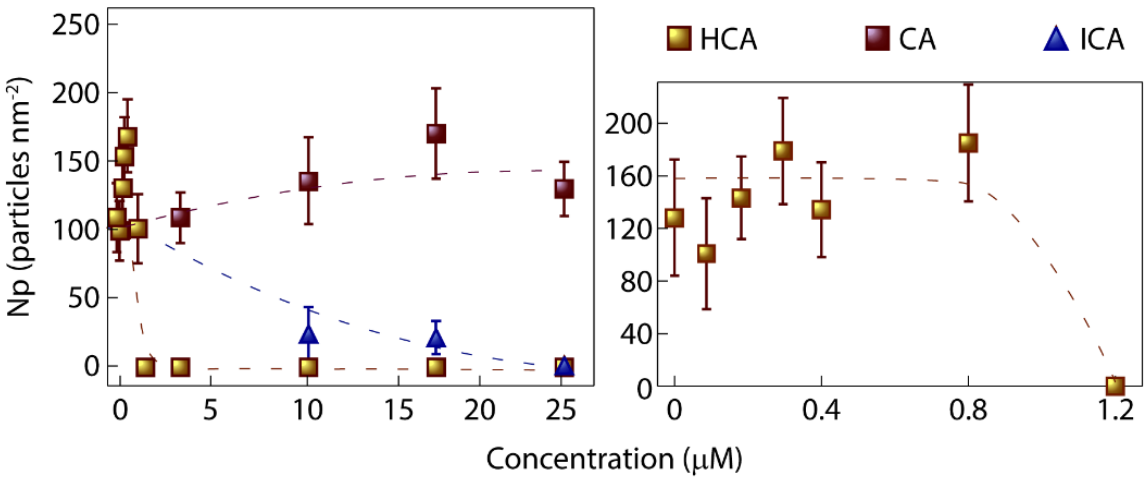

Figure A42. (left) Barite crystal number density obtained from bulk crystallization assays at 21.0 ± 0.5 °C in the presence of hydroxycitrate (HCA), isocitrate (ICA), and citrate (CA). (right) Enlarged region showing the effect of HCA at low modifier concentration.

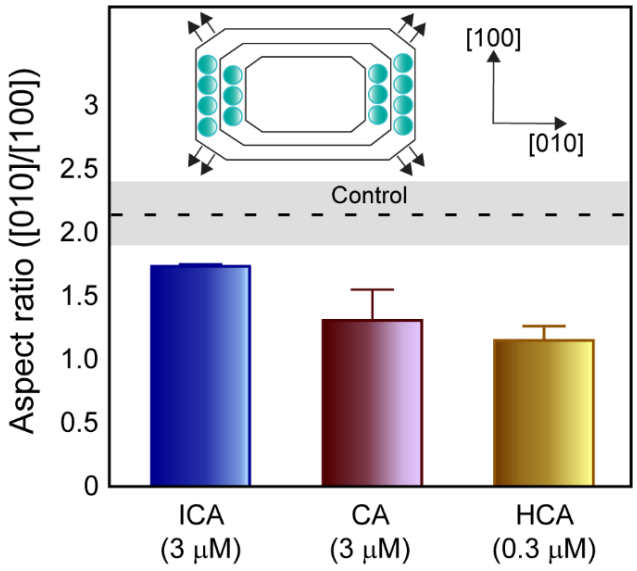

Figure A43. Length to width aspect ratio of barite crystals synthesized in the in presence and absence of 3 μM CA, ICA, and 0.3 μM HCA. Error bars equal one standard deviation.

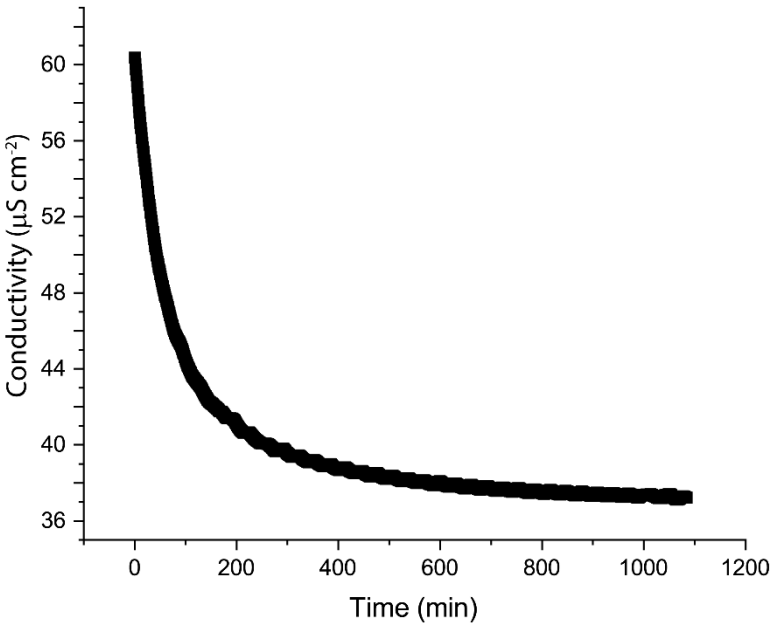

Figure A44. Temporal decrease in solution ionic conductivity during barite crystallization. Experiments were performed at room temperature 20 ± 1 °C under continuous stirring (300 rpm).

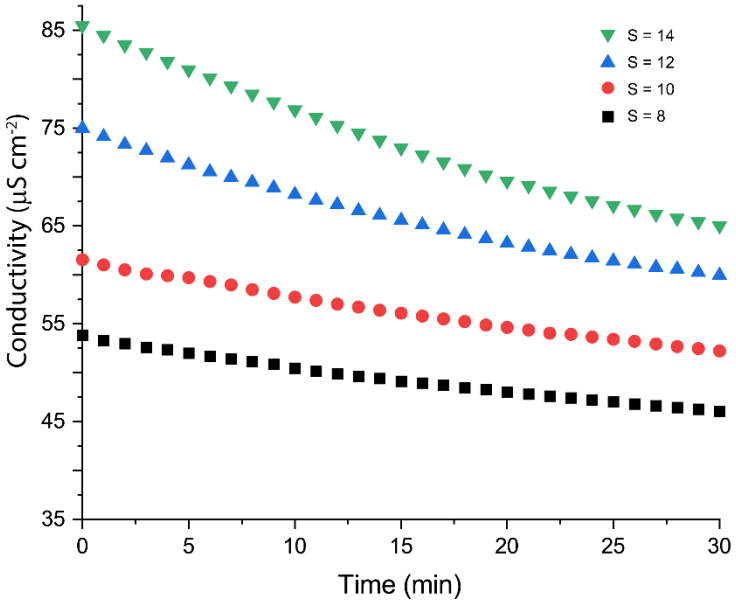

Figure A45. Temporal decrease in solution conductivity during barite crystallization at varying supersaturation performed at 20 ± 1 °C under continuous stirring (300 rpm).

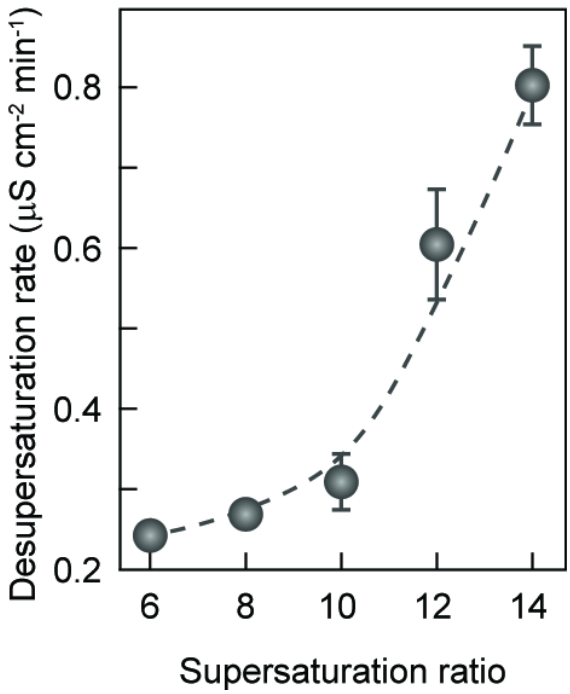

Figure A46. Desupersaturation rate as a function of supersaturation ratio measured from temporal changes in ionic conductivity during bulk crystallization assays.

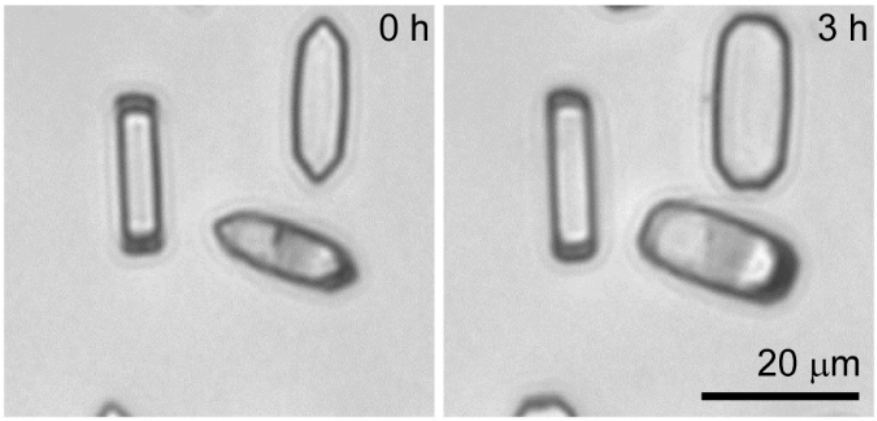

Figure A47. Brightfield optical micrographs of barite crystals growing in a microfluidic channel under flow (12 ml h^{-1}) of supersaturated growth solution (S = 7) containing 0.5 μM HCA.

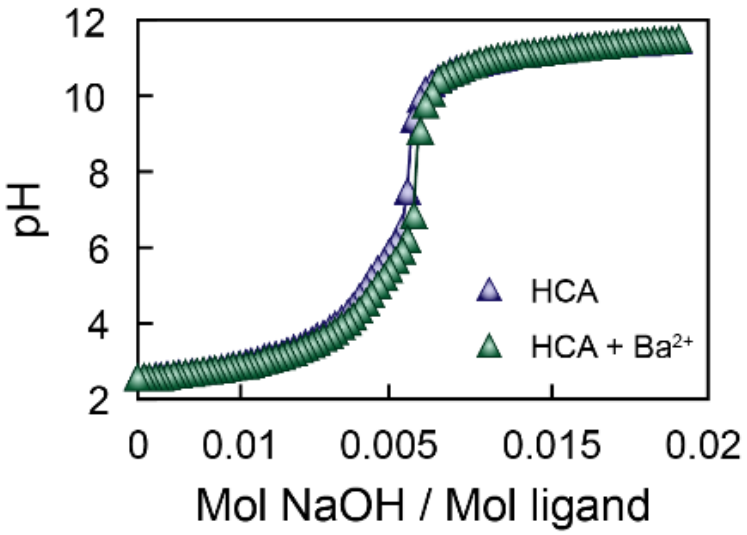

Figure A48. Titration of 1 mM HCA with the addition of 0.1 M NaOH in 25 µL incremements in the absence (grey triangles) and presence (green triangles) of 1 mM Ba^{2+}.

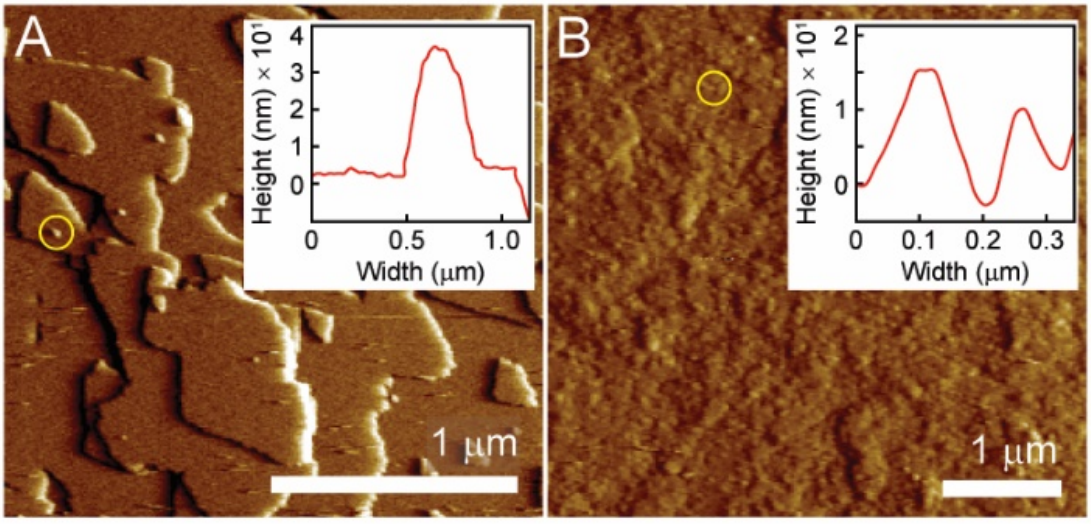

Figure A49. Representative images from *in situ* AFM measurements taken in contact mode displaying (A) 2D islands and (B) disordered protrusions. Insets: corresponding height profiles of the regions highlighted by yellow circles.

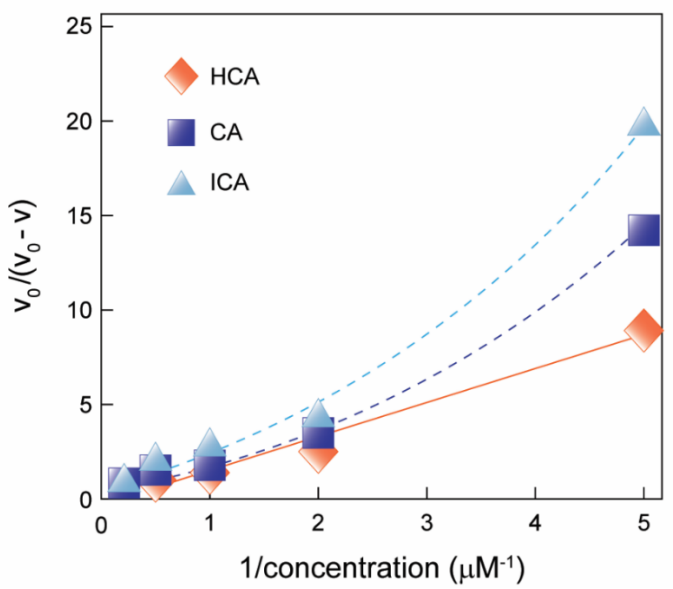

Figure A50. Scaling relationship between step velocity and inverse modifier concentration in accordance with previous literature.[15, 270]

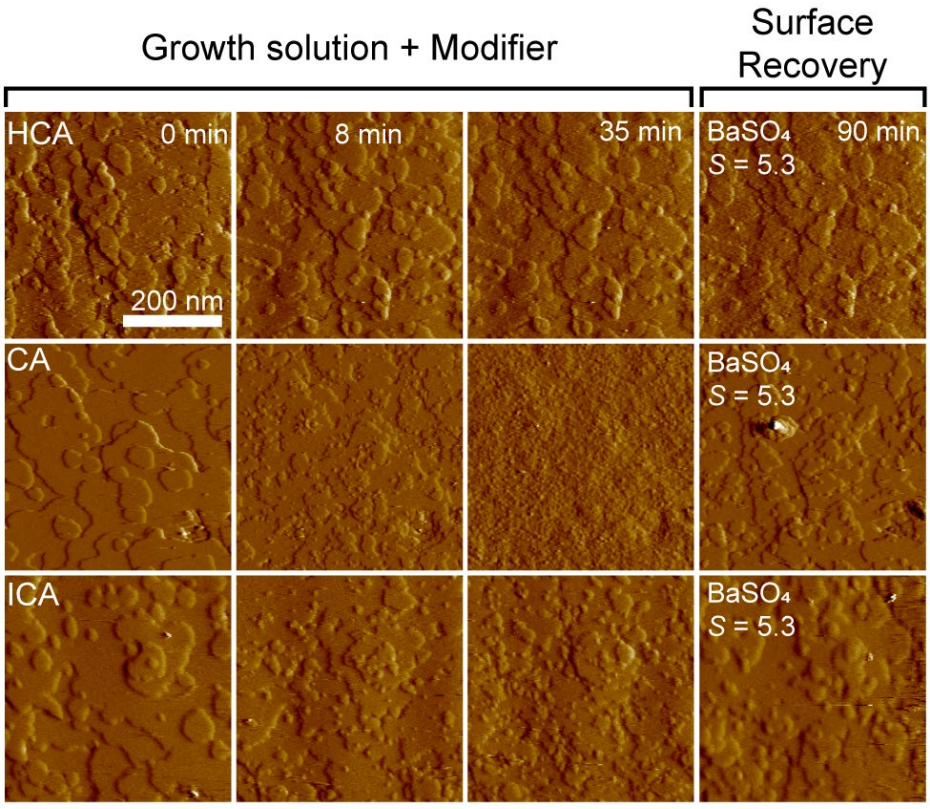

Figure A51. Time-elapsed AFM images of barite growth suppression in the presence of 5 μM HCA, CA, and ICA. The far right column shows surfaces after 55 min of surface growth recovery in supersaturated solutions (S = 5.3) without additives.

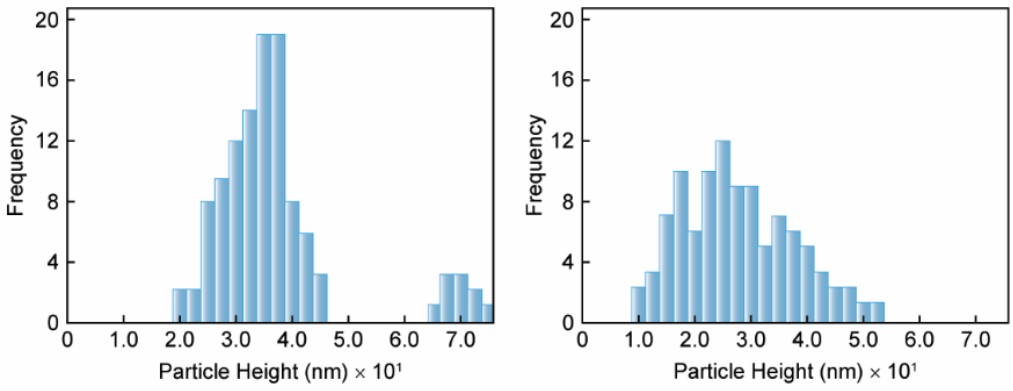

Figure A52. Height distribution for surface features in the presence of ICA at (left) 2 μM and (right) 5 μM. Measurements were obtained from multiple features during a single *in situ* AFM experiment.

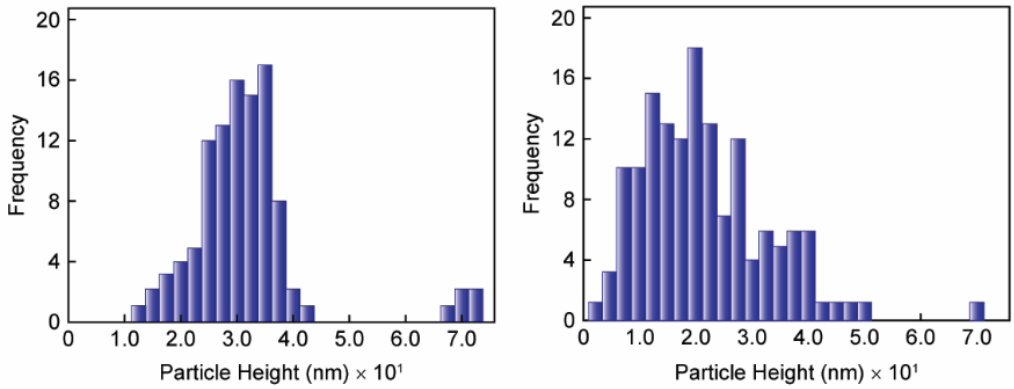

Figure A53. Height distribution for new growth features in the presence of CA at (left) 2 μM and (right) 5 μM. Measurements were obtained from multiple features during a single *in situ* AFM experiment.

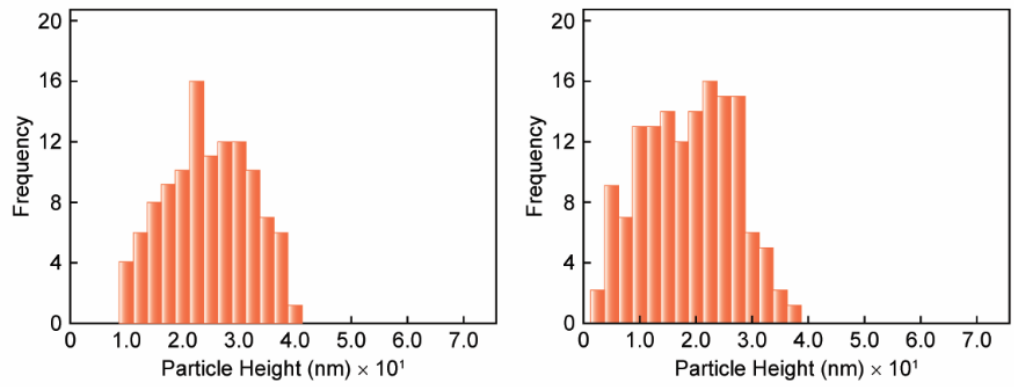

Figure A54. Height distribution for new growth features in the presence of HCA at (left) 2 μM and (right) 5 μM. Measurements were obtained from multiple features during a single *in situ* AFM experiment.

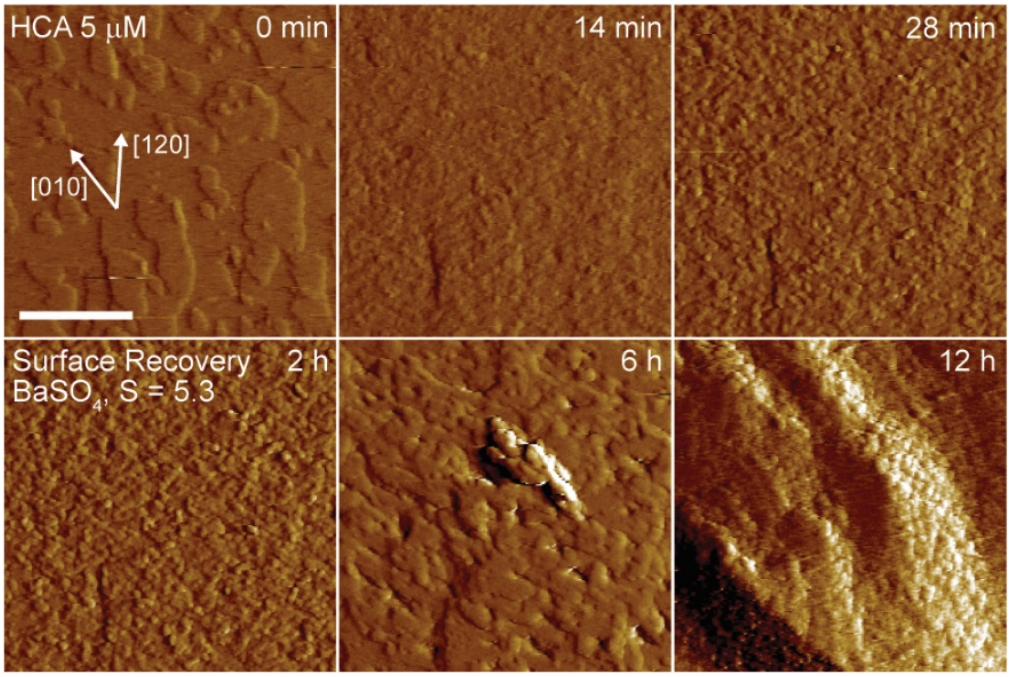

Figure A55. Time-elapsed *in situ* AFM images of (001) barite surface growth inhibition (top) in the presence of 5 μM HCA, followed by surface recovery (bottom) using supersaturated growth solution (S = 5.3) containing only Ba^{2+} and SO_4^{2-} ions. Scale bar equals 1 μm.

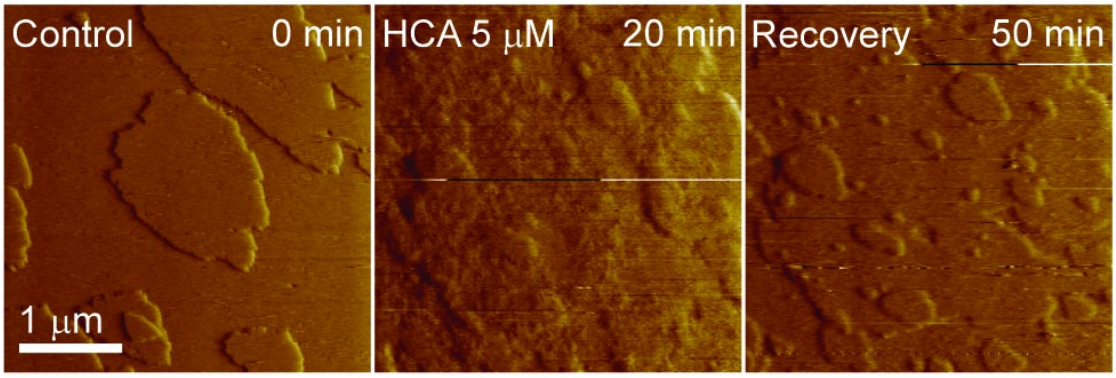

Figure A56. Time elapsed in situ AFM images of (001) barite surface growth inhibition in the presence of 5 mM HCA, followed by surface recovery using supersaturated growth solution (S = 6.5)

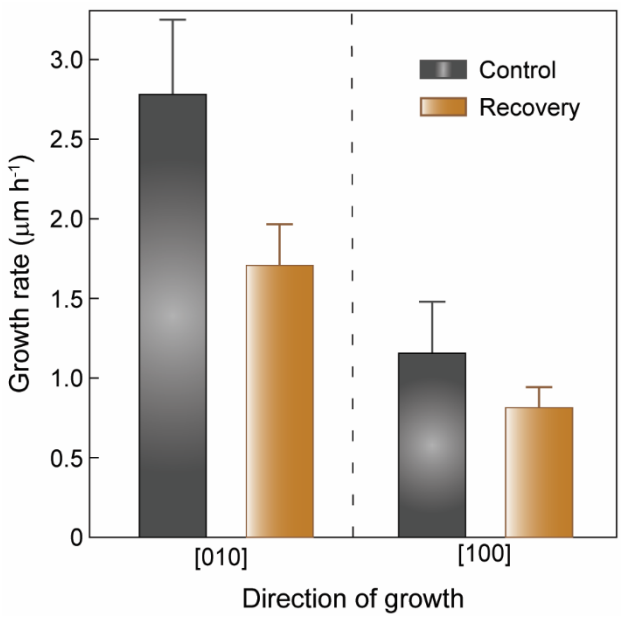

Figure A57. Growth rate of untreated barite crystals and crystals treated with 2 μM HCA in the [010] and [100] crystallographic directions under flow (12 ml h^{-1}) of supersaturated (S = 7) barium sulfate solution. Data are the average of at least 100 crystals from a single experiment.

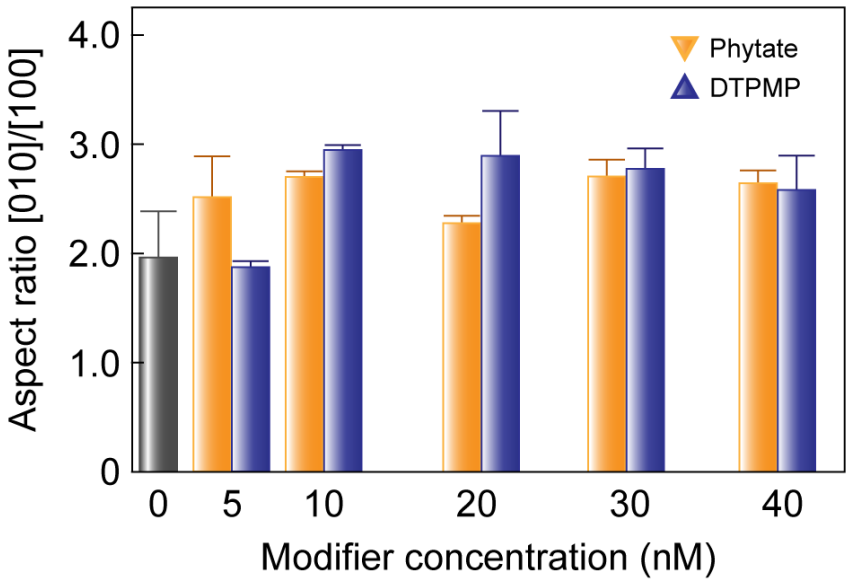

Figure A58. Length to width aspect ratio measurements for barite crystals grown in 24-h bulk assays in supersaturated growth media (S = 10) at room temperature in the presence and absence (gray bar) of inhibitors. Error bar equals one standard deviation.

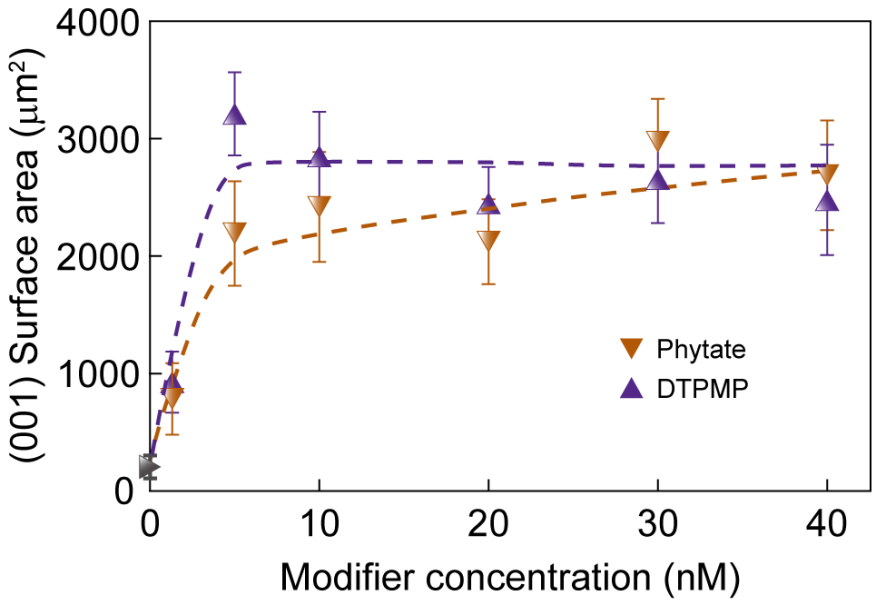

Figure A59. Barite (001) basal surface area measurements of crystals synthesized in quiescent bulk crystallization assays after 24 h using a supersaturated growth solution (S = 10) containing either phytate (orange symbols) or DTPMP (purple symbols) at various concentrations.

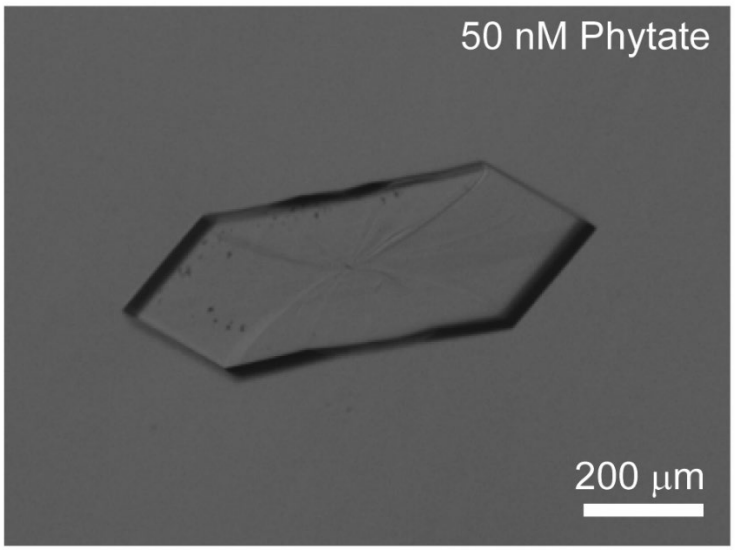

Figure A60. Representative optical micrograph of a barite crystal after a 14 day synthesis at room temperature in supersaturated growth solution (S = 10) containing 50 nM phytate.

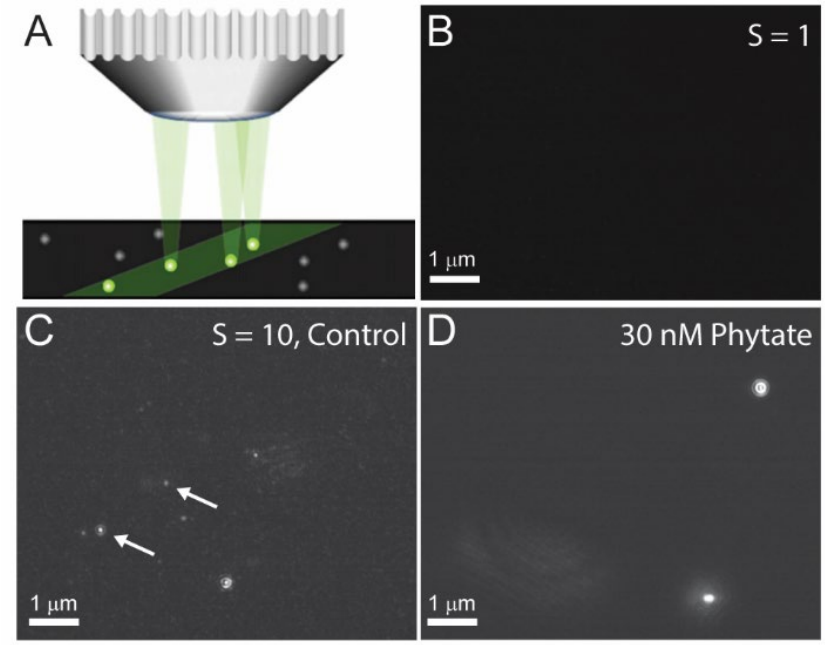

Figure A61. (A) Schematic of the oblique illumination microscopy (OIM) setup.[289] (B) Image of the thin film chamber filled with a saturated barium sulfate solution. (C) Snapshot of a supersaturated barite solution (S = 10). (D) Introduction of 30 nM phytate into the growth solution.

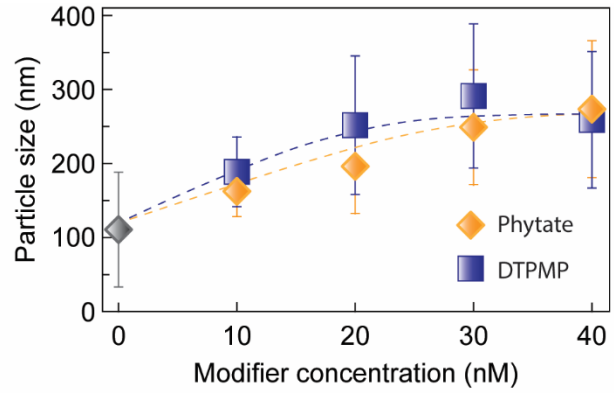

Figure A62. Barium sulfate particle size measured by OIM. Symbols are the average measurements of a minimum of 50 particles (single experiment) for modifier concentrations ≤ 20 nM.

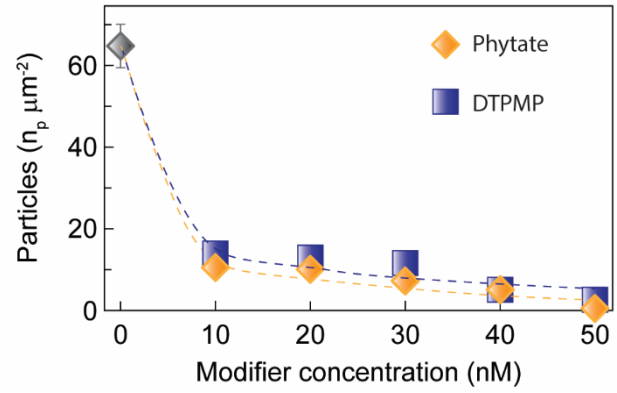

Figure A63. Particle number density of solutions assess using OIM. Symbols are the average of three individual experiments. Dashed lines are interpolated to guide the eye. Error bar spans two standard deviations and those not shown are smaller than the symbol size.

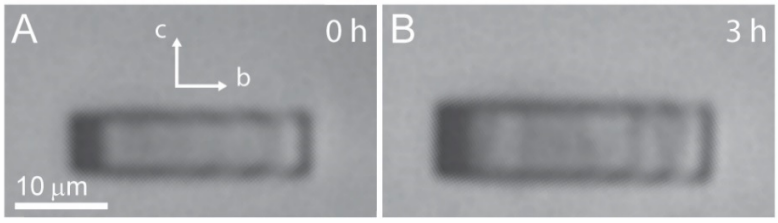

Figure A64. Brightfield optical micrographs of barite crystals in the a-orientation (A) before and (B) after exposure to a supersaturated growth solution (S = 7) containing 50 nM PA.